Design, Modeling, and Optimization of Flexible Hydrogen-based Power-to-X Processes

Entwurf, Modellierung und Optimierung von flexible wasserstoffbasierten Power-to-X Prozessen

Von der Fakultät für Maschinenwesen der Rheinisch-Westfälischen Technischen Hochschule Aachen zur Erlangung des akademischen Grades eines Doktors der Ingenieurwissenschaften genehmigte Dissertation

vorgelegt von

Simone Mucci

Berichter: Universitätsprofessor Alexander Mitsos, Ph.D.
Assistant Professor Dr.-Ing. Dominik Bongartz

Tag der mündlichen Prüfung: 8. Mai 2026

Diese Dissertation ist auf den Internetseiten der Universitätsbibliothek online verfügbar.

Titel: Design, Modeling, and Optimization of Flexible Hydrogen-based Power-to-X Processes

Autor: Simone Mucci

Reihe: Aachener Verfahrenstechnik Series
AVT.SVT - Process Systems Engineering
Band 45 (2026)

Herausgeber: Aachener Verfahrenstechnik
Forckenbeckstraße 51
52074 Aachen
Tel.: +49 (0)241 80 97717
Fax.: +49 (0)241 80 92326
E-Mail: secretary.svt@avt.rwth-aachen.de
https://www.avt.rwth-aachen.de

Volltext verfügbar: 10.18154/RWTH-2026-05188

This dissertation is submitted in partial fulfillment of the requirements for a jointly conferred doctoral degree with the doctoral titles of

Doktor der Ingenieurwissenschaften (Dr.-Ing.)
from the Faculty of Mechanical Engineering at RWTH Aachen University
and

Doctor of Engineering Science (Ph.D.): Chemical Engineering
from the Faculty of Engineering Science at KU Leuven.

Dedicata ai miei genitori

Preface

This dissertation results from the research I conducted during my time at the Chair of Process Systems Engineering (AVT.SVT) at RWTH Aachen University and at the Division of Chemical and Biochemical Reactor Engineering and Safety (CREaS) at KU Leuven. These years have been the most intense, formative, and rewarding that I have spent so far, and I am very grateful for this experience. This journey would not have been as exciting and enriching without the people I luckily had around me.

First, I would like to sincerely thank my Doktorväter, Professors Alexander Mitsos and Dominik Bongartz. Professor Mitsos offered me the life-changing opportunity to pursue a Ph.D. in his lab. His great mentorship and example of good practices and efficiency let me grow as a researcher and a person. Further, I am grateful that Professor Bongartz continued advising me after being appointed at KU Leuven. Without his curiosity, competence, and guidance, this would not have been possible.

Further, I would like to thank Professors Andreas Peschel, Erik Delarue, and Grégoire Léonard for their constructive feedback on this work, and my Vorsitzender, Professors Lucie Vandewalle and Stefan Pischinger, for their moderation at my doctoral defenses.

I would then like to thank all my colleagues at SVT. In particular, I would like to thank the SVT secretary team, Petra Eissa and Wanda Frohn, the bookkeeping and IT teams, and the Erasmus and CAPD teaching teams. Further, I thank my coauthors and the students I supervised, especially Dominik P. Goldstein, Elvis J. Sim, and Oliver Stollenwerk.

I would also like to make some special thanks. First, the GAEnG folk, i.e., Katharina M. Ebeling, Georgianna Prokopou, Jan F. Pyschik (aka jfp), Michael J. Rix, and J. Raphael Seidenberg. We spent a lot of great time together in the office with engaging discussions and outside it - All our events with and without GAEnG students, dinners, sports classes, mud runs, and trips created some amazing and lasting memories. I would also like to thank the Hochkultur guys, especially Sebastian Henzler, Jan Pavšek, jfp, and Tai Xuan Tan, for the nice cultural events we attended together.

Further, special thanks to my friends Raphael and Georgianna, as I could not have wished for better office mates, and to jfp for being a great friend and project partner within the H2Giga project DERIEL. I also sincerely thank Chrysanthi Papadimitriou for always being so positive and supportive, and for the great time we spent together; Tanuj Karia for the memorable time and excursions when visiting AVT.SVT and during conferences; Katharina, Marc-Daniel Stumm, Anna Taka, and Clara Witte for the enjoyable hat-crafting sessions; and Anita L. Ziegler, Marian Panofen, Philipp Ackermann, and Dr. Jörn Viell for the nice and insightful talks and collaborations.

I would then like to thank my colleagues at CREaS, who made me feel welcome during my research stays in Leuven. Special thanks to Aldwin L. G. Cara, Hongzhen Zhang, Zander Op De Beeck, Kenneth Simoens, Roel Leenhouts, Michiel Busschaert, and Kenzie De Smet for the nice time we spent together within and outside the office.

Finally, I want to deeply thank my family, especially my parents, Veronica and Carlo. Without their continuous support and love, I would not be the person I am today, and all this would not have been possible. I also thank my friends, Lisa di Chiara, Mirco di Chiara, Luca Donati, and Manuel Bercigli, for their support and the nice time in Italy.

Aachen, May 2026 *Simone Mucci*

Contents

Acronyms XIII

Summary XV

Kurzfassung XVII

Samenvatting XIX

Publications and Copyrights XXI

1. Introduction and Overview 1

2. Integrated and Flexible Power-to-X Processes - A Literature Review 5
- 2.1. Introduction . . . 6
- 2.2. Hydrogen supply . . . 9
  - 2.2.1. Water electrolysis: Technology overview . . . 9
  - 2.2.2. PEM water electrolyzers: Insight into the technology . . . 11
  - 2.2.3. Flexible operation of PEM water electrolyzers . . . 13
- 2.3. Carbon dioxide supply . . . 14
  - 2.3.1. Carbon dioxide sources . . . 15
  - 2.3.2. Carbon capture technologies . . . 15
  - 2.3.3. Flexible operation of carbon capture units . . . 17
- 2.4. Hydrogen-to-X . . . 18
  - 2.4.1. Methane . . . 19
  - 2.4.2. Methanol . . . 23
  - 2.4.3. Syngas . . . 26
- 2.5. System perspective: Process integration and flexibility . . . 30
  - 2.5.1. Process integration in Power-to-X processes . . . 30
  - 2.5.2. Flexibility of Power-to-X processes . . . 34
- 2.6. Conclusion . . . 35

3. Biomass Integration in Power-to-X Processes: Combustion vs. Gasification 39
- 3.1. Introduction . . . 40
- 3.2. Power- and Biomass-to-X process description . . . 41
- 3.3. Power- and Biomass-to-X process model . . . 43
  - 3.3.1. Biomass conversion unit . . . 43
  - 3.3.2. Electrolysis unit . . . 46
  - 3.3.3. Synthesis unit . . . 47
  - 3.3.4. Power cycle unit . . . 48
- 3.4. Power- and Biomass-to-Kerosene case study . . . 48
  - 3.4.1. Process description . . . 49

3.4.2. Process model . . . 51
3.5. Exergy analysis . . . 57
3.6. Results and discussion . . . 58
3.6.1. Power- and Biomass-to-X: Back-of-the-envelope analysis . . . 58
3.6.2. Power- and Biomass-to-X: Sensitivity analyses . . . 61
3.6.3. Practical considerations . . . 63
3.6.4. Power- and Biomass-to-Methanol: Validation with detailed models . 66
3.6.5. Power- and Biomass-to-Kerosene case study . . . 68
3.7. Conclusion . . . 74

4. Optimization of Power-to-Methanol Processes with Intermediate Storage 77
4.1. Introduction . . . 78
4.2. Process description . . . 80
4.2.1. Battery . . . 80
4.2.2. PEM water electrolyzer . . . 80
4.2.3. Hydrogen compression unit . . . 80
4.2.4. Hydrogen storage . . . 81
4.2.5. Methanol synthesis plant . . . 81
4.3. Process model . . . 81
4.3.1. Battery . . . 82
4.3.2. PEM water electrolyzer . . . 82
4.3.3. Hydrogen compression unit . . . 83
4.3.4. Hydrogen storage . . . 84
4.3.5. Methanol synthesis plant . . . 84
4.4. Case studies . . . 85
4.5. Optimization . . . 89
4.5.1. Optimization variables . . . 90
4.5.2. Operation constraints . . . 91
4.6. Results and discussion . . . 93
4.6.1. Grid-connected Power-to-Methanol case study . . . 93
4.6.2. Stand-alone Power-to-Methanol case study . . . 100
4.6.3. Discussion . . . 101
4.7. Conclusion . . . 105

5. Stochastic Optimization of Power-to-Methanol Processes with Intermediate Storage 107
5.1. Introduction . . . 108
5.2. Production cost sensitivity to optimal process design vs. scheduling . . . 109
5.2.1. Methodology . . . 110
5.2.2. Process description and model . . . 112
5.2.3. Case studies . . . 112
5.2.4. Results and discussion . . . 116
5.3. Numerical complexity reduction approaches . . . 122
5.3.1. Literature background . . . 122
5.3.2. Methodology . . . 124
5.3.3. Case study . . . 128
5.3.4. Results and discussion . . . 128

5.4. Conclusion . . . 139

6. Conclusion and Outlook **141**

Declaration of use of generative AI and AI-assisted technologies **147**

A. Additional Information to Chapter 3 **149**
A.1. Molar balances . . . 149
A.2. Energy balances . . . 150
A.3. Modeling assumption overview . . . 151
A.4. Exergy analysis . . . 152
A.4.1. Exergy related to heat flows . . . 152
A.4.2. Molar physical exergy . . . 153
A.4.3. Molar chemical exergy . . . 153
A.5. Additional results of the back-of-the-envelope analysis . . . 154
A.5.1. Energy analysis . . . 154
A.5.2. Exergy analysis . . . 156
A.6. Additional results of the sensitivity analyses . . . 158
A.6.1. Electrolyzer efficiency . . . 158
A.6.2. Power cycle efficiency . . . 158
A.6.3. Carbon feedstock composition . . . 159
A.7. Detailed model of the Power- and Biomass-to-Methanol processes . . . 163
A.7.1. Combustion-based Power- and Biomass-to-Methanol process . . . 163
A.7.2. Gasification-based Power- and Biomass-to-Methanol process . . . 165
A.7.3. Techno-economic analysis assumptions . . . 167
A.8. Detailed model of the Power- and Biomass-to-Kerosene processes . . . 168
A.8.1. RWGS unit . . . 168
A.8.2. Fischer-Tropsch unit . . . 169
A.8.3. Olefin oligomerization unit . . . 170
A.8.4. Techno-economic analysis assumptions . . . 171

B. Additional Information to Chapter 4 **173**
B.1. Power-to-Methanol process model . . . 173
B.1.1. Battery . . . 173
B.1.2. PEM water electrolyzer . . . 175
B.1.3. Hydrogen compression unit . . . 176
B.1.4. Hydrogen storage . . . 177
B.1.5. Methanol synthesis plant . . . 178
B.1.6. Cost models . . . 179
B.2. Hydrogen storage cost . . . 183
B.3. Methanol synthesis plant . . . 183
B.4. Methanol synthesis plant cost . . . 184
B.5. Scenarios . . . 186
B.6. Optimization results . . . 187
B.6.1. Grid-connected Power-to-Methanol case study . . . 187
B.6.2. Stand-alone Power-to-Methanol case study . . . 193

C. Additional Information to Chapter 5 **199**
C.1. Power-to-Methanol process with intermediate storage: Cost estimation . . 199
C.2. Additional results 200
C.2.1. Optimal design vs. scheduling: Design variables 200
C.2.2. Additional data analysis 201
C.3. Considered scenario clustering approaches 204
C.4. Reformulation of the optimization problem with DoF reduction 205
C.5. Process model for objective function under-estimation 207
C.6. Weekly scenarios: Effect of clustering approaches and number of scenario clusters 208

Bibliography **211**

Acronyms

AEM-WE	Anion Exchange Membrane Water Electrolyzer
ASF	Anderson-Schulz-Flory
A-WE	Alkaline Water Electrolyzer
AVT.SVT	Chair of Process Systems Engineering
BARON	Branch-And-Reduce Optimization Navigator
BtX	Biomass-to-X
CAMERE	Carbon dioxide hydrogenation to form Methanol via a Reverse-water-gas-shift reaction
CAPEX	Capital Expenditures
CC	Carbon Capture
CDS	Combined Design and Scheduling
CEPCI	Chemical Engineering Plant Cost Index
CREaS	Department of Chemical Engineering, Division of Chemical and Biochemical Reactor Engineering and Safety
DAC	Direct Air Capture
DME	Dimethyl Ether
DoF	Degrees of Freedom
DSM	Demand-Side Management
FT	Fischer-Tropsch
GAMS	General Algebraic Modeling System
GHG	Greenhouse Gases
IEA	International Energy Agency
LCOM	Levelized Cost Of Methanol
LHHW	Langmuir-Hinshelwood-Hougen-Watson
LHS	Latin Hypercube Sampling
LHV	Lower Heating Value
MEA	Monoethanolamine
MINLP	Mixed-Integer NonLinear Programming
MtO	Methanol-to-Olefins
OPEX	Operating Expenditures

ORC	Organic Rankine Cycle
PBtK	Power- and Biomass-to-Kerosene
PBtL	Power- and Biomass-to-Liquid
PBtMeOH	Power- and Biomass-to-Methanol
PBtX	Power- and Biomass-to-X
PCA	Principal Component Analysis
PEM	Polymer Electrolyte Membrane
PEM-WE	PEM Water Electrolyzer
PSA	Pressure Swing Adsorption
PtK	Power-to-Kerosene
PtL	Power-to-Liquid
PtMeOH	Power-to-Methanol
PtX	Power-to-X
PV	Photovoltaic
RWGS	Reverse Water Gas Shift
RWGS-CL	RWGS in Chemical Looping
SAF	Sustainable Aviation Fuel
S-CDS	Stochastic Combined Design and Scheduling
SO-WE	Solide Oxide Water Electrolyzer
TSA	Temperature Swing Adsorption

Summary

Power-to-X (PtX) and Power- and Biomass-to-X (PBtX) processes are promising alternatives to conventional production processes of bulk chemicals and fuels, which generally rely on fossil feedstocks. These processes can utilize renewable energy sources and sustainable feedstocks such as carbon dioxide and residual biomass to synthesize electricity-based products. Nevertheless, substantial challenges must be addressed to improve their efficiency and economic viability.

This dissertation addresses some of these challenges by investigating PtX and PBtX processes that synthesize some key carbon-based chemicals and fuels using hydrogen produced via low-temperature water electrolysis. In particular, after reviewing the suitability of PtX processes for process integration and flexible operation, several ways of utilizing residual biomass in PBtX processes, as well as some key trade-offs between flexible operation and intermediate storage technologies, are investigated, all being crucial aspects for improving process efficiency and viability.

Concerning the utilization of biomass in PBtX processes, two key thermochemical processing options, i.e., combustion and gasification, are investigated and compared. With relatively simple models, the thermodynamic advantages of biomass gasification over combustion for all considered products "X" are shown. The key trends are then confirmed for a Power- and Biomass-to-Methanol process modeled in detail. Nevertheless, the use of these relatively simple models could lead to misleading conclusions for other process comparisons, e.g., of kerosene production pathways, if the models are not adequately representative.

When investigating the trade-off between flexible operation and intermediate storage, a Power-to-Methanol (PtMeOH) case study is optimized with respect to its design and scheduling, simultaneously. The optimization results show that enabling flexible operation of the entire process can reduce the methanol production cost. In contrast, the need for intermediate storage depends on the economic assumptions, as its investment cost may not be recovered through the savings in the operating costs.

This trade-off is further investigated by optimizing the PtMeOH process with intermediate storage under electricity price scenario uncertainty. While enabling flexible operation of all process units consistently lowers the production cost for given process designs, no clear pattern emerges concerning the need for intermediate storage: different process designs with and without storage can result in similar production costs when flexible operation of all process units is enabled and scheduling is optimized. Still, both process design and scheduling should be optimized simultaneously. As these optimization problems often suffer from numerical intractability, a complexity reduction approach based on feature-based scenario clustering and degrees of freedom reduction is investigated.

This dissertation advances the understanding of hydrogen-based PtX and PBtX processes and highlights some key efficiency and economic drivers to improve their competitiveness against fossil-based alternatives. Also, some limitations in the applied and developed methods, specifically related to process model representativeness and computational speed-up consistency, are identified, thus indicating the need for further investigation.

Kurzfassung

Power-to-X (PtX) und Power- and Biomass-to-X (PBtX)-Prozesse sind vielversprechende Alternativen zu konventionellen Produktionsprozessen für Bulkchemikalien und Kraftstoffe, die im Allgemeinen auf fossilen Rohstoffen basieren. Diese Verfahren können erneuerbare Energiequellen und nachhaltige Rohstoffe wie Kohlendioxid und Restbiomasse zur Synthese von strombasierten Produkten nutzen. Dennoch müssen erhebliche Herausforderungen bewältigt werden, um ihre Effizienz und Wirtschaftlichkeit zu verbessern.

Diese Dissertation befasst sich mit einigen dieser Herausforderungen, indem sie die PtX- und PBtX-Prozesse untersucht, bei denen wichtige kohlenstoffbasierte Chemikalien und Kraftstoffe unter Verwendung von Wasserstoff aus Niedertemperatur-Wasserelektrolyse synthetisiert werden. Insbesondere werden nach einer Überprüfung der Eignung von PtX-Prozessen für die Prozessintegration und den flexiblen Betrieb verschiedene Möglichkeiten zur Nutzung von Restbiomasse in PBtX-Prozessen sowie einige wichtige Trade-offs zwischen flexiblem Betrieb und Zwischenspeicherung untersucht, die allesamt entscheidende Aspekte für die Prozesseffizienz und -wirtschaftlichkeit sind.

In Bezug auf die Biomassenutzung in PBtX-Prozessen werden zwei Verarbeitungsoptionen, nämlich Verbrennung und Vergasung, untersucht. Mit relativ einfachen Modellen werden die thermodynamischen Vorteile der Biomassevergasung gegenüber der Verbrennung für alle betrachteten Produkte "X" aufgezeigt. Die wichtigsten Trends werden für einen detailliert modellierten Methanolproduktionsprozess bestätigt. Dennoch könnten diese relativ einfachen Modelle zu irreführenden Schlussfolgerungen bei anderen Prozessvergleichen führen, z. B. bei der Kerosinproduktion, wenn sie nicht ausreichend repräsentativ sind.

Bei der Untersuchung des Trade-offs zwischen flexiblem Betrieb und Zwischenspeicherung wird eine Fallstudie zu Power-to-Methanol (PtMeOH) hinsichtlich Designs und Betrieb gleichzeitig optimiert. Die Ergebnisse zeigen, dass ein flexibler Betrieb des gesamten Prozesses zu einer Methanolproduktionskostensenkung führt. Der Zwischenspeicherungsbedarf hängt von den wirtschaftlichen Annahmen ab, da sich die Investitionskosten eventuell nicht durch die Betriebskosteneinsparungen amortisieren.

Dieser Trade-off wird weiter untersucht, indem der PtMeOH-Prozess unter Unsicherheit bezüglich der Realisierung des Strompreisszenarios optimiert wird. Während ein flexibler Betrieb aller Prozessanlagen die Produktionskosten senkt, ergibt sich kein klares Muster hinsichtlich der Notwendigkeit einer Zwischenspeicherung. Dennoch sollten das Prozessdesign und der -betrieb gleichzeitig optimiert werden. Da diese Optimierungsprobleme oftmals numerisch schwer zu lösen sind, wird auch ein Ansatz zur Komplexitätsreduzierung untersucht, der auf Szenario-Clustering und der Freiheitsgradereduzierung basiert.

Diese Dissertation vertieft das Verständnis der wasserstoffbasierten PtX- und PBtX-Prozesse und hebt einige wichtige Effizienz- und Wirtschaftlichkeitsfaktoren hervor, um ihre Wettbewerbsfähigkeit gegenüber fossilen Alternativen zu verbessern. Darüber hinaus werden einige Einschränkungen bei den betrachteten Methoden festgestellt, insbesondere in Bezug auf die Repräsentativität des Prozessmodells und die Konsistenz der Rechengeschwindigkeit, welche auf die Notwendigkeit weiterer Untersuchungen hinweisen.

Samenvatting

Power-to-X (PtX) en Power- and Biomass-to-X (PBtX)-processen zijn veelbelovende alternatieven voor conventionele productieprocessen voor bulkchemicaliën en brandstoffen, die in het algemeen gebaseerd zijn op fossiele grondstoffen. Deze processen kunnen namelijk van hernieuwbare energiebronnen en duurzame grondstoffen zoals kooldioxide en biomassa gebruik maken om op elektriciteit gebaseerde producten te synthetiseren. Er moeten echter nog aanzienlijke uitdagingen worden aangepakt om hun efficiëntie en economische haalbaarheid te verbeteren.

Deze doctoraatsthesis behandelt enkele van deze uitdagingen door onderzoek te doen naar PtX- en PBtX-processen die bepaalde belangrijke koolstofgebaseerde chemicaliën en brandstoffen synthetiseren met behulp van waterstof uit waterelektrolyse bij lage temperaturen. Na een evaluatie van het geschiktheid van PtX-processen voor procesintegratie en flexibele werking werden verschillende mogelijkheden om restbiomassa te gebruiken in PBtX-processen onderzocht, evenals enkele trade-offs tussen flexibele werking en tussentijdse opslag, die allemaal cruciale aspecten zijn voor efficiëntie en haalbaarheid.

Met betrekking tot het gebruik van biomassa in PBtX-processen werden twee verwerkingsopties onderzocht, namelijk verbranding en vergassing. Met relatief eenvoudige modellen werden de thermodynamische voordelen van biomassavergassing ten opzichte van verbranding voor alle onderzochte producten “X” aangetoond. De belangrijkste trends worden vervolgens bevestigd voor een gedetailleerd model van een methanolproductieproces. Niettemin kunnen deze relatief eenvoudige modellen tot misleidende conclusies leiden voor andered procesvergelijkingen, bijvoorbeeld voor de productie van kerosine, als ze niet voldoende representatief zijn.

Bij het onderzoek naar de trade-off tussen flexibele werking en tussentijdse opslag wordt een casestudy over Power-to-Methanol (PtMeOH) met betrekking tot het ontwerp en de werking gelijktijdig geoptimaliseerd. Hoewel een flexibele werking van het hele proces de productiekosten van methanol kan verlagen, hangt de noodzaak van tussentijdse opslag af van de economische factoren, aangezien de investeringskosten mogelijk niet worden terugverdiend door de besparingen op de exploitatiekosten.

Deze trade-off wordt verder onderzocht door het PtMeOH-proces te optimaliseren onder onzekerheid over het elektriciteitsprijsscenario. Hoewel de proceseenheden flexibel te laten werken de productiekosten consistent verlaagt, verschijnt er geen duidelijk patroon met betrekking tot de noodzaak van tussentijdse opslag. Toch moeten het procesontwerp en de procesvoering tegelijkertijd worden geoptimaliseerd. Aangezien deze optimalisatieproblemen vaak numeriek onoplosbaar zijn, onderzoeken we een benadering voor complexiteitsvermindering op basis van scenarioclustering en vermindering van de vrijheidsgraden.

Deze doctoraatsthesis verdiept het inzicht in op waterstof gebaseerde PtX- en PBtX-processen en belicht enkele belangrijke efficiëntie- en economische factoren om hun competitiviteit ten opzichte van fossiele alternatieven te verbeteren. Verder werden enkele beperkingen bij de onderzochte methoden geconstateerd, met name wat betreft de consistentie van de rekensnelheid, die wijzen op de noodzaak van verder onderzoek.

Publications and Copyrights

This dissertation is based on the research conducted by the author during his time at the Chair of Process Systems Engineering (AVT.SVT) at RWTH Aachen University between April 2021 and October 2025 and at the Department of Chemical Engineering, Division of Chemical and Biochemical Reactor Engineering and Safety (CREaS) at KU Leuven between November 2023 and October 2025. Some parts of this work have been previously published or submitted for publication, and the relevant material is incorporated into the chapters with permission, as outlined below. A detailed description of the contributions made by all authors is also provided.

- The introduction (Chapter 1) and Chapter 2 are mainly based on **S. Mucci**, A. Mitsos, and D. Bongartz. Power-to-X Processes based on PEM Water Electrolyzers: A Review of Process Integration and Flexible Operation. *Computers & Chemical Engineering*, 175:108260, 2023 [1]. Published by Elsevier Ltd. Copyright © 2023 The Authors.
  Reprinted (adapted) under the Creative Commons Attribution 4.0 International License (CC BY 4.0).
  Only parts of this publication are incorporated in this dissertation.

  Author contributions: *S. Mucci*: Conceptualization, Investigation, Visualization, Writing – original draft. *A. Mitsos*: Conceptualization, Funding acquisition, Writing – review & editing. *D. Bongartz*: Conceptualization, Funding acquisition, Supervision, Project administration, Writing – review & editing.

- Sections 3.1-3.3 and 3.5-3.7 in Chapter 3 and Appendix A are mainly based on **S. Mucci**, A. Mitsos, and D. Bongartz. Combustion versus Gasification in Power- and Biomass-to-X Processes: An Exergetic Analysis. *ACS Omega*, 9(49):48213–48231, 2024 [2]. Published by American Chemical Society. Copyright © 2024 The Authors.
  Reprinted (adapted) under the Creative Commons Attribution 4.0 International License (CC BY 4.0).

  Author contributions: *S. Mucci*: Conceptualization, Methodology, Software, Investigation, Visualization, Writing – original draft. *A. Mitsos*: Conceptualization, Methodology, Supervision, Funding acquisition, Project administration, Writing – review & editing. *D. Bongartz*: Conceptualization, Methodology, Supervision, Funding acquisition, Writing – review & editing.

- Sections 3.4, 3.6, and 3.7 in Chapter 3 include the work published in **S. Mucci**, D. P. Goldstein, D. Bongartz, and A. Mitsos. Exergo-Techno-Economic Comparison of Power & Biomass-to-Kerosene Pathways. *Computer-Aided Chemical Engineering, Proceedings of the 34th European Symposium on Computer-Aided Chemical*

Engineering / 15th International Symposium of Process Systems Engineering (ESCAPE34/PSE24), June 2-6, Florence, Italy, 53:2131–2136, 2024 [3]. Published by Elsevier. Copyright © 2024 Elsevier B.V.
Reprinted (adapted) with permission.

Author contributions: *S. Mucci*: Conceptualization, Methodology, Software, Investigation, Visualization, Writing – original draft. *D. P. Goldstein*: Conceptualization, Software, Investigation, Visualization. *A. Mitsos*: Conceptualization, Methodology, Supervision, Funding acquisition, Project administration, Writing – review & editing. *D. Bongartz*: Conceptualization, Methodology, Supervision, Funding acquisition, Writing – review & editing.

- Chapter 4 and Appendix B are mainly based on **S. Mucci**, A. Mitsos, and D. Bongartz. Cost-optimal Power-to-Methanol: Flexible Operation or Intermediate Storage? *Journal of Energy Storage*, 72:108614, 2023 [4]. Published by Elsevier Ltd. Copyright © 2023 The Authors.
  Reprinted (adapted) under the Creative Commons Attribution 4.0 International License (CC BY 4.0).

  Author contributions: *S. Mucci*: Conceptualization, Methodology, Software, Investigation, Visualization, Writing – original draft. *A. Mitsos*: Conceptualization, Methodology, Supervision, Funding acquisition, Writing – review & editing. *D. Bongartz*: Conceptualization, Methodology, Supervision, Funding acquisition, Project administration, Writing – review & editing.

- Chapter 5, primarily Sections 5.1, 5.2, and 5.4, and Appendix C are mainly based on **S. Mucci** and D. Bongartz. Stochastic Optimization of Power-to-Methanol: Production Cost Sensitivity to Process Design vs. Scheduling. *AIChE Journal*, 72(5):e70265, 2026 [5]. Published by Wiley Periodicals LLC on behalf of American Institute of Chemical Engineers. Copyright © 2026 The Authors.
  Reprinted (adapted) under the Creative Commons Attribution 4.0 International License (CC BY 4.0).

  Author contributions: *S. Mucci*: Conceptualization, Methodology, Software, Investigation, Visualization, Writing – original draft. *D. Bongartz*: Conceptualization, Methodology, Supervision, Funding acquisition, Writing – review & editing.

- Chapter 5, primarily Sections 5.2-5.4, and Appendix C are partially based on **S. Mucci** and D. Bongartz. Feature-Based Scenario Clustering and Selective Degrees of Freedom Reduction for Two-stage Stochastic Optimization of Power-to-Methanol. *Chemical Engineering Research and Design*, 223:311-330, 2025 [6]. Published by Elsevier Ltd. Copyright © 2025 The Authors.
  Reprinted (adapted) under the Creative Commons Attribution 4.0 International License (CC BY 4.0).
  Only parts of this publication are incorporated in this dissertation.

  Author contributions: *S. Mucci*: Conceptualization, Methodology, Software, Investigation, Visualization, Writing – original draft. *D. Bongartz*: Conceptualization, Methodology, Supervision, Funding acquisition, Writing – review & editing.

Additionally, during his time at AVT.SVT and CREaS, the author worked on the following articles, which are not included in this dissertation:

- S. Mucci, M.-D. Stumm, M. Rix, and A. Mitsos. Model-based Evaluation of Ammonia Energy Storage Concepts at High Technological Readiness Level. *Applied Energy*, 377:124495, 2025 [7].
- S. M. Krämer, A. S. Nielsen, S. Maier, S. Mucci, M. Hillestad, and O. S. Burheim. Power- and Biomass-to-Liquid Processes with Fuel-assisted Solid Oxide Electrolysis Cells and Water Gas Shift-adjusted Systems: A techno-economic Analysis. *Fuel*, 396:135290, 2025 [8].
- S. Mucci, J. F. Pyschik, E. J. Sim, A. Mitsos, and D. Bongartz. Combined Design and Operation Optimization of a Dynamic e-Syngas Fermentation Process. *In Preparation*, 2026 [9].

Some parts of this work have been presented by the author at the following national and international conferences: Aachen Hydrogen Colloquium (2022), Annual Conference of ProcessNet and DECHEMA-BioTechNet (2022), Fuel Science from Production to Propulsion (FSC) conference (2023), AIChE Annual Meeting (2023), European Symposium on Computer-Aided Process Engineering (2024), and H_2Giga-Abschlusskonferenz (2025). The references to the abstracts submitted to these conferences are hereby omitted.

During his time at AVT.SVT and CREaS, the author supervised or co-supervised the student theses of Christoph Mehler [10, 11], Oliver Stollenwerk [12], Boris König [13], Casper J. van Wersch [14], Jannik Bothe [15], S. Mohammad H. Rachi [16], Samuel M. Krämer [17], Margot Vander Elst [18], and Justus Danko [19].
The model developed by Oliver Stollenwerk in his bachelor's thesis [12] was extended and utilized to generate some of the results shown in Chapter 3.

Further, the author supervised the work of one student teaching assistant, i.e., Oliver Stollenwerk, and two student research assistants, i.e., Dominik P. Goldstein and Elvis J. Sim. The models developed by Dominik P. Goldstein under my supervision were then extended and utilized to generate some of the results shown in Chapter 3.

1. Introduction and Overview

Anthropogenic Greenhouse Gases (GHG) emissions are mainly responsible for global warming and climate change. Without the rapid implementation of ambitious mitigation policies, GHG emissions will lead to a global temperature rise higher than 1.5 °C compared to the period 1850-1900 by the end of the century [20].

Several economic sectors, e.g., industry and transport, heavily rely on energy-intensive processes and fossil feedstocks and energy sources, thus significantly contributing to GHG emissions (ca. 24 % and 21 % of the overall CO_2 emissions in 2022, respectively [21]). However, some of the currently produced carbon-based chemicals and fuels will likely be used even in a low-carbon society [21]. Therefore, developing more sustainable production processes is essential.

In combination with technological improvements and the optimization of existing processes, developing new processes using alternative and sustainable feedstocks and energy sources represents a promising pathway for defossilization [22]. Power-to-X (PtX) processes, where the power is obtained from renewable or low-carbon energy sources and the "X" denotes the final product (e-product), have great defossilization potential [23–25], especially thanks to the expected expansion of renewable generation capacity [21]. Moreover, several variants of "Power-to-X" can be found in literature based on the final e-product, e.g., Power-to-Heat [26, 27], Power-to-Chemicals [28–30], and Power-to-Fuels [27, 30–32], thus showing the versatility of these processes across different sectors.

Among the PtX processes, hydrogen-based PtX processes, where hydrogen is produced electrochemically by using renewable or low-carbon-footprint power and then converted into the final product "X", have recently gained increasing attention both in model-based [31–34] and experimental works (more than 100 research and development projects commissioned in Europe over the past two decades [35]). In fact, these e-products are relevant not only in the chemical and transport sectors, but also in the energy sector, where they can serve as energy carriers when stored and then converted to generate electricity [7, 27, 36, 37].

Hydrogen-based PtX processes often require a sustainable carbon source such as CO_2 captured from a point source or air [38], or biomass. In the latter case, the PtX processes are often called Power- and Biomass-to-X (PBtX) or bio-hybrid [39] processes. This transition in feedstock and energy source poses new challenges from a technological, economic, and environmental perspective. Furthermore, it offers the unique opportunity to investigate alternative production pathways and develop and design new sustainable production processes.

Further, the heavy reliance of PtX and PBtX processes on electricity, generally one of the main cost drivers in grid-connected plants, makes flexible process operation, also called Demand-Side Management (DSM) [40], particularly attractive for reducing production costs: the operating load of the process units is continuously adapted within their operating constraints, depending on time-varying electricity prices. Flexible operation can also be beneficial when the availability of raw materials or electricity is not constant over

time, as in stand-alone plants. Therefore, DSM offers the possibility to reduce the price gap between e-products and their fossil-based alternatives, especially when processes are designed considering information on how they will be operated.

In synergy with flexible operation, the use of storage has often been proposed as a way to deal with fluctuations and reduce operating costs, e.g., in multi-energy systems [41], biodiesel production [42], cryogenic air separation units [43], and PtX applications such as Power-to-Hydrogen [44] and Power-to-Methanol [45, 46]. However, the use of flexible operation and storage should be properly evaluated to capture the trade-off between the savings in the operating costs and the additional investment costs for storage and oversizing some process units, while meeting the production goals [22, 47].

Model-based analyses at the process level can help identify promising production pathways and designs of PtX processes. Moreover, their efficiency and economic viability can be improved via process optimization, including optimal sizing and operation of the key process units. For this purpose, the modeling approach and its level of detail should be tailored to the research questions, the information available on the specific processes, the considered boundaries and assumptions, as well as the numerical tractability of the models. For instance, relatively simple process models can be built for preliminary process screening to reduce the process alternatives to be modeled in detail. Nevertheless, the process models must retain sufficient representativeness, particularly when the process units exhibit nonlinear and nonideal behaviors.

Given the role that hydrogen-based PtX processes, hereafter referred to as PtX processes, can play in defossilizing several sectors, this work focuses on three essential aspects:

- A literature-based analysis of some key PtX processes to provide a better understanding of their perspectives for process integration and flexible operation as well as highlight some key challenges;
- A model-based comparison of several pathways that incorporate biomass in PtX processes to identify inherent thermodynamic and economic differences;
- An optimization-based investigation of the role of flexible operation and intermediate storage technologies to reduce the production cost of e-chemicals.

To address these aspects, we review open literature and build steady-state models of some PBtX processes as well as quasi-steady-state models of a Power-to-Methanol (PtMeOH) process with and without intermediate storage.

This work focuses on key C-based platform chemicals and fuels such as methanol and kerosene-like fuels, as they are currently widely consumed and will likely be needed in a low-carbon society. Further, all the investigated PtX processes consider low-temperature water electrolysis technology, specifically PEM Water Electrolyzers (PEM-WEs). This technology is relatively mature [48] and suitable for fast process scale-up and sector defossilization. Moreover, PEM-WEs are particularly suitable for flexible operation thanks to their fast dynamics and wide operating ranges [49].

This dissertation is structured as outlined in Figure 1.1, which visually represents the framework that is revisited and further developed in the following chapters as described below.

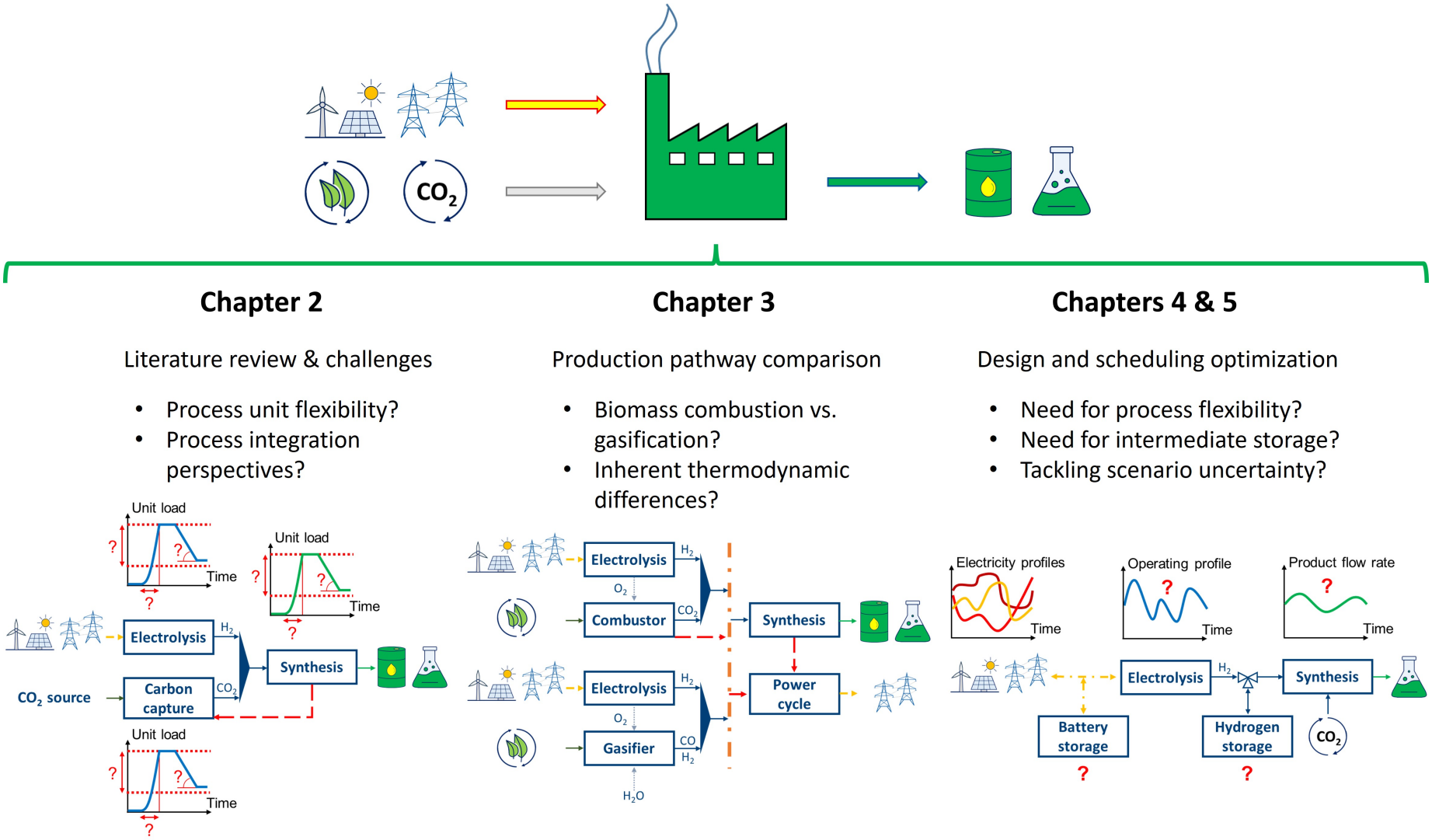


Figure 1.1.: Overview of the chapters and key questions related to the Power-to-X and Power- and Biomass-to-X processes investigated in this dissertation.

In Chapter 2, we establish a literature-based foundation for this work by reviewing the state of the technology of the key units of the main PtX processes that produce hydrogen and convert it in one step, i.e., Power-to-Methane, Power-to-Methanol, and Power-to-Syngas, with a focus on their potential for flexible operation. In particular, flexibility concepts of the process units are described, and the characteristic times for start-up and load variations, ramp rate limits, and operating ranges are collected. Furthermore, opportunities for mass and heat integration across the process units are discussed, as well as some key challenges that are addressed in the following chapters.

In Chapter 3, we investigate the potential of biomass utilization in PBtX processes. In particular, we build relatively simple steady-state models of combustion-based and gasification-based PBtX processes for the production of several molecules relevant to the chemical and transport sectors. These models are used to identify inherent efficiency differences among the pathways via an exergy analysis. The key trends obtained with the simple models are then validated with detailed models of a Power- and Biomass-to-Methanol process. Further, we analyze some limitations of this simplified modeling approach by comparing some Power- and Biomass-to-Kerosene (PBtK) processes that exhibit significant process nonidealities.

In Chapter 4, we investigate the role of flexible operation and the need for intermediate storage to reduce production costs. For this purpose, we model a Power-to-Methanol process with intermediate electric and hydrogen storage under the quasi-steady-state assumption. We then minimize the methanol production cost by solving two-stage programming problems, namely Combined Design and Scheduling (CDS) optimization problems.

In Chapter 5, we investigate how some of the key conclusions in Chapter 4 vary when the Power-to-Methanol process is optimized under uncertainty related to scheduling scenario realization in two-stage stochastic programming problems. In particular, we solve different approximations of the original Stochastic Combined Design and Scheduling (S-CDS) optimization problems. Moreover, we first assess how optimal process design and optimal scheduling affect the methanol production cost when considering multiple scheduling scenarios, namely electricity price profiles, simultaneously. Furthermore, we analyze the optimization results via a statistical analysis. Finally, we develop and investigate an approach based on feature-based scenario clustering and degrees of freedom reduction to tackle the generally high numerical complexity of S-CDS optimization problems.

Finally, Chapter 6 summarizes the key findings of this work and highlights aspects to be further investigated in order to enhance the current understanding and viability of PtX and PBtX processes, and speed up their industrial realization.

2. Integrated and Flexible Power-to-X Processes - A Literature Review

Figure 2.1 visualizes the focus of this chapter, i.e., a literature-based investigation of the extent to which hydrogen-based Power-to-X processes can be operated flexibly and the possible interfaces within their key process units. Through this analysis of PtX processes, we also identify some key challenges that will be addressed in the following chapters on the design, modeling, and optimization of hydrogen-based Power-to-X processes for the production of key fuels, e.g., kerosene, and platform chemicals, e.g., methanol, which have a significant potential for the defossilization of the transport and chemical sectors.

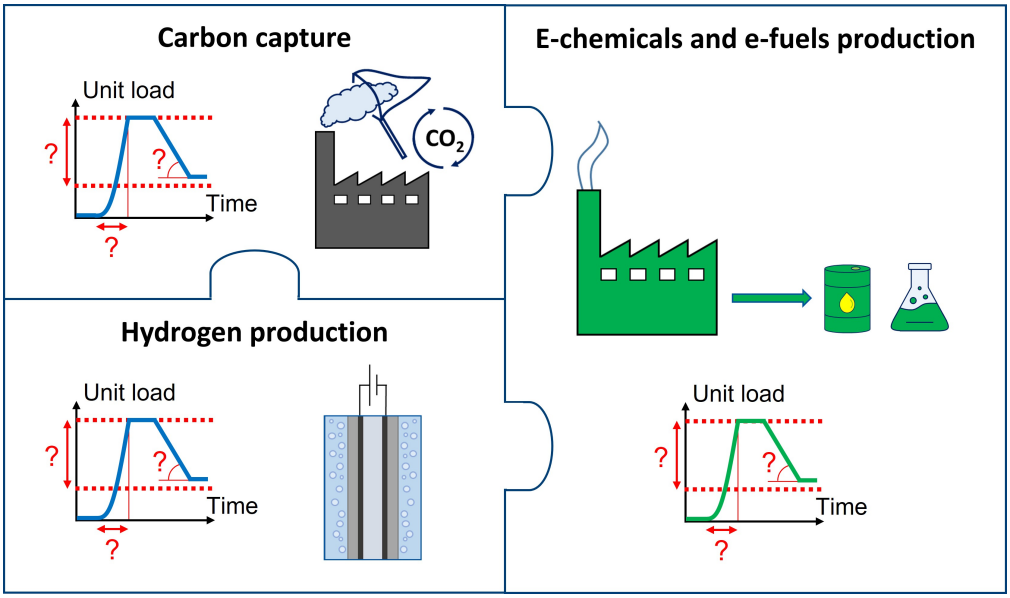


Figure 2.1.: Graphical representation highlighting the focus of Chapter 2, i.e., the literature review of hydrogen-based Power-to-X processes with respect to flexible operation and the opportunities for process integration.

2.1. Introduction

A core unit of Power-to-X (PtX) processes is generally hydrogen (H_2) production via water electrolysis. However, H_2 has a low volumetric energy density, is rather difficult to store on a large scale, transport, and handle, and needs a dedicated infrastructure [50]. These limitations of H_2, as well as the high demand for sustainable platform chemicals and fuels, motivate its further conversion into products with higher volumetric energy density, ideally suitable for existing infrastructure, in Power-to-Chemicals and Power-to-Fuel processes.

Flexible operation, also known as Demand-Side Management (DSM), can be a promising operating strategy for PtX processes [24] to deal with raw material availability, fluctuating electricity prices, and renewable power generation, if all process units are sufficiently flexible. Moreover, these fluctuating inputs can be handled differently according to the operation mode (steady-state vs. dynamic) of the individual process units, their flexibility, as well as the presence of intermediate storage.

In principle, if raw materials are constantly available but the (renewable) power input is fluctuating, every process unit of PtX processes can be operated at steady state thanks to an electricity storage (Figure 2.2 a). Without electricity storage, at least some process units need to be operated dynamically in stand-alone processes (in grid-connected processes, the process units can be operated in steady state despite the electricity price fluctuations). In the case the raw material availability also varies over time or the electrolysis unit is operated flexibly while the downstream conversion process is operated steadily, buffer tanks for raw materials and intermediates, e.g., carbon dioxide and hydrogen, are essential (Figure 2.2 b).

Operating the downstream conversion processes flexibly could be an alternative to large-scale (and expensive) intermediate storage (Figure 2.2 c). Furthermore, intermediate storage could be unnecessary if all units can be operated sufficiently flexibly. Nevertheless, even in the case of very flexible processes, intermediate storage could still be economically beneficial, since it enables operational strategies that reduce operating costs [46, 51].

While flexible operation reduces operating costs, renewable curtailment, and the need for intermediate storage, DSM also reduces the plant capacity factor, thus requiring the oversizing of some process units to meet the production goals. DSM may also cause losses in process efficiency, lower product quality, or increased degradation of the process units, e.g., water electrolyzer. Further, the operation mode raises constraints and concerns about the integration of heat and mass at the process scale. Therefore, flexible operation in PtX processes should be properly evaluated and optimized.

Recent literature includes several reviews on PtX processes. As regards the electrochemical hydrogen production (Power-to-Hydrogen), Carmo et al. [48] presented a comprehensive review of PEM Water Electrolyzers (PEM-WEs). However, a discussion of the flexibility of PEM-WEs and their integration into both the power grid and the synthesis of further products is largely missing. These aspects were also not covered by more recent reviews about PEM-WEs, which focused on catalysts and materials [52–54] and modeling [55–57]. Furthermore, most works focus on the main conversion device rather than the auxiliaries, such as the power converter or the purification units, which are essential to operate the plant. Buttler and Spliethoff [58] included relevant information about electrolysis flexibility in their comparison between the electrolyzer technologies, but a thorough discussion about the auxiliaries and the integration with other process units is missing. Only in a very recent work, Sayed-Ahmed et al. [59] thoroughly reviewed the above-mentioned aspects, especially the dynamic behavior and the related degradation of PEM-WEs.

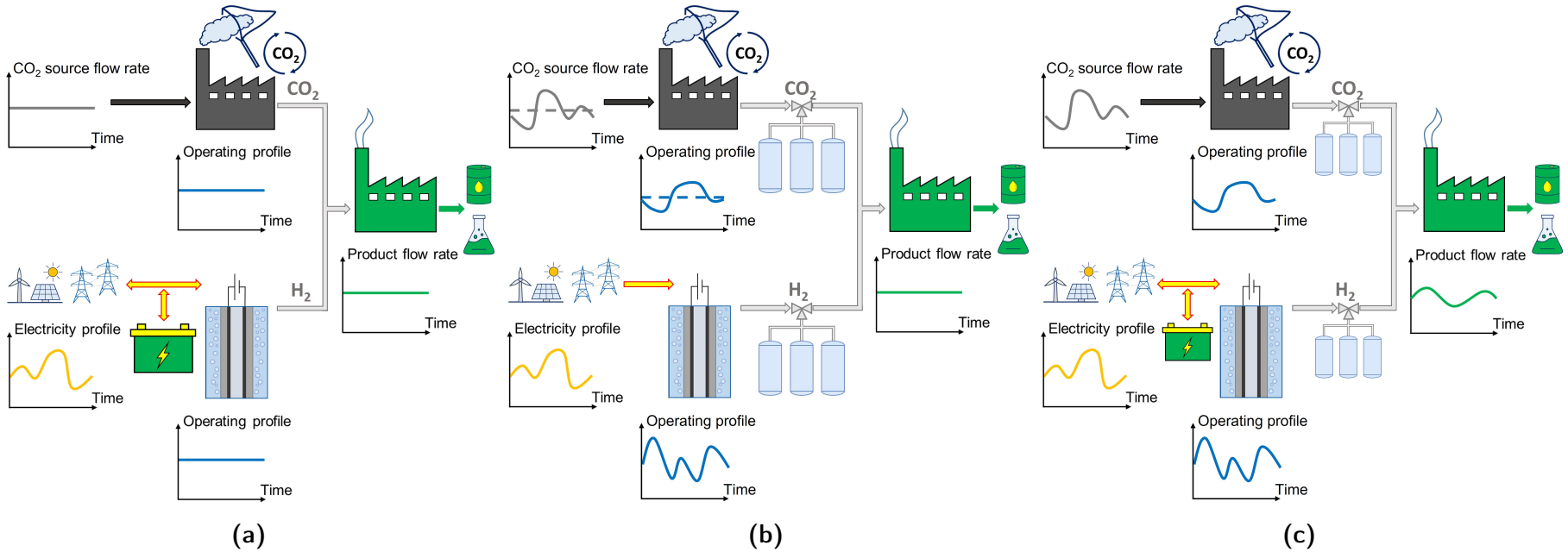


Figure 2.2.: Main Power-to-X operating concepts: (a) Every process unit is operated in steady state. Constant power input to the process units is possible thanks to large-capacity electric storage (battery). (b) The carbon capture and the electrolysis units are operated based on the CO_2 source and power availability, respectively, while the downstream conversion unit is operated in steady state. Storage allows a constant raw materials supply to the downstream conversion unit. If the CO_2 source is steady (gray dashed line), the CO_2 storage is not needed. (c) Every process unit is operated flexibly: raw materials are produced based on the source availability; smoother variations in the operation of the synthesis unit are possible thanks to small-capacity electric storage (battery) and raw material storage. The storage size is significantly lower than in case b); note that either the battery or the raw material storage can be omitted based on the process unit flexibility.

Several reviews and techno-economic analyses on PtX processes where hydrogen is an intermediate product can also be found in recent literature. Götz et al. [60], Peters et al. [61], and Rönsch et al. [62] conducted techno-economic reviews of Power-to-Gas and methanation. Foit et al. [63] reviewed the Power-to-Syngas process in which the co-electrolysis technology is used. Mbatha et al. [64] presented a thorough analysis of the Power-to-Methanol (PtMeOH) process, while Pérez-Fortes et al. [65] and Lee et al. [66] performed a techno-economic assessment of PtMeOH. Adnan and Kibria [67] compared different PtMeOH processes with a techno-economic analysis and a life cycle assessment. Álvarez et al. [68] mainly focused on catalysts for direct hydrogenation of carbon dioxide to formic acid, methanol, and Dimethyl Ether (DME). Saeidi et al. [69] reviewed catalysts, operating conditions, and reactor types for the production of methane, methanol, and heavier hydrocarbons. Several works also investigated the production of nitrogen-based chemicals, e.g., ammonia [70, 71].

Moreover, several techno-economic comparisons between e-products are available. For instance, Bongartz et al. [31] compared hydrogen, methane, methanol, and DME for light-duty transportation. Brynolf et al. [32] compared methane, methanol, DME, gasoline, and diesel. Tremel et al. [72] compared green synthetic natural gas, methanol, syncrude, diesel, DME, and ammonia; methane, methanol, ammonia, and urea production processes were compared by Bargiacchi et al. [73], while methane, methanol, DME, liquid hydrocarbons, olefins, aromatics, ammonia, and urea were compared by Allgoewer et al. [30].

The above-mentioned works focus on the technology and its cost. Few works consider the environmental impact [27, 74, 75] or account for all these aspects [30, 34, 67, 76, 77], but they still do not focus on process flexibility and process integration. Only very recent works started analyzing the flexibilization potential, such as Sayed-Ahmed et al. [59] for Power-to-Hydrogen processes, and Mbatha et al. [78], Qi et al. [79], and Svitnič and Sundmacher [46] for PtMeOH processes. Thus, we aim at complementing existing reviews on Power-to-X to help answer open research questions like:

- Which PtX process units can be operated flexibly? How fast can these units change the load? What are their operating limits?
- Which are the interfaces between the process units in terms of temperature, pressure, and purity? Should the components be mass and heat integrated, and how does their integration affect the process response under dynamic operation?
- Is intermediate storage needed? And, if yes, what kind of storage is economically beneficial, and how large should storage be? What is the trade-off between intermediate storage need and process flexibility?

Considering these research questions, this chapter aims at i) reviewing literature about the dynamic operation of some key Power-to-X process units to determine the main flexibility indicators, i.e., start-up times, ramp rates, operating range, and settling time; and ii) identifying potential matches and interfaces among the process units. In particular, we focus on Power-to-Methane, Power-to-Methanol, and Power-to-Syngas processes as they are the key C-based products or intermediates of the chemical and transport sectors that can be synthesized from hydrogen in one step (for Power-to-Ammonia processes, we refer to Mucci et al. [1]). Also, we consider the electrolysis and carbon capture units that provide raw materials for the synthesis of these products. Therefore, in this chapter, we

answer the questions related to process unit flexibility and interfaces, except for the effect of process unit integration on process dynamics, as this would require detailed modeling, which goes beyond the scope of this chapter. An answer to the third group of questions is largely lacking in the literature, which is why we investigate in detail the need for intermediate storage and flexible operation, as well as their interplay, for a Power-to-Methanol case study later in Chapters 4 and 5.

The remainder of this chapter is structured as follows: in Sections 2.2 and 2.3, hydrogen and carbon dioxide supplies are analyzed, respectively. Section 2.4 treats Hydrogen-to-X processes. Section 2.5 focuses on process flexibility and process integration, while, in Section 2.6, the key conclusions are summarized and some key challenges that are addressed in the following chapters are identified.

2.2. Hydrogen supply

Hydrogen can be used for several applications, e.g., in the steel and chemical industries, as a fuel or intermediate for transportation, and for heat and power generation. The International Energy Agency (IEA) [80] estimated an overall H_2 demand of about 100 Mt in 2024.

Currently, most hydrogen is produced from fossil fuels and only 2 % via electrolysis, mainly via chlor-alkali electrolysis [50], where hydrogen is a by-product. In other words, dedicated water electrolysis for H_2 production is still negligible (around 0.1 Mt in 2024 [80]). This is due to historical (long industrial experience in reforming) and economic reasons (high cost of electricity compared to natural gas, as well as high investment costs for the electrolyzers). Nevertheless, the currently limited installed capacity of electrolyzers (around 4 GW in 2025 [80]) is expected to quickly grow (IEA estimates that ca. 65 GW of electrolyzer capacity is confidently expected to be built or operating worldwide by 2030 [80]), thus significantly contributing to reducing GHG emissions related to hydrogen production.

In the following subsections, we provide an overview of the main water electrolysis technologies before focusing on PEM Water Electrolyzers.

2.2.1. Water electrolysis: Technology overview

Water molecules can be split into their constitutive elements by supplying a sufficient amount of energy:

$$H_2O \rightarrow \frac{1}{2} O_2 + H_2.$$

In water electrolysis, this overall reaction is carried out electrochemically at two electrodes, i.e., the anode and the cathode, at which oxidation and reduction reactions occur, respectively. The main water electrolysis technologies are briefly described in the following.

2.2.1.1. Alkaline water electrolysis

Alkaline Water Electrolyzers (A-WEs) are the most mature electrolysis technology [50]. A highly-concentrated alkaline aqueous solution (generally 20-30 wt.% of KOH [81]) is fed to

the cathode, where water molecules are split into hydrogen molecules and hydroxide ions. At the anode, hydroxide ions are oxidized to form oxygen and water.

Two main commercial versions can be identified based on how the electrodes are separated: i) in the conventional one, a diaphragm separates the electrodes; ii) in the so-called Anion Exchange Membrane Water Electrolyzers (AEM-WEs), the electrodes are divided by a membrane.

Currently, the typical current density range of A-WEs goes from 0.05 to 0.70 A cm^{-2} [81], even though this range is often narrower (0.2-0.4 A cm^{-2} [48]). This drawback has been partially overcome by AEM-WEs, which can be operated up to 1.5 A cm^{-2} [82].

A-WEs have longer lifetimes and lower investment costs than other electrolyzer technologies thanks to the absence of noble metals such as platinum and iridium [81]; similarly, AEM-WEs can avoid noble materials. At typical operating points, A-WEs are more efficient than PEM-WEs (63-70 % compared to 56-60 % [50], both based on the Lower Heating Value (LHV)).

Low partial-load limits (10 % [50]) are achievable, even though the practical limits are generally higher for safety reasons related, for instance, to hydrogen crossover (20-40 % [48]). Nevertheless, A-WEs have difficulties in tracking power fluctuations related, for instance, to renewable power supplies [83], because of the relatively high thermal inertia and settling times compared to other technologies. This recently led to increased investments in developing other electrolysis technologies, in particular PEM-WEs.

2.2.1.2. PEM water electrolysis

PEM Water Electrolyzers were introduced in the 1960s [50], but a new impulse to their development took place in the last few decades, making Polymer Electrolyte Membrane (PEM) water electrolysis plants commercially available at the MW-scale [84]. The polymeric membrane divides the anode side, where water is fed and oxygen forms, and the cathode side, where the produced hydrogen is collected.

Despite the generally lower efficiency and lifetime than A-WEs, their wide operating range and capability to be fast-responsive [49, 85] (see Section 2.2.3) make this technology particularly promising, especially if coupled with renewable sources.

High operating current densities (up to 2 A cm^{-2} or more [86]) are possible. Furthermore, the estimated enhancement of the efficiency (from 56-60 % to 63-68 % by 2030 [50], based on the LHV) and the expected drop of the Capital Expenditures (CAPEX) [86, 87] could potentially make PEM-WEs cost-effective.

2.2.1.3. Solid oxide water electrolysis

Solide Oxide Water Electrolyzers (SO-WEs) are technologically less mature than the other electrolysis technologies [88]. In SO-WEs, an oxide-ion conducting ceramic material separates the anode and cathode. Water is fed to the cathodic side, where the produced hydrogen is collected.

SO-WEs do not require noble materials and are not very sensitive to impurities in the feed stream. High operating current densities have been reached experimentally (up to 3.6 A cm^{-2} [88]). Furthermore, SO-WEs are reversible and can be used as solid oxide fuel cells generating electricity.

As opposed to the other electrolysis technologies, SO-WEs are operated at high temperatures (800-1000 °C [50]). On the one hand, higher temperatures reduce the amount of electricity required to split water, thus enabling higher efficiencies (74-81 %, based on the LHV [50]). On the other hand, thermal management is more complex.

Despite these appreciable features that make this technology promising, the stack lifetime is still low [50], and the thermal management and the scale-up of the electrolysis units remain key issues.

2.2.2. PEM water electrolyzers: Insight into the technology

PEM-WEs are considered the most promising technology concerning flexible PtX processes thanks to their fast responsiveness and shorter start-ups compared to the other technologies, and their wide operating ranges [59]. This subsection focuses on the key aspects of the technology.

2.2.2.1. PEM-WE cell

PEM-WEs have a so-called "sandwich structure" since they are composed of several layers, namely the membrane, the electrodes, the porous transport layers, and the bipolar plates.

The PEM cell core is a thin (20-300 µm [48]) Polymer Electrolyte Membrane that separates the anode from the cathode and is ideally only selective to protons (H^+). In reality, oxygen and hydrogen molecules, water, and cationic impurities (like Na^+, K^+, Ca^{2+}, Cu^{2+}, Fe^{3+}, and Ni^{2+}) succeed in crossing the membrane.

The membrane is coated with a conductive layer on each side acting as an electrode, where the electrochemical reaction occurs. The union of the membrane and the electrodes is often called membrane electrode assembly or catalyst-coated membrane from the production technique [48].

Catalysts represent one of the most challenging aspects of PEM-WEs since they must be active and stable [54]. Unfortunately, only noble, scarce, and expensive materials, i.e., iridium at the anode and platinum at the cathode, perform well in PEM-WEs. Research is active to find catalyst alternatives, set recycling strategies, and reduce the catalyst loadings to both lower the investment costs and avoid a shortage of noble materials for the expected large-scale electrolyzer production [89]. Many studies are summarized in two recent reviews [48, 52].

Porous transport layers, sometimes called gas diffusion layers, aim at distributing the reactants homogeneously on the catalyst layer and efficiently evacuating the produced gases from the reactive sites.

Bipolar plates have a threefold role in PEM-WEs: i) they transport the reactants and the products into and out of the cell, respectively, through the flow channels inside the plates, ii) they conduct electrons and heat, and iii) they physically separate adjacent cells of a stack connected in series. Parallel, single-serpentine, and multiple-serpentine flow channel layouts are the most common [90].

2.2.2.2. Stack set-up and auxiliary units

In PEM-WEs, several cells are connected in series to form a stack, and several stacks can be connected both in series and in parallel. Several additional units, e.g., pumps, sensors,

valves, and power conversion and control units, are essential to operate electrolyzers [91]. A simplified scheme is displayed in Figure 2.3.

The pre-treatment of the feed water with ion-exchange resins plays an essential role to reduce cell poisoning, which significantly affects the electrolyzer performance and lifetime. Nevertheless, the membrane electrode assembly can be partially reactivated by treatments with an H_2SO_4 solution when contaminated [92, 93].

Pumps provide fresh water to the cell (generally only at the anode) in over-stoichiometric conditions to avoid membrane dehydration and to remove the produced gases from the cell. The excess of water also acts as a cooling medium.

The hot material streams at the outlet of the cell contain two phases, i.e., liquid and gas, which are then separated. To reduce the steam content in the gaseous phase, the streams can be cooled down to either ambient temperature or below, if a refrigeration cycle is used. Further purification treatments can be necessary to meet the typically high purity specification of the hydrogen [94] and oxygen streams. For instance, oxygen traces can be eliminated from the hydrogen stream via catalytic conversion as in the research facility "Energiepark Mainz" [49]. Pressure Swing Adsorption (PSA) or Temperature Swing Adsorption (TSA) technologies can be used to further dry the hydrogen stream and increase its purity [95]. Extremely pure hydrogen streams ($>$ 99.999 %) can be commercially achieved [96, 97].

Power electronics for high-power applications and proper control systems acting on the AC-DC (or DC-DC if directly coupled with a DC power source) converters enable operating water electrolyzers flexibly and providing ancillary services to the grid. Furthermore, special care needs to be paid to the power quality provided to the cell to avoid additional losses if the electrolyzer is coupled to the grid via an AC-DC converter [98, 99].

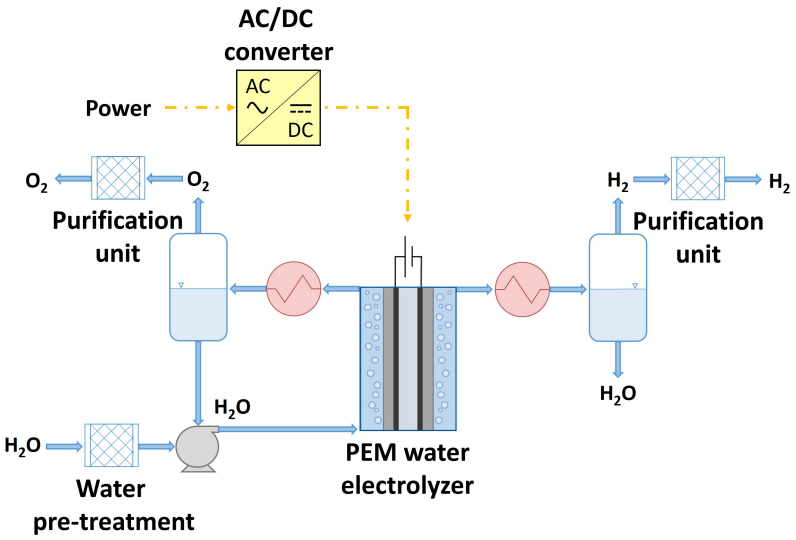


Figure 2.3.: Sketch of the main auxiliaries of a PEM water electrolysis unit.

2.2.2.3. Electrolyzer pressurization

The pressurization of hydrogen is an important aspect to consider for an efficient integration of water electrolyzers into more complex systems. In fact, high-pressure hydrogen is

needed for several applications, e.g., when feeding hydrogen into a pipeline (up to 85 bar), hydrogen for chemical synthesis processes (up to 250 bar), hydrogen storage in salt caverns underground (up to 200 bar), or hydrogen storage for hydrogen car refueling (350-700 bar).

Three main approaches can be considered to pressurize hydrogen: i) compress hydrogen inside the PEM-WE (electrolyzer with a pressurized cathodic side), ii) compress hydrogen outside the PEM-WE in an electrochemical hydrogen compressor [100], iii) compress hydrogen in a mechanical (multi-stage) compressor. Combinations of the above-mentioned approaches are also possible if, for instance, the PEM-WE cannot reach a sufficiently high operating pressure. In this case, hydrogen can be produced by a pressurized PEM-WE and then compressed in a different device to reach the desired pressure. The anodic side can also be pressurized (balanced configuration) to reduce the mechanical stress on the membrane and store oxygen more easily, but a higher energy demand is needed.

Determining the best configuration in terms of energy demand is not trivial. In hybrid configurations, e.g., pressurized cathode and mechanical compressor, the optimal ratio between these two compression steps mainly depends on the final pressure level [94, 95] and the current density [95]. Bensmann et al. [94] showed that the optimal cathodic pressure is lower than around 20 bar for delivery pressures up to 100 bar. A similar result was obtained by Bornemann et al. [101] for a delivery pressure of 200 bar. Analogous findings were obtained by Tjarks et al. [95] for delivery pressures up to 750 bar. However, whether the positive effect of high pressure on the reduction of some overpotentials [102] is taken into account in their evaluations is unclear. Recent works [103, 104] compared electrochemical compression against mechanical compression for different hydrogen pressure levels and a hydrogen refueling station case study, but the interplay between hydrogen production and its pressurization was not investigated. Although technological improvements are needed to be competitive against mechanical compression in terms of efficiency [103, 104], electrochemical hydrogen compression is promising because it can reach high pressures (up to 1000 bar) in one stage without any moving parts [100, 105] and has relatively low investment costs [104].

The cathodic pressure of PEM-WEs affects not only the energy demand but also hydrogen crossover backward to the anode [59, 106]. The operating temperature also affects the crossover [59]. High amounts of hydrogen at the anode reduce the Faradaic efficiency [107, 108] and pose safety issues due to the low flammability threshold of hydrogen in oxygen (4 vol.% [48]). Thicker membranes [106, 109] and the positioning of a third electrode inside the membrane to force the conversion of the crossing hydrogen into water or hinder hydrogen crossover [110] can mitigate this risk. If hydrogen compression is carried out in an electrochemical compressor afterward, hydrogen crossover does not generate any safety issue since there is no oxygen at the anode. In contrast, the efficiency reduction due to hydrogen crossover still stands [103].

2.2.3. Flexible operation of PEM water electrolyzers

In hydrogen-based PtX processes, the renewable power input can vary over time, thus requiring flexible operation of the water electrolyzer, unless electric storage is considered (Figure 2.2 a). Further, the capability of PEM-WEs to perform quick load variations could potentially enhance their performance since sudden current changes can promote bubble detachment, thus improving mass transport [59]. Nevertheless, the benefits should be carefully evaluated, also accounting for the higher cell degradation risk [59].

The following paragraphs deal with the flexibility of PEM-WEs. The key parameters of their flexibility are summarized in Table 2.2.

Start-up and shutdown

Start-ups and shutdowns for PEM-WEs could be quite frequent if water electrolyzers are directly coupled with renewable power plants. It has been experimentally tested that PEM-WEs have short start-up and shutdown times (minute scale [49]). However, the effects of their flexible and alternating operation on cell degradation are still unclear. Furthermore, shutdowns and idle phases can be critical; having small bias currents and low cell voltages instead of idle periods seems to reduce degradation [59, 111], as for A-WEs.

Load changes

PEM-WEs have an extremely wide operating range (5-100 % [96]). Operation at loads higher than the nominal is also possible (150 % [49] - 160 % [50]), but only for short periods because of cooling reasons [49].

Several dynamic models have been built to assess the flexibility and fast-responsiveness of PEM-WEs and which ancillary services they could provide. Gusain et al. [112] built a simplified PEM-WE model to show that relatively large electrolyzer systems, e.g., 10 MW, can provide ancillary services on a large scale. They also pointed out that degradation phenomena over time should be accounted for in long-term assessments to avoid overestimating the real flexibility [112]. Alshehri et al. [113] showed that PEM-WEs can participate in the European electrical ancillary markets and can contain frequency imbalance even in a low-inertia grid by providing primary regulation. Veerakumar et al. [114], using a synthetic model of the north Netherland network for the year 2030, showed that a properly controlled large-scale electrolyzer (300 MW) can quickly damp frequency imbalances. Furthermore, the use of small-scale PEM-WEs aggregated in virtual power plant concepts can enhance grid flexibility [115].

PEM-WEs flexibility has been tested not only via dynamic models but also experimentally. Koponen et al. [116] showed that their small-scale PEM-WE (4.5 kW) could not follow extremely fluctuating power profiles due to the ramp limit (0.4 % s^{-1} [116]); this problem can be solved by coupling the electrolyzer with fast-responsive storage technologies like supercapacitors [116]. In contrast, some industrial-scale products can reach higher ramp rates, e.g., 10 % s^{-1} [96]. For a medium-scale pilot plant (4 MW) [49], it was experimentally shown that ancillary services up to the primary control reserve can be provided. Nevertheless, the economic profitability of having such a high responsiveness is still under debate [49, 117].

2.3. Carbon dioxide supply

To reduce the environmental impact of the chemical and transport sectors, alternative carbon sources are necessary for producing carbon-based chemicals and fuels. Carbon dioxide and residual biomass are often considered promising carbon (and energy) feedstocks for PtX and PBtX processes.

In PBtX processes, biomass is generally converted into an intermediate stream, e.g., carbon dioxide or synthesis gas, which is further converted into the product "X". Depending on the biomass conversion technology, the intermediate stream is concentrated to reduce

the amount of inert components. For instance, in combustion-based PBtX processes, carbon dioxide is captured from the flue gases.

As even PBtX processes can require carbon dioxide separation, the following subsections focus on carbon dioxide separation technologies. Further, the potential and the key challenges of biomass utilization as a carbon and energy feedstock PBtX processes are discussed in more detail in Chapter 3.

2.3.1. Carbon dioxide sources

Carbon dioxide sources can be classified into three main categories, i.e., biogenic, fossil-based, and air. To reduce the net worldwide CO_2 emissions related to anthropogenic activities, carbon capture and utilization, e.g., in PtX processes, is a promising solution in the medium-to-long term [21].

As the amount of captured CO_2 is much lower than the potential availability and demand (0.05 Gt of captured and used CO_2 vs. 37 Gt of emitted CO_2 just in the energy sector in 2022 [21]), classifying which CO_2 sources should be prioritized for capture is important to maximize overall CO_2 emissions abatement (thus including the emissions related to the CO_2 capture itself). Von der Assen et al. [38] ranked the current CO_2 sources according to an environmental merit-order. Even though Carbon Capture (CC) requires substantial amounts of energy, they verified that CC reduces CO_2 emissions compared to the status quo without capture for all the analyzed sources (power plants, hydrogen, ammonia, ethylene oxide, pulp and paper, steel and iron, cement plants, refineries and gas processing plants, and direct air capture) [38]. The largest reduction can be obtained from fossil-based hydrogen, ammonia, and ethylene oxide production processes [38]. Other authors [74] confirmed that carbon dioxide from hydrogen production plants has the lowest cradle-to-gate impact.

CO_2 capture from point sources is less energy-demanding than Direct Air Capture (DAC) because of the low CO_2 concentration in air (around 400 ppm). Nevertheless, CC via DAC has a negative value of CO_2 emissions [38, 118]. Furthermore, such CO_2 source will be available even in a low-carbon economy and has the advantage of being geographically unconstrained. This would allow the conversion of captured CO_2 with green hydrogen into valuable e-products where renewable power is produced (without transporting electricity).

2.3.2. Carbon capture technologies

Based on the position of the CC unit in the CO_2-emitting plants, CC is generally classified as pre-combustion, oxy-combustion, and post-combustion capture [119, 120]. In pre-combustion capture, a carbon-based feedstock is first converted into a suitable intermediate product from which CO_2 is then separated. In post-combustion capture, CO_2 is captured from the flue gas after the carbon-based feedstock combustion. In oxy-combustion, carbon and hydrogen atoms are oxidized with pure oxygen (and recycled flue gas) instead of air; as nitrogen and argon are not present in the mixture, an almost pure CO_2 stream is obtained after water condensation. Oxy-combustion is promising for CC, especially when coupled with electrolysis: the main side product of water electrolysis is oxygen, which could be used to substitute the combustion air. Several benefits can be named, e.g., no nitrogen oxides emissions, the absence of the energy-intensive CC unit, and a lower need for oxygen purification (hydrogen traces in oxygen provide additional thermal energy when burned).

Several CC technologies are available, e.g., chemical absorption, chemical adsorption, PSA, selective membranes, and cryogenic separation [119, 121]. Further separation concepts with lower technological readiness levels have been proposed, like the use of molten carbonate fuel cells [122] and biological capture methods, e.g., dedicated microalgae plantations where microalgae grow by capturing CO_2 from flue gases [119, 123] and are then used as biomass feedstock.

Absorption in Monoethanolamine (MEA) solutions is the most mature CC technology (Figure 2.4). The relatively low temperature for solvent regeneration (lower than 150 °C) makes this technology particularly suitable for heat integration with several exothermic downstream synthesis processes (see Section 2.5). Also, MEA has often been considered the benchmark for new CC solvents because they are cheap, stable, and fast-reactive. However, they require a significant amount of thermal energy for regeneration (stripping phase), and their corrosiveness and viscosity limit the CO_2 mass fraction in aqueous solutions to ca. 40 % [124]. Other pure solvents, e.g., ammonia [125] and piperazine [126], have been proposed as alternatives, but none of these outperforms MEAs overall. In contrast, some solvent blends seem particularly promising. For instance, CESAR 1, a mixture of 2-amino-2-methyl-1-propanol and piperazine, has been shown to require less thermal energy for regeneration and lower CO_2 separation costs than conventional CC with MEAs [127]. Finally, the choice of solvent also depends on the partial pressure of CO_2 in the gas [128].

Since absorption and stripping are exothermic and endothermic reactions, respectively, inter-cooling of the absorber and inter-heating of the stripper enhance the capture rate and reduce the thermal duty. Given the high energy demand and cost of these units, there is much interest in optimizing CC via MEA solutions. For example, a reduction of the thermal duty from 3.8 MJ $kg_{CO_2}^{-1}$ to 3.1 MJ $kg_{CO_2}^{-1}$ was achieved with the introduction of an absorber inter-cooling, a stripper inter-heating, and a CO_2-rich feed split before thermal regeneration [129]. Further, the CC unit design was optimized via superstructure by Lee et al. [124] to minimize CO_2 capture costs. The resulting optimal design included several absorber intercoolers, cold solvent split, vapor recompression, and internal heat integration, and could reduce the thermal duty to 2.2 MJ $kg_{CO_2}^{-1}$, although it slightly increased the specific electricity demand.

Adsorption on solid materials, generally CaO-based, is another mature technology. These sorbents can be used for both pre-combustion and post-combustion capture (or pre-conversion and post-conversion if no combustion is performed). CaO sorbents have a high theoretical CO_2 sorption capacity [130] enabled by chemical adsorption according to the following reaction:

$$\mathrm{CaO\,(s) + CO_2(g) \rightarrow CaCO_3(s)},$$

where CO_2 is captured at around 650 °C at atmospheric pressure and desorbed at around 950 °C, thus requiring an energy input.

Research on solid sorbent materials for CC is still active. ZrO_2-modified CaO materials, for example, were proven to enhance the sorbent stability over time without highly affecting the sorption capacity [130], and the NiCaO material, despite a lower sorption capacity, was proven to release methane at 500 °C [131, 132] or carbon monoxide at 700 °C [132] if fluxed with hydrogen. The latter could be an interesting alternative for producing syngas (see Section 2.4.3). Other adsorbent materials, e.g., zeolites and metal-organic frameworks [133], are also particularly promising, as they require significantly lower desorption

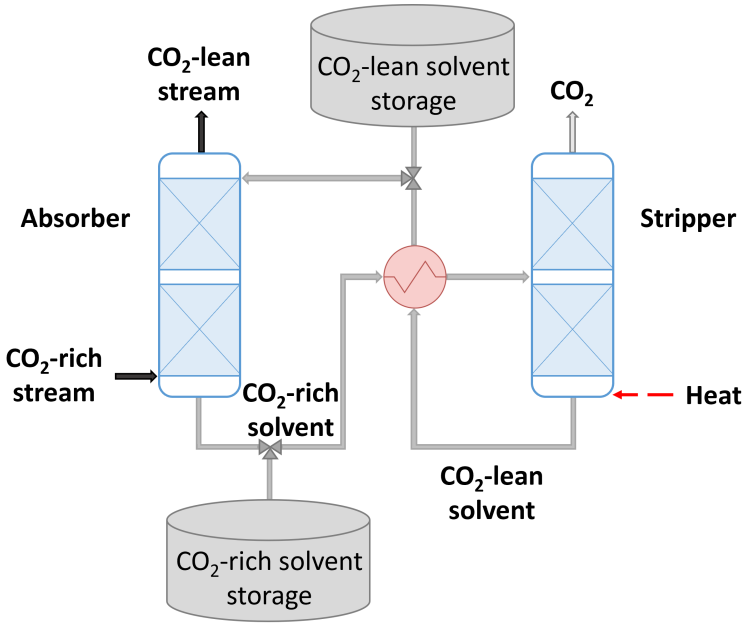


Figure 2.4.: Simplified sketch of a solvent-based carbon capture unit (chemical absorption) with solvent storage.

temperatures, thus easing process integration. Alternatively, processes that combine CO_2 capture and its electrochemical conversion into valuable products, e.g., CO and formic acid, are also under development [134].

2.3.3. Flexible operation of carbon capture units

Flexible operation of carbon capture units based on the availability of the carbon source or CO_2 demand of the downstream conversion process would reduce the need for intermediate storage. However, it could complicate heat integration with other process units.

The next paragraphs deal with the flexibility of CC units via chemical absorption, as the most established technology. The key parameters of their flexibility are summarized in Table 2.2.

Start-up

Two main cold start-up procedures are mentioned in literature [135]: air instead of the flue gas enters the absorber in the first phases of the start-up; the flue gas enters the absorber directly, and the flow rate of the MEA solution is adjusted consequently. Gaspar et al. [135] simulated the second procedure and noted that, after around 20-30 minutes, the CO_2 removal factor is approximately at the design value. However, some residual fluctuations of some control variables remained, and longer times would be needed to reach the steady state.

Load changes

As regards the operating load range, a properly designed control system can handle wide variations (50-130 % [135]) of the flue gas flow rate while keeping the CO_2 removal factor almost constant. The main risk of further extending the load range is the flooding or drying of the columns.

Several studies about flexible operation of CC units can be found in the literature. These include models to investigate the solvent loss for entrainment and degradation [136], load changes [135, 137, 138], variation of the carbon dioxide content in the flue gas [139], insufficient steam at the reboiler for regeneration [137], and integration of a buffer tank [126].

Most of the above-mentioned simulation-based studies compare two solvents, i.e., MEA and piperazine: plants using MEA solutions provide faster responses (up to 2-3 times faster) both for step [138, 139] and ramp [137, 138] variations. For a CC process designed to remove 1 t h^{-1} of CO_2 from flue gas, settling times in the range 1-2 h [138] or even shorter (around 0.2-0.5 h) [135, 139] could be achieved depending on the changed variable and considered solvent. Similar settling times were found by Mostafa et al. [140] for the absorber of a CC unit with MEA solutions for a large-scale PtX plant. Furthermore, MEA and piperazine provide inverse response behavior under certain step changes in the desorber, thus making control more challenging [126, 139]. The longer settling times (around 6 h [140]) of the desorption phase could be a bottleneck unless solvent storage is used [135].

Experimental campaigns were carried out at the amine-based CC test rig at the Klemetsrud waste incinerator in Oslo [141]. However, these tests focused more on pollutant emissions and solvent degradation than on the assessment of the unit flexibility. Fagerlund et al. [141] remarked that sudden variations of the load or high presence of dust in the flue gas result in higher emissions of amines in the flue gas.

Alternative designs and operating strategies could enhance CC flexibility. Having smaller CC units in parallel, for example, could enhance capture flexibility [125] and be particularly suitable when the processed gas flow rate is high. Flue gas bypass and solvent storage tanks (Figure 2.4) could also enhance the CC unit efficiency and flexibility in off-design conditions [126, 135, 142]. In particular, storing CO_2-rich solvent in buffer tanks instead of CO_2 in pressurized vessels could be advantageous. This decoupling strategy could be particularly suitable when a downstream conversion process with slow characteristic times provides the heat for CO_2 stripping. However, the costs would unavoidably be higher because of the tank inventories and the additional amount of solvent.

2.4. Hydrogen-to-X

As discussed in Section 2.1, flexible operation of the downstream conversion processes of CO_2 and H_2 (Hydrogen-to-X) could lead to savings in operating costs and reduce the size and cost of storage tanks. Knowing how flexible such downstream conversion processes are could be particularly important to reduce production costs. In fact, process flexibility parameters can be considered to optimize the design of the processes and their scheduling.

In this section, we analyze the production processes of some key C-based chemicals produced with hydrogen in one step, namely methane, methanol, and syngas, and their process flexibility. The choice of these chemicals is motivated by their wide utilization as platform chemicals, and thus their defossilization potential; however, their life cycle emissions have not been assessed in this dissertation. Further, the related PtX processes have medium-to-high technological readiness level. For instance, demonstration plants for Power-to-Methane at the MW scale have been built [35]. Power-to-Methanol technology is at the commercialization phase already [143, 144]. A 150 kW Power-to-Syngas plant with a solid oxide electrolyzer to synthesize liquid fuels via the Fischer-Tropsch process has been built [35]; in contrast, the production of syngas via catalytic Reverse Water Gas

Shift (RWGS) for liquid fuels synthesis is currently tested at smaller scales [145].

Further, the synthesis processes of these chemicals have high theoretical conversion efficiencies (see Table 2.1), which means that most of the chemical energy in hydrogen can be stored in the product. The theoretical conversion efficiency in terms of LHV (η_{LHV}) is calculated as follows [72]:

$$\eta_{\mathrm{LHV}} = \frac{p \cdot \mathrm{MW_P} \cdot \mathrm{LHV_P}}{h \cdot \mathrm{MW_{H_2}} \cdot \mathrm{LHV_{H_2}}},$$

where MW and LHV are the molecular weight and the lower heating value, respectively, p and h are the stoichiometric numbers of the direct synthesis reaction for the product and hydrogen, respectively. The theoretical conversion efficiency can be higher than one only if the reaction is endothermic, as for syngas production via RWGS.

Table 2.1.: Theoretical conversion efficiency in terms of LHV for the considered products.

	MW kg kmol^{-1}	LHV MJ kg^{-1}	η_{LHV} -
Methane	16	50.0	0.833
Methanol	32	19.9	0.884
Syngas*	2-28	120.0-10.1	1-1.178

* Ranging from pure H_2 to pure CO.

2.4.1. Methane

The production of methane via Power-to-Methane (often also called Power-to-Gas) processes is gaining growing interest, as proven by the more than thirty projects funded in Europe in recent years [146]. Thanks to the existing infrastructure, e-methane can be injected, stored, distributed, and then converted to heat and electricity or used as fuel.

Methane synthesis can be catalyzed both chemically and biologically [60]. The first case requires high-activity and selective catalysts; the second requires microorganisms that can convert CO_2 and H_2. Given such catalysts or microorganisms, methane production is a highly efficient one-step process; this makes its production cheap and competitive compared to other alternatives like methanol [147].

2.4.1.1. Catalytic methane production

Two process routes are possible for catalytic methanation: direct and indirect. In the direct one, the most common, CO_2 is hydrogenated to produce methane. In the indirect one, CO_2 is reduced to carbon monoxide in a RWGS step (also see Section 2.4.3.1) before being converted to methane. Direct electrochemical synthesis from CO_2 and water is also possible [148].

Reaction and operating conditions

The synthesis reaction in which carbon dioxide is directly hydrogenated to form methane is known as the Sabatier reaction:

$$CO_2 + 4H_2 \rightarrow CH_4 + 2H_2O.$$

The reaction is exothermic and a typical temperature range is 200-550 °C [60]; the operating range depends on the catalyst. Several metals such as Ni, Ru, Pt, and Co can be used as catalysts [62]. Nickel is the most used because of its activity, but it can be poisoned if the feed contains contaminants such as sulfur [149]. The reaction can be carried out in a wide pressure range (1-100 bar [60]). High pressures enhance the conversion according to Le Chatelier's principle. The feed typically has a stoichiometric CO_2:H_2 ratio [60].

High CO_2 conversion rates are achievable, and recycle streams are generally not needed. The selectivity of methanation is very high, since only small amounts of side-products like CO, C_2H_6, CH_3OH, and CH_3OCH_3 are produced [150]. Among these, carbon monoxide is the main side product, but high pressures (e.g., 10 bar) strongly hinder its formation [150]. Also, increasing the pressure reduces the risk of carbon deposition [150].

Reactor configurations and process concepts

For the methanation of both CO_2 and CO, several reactor types have been proposed, e.g., fixed-bed, fluidized-bed, three-phase (a slurry reactor in which the gaseous stream reacts over solid catalyst particles dispersed in a liquid phase), and structured reactors [60].

Thermal management is a key point for all methanation reactors, especially when CO is used due to the higher exothermicity [151]. Beyond the risk of thermal runaway, hot spots could damage the catalyst and compromise the reactor performance. The risk of hot spot formation can be reduced by introducing a diluent at the expense of having larger components. A common diluent is methane itself (e.g., when using CO_2 from biogas), which luckily hardly affects CO_2 conversion [150]. The injection of fresh reactants at the inlet of each reactor (in a series reactor configuration) [149] or an inhomogeneous catalyst distribution over the reactor can also help mitigate this risk [152].

One of the most widely used configurations consists of multiple adiabatic fixed-bed reactors with intercooling, since it avoids excessive temperatures inside the reactor [153]. El Sibai et al. [154] economically optimized a multiple adiabatic fixed-bed reactor, also accounting for the downstream separation units to meet purity specifications. They found that a configuration with three reactors and two intercoolers for water condensation was optimal.

The use of the cooled-reactor technology generally reduces the number of reactors and intercooling units in series. High-temperature-resistant diathermic oil can be used for heat removal [149], but hot spots can still occur. Other reactors like fluidized-bed reactors avoid the problem of hot spots thanks to the high degree of mixing, but friction has to be considered [153].

Further reactor types with a lower technological readiness level have also been proposed, e.g., hydrophilic membrane reactor [155] and the sorption-enhanced synthesis [156], where steam is removed in situ.

Regardless of the reactor type, the methane stream has to be purified. Most of the water can be separated via condensation. Further purification is needed to remove the small amount of unreacted CO_2 and the residual water if there are strict purity constraints on methane, as for injecting methane into the gas grid. A compression unit is usually included to reach the desired delivery pressure.

Finally, the direct integration of carbon capture and methanation could also be an alternative, e.g., if a Ni/CaO adsorbent is fluxed with hydrogen at a relatively low temperature (500 °C) [131, 132].

2.4.1.2. Biological methane production

Specific species of microorganisms (methanogens) can convert CO_2 and H_2 into methane in biological reactors [60]. Recent studies [157, 158] have shown that the direct injection of hydrogen into the anaerobic digester, which produces biogas (a mixture of CO_2 and CH_4), promotes the conversion of the residual CO_2 into methane since hydrogenotrophic bacteria are present. Up to 90 % of the injected hydrogen can be converted into methane, thus increasing methane production by over 20 %, although the increase of pH causes partial inhibition of methanogenesis from biomass [158]. This limitation can be overcome by feeding biogas and hydrogen into different reactors.

On the one hand, the low temperatures (< 100 °C) and pressures (< 10 bar), as well as the high selectivity of biological methanation reactors, are very attractive; on the other hand, biological processes are complex and difficult to operate. Furthermore, they have relatively low space-time yields [60]. Also, biological methanation from biogas is more suitable for small-to-medium size plants because of the typical size of anaerobic digesters [60].

Further, the economic viability of biological methanation is uncertain. The cost of biological methanation plants from biogas was found to be higher than the catalytic ones by Uebbing et al. [159], who solved a superstructure optimization problem. Nevertheless, further configurations, e.g., the direct injection of hydrogen into the anaerobic digester, should be considered for a holistic assessment.

2.4.1.3. Flexible operation of methanation plants

Process flexibility parameters are essential to optimize the process design while accounting for its operation and improve its off-design behavior. To this end, approaches like multi-period design optimization [152] or integrated process design and control [160] have been proposed for methanation. The optimization of both the process size and intermediate storage and plant has also been carried out [51].

Dynamic evaluations in the literature generally focus on the reactor behavior; only a few, e.g., Uebbing et al. [147], included the purification units. Several aspects of the reactor dynamics, such as start-ups, shutdowns, step and ramp tests, are reviewed in the following, and the key parameters are collected in Table 2.2.

Start-up and shutdown

Bremer et al. [161] proposed a 2D dynamic model of the first block of a 5 m-long fixed-bed tubular reactor with a cooling jacket to investigate and optimize the start-up procedure. The examined start-up procedure starts with a temperature step in the cooling stream that temporarily heats the reactants [161]. The results show that the time to reach the steady state is much higher than the residence time because of thermal inertia (around 500 s vs. around 5 s [161]).

Jürgensen et al. [150] simulated the warm start-up of a cooled multi-tubular reactor in Aspen Dynamics starting from a standby mode in which only hydrogen was fed into the reactor, and they validated the model against experimental data. They showed that the steady state is reached after around five times the residence time in the reactor, and that the product purity requirements are not met during this period. If the CO_2 source is biogas, the impure methane can be recycled back into the biogas reactor [150]. Similarly, Matthischke et al. [162] investigated the warm start-up behavior of a 1 m-long fixed-bed

reactor, both in adiabatic and cooled configurations with a recycle. They showed that the cooled reactor is faster than the adiabatic reactor in case of a warm start from 280 °C (around 200 s vs. around 400 s [162]) because less energy is required to heat the reactor.

The period after which a warm start-up is still possible was identified by Rönsch et al. [163] for a carbon monoxide methanation reactor with insulation. After four hours, the simulated temperature fell below 550 K, thus requiring reactant preheating to re-initiate the methanation reaction [163, 164].

The reactor temperature also plays a relevant role during the plant shutdown and idle periods. Before the shutdown, the reactor has to be fluxed with an inert gas like nitrogen or hydrogen [60, 163], and the reactor temperature should not fall below 503 K (depending on the catalyst) to avoid catalyst deactivation [163]. These aspects complicate the intermittent use of the reactor; thus, flexible but continuous operation should be preferred.

Biological reactors are less suitable for frequent start-ups and shutdowns than catalytic reactors since these reactors are characterized by long characteristic times. Immediate shutdowns of these plants are possible, but the restart could take more than 500 hours [60]. Depending on the microorganism, shorter start-up times are possible. For instance, only a few minutes are needed for the warm start-up if the plant restart is carried out within a few hours [25].

Load changes

The reactor concept affects the minimum reactor load and its flexibility. The minimum load of both adiabatic fixed-bed and cooled reactors is ca. 40 % of the nominal load [51], while it ranges between 10 % and 20 % for three-phase reactors [60].

The inlet temperature of the reactants is one of the most important variables to be controlled in methanation, especially if flexible. This temperature affects the position of the temperature peak in the reactor [164], and the stability of the reaction. In fact, for methanation reactors, a temperature hysteresis cycle exists: the ignition temperature is higher than the extinction temperature of the reaction and, therefore, a bi-stability region exists. Sun and Simakov [164] claimed that it would be preferable to avoid the bi-stability operating region for practical applications since sudden variations of the feed temperature could cause the extinction of the reaction. However, the stable operating region, hence flexibility, can be extended with a suitable control system, e.g., a cooling jacket with controlled coolant temperature or mass flow rate [165].

Several factors can affect the settling time after load variations. Matthischke et al. [166] pointed out that thermal inertia causes slower temperature responses than concentration responses [166]. Because of the importance of thermal inertia, even the design of the catalyst particles affects the dynamic behavior [167]. Similarly, reactor designs, as well as their size, can affect the process dynamics and responsiveness.

Further, product recycles could offer a further degree of freedom for controlling transients and increasing robustness to variations of the mass flow rates, although they are generally not necessary for methanation reactors. For instance, faster load variations can be achieved by adjusting the recycle ratio [166]. Also, recycles can contribute to extending the reactor flexibility and the operating range by reducing the risk of temperature hot spots and catalyst deactivation. Similarly, catalyst dilution over the reactor has been experimentally tested in a lab-scale (around 10 kW capacity) fixed-bed reactor to reduce temperature peaks [168] and potentially extend the operating range.

Several studies, both simulation-based and experimental, on load changes of methanation

plants can be found for different reactor types. Matthischke et al. [166] experimentally investigated the performance of a lab-scale fixed-bed reactor without recycle under ramp variations of the inlet flow. Ramp rates up to around 4 % min^{-1} were used [166]. Similar ramp rates (around 3 % min^{-1}) were suggested to be suitable for load changes without affecting the gas quality at the reactor outlet in a different study [51]. Ramp rates up to 10 % min^{-1} have also been reported [169].

A reactor with alternating cooling and reaction channels was simulated by Kreitz et al. [170] under variable hydrogen feed flow rates. Although the CO_2 flow rate was modified proportionally to the hydrogen flow rate, the purity requirements were not always met in their study [170]. Thus, they suggested inserting a purification unit, modifying the reactor design, or controlling other variables, e.g., the coolant temperature [170].

Lefebvre et al. [151] experimentally investigated a lab-scale slurry bubble column reactor, a promising alternative to the adiabatic fixed-bed reactor, under flexible operation, since the nearly isothermal temperature profile avoids the hot spot risk. It was noticed that the settling time changes if the step change of the gas velocity is positive or negative (around 10 and 40 minutes, respectively [151]). A similar behavior was experienced by Hermann et al. [168] in a lab-scale fixed-bed reactor. Hervy et al. [171] experimentally tested the flexibility of a demonstration-scale (400 kW capacity) fluidized bed reactor by varying pressure, reaction temperature, and H_2:CO_2 inlet ratio and showed that a stable regime and maximum conversion were reached in less than 30 minutes after the variation.

The dynamic behavior of a simplified model of a reactor under periodic inputs was investigated in silico by Güttel [172]. The reactor could self-stabilize and damp the fluctuation amplitude, especially when its period was lower than the residence time [172].

Concerning the flexible operation of biological methanation processes, only a few studies have been performed. In the model-based analysis with step tests performed by Bensmann et al. [157], the biological reactor exhibited slow dynamics (multiple days to reach the new steady state). Also, it was shown that biological reactors can operate during transients in conditions that are unfeasible at steady state [157].

Further, the high volumes and the slowness of biological reactors could also be advantageous in the case of highly fluctuating hydrogen flow rate, e.g., due to renewable power generation. In fact, biological reactors can act as hydrogen storage and dampen flow rate fluctuations. Moreover, certain microorganisms can survive a temporary interruption of the feed stream, thus allowing an operating range from 0 % to 100 % [25] (although the typical operating range is 60-100 % [25]).

2.4.2. Methanol

Methanol is one of the most produced chemicals since it can be used as a raw material for the synthesis of other chemicals (e.g., formaldehyde, formic acid, and acetic acid) and fuels (e.g., DME and kerosene), and its demand is expected to grow [50].

With its high energy density in terms of volume (nearly 80 % more than liquid hydrogen) and simple handling due to its liquid form, and its relatively easy synthesis process, methanol represents one of the most investigated uses of green hydrogen. Furthermore, e-methanol could be used as an energy and hydrogen storage medium [37].

2.4.2.1. Methanol production

Methanol can be produced from carbon dioxide and hydrogen either directly or indirectly. In the indirect route, CO_2 is reduced to carbon monoxide in a RWGS step (also see Section 2.4.3.1) and then converted to methanol. This process is also known as Carbon dioxide hydrogenation to form Methanol via a Reverse-water-gas-shift reaction (CAMERE) [173] and aims at using the know-how of methanol production from syngas. In the direct pathway, methanol is produced in one step. This leads to obvious benefits in terms of plant complexity, higher energy efficiency, and better economic feasibility [174]; thus, the direct pathway is the main focus of this subsection.

Reaction and operating conditions

Methanol synthesis from H_2 and CO_2 is an exothermic catalytic reaction that can be described by the following reaction network: i) CO_2 hydrogenation, ii) RWGS, and iii) CO hydrogenation:

$$\begin{aligned} CO_2 + 3H_2 &\rightarrow CH_3OH + H_2O \\ CO_2 + H_2 &\rightarrow CO + H_2O \\ CO + 2H_2 &\rightarrow CH_3OH. \end{aligned}$$

The operating temperature ranges between 220 °C and 280 °C [175] depending on the catalyst. High pressures allow higher conversions, since the overall number of moles decreases from the inlet to the outlet (Le Chatelier's principle). The operating pressure generally ranges between 50 bar and 100 bar.

Other than CO and H_2O, further components such as methane, ethers, formiates, aldehydes, and ketones, which are not generally included in the reaction scheme, form in traces and are removed via distillation. The amount of these side-products for the one-step route is lower than for the CAMERE process thanks to the lower reaction exothermicity that leads to fewer hot spots [175, 176]. However, the equilibrium conversion for the CAMERE process is higher than for the one-step process, since part of the water is removed from syngas before entering the methanol synthesis reactor.

Reactor configurations and process concepts

The reactors for methanol production generally have a multi-tube design and are externally cooled by evaporating water on the shell side. The generated steam can be exported for heat integration.

Since the one-pass conversion for methanol production is relatively low, a relevant fraction of unreacted gases is recirculated after the separation of crude methanol (a mixture of methanol and water) via condensation. Recycle streams are bigger in the one-step process than in the CAMERE one because of the lower conversion per pass, which has clear implications on the unit size and costs. Methanol is then separated from water via distillation to meet the purity requirements (generally higher than 99 wt.%). The higher water content in crude methanol of the one-step process increases the thermal duty of the distillation unit. Nevertheless, the direct pathway is more efficient [174] and does not require the RWGS unit.

Alternative reactor concepts, which are currently at a lower technological readiness level, are studied to increase the conversion per pass. Selective in-situ product removal is beneficial to shift the equilibrium toward the products. Selective water removal could be

particularly effective, especially for the one-step process where the water content is particularly high. For instance, a commercial copper-based catalyst combined with a molecular sieve for in-situ water removal was proven to increase methanol production [177]. Unfortunately, steam removal via adsorption cannot occur steadily because of the sorbent material saturation; therefore, periodical desorption phases are required. These drawbacks can be overcome if steam removal is performed via water-selective membranes [178].

2.4.2.2. Flexible operation of methanol plants

In the following paragraphs, the studies about the flexibility of methanol processes are reviewed, and the key flexibility parameters are summarized in Table 2.2. Information about the methanol process flexibility will then be used for optimizing the design of a flexible Power-to-Methanol process (Chapters 4 and 5).

Start-up and shutdown

Start-up and shutdown processes of methanol plants are rarely discussed in literature at the time of writing. During the start-up, the reactor has to be heated, e.g., via steam, but, to the best of our knowledge, there is no information about the start-up duration. Further, the effects of frequent start-ups are not reported in literature, since conventional plants are generally operated at steady state. However, it is mentioned that the catalyst suffers from deactivation, especially during idle periods, and it can take more than three days to fully recover its performance from 90 % of its activity [33].

Load changes

Dieterich et al. [33] reported that some commercial plants have a wide operating range (20-100 %); lower part-load limits might be problematic because the higher residence time inside the reactor could increase the risk of hot spots [179]. Nevertheless, this does not generally occur in reactors cooled via water evaporation thanks to the excellent heat transfer coefficient [33]. Also, wider operating ranges, e.g., 10-120 %, are possible if the process is designed to be operated flexibly [144].

Methanol production processes are particularly responsive since their load can be varied with relatively high ramp rates (5-13 % min^{-1}) [33]. Several setups under different operating regimes have been investigated to assess the influence of several operating strategies. For instance, Manenti et al. [180] noted from their model of a large-scale cooled fixed-bed multi-tubular reactor that a step variation of the shell temperature significantly affects the performance, while a step variation of the feed temperature does not. Furthermore, the settling times for step changes are on the minute scale [180, 181], thus making methanol reactors fast-responsive. In contrast, longer settling times, i.e., ca. 1 h, were obtained by Mbatha et al. [78] by modeling the methanol production process in Aspen Plus Dynamics. Furthermore, heat integration within the methanol synthesis unit can also induce thermal oscillations [78], thus increasing the settling time.

Seidel et al. [182] optimized a dynamic model of an isothermal reactor with respect to two objective functions (methanol outlet flow rate and methanol yield based on the total carbon in the feed) by simultaneously and periodically varying the CO concentration in the syngas feed stream and the total feed flow rate. They showed that this periodic feeding strategy improved the average performance over a period compared with the steady-state operation. For this evaluation, a kinetic model validated against experimental data

of dynamic tests [183, 184] was embedded in the model to better predict the catalyst dynamics. Similar performance improvements were obtained for a non-isothermal fixed-bed reactor [185].

A similar strategy was previously proposed by Velardi and Barresi [186] for a ring-reactor concept in which the feed stream is fed into one of the three adiabatic reactors without intercooling connected in series. Periodically shifting the feed position forces the reactor network to work dynamically. This strategy allows a more uniform use of the catalyst, the use of catalyst thermal inertia to heat the reactants, and the enhancement of methanol concentration [186, 187]. Furthermore, Velardi and Barresi [186] noted in their simulations that short switching times for the variation of the feed position are beneficial in terms of conversion. Nevertheless, proper switching times and controllers are required to maintain the reaction stable and avoid its extinction [187].

As an alternative to periodic feeding, fresh feed streams, e.g., hydrogen, can be injected along the reactor (or between the reactors if in series) to cool the mixture, improve thermal management, and thus reduce the formation of by-products, such as methane, in adiabatic reactors due to hot spots [188].

Other types of reactor networks, e.g., modular reactors in which some reactors can be bypassed in case of reduced feed rates, may offer additional flexibility but require higher investment costs [64].

The presence of distillation units in conventional methanol production is likely to be a bottleneck for fast transients without a significant impact on methanol purity. This problem could be partially circumvented with dedicated column designs or the introduction of intermediate storage for crude methanol [189]. At the same time, the latter would complicate heat integration and increase the investment costs [45] because additional tanks and controllers are required.

2.4.3. Syngas

Syngas or synthesis gas, a mixture mainly composed of carbon monoxide and hydrogen, is an important intermediate for the synthesis of several chemicals such as methanol and liquid fuels (also see Chapter 3). Currently, syngas is predominantly produced from fossil fuels, i.e., via methane steam reforming or coal gasification, but its production from CO_2 may be an alternative.

2.4.3.1. Syngas production

Syngas can be produced either electrochemically or chemically. CO_2 electrolyzers can produce syngas with a different H_2:CO ratio based on the operating conditions [63, 190, 191]. In the chemical route, syngas is produced via Reverse Water Gas Shift (RWGS) by reducing CO_2 to CO via hydrogenation. The H_2:CO ratio of syngas depends on the requirements of the downstream synthesis process, e.g., around 2:1 for methanol, DME, or Fischer-Tropsch (FT) synthesis.

The chemical route to syngas will be the focus of the following paragraphs.

Reaction and operating conditions

Carbon dioxide reduction occurs chemically through the RWGS reaction:

$$CO_2 + H_2 \rightarrow CO + H_2O.$$

As the RWGS reaction is endothermic, high temperatures are necessary to shift the equilibrium towards products. If the reactor is operated with conventional catalysts below 600 °C, methanation occurs instead of RWGS. Above 700 °C, the main product is carbon monoxide and only traces of methane are produced at atmospheric pressure. Although the equilibrium yield of the RWGS reaction does not depend on pressure (equimolar reaction), the formation of side products like methane does. At high pressures, methanation is relevant at higher temperatures; therefore, the operating temperature of RWGS should be even higher (at least 800 °C) to hinder its formation [192], making heat integration with other process units challenging (see Section 2.5).

Due to the kinetic limitations, several studies have been performed to improve catalyst selectivity and yield and achieve reasonable conversion rates at milder temperatures while avoiding methanation. A quite recent and detailed review of catalysts and kinetic mechanisms was carried out by Daza and Kuhn [193].

Reactor configurations and process concepts

The main RWGS reactor technologies are fixed and fluidized beds. Typically, fixed-bed reactors are preferred because of their simple design. However, they have some drawbacks, such as the need to shut the plant down for replacing the degraded catalyst and a slower response under flexible operation [194].

Fixed-bed reactors can be both adiabatic and heated. In adiabatic reactors, the inlet gas is at high temperatures (up to 1000 °C) and it gradually cools down (e.g., to around 800 °C) during the conversion, because of the endothermic reaction [192]. The achieved CO_2 conversion is around 80 %, and the residence time could be lower than 0.1 s, thus allowing high mass flow rates in compact devices. In fire-heated and electrically-heated reactors, heat fluxes and reactor temperature profiles can be used to optimize the conversion.

Achieving high CO_2 conversion is possible via stream recycling. For this purpose, the crude syngas at the reactor outlet is generally dehydrated via condensation and then partially recycled back to the reactor (see, for instance, Figure A.9). The feed of over-stoichiometric H_2 in the RWGS reactor promotes CO_2 conversion, thus reducing the recycle stream, and allows adjusting the H_2:CO ratio. However, it also promotes side-product formation, e.g., methane. Therefore, the excess of hydrogen in the feed stream has to be properly evaluated (see an example in Appendix A.8.1).

According to the syngas purity requirements, CO_2 and side products might need to be separated. Membranes and adsorption methods are generally preferred over absorption and cryogenic methods [195]. However, CO_2 removal is not always essential since several downstream processes, e.g., methanol synthesis [196], can tolerate or even convert CO_2.

RWGS in Chemical Looping (RWGS-CL) is an alternative RWGS technology. The hydrogen and carbon dioxide streams are fed into different reactor chambers containing a catalyst matrix (generally iron). H_2 oxidation and CO_2 reduction occur on the catalyst matrix: H_2 is oxidized by removing oxygen atoms from the iron matrix; CO_2 is reduced by supplying oxygen atoms into the matrix. The two streams are then periodically inverted. The unreacted CO_2 is then separated from carbon monoxide and re-fed into the reactor; the unreacted H_2 is dehydrated and recycled into the reactor or mixed with the CO stream to adjust the syngas composition.

RWGS-CL circumvents the formation of side products like methane since H_2 and CO_2 are not in direct contact [193]. Furthermore, it is particularly suitable for the production of almost pure carbon monoxide [197] since there is no direct addition of H_2, and the CO_2 can

be separated, e.g., via membranes. The energy demand for CO_2 separation from syngas in RWGS-CL is lower than in common RWGS [197], though it is a less mature technology.

Wenzel et al. [198] experimentally investigated an isothermal RWGS-CL with a modified iron oxide oxygen carrier material and proposed a kinetic model for the temperature range 750-850 °C. Research on catalysts for RWGS-CL is quite active. For example, the use of BaFe-hexaferrite allows stable operation at 350-450 °C [199]. The best design for a RWGS-CL reactor is also an object of interest [200].

Finally, promising outcomes could also come from the integration of the CO_2 capture and the CO_2 reduction process. For example, some adsorbent materials, e.g., Ni/CaO can capture carbon dioxide and release carbon monoxide with good selectivity if treated with hydrogen at temperatures around 700 °C [132]. Further, the CO_2 reduction phase can also occur electrochemically if a suitable electrolyte solution with CO_2 absorption properties is used for carbon capture [134].

2.4.3.2. Flexible operation of syngas plants

To our knowledge, the behavior of conventional catalytic RWGS units under flexible operation has not been investigated in the literature yet. This is likely since syngas is a gaseous intermediate, thus more difficult to store. Therefore, flexible operation of syngas production is likely only an option if the downstream process that converts syngas also operates flexibly.

Despite the lack of studies about flexible operation of conventional catalytic RWGS processes, a few considerations can be made. As the process is endothermic, the flexible operation does not lead to hot spots at partial load. However, high conversion rates due to higher residence times could lead to an excessive reactor temperature reduction, which could lead to catalyst deactivation. Thus, thermal management could be a crucial factor, especially if heat is provided by another process. Furthermore, the presence of a recycle is likely to allow an extension of the operating range, a shortening of transient times, and a damping of fluctuations in analogy with flexible methanation (Section 2.4.1.3).

In contrast, some information is available about the flexibility potential of RWGS-CL reactors, which are an intrinsically dynamic technology: the yield changes over time even for steady feed streams since the catalyst matrix gradually saturates [200].

RWGS-CL reactors could be particularly promising for the conversion of green H_2 thanks to their inherent decoupling of H_2 conversion and CO generation. To ensure the continuous operation of the system, the number of oxygen atoms deposited by CO_2 in the matrix is required to be equal to the number of oxygen atoms captured by H_2 when the feed streams are switched. This constraint can still be met if the H_2 flow rate is variable over time (e.g., according to the availability of renewable electricity): only the integral stoichiometric CO_2:H_2 ratio over a phase duration, and not the instantaneous stoichiometric ratio, must be constant. Thus, in case of temporary insufficient H_2 supply, H_2 could be used to adjust the H_2:CO ratio of syngas instead of also feeding the RWGS-CL reactor to remove oxygen from the matrix. Furthermore, this technology could potentially deal with variable H_2 production without the need for hydrogen storage.

Table 2.2.: Summary of the main flexibility parameters for the considered process units, besides the syngas production unit due to lack of data. Note that these parameters are configuration- and technology-dependent and might vary over time thanks to technological development. Also, their value can be affected by the process (unit) size.

	PEM water electrolyzer	Carbon capture with MEAs	Methane synthesis #	Methanol synthesis
Load range*	0-160 % [50]**	50 [135, 140] -130 % [135]	40-100 % [51, 60]	20-100 % [33]; 10-120 % [144]***
Max ramp rates	3.3 % s^{-1} [49]***-10 % s^{-1} [96]	N.A.	3-10 % min^{-1} [51, 169]; 4 % min^{-1} [166]***	5-13 % min^{-1} [33] or higher [144]***
Settling times	Few seconds [49]***	1-2 h [138]	Few minutes [168]***	$<$ 1 min [181]*** [180]; ca. 1 h [78]
Cold start-up time	Few minutes [49, 96]*** [59, 116]	20-60 min for absorption [135]; Up to 6 h for stripping [140]	Few minutes [161]	N.A.
Warm start-up time	$<$ 1 min [49]***[59]	N.A.	200-400 s [162]	N.A.

Catalytic in fixed-bed reactor. Other reactor types have different flexibility parameters.
* Relative to the nominal load.
** Operation at loads higher than the nominal one is possible, but only for short periods because of cooling reasons [49].
*** From experimental tests. (In the absence of this symbol ***, data are from simulations, or their origin is unknown).
N.A. Data not available.

2.5. System perspective: Process integration and flexibility

In the previous sections, we investigated individually the production of hydrogen and the separation of carbon dioxide, as well as their main one-step conversion processes. A similar approach is often found in the literature: most studies propose thorough models of just one process step or component by moving the others outside the system boundaries. In contrast, considering heat integration and interfaces between the process steps in terms of stream temperature, pressure, and purity levels could significantly change the optimal design and make PtX processes more competitive.

2.5.1. Process integration in Power-to-X processes

In the past few years, only a few analyses of integrated Power-to-X processes could be found in literature. Nevertheless, several comprehensive studies have been recently performed, thus tackling some of these system perspective shortcomings. For instance, Adelung et al. [201] built a model of a Power-to-Liquid (PtL) process including the electrolyzer, the CO_2 absorption unit, an oxy-fuel burner, and an RWGS unit to maximize the PtL efficiency by varying the operating conditions and performing heat integration among the units via pinch analysis. Hannula et al. [202] modeled a PtL process composed of a water electrolyzer, a RWGS unit, and a FT reactor, and investigated different ways of supplying high-temperature heat to the RWGS unit and the option of recycling FT tail gas into the RWGS to improve the carbon and energy efficiency. Similarly, Marchese et al. [203] presented an Aspen Plus model including a DAC unit, an RWGS unit, and a FT process to assess different configurations for the off-gas recirculation.

A few more process integration and optimization examples can be found for other processes, e.g., methanol production. For instance, heat integration between the one-step methanol production process and the carbon capture unit reduced its net thermal demand by 36 % in Van-Dal et al.´s case study [196]. Also, Mbatha et al. [78] investigated several PtMeOH process configurations with methanol synthesis reactors in series and parallel to assess their efficiency and dynamic response. Further, recent works [45, 46] focused on the optimization of PtMeOH processes in which both the electrolyzer and the methanol plant are operated flexibly.

However, most of these simulation-based studies neither consider nor optimize several heat and material interfaces that would improve the overall process efficiency. In the following paragraphs, the main interfaces between the PtX process units are discussed.

2.5.1.1. Material streams interfaces

Purity levels of the material streams at the interface between process units should be established according to the requirements, characteristics, and catalyst tolerance of the downstream processes. For instance, high-purity hydrogen might be unnecessary at the interface of the electrolysis unit in PtX processes, when it requires further compression or is mixed with a carbon dioxide stream that has some residual water. In contrast, oxygen, even if in traces, should be removed from the hydrogen stream, since it often poisons catalysts.

Temperature levels at the interfaces also play a relevant role, especially in energetic and economic evaluations. Some heat exchangers, e.g., coolers after the last compression stage, might be unnecessary if the material stream is heated afterward.

Also, the optimal process design can change depending on the operating temperature and pressure of the PtX units [101]. For instance, as mentioned in Section 2.2.2 for hydrogen pressurization, the optimal production pressure can change if the pressurization unit is considered in a design optimization problem. For example, for a given synthesis process, high pressures may improve the conversion, thus reducing the size of the conversion unit, but also increase the size and operating costs of the compression unit. The choice of the optimal operating pressure is even more important in the case of side-product formation or further processing of the product, as for syngas production via RWGS (see Section 2.4.3.1 and Appendix A.8.1) in FT synthesis plants.

Further, side products of the units could also play a relevant role in improving both efficiency and economic profitability. Oxygen, the main side product of water electrolysis, could be either sold or used for other applications, e.g., wastewater treatment plants [189], peroxide products [189], blast furnaces for steel production [50, 204], chlorine production via chlor-alkali electrolysis in the oxygen mode to reduce the power demand [205–208], and medical purposes [204, 209]. In particular, the sale of oxygen in the healthcare sector seems to be particularly beneficial to reduce the levelized cost of hydrogen [204], thus the e-product cost. Nevertheless, some technical challenges related to handling wet oxygen in the purification process need to be addressed since it is highly corrosive.

Also, oxygen could enrich or replace the combustion air of C-based fuels to reduce equipment size and ease CO_2 capture or improve the syngas quality if they are gasified [210]. A fraction of the produced oxygen could also be used to oxidize purge streams, which are always present in chemical plants (Figure 2.5). In this way, heat can be recovered and CO_2 easily captured and possibly recycled, thus reducing the direct CO_2 emissions of the process.

Finally, in some processes, purge streams such as tail gases of FT processes could be valorized via electrochemical oxidation, e.g., in fuel-assisted SO-WEs [8, 211], instead of being directly combusted for environmental and heat recovery purposes.

2.5.1.2. Heat streams interfaces

Heat integration is essential for achieving high energy efficiencies. Several integration options are available among the units of the considered Power-to-X processes. However, challenges arise in the case of flexible operation or the presence of intermediate storage. Thus, specific studies should be carried out.

The temperature of the exothermic reaction of both methane and methanol (see Table 2.3) allows exporting heat to other units, e.g., to the stripper of the CC unit (temperatures around 120 °C), the distillation column for methanol purification (temperatures around 100 °C), or the TSA unit for the purification of gases (the temperature depends on the adsorbent material and the component that has to be removed). For some energy-demanding applications like CO_2 stripping, reaction heat may not be sufficient. Nevertheless, additional low-to-medium temperature heat could be provided by other process units or generated via heat pumps or burning purge streams.

In contrast, the large amount of low-temperature heat from water electrolyzers is more difficult to use. Water electrolyzers could be coupled, for example, with anaerobic digesters

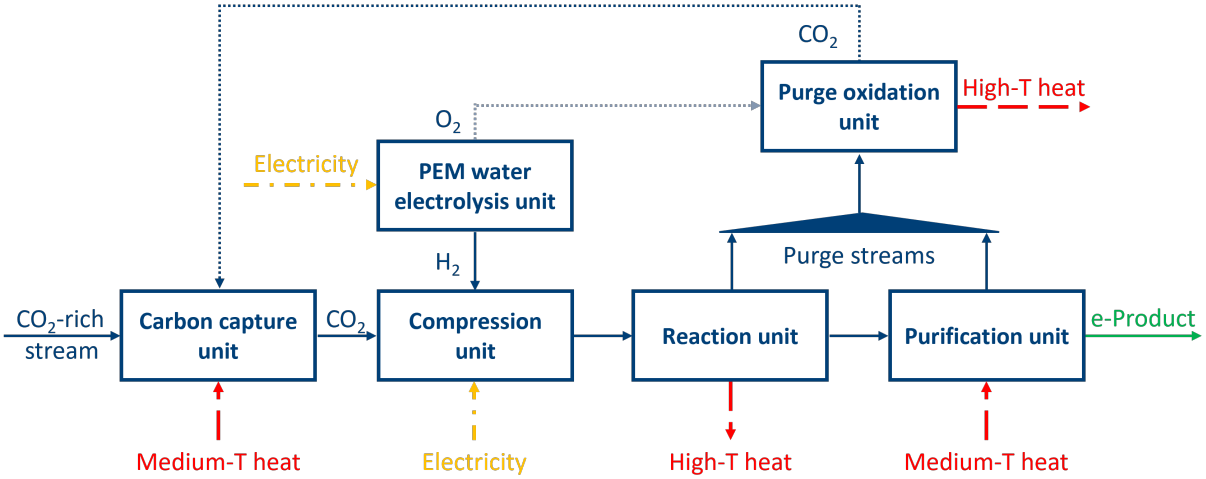


Figure 2.5.: Simplified sketch of a general Power-to-X process with an exothermic reaction unit for C-based chemicals production. The use of oxygen for the purge stream oxidation and the recycling of the resulting CO_2 stream are displayed (dotted lines). In contrast, the use of oxygen in the upstream CO_2-emitting unit, heat integration among the units, as well as heat recovery and conversion, are not shown.

when the produced biogas is upgraded to methane via hydrogenation (see Section 2.4.1.2), or low-temperature district heating. Alternatively, low-temperature waste heat could be upgraded with respect to temperature via heat pumps to meet industrial low-to-medium temperature heat demands [212] or converted into electricity via Organic Rankine Cycles (ORCs) [7, 213].

As regards conventional catalytic RWGS, the high operating temperature of the endothermic reactor makes heat integration more challenging: the most common downstream processes using syngas, e.g., the FT process, cannot provide such high-temperature heat. Furthermore, the heat from purge stream combustion would not likely be sufficient to run the catalytic RWGS. Alternatively, the reaction energy could be supplied via biomass combustion, tail gas combustion, or electric heating (the latter has been demonstrated only in pilot plants [25]). In the case the energy source is shifted to electricity instead of waste heat, co-electrolysis also represents a promising alternative for syngas production.

Table 2.3.: Summary of the main characteristics and possible interfaces of the process units of Power-to-X processes.

	PEM water electrolyzer	Carbon capture with MEAs
Input stream	Water	Flue gas after combustion
Input stream quality	High purity water	No specific requirements
Output stream quality	99.999 % H_2 if O_2 traces and H_2O are removed	$>$ 98 % CO_2 [140], saturated by steam with MEA traces
Useful side products	Oxygen	-
Typical operating temperature range	50-80 °C [50]	40-60 °C for the absorber; ca. 120 °C for the stripper [124]
Typical operating pressure range	1-30 bar [48]; 30-100 bar [50]	1-3 bar
Main energy inputs	Electricity: 4.2-5.6 kWh $Nm^{-3}_{H_2}$ [48]	Electricity: 80-130 kJ $t^{-1}_{CO_2}$ [124]; Heat: 2.2-3.8 GJ $t^{-1}_{CO_2}$ [124]

(a) Hydrogen and carbon dioxide supply processes.

	Methane synthesis (catalytic)	Methanol synthesis	Syngas synthesis (conventional RWGS)
Input stream	Syngas or CO_2-H_2 mixture	Syngas or CO_2-H_2 mixture	CO_2-H_2 mixture
Input stream quality	No components poisonous for the catalyst	No components poisonous for the catalyst	No components poisonous for the catalyst
Output stream quality	The achieved purity depends on the requirements. High purity if CO_2 and H_2O are removed	The achieved purity depends on the requirements. High purity ($>$ 99.9 %) if CO_2 and H_2O are removed	The achieved composition depends on the requirements
Useful side products	-	-	-
Typical operating temperature range	300-550 °C [60]	220-280 °C [175]	700-1000 °C [193]
Typical operating pressure range	1-100 bar [60]	50-100 bar [175]	1-10 bar
Main energy inputs	-	Electricity for reactant compression; Heat for distillation unit	Heat for the endothermic reaction

(b) Hydrogen-to-X processes.

2.5.2. Flexibility of Power-to-X processes

Despite the experience gained in the existing PtX plants [35], dedicated experimental studies of their overall flexibility are still missing. However, as shown in the previous sections, each unit of the considered PtX concepts is suitable for flexible operation to a certain extent depending on the process technology and configuration. Moreover, the process size affects the process responsiveness, as not all design parameters scale proportionally with it, e.g., surface-to-volume ratios, and some heat transfer and fluid dynamics effects could play different roles at different scales.

The water electrolysis unit can handle highly fluctuating power profiles while all the other process units are at least one order of magnitude slower (Table 2.2). This means that the less-responsive units slow the load variation of the electrolyzer unless buffer tanks for raw materials are considered. In fact, intermediate storage can decouple the operation of fast-responsive units like the electrolyzers from the less-responsive ones and dampen high-frequency fluctuations (Figures 2.2 b-c).

Beyond process unit responsiveness, wide operating ranges can positively affect the economics of flexible PtX processes. However, the different operating ranges across the process units affect the flexibility of the entire PtX plants, as shown by Herrmann et al. [214] for a Power-to-Methane case study without storage. Nonetheless, the use of intermediate storage could also overcome some of these limitations.

Several solutions on different scales (from the catalyst to the plant scale) could be considered to enhance flexibility [215]. In fact, most of the current chemical processes were designed according to the steady-state operation paradigm, thus meaning that additional flexibility could be gained by designing them with this operation paradigm shift in mind, as shown, for instance, by Fahr et al. [216] when designing a large-scale ammonia synthesis process. Moreover, novel optimal designs that integrate information about operation and uncertainties [22], e.g., the electricity availability and price, could make PtX processes more flexible and economically viable.

Among the considered PtX routes, Power-to-Methane and Power-to-Methanol processes were shown to be quite flexible in terms of operating range and possible ramp rates. In particular, the wide operating range allows a sensible reduction of start-up and shutdown procedures and/or storage needs. Their operating ranges could potentially be extended by applying strategies, e.g., increasing the inert or product fractions in the feed stream and decreasing the operating pressure of the reactors, which have been proposed and assessed for other exothermic reactors, e.g., ammonia reactors [71, 216]. Thus, these plants have the potential to handle quite fluctuating inputs with little or no intermediate storage for raw materials.

Although intermediate storage might not be needed in fast-responsive plants, it could still play a role in reducing operating costs and tackling variability: the reactants could be produced in excess during cheap electricity price hours or renewable power availability and stored to be converted into chemicals at a later time. However, the best process configuration highly depends on the case study, plant location, and investment costs for storage. Despite this crucial role, the optimization of storage capacity in PtX concepts has been considered in only a few recent works [45, 46, 51, 217, 218]. Therefore, the trade-off between flexible operation and need for intermediate storage in the optimal design of PtX processes is extensively investigated for a PtMeOH case study in Chapters 4 and 5.

Finally, dedicated studies and experimental works on the flexibility of entire PtX pro-

cesses should be performed to assess, and eventually exploit, the real potential of these technologies. Also, the role of process integration between the process units should be investigated, because it could affect flexibility and operation in off-design conditions.

2.6. Conclusion

In this chapter, we reviewed from a system perspective the main technologies involved in some key hydrogen-based Power-to-X processes with high defossilization potential in the chemical, transport, and energy sectors. In particular, we considered hydrogen production via PEM-WEs and CO_2 capture, and the main one-step C-based Hydrogen-to-X processes, i.e., methane, methanol, and syngas production. Moreover, we analyzed their flexibility and process integration perspectives to achieve higher efficiencies and cost-effectiveness.

From this analysis, the following conclusions about process unit flexibility can be drawn:

- PEM Water Electrolyzers, if equipped with suitable power electronics, can be flexibly operated up to providing ancillary services. Nonetheless, further research is needed to shed light on their degradation under flexible operation.
- Flexible operation of Carbon Capture processes is possible, although the response times are longer than for PEM-WEs.
- The investigation of the flexibility potential of Hydrogen-to-X processes is still at an early stage. Also, only a few works are experimental, which means that the validity of some of the findings should still be assessed experimentally. Furthermore, the flexibility ranges are often configuration-, technology-, and size-dependent. Under these caveats, the main parameters of the flexibility of the plant units at the current state have been summarized in Table 2.2, and some interesting aspects can be pointed out:
  - Chemical e-methane production seems to be suitable for flexible operation even on short time scales (minutes) if hot spots and reaction extinction are avoided via proper thermal management of the reactor. Warm and cold start-ups can be potentially carried out in a few minutes. However, their impact on catalyst deactivation should be investigated.
  - Biological methanation is not suitable for quick load variations of the methane production rate. However, the large size of reactors could serve as buffers in case of fluctuating hydrogen production rates if the reaction time of the biological system is much higher than the time of fluctuations. Furthermore, some microorganisms can survive short feed stream interruptions [25], thus meaning biological methanation could be suitable for direct coupling to renewable hydrogen production.
  - E-methanol processes are suitable for flexible operation since they have wide operating ranges and high ramp rates. Storing crude methanol and operating the distillation column as steadily as possible could be an interesting option to quickly vary the reactant feed flow rates, while still meeting the purity requirements. In that case, the main problem could arise from the typical heat integration between the reboiler and the synthesis reactor. Also, frequent idle

periods and start-ups do not seem appropriate, since the catalyst can suffer from deactivation.

– Literature about the flexibility of catalytic e-syngas production plants is almost absent, since syngas is an intermediate and is not easy to store as a gas. For this reason, flexible operation of e-syngas production should be considered together with the downstream synthesis process. Among the syngas production technologies, RWGS in Chemical Looping (RWGS-CL) seems to be particularly suitable for handling variable hydrogen inputs.

The considered PtX process units can therefore be operated flexibly and deal with fluctuating inputs to some extent, thus reducing the need for intermediate storage if directly coupled to renewable power generation. However, model-based and experimental investigations of the flexible operation of entire PtX processes are still rare to date. These analyses would increase the process understanding and enable the improvement of their overall system efficiency and economic competitiveness. Also, designing PtX processes while considering the presence of intermediate storage and information about their operation could potentially reduce production costs and the price gap with conventional fossil-based processes.

Further research should also shed light on catalyst degradation under flexible operation, since this aspect can affect the process economics and the optimal plant design and operation. For instance, if the electrolyzer degradation due to highly fluctuating power profiles is severe, the use of a small battery to smoothen such input power profiles could be investigated from an economic perspective. Also, the use of multiple electrolyzers designed to serve different operating purposes [79], e.g., steady-state vs. flexible operation to cover a base hydrogen production and exploit fluctuating power generation or electricity price profiles, respectively, could be investigated for large-scale PtX processes.

Finally, the economic competitiveness of PtX processes could be improved by optimizing the stream interfaces (e.g., purity, temperatures, and pressures) and mass and heat integration among the process units. Nevertheless, to date, relatively few studies consider process integration among different process units of PtX plants. We therefore highlighted the main opportunities for heat and stream integration for the investigated PtX processes. However, highly integrated processes are generally less flexible. Therefore, the performance of the identified optimal solutions needs to be investigated through dynamic models and experiments to assess their viability.

Among the identified literature shortcomings and challenges, in this work, we focus on two essential aspects that can significantly improve the economic competitiveness of hydrogen-based PtX processes:

- The analysis of some mass- and energy-integrated PtX concepts that consider biomass as carbon and energy feedstock (Chapter 3), since biomass utilization can reduce the size of water electrolyzers and the related electricity demand, which generally affect the production cost of e-chemicals and e-fuels significantly.

- The role of flexible operation and intermediate storage, as well as their interplay, in reducing the production costs when optimizing the design of a PtX process while simultaneously optimizing its scheduling for single and multiple scenarios (Chapters 4 and 5, respectively).

In contrast, degradation phenomena due to flexible operation and their effect on optimal process design, the optimal choice of electrolyzers in PtX processes, as well as the impact of heat integration on process flexibility, are not analyzed further in this work. These analyses would require dynamic models for the short time scales and very detailed process unit models, thus going beyond the scope of this dissertation, which investigates key trade-offs at the system level with steady-state or quasi-steady-state models.

3. Biomass Integration in Power-to-X Processes: Combustion vs. Gasification

As mentioned in Chapter 2, the production cost of e-chemicals and e-fuels in Power-to-X processes is generally affected by the high cost of the electrolysis units as well as the related energy demand. The utilization of biomass as an alternative feedstock can improve the economic viability of such processes if its energy content is properly exploited.

In this chapter, we therefore explore the potential of using biomass as a carbon and energy feedstock in Power-to-X processes (instead of captured carbon dioxide) by modeling and comparing two technologically mature thermochemical conversion pathways for integrating biomass into Power-to-X processes, as visualized in Figure 3.1. Moreover, this analysis identifies thermodynamic efficiency limits for mass and energy-integrated Power- and Biomass-to-X processes. Also, it shows that relatively simple steady-state models are sufficient to highlight inherent thermodynamic differences between combustion-based and gasification-based Power- and Biomass-to-X processes. Nonetheless, this modeling approach, which could be particularly suited for process screening before detailed modeling of promising processes, can exhibit some limitations when the production processes present significant nonidealities, as highlighted in a Power- and Biomass-to-Kerosene case study.

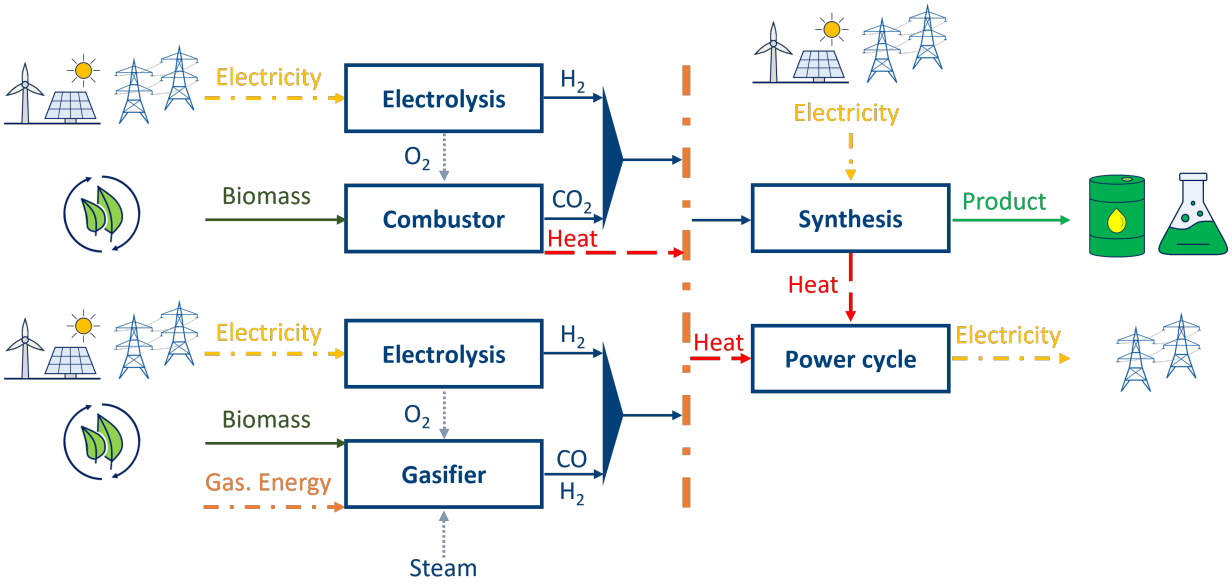


Figure 3.1.: Graphical representation highlighting the focus of Chapter 3, i.e., the comparison of combustion-based vs. gasification-based Power- and Biomass-to-X processes.

3.1. Introduction

In addition to low-carbon-footprint electricity, the synthesis of C-based products via Power-to-X processes requires a sustainable carbon source. As mentioned in Section 2.3, CO_2 captured from point sources or directly from air is often considered as carbon feedstock in PtX processes. However, as CO_2 has no valuable energy content, most of the energy demand of PtX processes is generally supplied via electricity. In contrast, residual biomass also has a valuable energy content that can be exploited in so-called Biomass-to-X (BtX) processes.

There are two biomass conversion pathways, i.e., biochemical and thermochemical, for producing chemicals in these BtX processes. Both biomass conversion pathways have advantages and disadvantages depending on the biomass feedstock and the target product. Further, synergies between these conversion pathways can be established, as thermochemical conversion can complement biochemical conversion. For instance, some biomass fractions can be directly and rather easily used for the production of valuable products, e.g., fermentable sugars, levulinic acid [219], and cellulose nanofibers [220], thus exploiting the existing functionalized molecular structures [221], while the residual fractions, e.g., lignin, require more intense conversion processes, e.g., termochemical conversion processes [222].

Several thermochemical conversion processes of biomass, e.g., pyrolysis, have been proposed, but combustion and gasification processes are the most mature [223, 224]. Combustion and gasification processes can convert almost any biogenic feedstock into some base intermediates, such as CO_2, CO, and H_2, which can then be used to synthesize chemicals. When green hydrogen is added to these bio-based intermediates, the combination of BtX and PtX is called Power- and Biomass-to-X (PBtX) or bio-hybrid process [39]. This combination can improve the conversion of bio-based carbon feedstocks and the cost-effectiveness [225]. For instance, ethanol production in PBtX processes resulted in a better trade-off of economic and environmental objectives than its production in either PtX or BtX processes [39]. Techno-economic trade-offs have also been shown for Power- and Biomass-to-Liquid (PBtL) processes [225–227].

Many works can be found in literature about these thermochemical conversion technologies, especially gasification [210, 223, 228, 229], and their modeling [224, 230]. For instance, different types of gasification processes have been compared concerning energy and exergy efficiency [230, 231]. Also, gasification units have been considered in BtX processes [232, 233]. However, a systematic comparison of the main thermochemical biomass conversion processes in the PBtX context that sheds light on their fundamental thermodynamic differences in the process efficiency is still missing. Although combustion-based PBtX processes are expected to be less efficient than gasification-based processes since the carbon atoms are first fully oxidized and then reduced, they offer practical advantages, e.g., in flue gas cleaning. Therefore, we want to quantify the efficiency differences between combustion-based and gasification-based PBtX processes when considering empirical parameters for the key process units, and identify the underlying thermodynamic reasons for such efficiency differences.

To this end, we perform a "back-of-the-envelope" analysis for PBtX processes synthesizing products with different C:H:O ratios, i.e., methane, methanol, dimethyl ether (DME), and dodecane. In particular, we model integrated PBtX processes composed of a biomass conversion unit based on either combustion or gasification, a low-temperature water electrolyzer, and a product synthesis unit. Additionally, a power cycle unit is considered to

convert heat from the exothermic units into electricity to reduce the net electricity demand of the PBtX process.

In this analysis, the process units are modeled with steady-state mass and energy balances. We intentionally keep the models simple and general, e.g., not dependent on reactor configurations, operating conditions, and catalyst performance, which might change due to technological improvements, in order to identify inherent efficiency differences between the considered PBtX processes and highlight their potential and limitations. Thus, the process efficiencies calculated with these simple and general models represent an upper limit for the efficiency achievable by real PBtX processes.

An exergy analysis is performed to compare combustion-based and gasification-based PBtX processes and identify the units that cause the main losses. Also, we evaluate the influence of some key process parameters, namely the electrolyzer and power cycle efficiencies, and the carbon feedstock composition, via a sensitivity analysis. Further, we discuss practical aspects that can affect the efficiency beyond the fundamental thermodynamic effects, as well as the cost.

Although the performed analysis based on relatively simple (or even simpler) models can be particularly effective to understand underlying thermodynamic differences and screen process alternatives in preliminary process design stages, it could exhibit some limitations when real processes deviate significantly from the considered simplifying assumptions, e.g., because of process nonidealities. We therefore verify the results obtained for the two biomass conversion pathways with the relatively simple models for a Power- and Biomass-to-Methanol (PBtMeOH) and a Power- and Biomass-to-Kerosene (PBtK) process modeled in detail. Moreover, these processes present significant differences: methanol synthesis does not present significant nonidealities (see Section 2.4.2.1), while kerosene-like fuel synthesis, e.g., via the conventional Fischer-Tropsch (FT) synthesis, often produces significant amounts of side products [25, 234, 235].

As synthetic kerosene is expected to play a significant role in the defossilization of the aviation sector [21, 236], we also investigate two promising pathways for kerosene production in combustion-based and gasification-based PBtK processes. Moreover, we first test the effectiveness of the "back-of-the-envelope" analysis for comparing Fischer-Tropsch (FT)-based and Methanol-to-Olefins (MtO)-based kerosene production pathways, and then benchmark the results against the outcomes of the detailed PBtK process models.

The remainder of this chapter is structured as follows: in Sections 3.2 and 3.3, the processes and the models considered for the back-of-the-envelope analysis are described, respectively. In Section 3.4, the PBtK case study as well as its model are introduced. Sections 3.5 and 3.6 present the main assumptions for the exergy analysis and the main results. Finally, the conclusions are drawn in Section 3.7.

3.2. Power- and Biomass-to-X process description

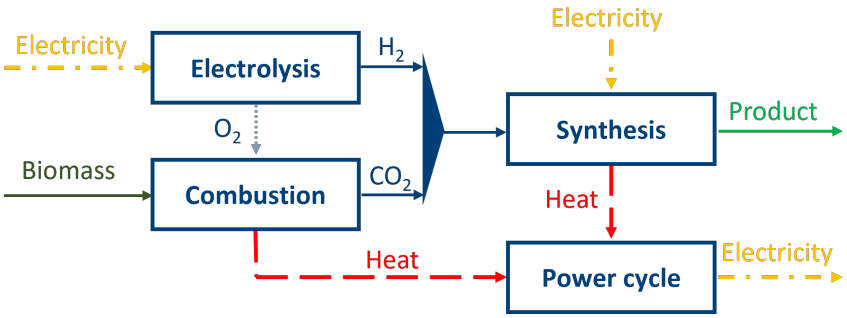
The considered PBtX processes are composed of four key units, i.e., the biomass conversion, the water electrolysis, the product synthesis unit, and the power cycle (Figure 3.2), which are mass and energy integrated.

Biomass is oxidized via either combustion or gasification by using pure oxygen (the side product of water electrolysis) or steam. The resulting stream is mostly composed of either CO_2 and water (in case of combustion) or syngas (in case of gasification). Although oxygen-

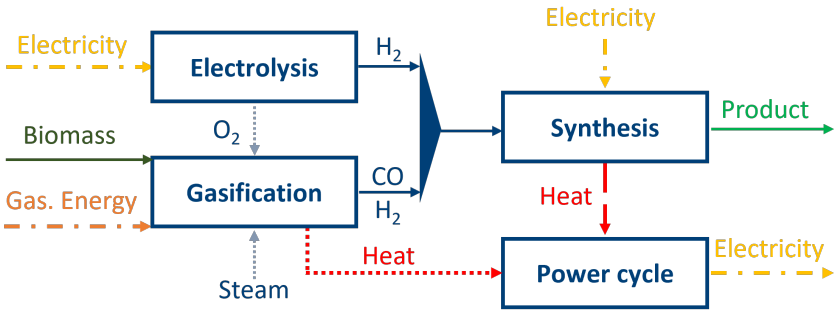
based gasification generally also occurs in the presence of some steam due to the residual moisture of biomass, the combination of oxygen and steam is not considered to isolate the effects of the pure oxidizing agents on syngas production and process efficiency. Also, the use of air as an oxidizing agent is not considered, since nitrogen would dilute the CO_2 or syngas stream, thus requiring an additional energy-intensive separation unit in real plants. Moreover, considering oxygen instead of air does not introduce any energy or economic penalties, e.g., for air separation. In fact, a sufficient oxygen stream is generally available in PBtX processes, thus highlighting the benefits of process integration (Section 2.5.1).

For combustion-based PBtX processes, the purified CO_2 stream at the outlet of the combustion unit is fed into the synthesis unit together with hydrogen produced by the low-temperature water electrolysis unit to adjust the H:C ratio of the mixture. The reactant stream is then converted into the target product in the synthesis unit, where it is separated from the side products. Similarly, for gasification-based PBtX processes, the purified syngas stream at the outlet of the gasification unit is supplied to the synthesis unit after adjusting the H:C ratio with additional hydrogen to synthesize the target product.

Additionally, the power cycle unit converts part of the high-temperature thermal energy of the exothermic units into electricity, thus reducing the net electricity demand of the overall PBtX process.



(a) Sketch of the PBtX process with biomass combustion.



(b) Sketch of the PBtX process with endothermic biomass gasification.

Figure 3.2.: Block flow diagrams of Power- and Biomass-to-X processes using (a) combustion or (b) gasification (the considered gasification agents, i.e., water and oxygen, are marked with dotted arrows). In case the gasification process is exothermic due to the operating conditions and the amount of supplied oxidizer, no additional energy input is needed, and the produced heat can be supplied to the power cycle (dashed arrow in (b)). Note: only the major material and energy streams are shown in the block flow diagrams.

3.3. Power- and Biomass-to-X process model

The models of the PBtX process units for the back-of-the-envelope analysis are based on steady-state mass and energy balances, and are written in Matlab. Ideal overall reaction conversion values (100 %) and no side reactions are assumed within the process units. This approach has the key advantage that the results are not affected by kinetics, whose performance depends on the chosen catalyst, reactor technology, and operating conditions, while it can still capture some inherent differences in efficiency between the considered processes. Furthermore, many real synthesis processes using selective catalysts approximate full conversion through recycling most of the unreacted reactants [31].

The process efficiencies calculated with these relatively simple models represent the upper limits in performance determined by the thermodynamics of the processes. To verify and validate the key trends, a more detailed model has also been built in Aspen Plus for a Power- and Biomass-to-Methanol case study (see Section 3.6.4).

In the following subsections, the main modeling equations and assumptions are discussed. A summary of the considered reactions and main assumptions is reported in Tables A.1 and A.2.

3.3.1. Biomass conversion unit

Biomass is converted into a suitable gaseous intermediate via either combustion or gasification to be fed into the synthesis unit. In the following, the models of the biomass feedstock and biomass conversion units are described.

3.3.1.1. Biomass

For all the considered biomass conversion processes, the inlet biomass is assumed to be composed of C, H, O, N, and S atoms and represented by the pseudo-molecule $C_xH_yO_zN_wS_t$, where x, y, z, w, and t are the molar fractions calculated from the ultimate analysis. Woody biomass (ultimate analysis in Table 3.1) is considered as the reference biogenic feedstock for the results in Section 3.6 and 3.6.5. Moreover, the feedstock is assumed to be dry and without ashes. In practice, the moisture in the biomass adds an energy penalty due to the heat required for its evaporation (heat from water condensation in the flue gas is generally not recovered). Also, the energy demand for biomass pre-treatment as well as for flue gas cleaning, including ash removal, is neglected. These modeling choices thus lead to identifying an upper bound to the overall PBtX efficiencies.

Table 3.1.: Ash-free dry biomass composition in wt.% (ultimate analysis) [237].

	x_C	x_O	x_H	x_N	x_S
Woody biomass (mean)	52.1	41.2	6.2	0.4	0.1

The higher heating value (HHV_{bio}) of the dry biomass is calculated via the correlation proposed by Sheng and Azevedo [238]:

$$HHV_{bio} = \left(-1.3675 + 0.3137 \cdot \frac{x_C}{\%} + 0.7009 \cdot \frac{x_H}{\%} + 0.0318 \cdot \frac{x_{O^*}}{\%}\right) \cdot \frac{MJ}{kg},$$

where x_C, x_H, and x_{O^*} are the mass fractions of carbon, hydrogen, and equivalent oxygen (sum of oxygen and other elements in the organic matter) from the ultimate analysis. The calculated HHV_{bio} of the dry ash-free woody biomass with the above composition is 20.7 MJ kg^{-1}.

The biomass lower heating value (LHV_{bio}) is then obtained by subtracting the energy for condensation of the water in the biomass oxidation products at 25 °C. The estimated LHV_{bio} of such biomass is 19.3 MJ kg^{-1}.

3.3.1.2. Combustion unit

In the model of the combustion unit, biomass is completely oxidized. The carbon, hydrogen, and sulfur atoms are oxidized to CO_2, H_2O, and SO_2, respectively, while the nitrogen atoms form N_2 (see Table A.1 for the reaction and Figure 3.3 for a sketch summarizing the molar flow rates).

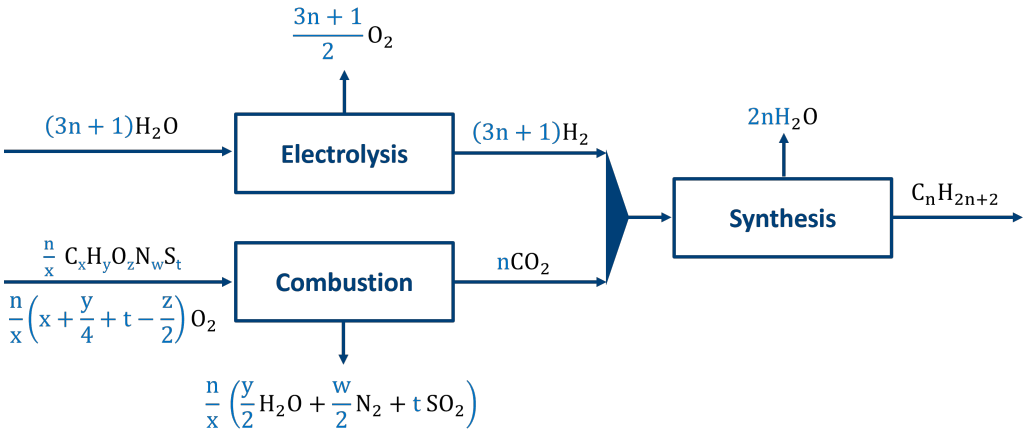


Figure 3.3.: Molar flow rates in the PBtX process with biomass combustion for the production of alkanes. The stoichiometric coefficients are shown in blue.

The oxygen contained in the biomass is used for the oxidation of biomass. Any additional oxygen that is needed to achieve the desired conversion is provided by the electrolysis unit (Subsection 3.3.2). In fact, the model shows that the electrolysis unit can always supply enough oxygen for the considered oxidation processes, although the electrolysis unit aims at satisfying the hydrogen demand of the product synthesis unit.

The maximum temperature assumed in the combustion unit is 1000 °C. The relatively low combustion temperature is motivated by the generally low melting point of biomass ashes. As the flame temperature of stoichiometric oxy-combustion is too high, a recycle of cold product gases within the unit is assumed to reach the desired combustion temperature. Nevertheless, the choice of the combustion temperature value does not affect the energy efficiency of the modeled unit, but only the exergy flows. In fact, the energy efficiency of the combustion unit, defined as the ratio between the energy output, i.e., the generated heat, and the energy input, is equal to 100 % under the considered modeling assumptions (ideal components and reactions, chemical energy of biomass estimated via the LHV, no compression energy for cold product gas recycle, and no heat losses). In contrast, lower energy efficiencies are achieved when nonidealities are considered as, e.g., in the detailed PBtMeOH model (see Section A.7).

The produced CO_2 is then separated from the N_2, SO_2, and H_2O before being supplied to the synthesis unit. No energy demand for CO_2 separation is considered in the energy balance. In real processes, SO_2 can be mostly removed with H_2O via condensation, while the small amount of N_2 can be either separated or not, since N_2 is generally an inert gas in CO_2 conversion processes. Furthermore, the need for separation might also depend on the tolerance of the catalyst of the downstream synthesis unit.

The whole energy content of biomass is transferred into the power cycle (Figure 3.2 a and Subsection 3.3.4) by cooling the flue gases from the operating to the ambient temperature. The CO_2 stream, which is assumed to be at ambient conditions at the interface to the synthesis unit, has no useful energy content (LHV=0). Further details and assumptions on the energy balance can be found in Appendix A.2.

3.3.1.3. Gasification unit

In the model of both oxygen-based and steam-based gasification units, we assume that all the carbon and hydrogen atoms in the biomass are converted to CO and H_2, while nitrogen and sulfur atoms form N_2 and SO_2, respectively. However, how carbon is oxidized differs among the two considered gasification processes. In particular, in the model of oxygen-based gasification, oxygen is added to partially oxidize all the carbon atoms as in Reaction (3.1). In the model of steam-based gasification, Reaction (3.1) occurs until the oxygen content in the biomass is depleted. Steam is then added to partially oxidize the remaining carbon and generate hydrogen as in Reaction (3.2). The overall conversion reactions and a sketch summarizing the molar flows for the two case studies can be found in Table A.1 and Figure 3.4, respectively.

$$\mathrm{C} + \frac{1}{2}\,\mathrm{O_2} \rightarrow \mathrm{CO} \tag{3.1}$$

$$\mathrm{C} + \mathrm{H_2O} \rightarrow \mathrm{CO} + \mathrm{H_2}. \tag{3.2}$$

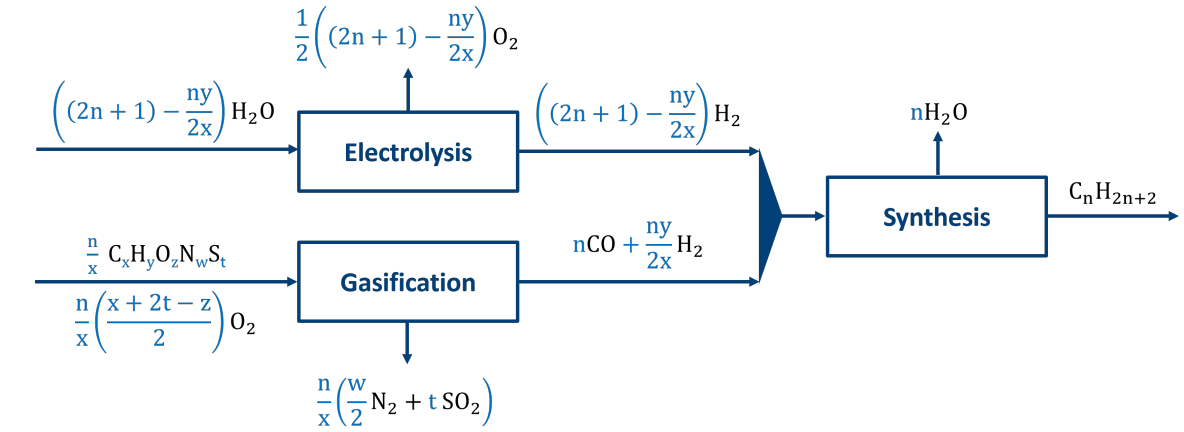
Depending on the biomass composition, operating conditions, and assumed conversion, biomass gasification can be exothermic or endothermic. If the biomass gasification process is endothermic (the typical operating condition), an energy input ($\dot{E}_{\mathrm{gas}}$) has to be supplied to drive the process. $\dot{E}_{\mathrm{gas}}$ results from the energy balance below:

$$\dot{E}_{\mathrm{gas}} + \dot{n}_{\mathrm{bio}} \cdot \mathrm{MW}_{\mathrm{bio}} \cdot \mathrm{LHV}_{\mathrm{bio}} = \dot{n}_{\mathrm{CO}} \cdot \mathrm{MW}_{\mathrm{CO}} \cdot \mathrm{LHV}_{\mathrm{CO}} + \dot{n}_{\mathrm{H_2}} \cdot \mathrm{MW}_{\mathrm{H_2}} \cdot \mathrm{LHV}_{\mathrm{H_2}},$$

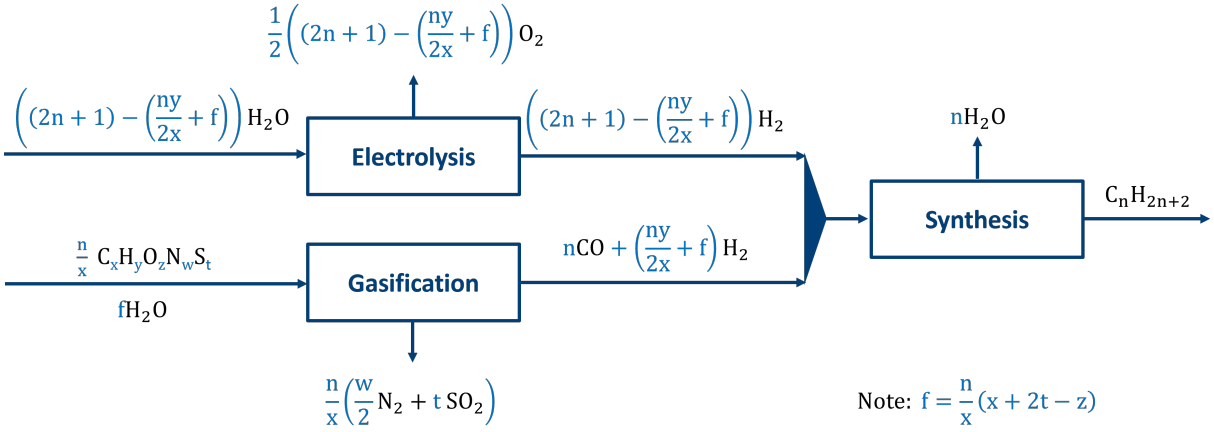
where $\dot{n}$ and MW are the molar flow rates and the molecular weights, respectively. If the biomass gasification process is exothermic, biomass represents the sole energy input and the biomass conversion unit produces high-temperature heat that is supplied to the power cycle (Figure 3.2 b).

Among the two considered gasification processes, steam-based gasification is expected to have a higher energy demand (when endothermic) than oxygen-based gasification because Reaction (3.2) is endothermic.

The whole energy demand $\dot{E}_{\mathrm{gas}}$, including heat for steam production, is considered to be supplied via electricity as the assumed gasification temperature is relatively high (900 °C, a typical value for biomass gasification [210]). Alternatively, other high-temperature heat sources, e.g., heat from the combustion of purge streams or solar energy stored in molten salts, could be used. In contrast, reversed Brayton-Joule cycles or heat pumps cannot



(a) PBtX process with biomass oxy-gasification.



(b) PBtX process with biomass steam-gasification.

Figure 3.4.: Molar flow rates in the PBtX process with biomass oxy-gasification (a) and steam-gasification (b) for the production of alkanes. The stoichiometric coefficients are shown in blue.

commercially achieve the target temperature of 900 °C [239]. Heat for steam production could also be supplied via heat integration with the synthesis unit, but this option has not been considered.

Similarly to the combustion unit, no energy demand for separating N_2 and SO_2 from H_2 and CO is considered. More details on the models and energy balances can be found in Appendix A.2.

3.3.2. Electrolysis unit

The electricity demand of the water electrolyzer ($P_{\text{el, WE}}$) is calculated by assuming a first law efficiency of the electrolyzer equal to $\eta_{\text{el, WE}} = 0.6$, a typical value for the mature low-temperature electrolysis technology [48], as follows:

$$P_{\text{el, WE}} = \frac{\dot{n}_{H_2} \cdot \text{MW}_{H_2} \cdot \text{LHV}_{H_2}}{\eta_{\text{el, WE}}}.$$

We assume an operating temperature of 60 °C, a typical value for low-temperature water electrolysis (Table 2.3).

The electrolysis unit produces excess heat since it is operated above the thermo-neutral voltage, as in typical operating conditions. The excess low-temperature waste heat could be used for biomass drying, for district heating, electricity production via ORCs, or upgraded with respect to temperature for industry applications [212, 240]. However, we assume that this excess heat is wasted due to its low temperature level.

The nominal hydrogen flow rate, which also affects the size of the electrolysis unit, depends on the considered pathway (combustion or gasification), target product, and biomass composition, since it is calculated according to the stoichiometry of the synthesis reactions. In particular, the gasification pathway requires a lower hydrogen flow rate (compare Figures 3.3 and 3.4).

3.3.3. Synthesis unit

The inlet stream of the synthesis unit is a CO_2-H_2 mixture or syngas for the biomass combustion and gasification pathways, respectively. The product is synthesized according to the reaction stoichiometry by assuming ideal conversion and no side reactions. For many products, real processes can achieve very high selectivity and almost complete conversion either in a single pass or by recycling unreacted reactants.

We consider the synthesis of four target products with significantly different C:H:O ratios and with high relevance for the chemical and transport sectors: the simplest alkane (methane), alcohol (methanol), and ether (DME), and a long-chain hydrocarbon representing the kerosene range of hydrocarbons (dodecane).

The synthesis reaction changes according to the feed stream composition (CO_2-H_2 mixture or syngas) and the considered product. For alkanes, the overall synthesis reactions from a CO_2-H_2 mixture and syngas are:

$$\mathrm{n\ CO_2} + (3\,\mathrm{n} + 1)\,\mathrm{H_2} \rightarrow \mathrm{C_nH_{2n+2}} + 2\mathrm{n\ H_2O}$$
$$\mathrm{n\ CO} + (2\,\mathrm{n} + 1)\,\mathrm{H_2} \rightarrow \mathrm{C_nH_{2n+2}} + \mathrm{n\ H_2O}.$$

The synthesis reactions for the other products can be found in Table A.1.

The exothermic synthesis reactions are assumed to occur at a typical (constant) reaction temperature. In particular, the considered reaction temperature is 400 °C for methane [60], 250 °C for methanol [175], 300 °C for DME [241], and 250 °C for dodecane [226] synthesis via low-temperature FT synthesis.

The energy demand for the compression of the reactants up to a typical reaction pressure is considered. In particular, the considered reaction pressure is 10 bar for methane [60], 75 bar for methanol [4], 10 bar for DME [241], and 25 bar for dodecane [226]. The electric energy demand is estimated by simulating a multi-stage compressor with intercooling in Aspen Plus. The heat removed in the intercooling section of the multi-stage compressor is not recovered, since there is no net heat demand within the synthesis unit or the other modeled process units (see modeling assumptions in Section A.2). Furthermore, compared to other PBtX process energy streams, this heat stream has a relatively low absolute value and average temperature level (ca. 100 °C); therefore, implementing a more advanced heat integration and conversion scheme would only result in a marginal improvement of the exergy efficiencies for the considered PBtX models.

No energy for product separation, e.g., via distillation, is considered in the energy balance. This assumption allows identifying thermodynamic efficiency limits that do not

depend on specific separation processes. Moreover, neglecting this contribution does not lead to a large overestimation of process efficiencies since the exergy efficiency of the product synthesis process is generally high (ca. 80-90 % as calculated by Bongartz et al. [31] with more detailed models of the production process of methane, methanol, and DME from a CO_2-H_2 mixture). Further information and assumptions on the energy balances can be found in Appendix A.2.

3.3.4. Power cycle unit

For all the considered pathways, the heat from the main exothermic units is converted into electricity in a power cycle unit, thus reducing the net electricity demand of the corresponding PBtX process. The first-law efficiencies of 40 % and 30 % are considered for the high-temperature (combustion and gasification unit) and medium-temperature (synthesis unit) heat sources, respectively. These efficiencies are comparable to the efficiency of a coal power plant and a steam power cycle using a high-quality residual heat source [213], respectively.

In contrast, the thermal energy from water electrolysis and water condensation in the biomass oxidation products and from compressing the synthesis unit reactants is not recovered and converted into electricity due to its low exergy content.

3.4. Power- and Biomass-to-Kerosene case study

Sustainable Aviation Fuels (SAFs), namely kerosene-like fuels, represent a promising short-to-medium term solution to defossilize the aviation sector thanks to their relatively high volumetric and gravimetric energy density, as opposed to hydrogen and batteries, respectively [236]. Also, kerosene-like fuels would not require replacing the existing aviation fleet.

Several pathways have been proposed for the synthesis of kerosene from hydrogen and either CO_2 (Power-to-Kerosene [203, 242–248]) or biomass (Power- and Biomass-to-Kerosene [8, 211, 225, 227, 249, 250]). Some of these, e.g., kerosene produced via the conventional Fischer-Tropsch (FT) process, have been formally approved for civil aviation (ASTM D7566 and D1655 [251, 252]) and the produced SAFs can be used as drop-in fuels.

As an alternative to the conventional FT process, a modification of the Methanol-to-Gasoline process, which is often called Methanol-to-Olefins (MtO) or Methanol-to-Jet process from the name of the intermediates or product, respectively, has been proposed [25, 242]. While the conventional FT pathway is often considered in PBtK processes, only a few very recent works [236, 250] focused on the modeling of the MtO pathway for kerosene production in the context of PBtK. Therefore, it is still unclear whether kerosene production via the MtO process is more efficient and has a lower production cost than kerosene produced via the conventional FT process. Further, an analysis that identifies the process units that mainly contribute to energy degradation in these processes is missing.

To cover these literature shortcomings, we model and compare a combustion-based and gasification-based PBtK process based on the FT and MtO pathways. Moreover, we compare the results of the relatively simple models (see modeling assumptions in Section 3.3) against the results of detailed PBtK models to assess whether the simpler modeling approach leads to similar conclusions.

3.4.1. Process description

For the investigated PBtK processes, we consider a biomass conversion unit (combustion or gasification unit), a hydrogen production unit, a kerosene synthesis unit, and a power cycle.

For the PBtK processes modeled with relatively simple models, the description of the process units is analogous to the one in Subsection 3.2. For the PBtK processes modeled in detail, the description of the processes is provided in the following paragraphs.

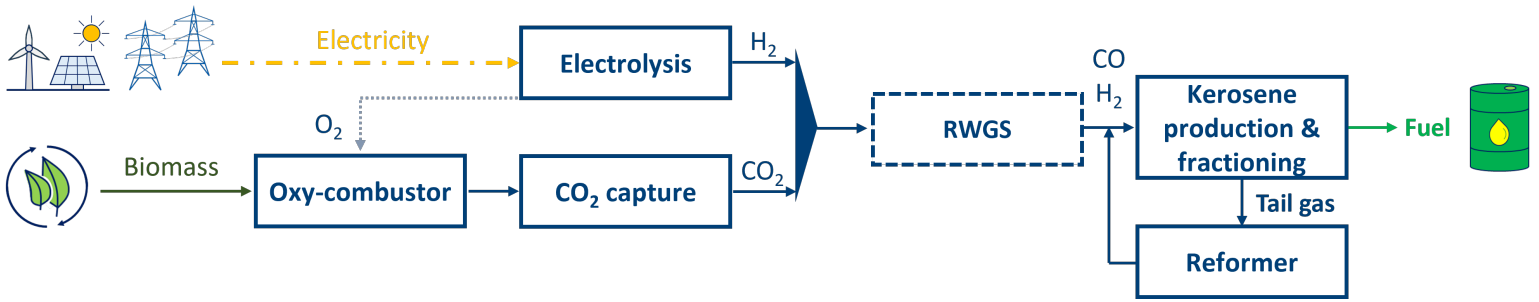
In the combustion-based PBtK process (Figure 3.5 a), biomass is oxidized using oxygen in slight excess to promote its conversion. This choice leads to high concentrations of CO_2 in the flue gas. Nevertheless, a CC unit is needed to obtain a pure CO_2 stream, since the residual oxygen in the flue gas can poison the catalyst of the downstream conversion units. The captured CO_2 stream is then mixed with the H_2 produced via low-temperature water electrolysis to adjust the CO_2:H_2 ratio according to the kerosene production pathway, i.e., either FT or MtO.

In the conventional FT pathway, the CO_2-H_2 stream is first converted to syngas in a RWGS unit and then supplied to the FT synthesis unit [25, 235, 242]. The produced hydrocarbon mixture is separated according to the carbon chain length via distillation. In particular, C_{5-7} (gasoline range), C_{8-16} (kerosene range), and C_{17-19} (diesel range) hydrocarbons are recovered. Lighter and heavier hydrocarbons are reformed and hydrocracked, respectively, to increase the selectivity of the process to the hydrocarbon range of interest.

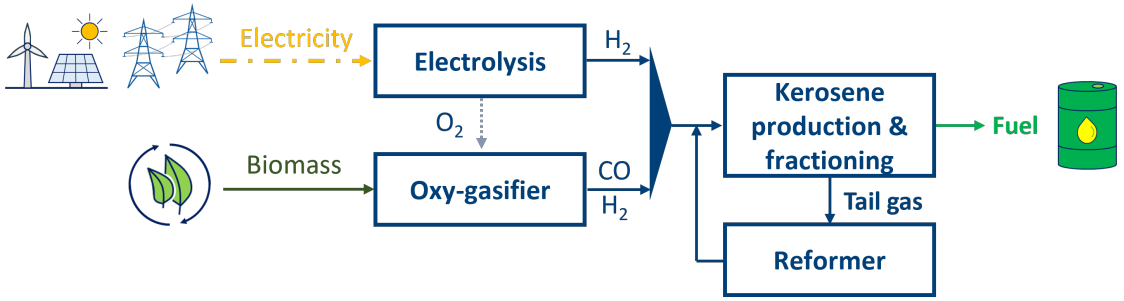
In the MtO pathway, the CO_2 stream is converted to methanol via direct hydrogenation (Subsection 2.4.2). The produced crude methanol is directly converted to short-chain olefins, which are then oligomerized [25, 242]. Finally, the long-chain olefins are converted into alkanes via hydrogenation [25, 242] before fractioning the resulting hydrocarbon mixture according to the hydrocarbon C-chain length.

In the gasification-based PBtK process (Figure 3.5 b), the main difference stands in the biomass conversion unit: biomass is partially oxidized to produce syngas instead of CO_2. Therefore, the CC and RWGS units are not included.

Finally, heat integration among the process units is carried out to reduce the hot utility demand to zero, thus improving the overall process efficiency. Furthermore, the residual process heat is supplied to either a steam power cycle or an ORC in the combustion-based and gasification-based processes, respectively, to reduce the process net electricity demand.



(a) Sketch of the combustion-based PBtK processes.



(b) Sketch of the gasification-based PBtK processes.

Figure 3.5.: Sketch of the combustion-based (a) and gasification-based (b) Power- and Biomass-to-Kerosene processes for both the FT and MtO pathways. Note that, in the combustion-based PBtK process via the MtO pathway, the RWGS unit (dashed) is not present since direct hydrogenation of CO_2 to methanol is considered. Also, note that heat integration among the units as well as the power cycle unit is not displayed to provide a clearer process representation.

3.4.2. Process model

The models of the PBtK process units for the back-of-the-envelope analysis are based on steady-state mass and energy balances, and ideal overall reaction conversion and selectivity values, as described in Section 3.3. Further, dodecane has been assumed as the representative hydrocarbon for a kerosene-like fuel.

The relatively simple FT-based and MtO-based PBtK process models only differ for the synthesis unit model: kerosene synthesis in the FT and MtO pathways is modeled as one and four sequential conversion steps, respectively (Figure 3.6). Each conversion step is modeled with an independent synthesis unit operated at typical reaction temperature and pressure conditions. Further information on these relatively simple unit models is provided in Section 3.3, and is therefore hereby omitted.

The following subsections describe the detailed steady-state models built in Aspen Plus of the considered PBtK processes.

3.4.2.1. Biomass conversion unit

Woody biomass (ultimate composition in Table 3.1) with 3.5 wt.% ashes and 10 wt.% moisture is modeled in Aspen Plus as a non-conventional component.

To model the biomass conversion processes, two reactor blocks are required in Aspen Plus. In the first reactor, biomass is decomposed into conventional components, e.g., C, H_2, and O_2. In the second reactor, the resulting components are oxidized either partially or fully based on the considered process, i.e., combustion and gasification. The two reactors are connected via a heat flow, so that the second reactor can supply the energy needed for biomass decomposition.

In the following paragraphs, a detailed description of the biomass combustion and gasification units is provided.

Combustion unit

In the biomass combustion unit, biomass is fully oxidized by using pure oxygen. Oxygen is fed in excess as recommended in the best references for large combustion plants [253] to achieve high biomass conversions (assumed 100 % conversion). Moreover, the excess of oxygen has been calculated to have a residual oxygen concentration in the dry flue gases of ca. 5 %.

To maintain an operating temperature of ca. 1000 °C, a typical temperature to avoid ash melting, a partial recycle of flue gases is considered to dilute the reactants and reduce the adiabatic flame temperature, which is relatively high due to the use of pure oxygen as the oxidizing agent. The recycle of relatively warm flue gases also allows preheating the reactants to ca. 175 °C. Such preheating temperature is within typical operating ranges (see, for instance, the Oxyplant in Schwarze Pumpe [254])

The ashes are assumed to be entirely removed from the flue gases after the combustion unit, e.g., via a cyclone. Also, no energy demand and costs for the flue gas cleaning treatment are considered.

The hot flue gases supply heat to the key high-temperature endothermic units, e.g., the RWGS unit. The residual high-quality heat is supplied to a power cycle (see Subsection 3.4.2.4) to reduce the net electricity demand of the PBtK plant.

As oxygen is generally poisonous for catalysts, a pure CO_2 stream is separated from the cold flue gases via amine washing (Subsection 2.3.2). A CO_2 capture rate of 90 %

is assumed in the built CC unit model based on Lee et al. [124]. The low-temperature heat for CO_2 stripping is supplied via heat integration. The captured CO_2 stream is then supplied to either the RWGS unit or the methanol synthesis unit, while the remaining flue gas is released via stack at a temperature above 100 °C.

To avoid the presence of a CC unit, biomass oxidation could be performed by supplying a slightly under-stoichiometric amount of oxygen. This process design choice reduces the investment costs, but also slightly reduces biomass conversion. Furthermore, it reduces the risk of catalyst poisoning if the oxygen content is not depleted due to incomplete combustion caused by poor mixing. This process configuration is not considered for the investigated combustion-based PBtK processes. In contrast, it is considered for the combustion-based PBtMeOH process (Subsection 3.6.4).

Gasification unit

In the biomass gasification unit, biomass is partially oxidized by using a mixture of oxygen and steam (ca. 0.87:0.13 ratio). Due to the scarcity of the oxidizing agent, biomass conversion is incomplete (assumed conversion of 95 %).

To avoid external heat sources and have an operating temperature of 900 °C, oxygen is fed in excess compared to the reaction stoichiometry (see Table A.1) to promote exothermic reactions, e.g., Reaction (3.1). The composition of the produced syngas is determined via an RGibbs reactor, which calculates the chemical equilibrium at the reaction conditions.

Similar to the combustion unit, the ashes and the unreacted biomass are assumed to be entirely removed from syngas after the gasifier. Also, no further flue gas cleaning is modeled.

The high-quality thermal energy of the syngas exiting the gasifier is used to supply heat to the endothermic units, e.g., the purge stream reformer, and to preheat the gasifier reactants to ca. 430 °C. The reactant preheating aims at reducing the excess of the oxidizing agent in the gasifier, thus improving the syngas quality. The residual low-temperature heat is partially converted into electricity in an ORC (Subsection 3.4.2.4).

Differently from the biomass combustion unit, no direct recycle of the flue gases (syngas) is carried out, since there is no need to reduce the reactor temperature. Nonetheless, a CO_2 stream is separated from syngas via a PSA unit and recycled into the gasifier for the gasification-based PBtK process via FT synthesis. This choice aims at reducing the downstream synthesis process size, since CO_2 does not generally react over conventional syngas-based catalysts for FT synthesis, and increasing the fuel production (carbon losses are reduced). Furthermore, CO_2 shifts the equilibrium in the gasifier, and reduces the need for external oxidizing agents. In contrast, CO_2 is not separated in the gasification-based PBtK process via MtO, since CO_2 is generally converted into methanol over conventional catalysts.

As the operation of the PSA unit is intrinsically dynamic, we consider average values for the key operating conditions based on the results of the detailed model proposed by Santos et al. [255] for a similar application. In particular, we consider a syngas inlet pressure of ca. 20 bar and a discharge pressure for CO_2 of 1.5 bar. An average pressure drop of ca. 3 bar is assumed on the syngas side. The considered selectivity values are collected in Table 3.2.

Table 3.2.: Considered selectivity values for the PSA unit (syngas side). Values based on Santos et al.'s work [255].

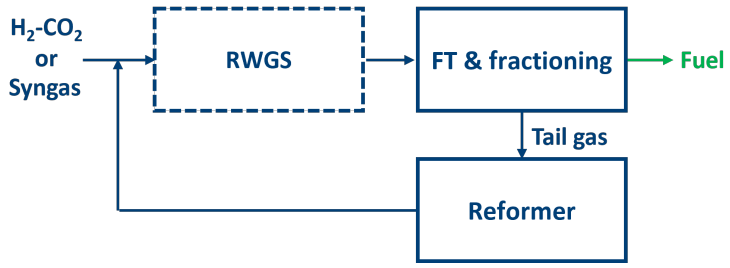
	CO	H_2	CO_2	CH_4	H_2O
Selectivity (%)	73.1	98.6	20.1	43.9	98.6

3.4.2.2. Water electrolysis unit

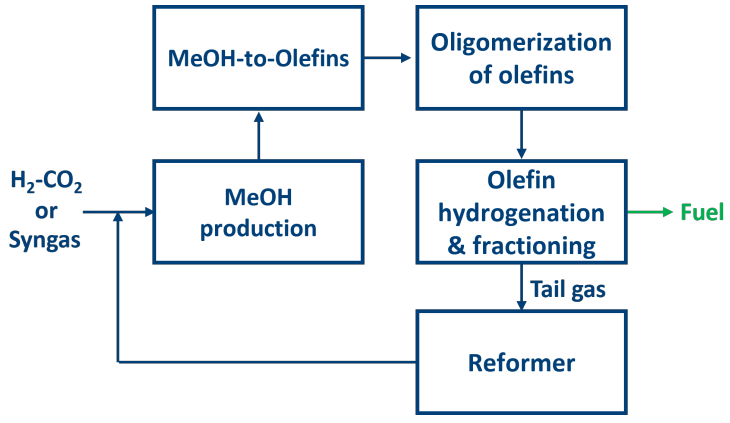
For the low-temperature water electrolysis unit, we consider a PEM-WE, and we assume an efficiency equal to 60 % and 59 % (based on the LHV) when H_2 is produced at atmospheric or high pressure (25 bar), respectively, based on the pathway. The size of the electrolysis unit depends on the considered pathway.

3.4.2.3. Kerosene synthesis unit

In the following paragraphs, the model of the two kerosene production pathways, i.e., the FT and MtO pathways (Figure 3.6), is described.



(a) FT pathway.



(b) MtO pathway.

Figure 3.6.: Sketch of the Fischer-Tropsch (a) and Methanol-to-Olefins (b) pathways for a H_2-CO_2 and syngas feed stream. Note that the RWGS unit (dashed) is not present in the gasification-based PBtK process via the FT pathway.

Fischer-Tropsch pathway

Although newly developed catalysts can directly convert CO_2 via hydrogenation [244, 245], the modeled FT pathway considers a conventional catalyst tailored for syngas. In particular, in combustion-based processes, syngas is produced from CO_2 via catalytic RWGS (see Appendix A.8.1 for further details on the RWGS unit model), while, in gasification-based processes, it is directly produced via biomass gasification (Figure 3.6 a).

Syngas conversion via FT synthesis is modeled analogously for the combustion-based and gasification-based PBtK processes. In particular, syngas is fed into a slurry bubble FT synthesis reactor with a Co-based catalyst [227] and converted into long-chain hydrocarbons. The kinetic model developed by Todic et al. [234] is embedded in the FT reactor model via a Fortran routine as in the work of Habermeyer et al. [227] (see Appendix A.8.2 for additional details). The implemented model considers an Anderson-Schulz-Flory (ASF) distribution for alkane and alkene formation with a carbon chain up to 30 carbon atoms. This kinetic model accounts for the deviation of methane and ethylene from the ASF distribution. In contrast, it neglects the formation of some side products, such as oxygenates and aromatics.

Syngas with a substoichiometric H_2:CO ratio (below 2) is considered to reduce methane formation as well as the hydrogen content in the purge stream. Further, an operating pressure of 25 bar and a relatively low operating temperature (225 °C) are chosen for the FT reactor. Moreover, low-temperature FT synthesis allows producing fuel mixtures, or syncrude, with a higher content of alkanes [25, 235], which is preferable for kerosene-like fuels.

The produced syncrude is cooled down to preheat the reactants for the FT synthesis and then fractioned via distillation. In particular, the liquid fractions corresponding to the gasoline range (C_5-C_7 hydrocarbons), kerosene range (C_8-C_{16} hydrocarbons), and diesel range (C_{16+} hydrocarbons) are separated from light and heavy hydrocarbons.

In conventional refining plants, the separated liquid fractions are generally further processed and purified to meet the fuel purity and property requirements. These additional process units have not been considered in the developed models, since the considered kinetic model for FT does not predict the formation of branched hydrocarbons and key side products such as oxygenates and aromatics; thus, the sizing of these units would have been subject to strong assumptions.

Light hydrocarbons are converted into syngas in a steam reformer, modeled as an RGibbs reactor, operated at 10 bar and ca. 800 °C, and then recycled into the FT synthesis reactor. Recycling the light hydrocarbon stream directly into the RWGS to be reformed is possible [202], but it exposes the catalyst to higher risks of carbon deposition. Therefore, this design option has not been considered. To drive the endothermic reforming reactions, high-temperature heat is supplied via heat integration. In particular, heat is recovered from either the biomass combustion or gasification units or from a combustion unit, where a fraction of the light hydrocarbons is combusted before being purged.

Heavy hydrocarbons are hydrocracked, and the resulting stream is recycled within the fractioning section to increase the process selectivity to the kerosene fuel range. Although kinetic-based models have been proposed for the hydrocracking reactor, e.g., by Gambaro et al. [256], including uneven cracking probability based on the carbon number and C-C bonds, a simpler modeling approach has been chosen. In the implemented hydrocracker model, 70 % of the alkenes are hydrogenated, and 70 % [257] of the long-chain hydrocarbons

are cracked in the middle of their carbon chain by assuming an even cracking probability across the considered carbon range. Also, only primary cracking is assumed.

Methanol-to-Olefins pathway

The MtO pathway requires more conversion steps than the FT pathway (Figure 3.6). In particular, methanol is produced from either a CO_2-H_2 mixture (combustion-based PBtK process) or syngas (gasification-based PBtK process). Methanol is then converted into short C-chain olefins via dehydration (Reaction 3.3). Short C-chain olefins are oligomerized to increase the C-chain length (Reaction 3.4), before being hydrogenated to alkanes (Reaction 3.5) and fractioned.

$$n\mathrm{CH_3OH} \rightarrow \mathrm{C}_n\mathrm{H}_{2n} + n\,\mathrm{H_2O} \tag{3.3}$$

$$m\mathrm{C}_n\mathrm{H}_{2n} \rightarrow \mathrm{C}_{\mathrm{n\cdot m}}\mathrm{H}_{2\mathrm{n\cdot m}} \tag{3.4}$$

$$\mathrm{C}_{\mathrm{n\cdot m}}\mathrm{H}_{2\mathrm{n\cdot m}} + \mathrm{H_2} \rightarrow \mathrm{C}_{\mathrm{n\cdot m}}\mathrm{H}_{2\mathrm{n\cdot m+2}} \tag{3.5}$$

The methanol synthesis unit is modeled similarly to what is described in Appendix A.7. However, no methanol purification via distillation is considered since the methanol oligomerization catalyst can generally handle methanol-water mixtures as feed streams [25, 236, 258, 259]. This highlights once more the importance of considering a holistic approach for process system design (Subsection 2.5.1).

Crude methanol conversion into short C-chain olefins, i.e., C_2-C_5, is modeled via a conversion reactor. In particular, the reactor is operated at nearly atmospheric pressure and at 375 °C, which conditions allow a methanol conversion of ca. 100 % over a SAPO-34 catalyst [258]. Furthermore, all produced C_x compounds are assumed to be alkenes, and the formation of other side products is neglected due to the generally high catalyst selectivity.

The oligomerization of short C-chain olefins is modeled via a single conversion reactor. In other works [246, 247], short C-chain olefins are first separated based on their C-chain length; these are then oligomerized as pure olefins in different reactors, and the resulting olefin streams are mixed. Although this approach enables optimizing the reaction conditions and the catalyst for every oligomerization reactor, significantly higher investment costs are required for the additional process units. Thus, this process configuration has not been modeled. In contrast, the oligomerization of the short C-chain olefin mixture is modeled under the assumption that the considered oligomerization reactions occur in parallel.

Although the oligomerization of olefin mixtures is indeed possible [235], kinetic models, e.g., based on an adjusted ASF distribution [248, 250], are seldom available in literature [25]. In the lack of suitable kinetic models, the oligomerization reactor has been modeled as a conversion-based reactor. The conversion factors of the oligomerization reactions are estimated from experimental works on the oligomerization of pure olefins (ethene [260], propene [261], butene [262], pentene [263], and hexene [261]) over acidic zeolite catalysts operated at similar reaction conditions (ca. 40 bar and 225 °C). The considered conversion factors are reported in Table A.9. Due to the relatively low conversion per pass, short C-chain olefins are separated via distillation and then recycled into the oligomerization reactor.

Finally, long C-chain olefins are converted into paraffins via hydrogenation [236, 264] (assumed conversion of 99 % at 30 bar and 320 °C), before being separated. Similarly to

the modeled FT pathway, light hydrocarbons are reformed, and the produced syngas is supplied to the methanol plant. In contrast, long C-chain hydrocarbons such as C_{20+} and waxes are generally not produced given the high selectivity of the MtO pathway.

3.4.2.4. Power cycle unit

Residual process heat is supplied to the power cycle unit to reduce the net electricity demand of the PBtK processes. Due to the different quality and quantity of residual heat, a steam power cycle and an ORC are modeled for the combustion-based and gasification-based processes.

In combustion-based PBtK processes, residual high-temperature heat from the combustion unit and reforming unit, as well as medium-temperature heat from the other process units, is supplied to the steam power cycle. The steam power cycle is designed with three levels of steam pressure (100 bar, 35 bar, and 3 bar). The condensation pressure is set to 0.075 bar ($\approx$ 40 °C). The three turbine stages are modeled with an isentropic and mechanical efficiency of 90 %. Moreover, the maximum turbine inlet temperature is assumed equal to 550 °C; a minimum steam quality of 98 % at the turbine outlets is considered. Higher maximum pressures and temperatures are technologically possible and applied in conventional steam power cycles. However, they require more expensive equipment, which is generally not worth it for power cycles converting waste heat. Finally, some low-pressure steam is drawn before the final expansion turbine stage to supply heat to the reboiler of the stripping column of the CC unit (Subsection 3.4.2.1).

The preliminary process design of the steam power cycle (sketch in Figure 3.7) was obtained by maximizing the electric power output via black-box optimization (similarly to what is described for the RWGS unit in Appendix A.8.1) for a similar case study, i.e., a Power-to-Kerosene (PtK) process, which is not shown in this thesis. The preliminary design was then adapted to the specific case study.

In the gasification-based PBtK processes, a lower amount of lower-quality residual heat is available. An ORC with an efficiency of 15 % [213] is considered for power generation. No detailed model is built for the ORC unit.

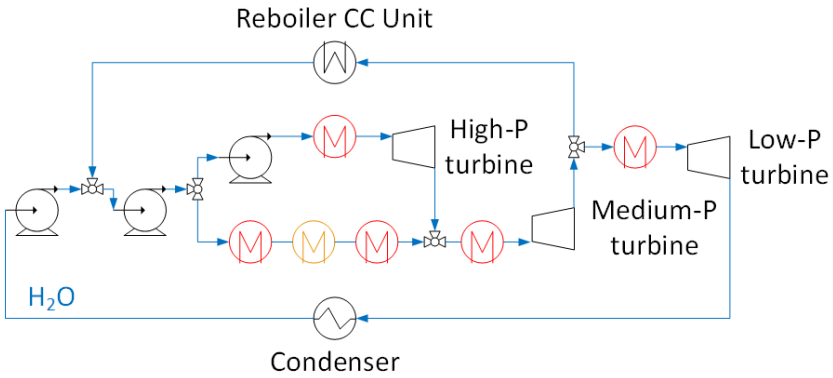


Figure 3.7.: Simplified sketch of the modeled steam power cycle. High-temperature heat is provided via heat integration with the flue gases and exothermic process units (heat exchangers marked in red and orange, respectively).

3.5. Exergy analysis

An exergy analysis of the PBtX processes is performed to compare the biomass combustion and gasification pathways and identify the process units that are mainly responsible for energy degradation.

The exergy balance of each process unit can be written as follows:

$$\sum_{j=1}^{\mathrm{Q_{in}}} \dot{\varepsilon}_{\mathrm{q\ in},\,j} + \sum_{j=1}^{\mathrm{M_{in}}} \dot{\varepsilon}_{\mathrm{m\ in},\,j} = \sum_{j=1}^{\mathrm{Q_{out}}} \dot{\varepsilon}_{\mathrm{q\ out},\,j} + \sum_{j=1}^{\mathrm{M_{out}}} \dot{\varepsilon}_{\mathrm{m\ out},\,j} + \dot{W} + \dot{\varepsilon}_{\mathrm{loss}}, \tag{3.6}$$

where $\dot{\varepsilon}_{\mathrm{q}}$ and $\dot{\varepsilon}_{\mathrm{m}}$ are the exergy flows related to heat flows and material streams, respectively, $\dot{W}$ the work exchange, and $\dot{\varepsilon}_{\mathrm{loss}}$ the exergy losses for the considered unit. In this work, the term $\dot{\varepsilon}_{\mathrm{loss}}$ accounts for not only the irreversibilities, e.g., mixing of the reactants, but also the exergy in the side products, namely water, N_2, and SO_2.

For the back-of-the-envelope analysis, the exergy flow related to heat flows in the process units ($\dot{\varepsilon}_{\mathrm{q}}$) is calculated by considering the typical reaction temperature of each unit as described in Appendix A.4.1. In contrast, the exergy flows due to the preheating of the reactant stream and the cooling of the product streams are not considered since perfect heat integration within the unit is assumed to minimize the energy demand and the exergy loss (see Appendix A.2 for more details on heat integration of the units). For the exergy analysis carried out with the detailed PBtMeOH and PBtK process models, $\dot{\varepsilon}_{\mathrm{q}}$ has been estimated more accurately (see Appendix A.4.1).

The exergy flow related to material streams ($\dot{\varepsilon}_{\mathrm{m}}$) is composed of four contributions, i.e., kinetic, potential, physical, and chemical. The kinetic and potential contributions are often negligible. The physical contribution, which is related to the stream temperature and pressure, is null since we assume that all the material streams at the unit interfaces are at ambient conditions (T_0=298 K, P_0=1 bar) for the back-of-the-envelope analysis. In contrast, the physical exergy contribution is estimated as described in Appendix A.4.2 for the detailed PBtMeOH and PBtK process models. The chemical contribution of $\dot{\varepsilon}_{\mathrm{m}}$ is calculated as in Appendix A.4.3.

The chemical exergy related to the oxygen and water feed streams is also considered. Recycling the produced water in the synthesis and combustion units, as well as the oxygen, reduces the net exergy demand of reactants ($\dot{\varepsilon}_{\mathrm{rectants,\,net}}$), although it plays a marginal role in the overall process efficiency. In contrast, the exergy demand for separating the target product from the side products is neglected in the back-of-the-envelope analysis.

The overall exergy efficiency for the PBtX processes is calculated as follows:

$$\eta_{\mathrm{ex,\,PBtX}} = \frac{\dot{\varepsilon}_{\mathrm{product}}}{\dot{\varepsilon}_{\mathrm{biomass}} + \dot{\varepsilon}_{\mathrm{reactants,\,net}} + \dot{W}_{\mathrm{net}}},$$

where $\dot{\varepsilon}_{\mathrm{product}}$ is the exergy content of the product, $\dot{\varepsilon}_{\mathrm{biomass}}$ the exergy content of biomass, $\dot{\varepsilon}_{\mathrm{rectants,\,net}}$ the exergy content of the other reactants (water and oxygen), and $\dot{W}_{\mathrm{net}}$ the net electricity demand, which also includes heat for gasification ($\dot{E}_{\mathrm{gas}}$) in case it is endothermic.

3.6. Results and discussion

In the following, the results of the exergy analysis performed by using relatively simple combustion-based and gasification-based PBtX process models are presented. Furthermore, a sensitivity analysis of the key process parameters is performed, and the key aspects of the practical implementation of these processes are discussed. Finally, we discuss the suitability and limitations of these relatively simple process models by comparing the results with those obtained via detailed process models for a PBtMeOH and PBtK case study.

3.6.1. Power- and Biomass-to-X: Back-of-the-envelope analysis

Among the different target products, the production processes of methane and dodecane have the lowest exergy efficiency (Figure 3.8). The main reason is that their production needs the highest number of hydrogen moles per mole of carbon. In contrast, the production processes of methanol and DME have the highest exergy efficiency since a lower number of hydrogen moles is needed based on the reaction stoichiometry (Table A.1). Nonetheless, it is important to mention that the calculated exergy efficiencies represent an efficiency benchmark for real PBtX processes due to the considered models, which combine nearly ideal assumptions, e.g., no side reactions and perfect heat integration, and empirical efficiency parameters (see Section 3.3 and Table A.2).

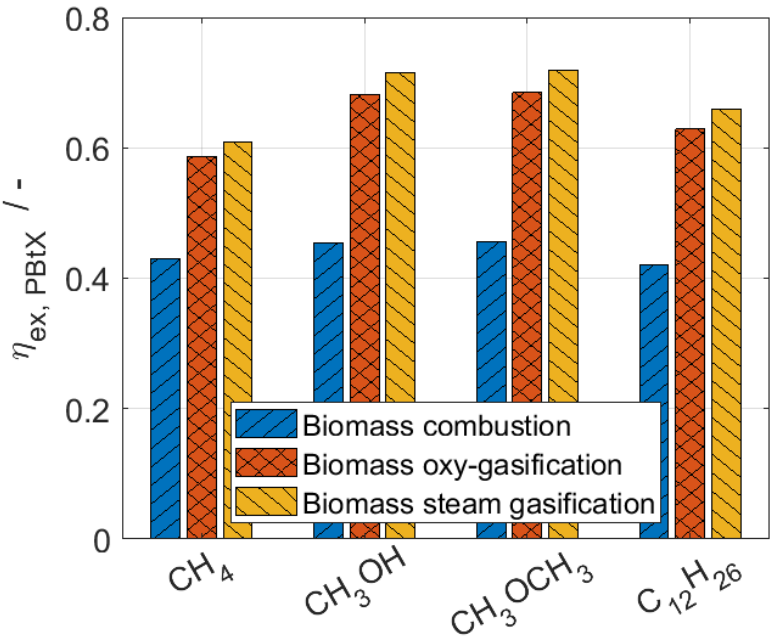


Figure 3.8.: Exergy efficiency of Power- and Biomass-to-X processes with biomass combustion and gasification for different products "X". Woody biomass is considered as carbon feedstock [237].

The results also show that gasification-based PBtX processes are significantly more efficient than combustion-based ones (around 15-20 percentage points) under the considered assumptions (Figure 3.8). A part of this efficiency difference is due to the high exergetic

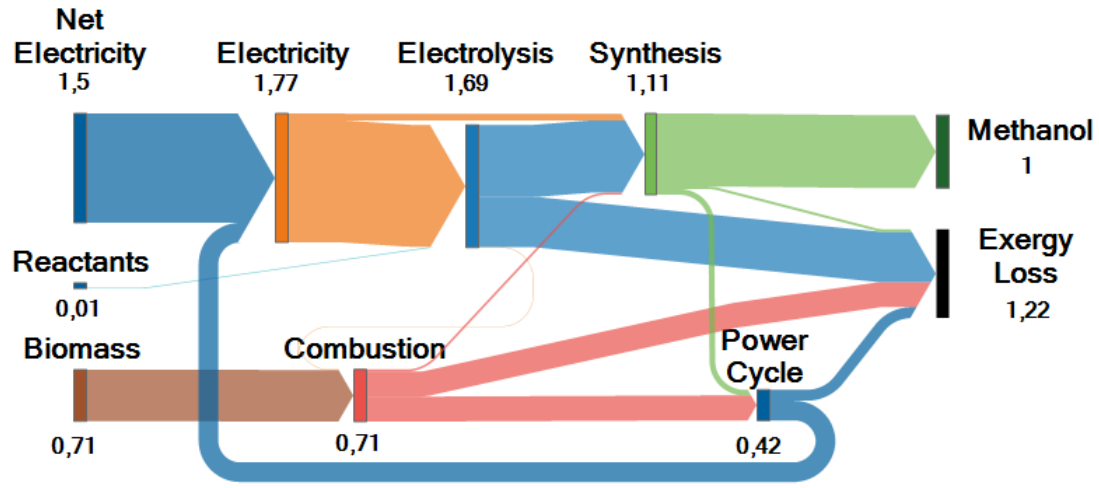
losses of the combustion unit: although the energy efficiency is assumed to be 100 %, the conversion of chemical to thermal energy causes significant energy degradation, resulting in an exergy efficiency of the combustor lower than 55 % (Figure 3.9 a for PBtMeOH). In contrast, gasification processes avoid the conversion of high-quality chemical energy into lower-quality thermal energy since the energy of biomass is transferred into the produced syngas, thus leading to higher exergy efficiencies (around 85 % in Figure 3.9 b-c).

Further, gasification-based processes can already produce part of the hydrogen needed for the downstream synthesis unit and do not require additional hydrogen to convert CO_2 into CO (RWGS reaction) due to the different reaction stoichiometry. The combination of these two effects significantly reduces the amount of hydrogen supplied by the electrolyzer, which is responsible for large exergy losses, and thus the energy input supplied via electricity. In fact, the higher electricity production in the power cycle of the combustion-based pathway cannot offset the higher electricity demand of the electrolyzer, thus leading to a higher net electricity input (> 45 % for methanol production) and a lower exergy efficiency.

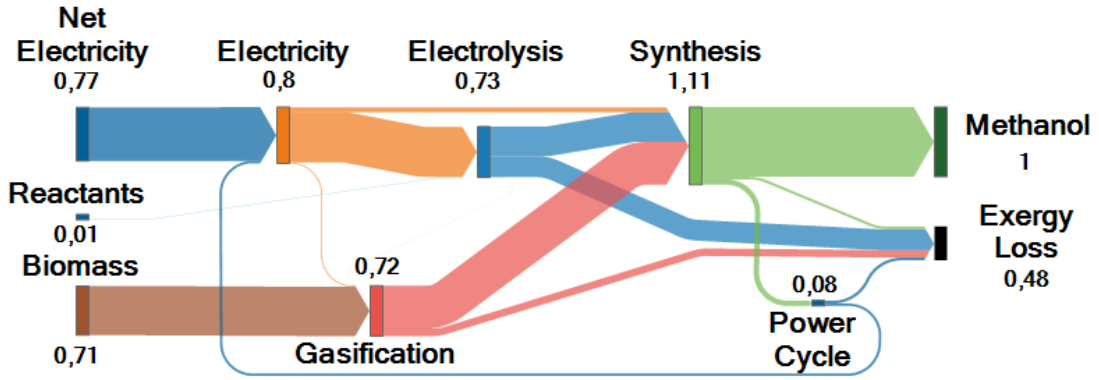
Among the considered gasification processes, steam-based gasification processes are more efficient, since syngas with a higher H_2:CO ratio can be produced despite the higher energy demand to drive the gasification process. The efficiency difference is mainly due to the lower exergy losses in the electrolysis unit (ca. 30 % lower hydrogen demand for PBtMeOH processes), since the exergy efficiency of the gasification unit is similar for the two cases (around 85 %).

The result that steam-based gasification is more efficient than oxygen-based gasification aligns with the findings of Brown et al. [230] who compared gasification processes with different gasifying agents for electricity production: the exergy efficiency of the gasification unit using oxygen and steam as gasifying agents does not differ significantly (ca. 73 %-77 %). The lower exergy efficiencies are due to the more detailed models and different operating conditions in Brown et al. [230].

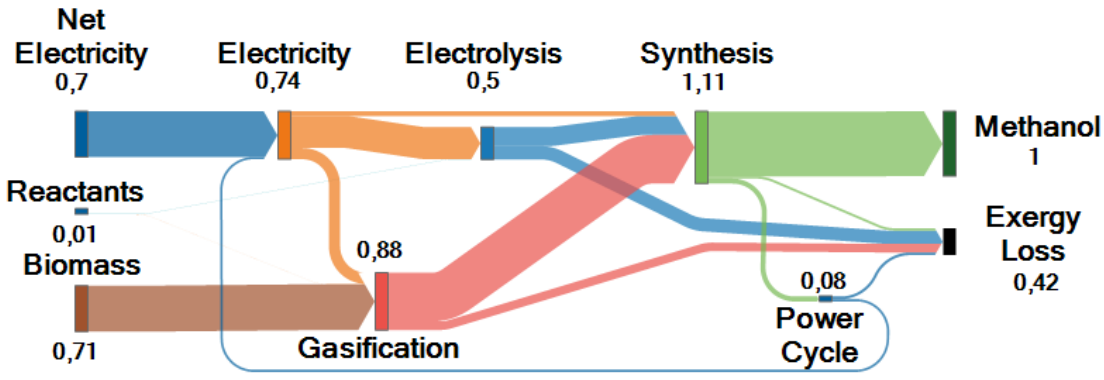
For the sake of completeness, the results of a similar analysis based on energy instead of exergy are reported in Appendix A.5. In contrast, the exergy and energy flows for the other products, i.e., methane, DME, and dodecane, are available in the Supporting Information of Mucci et al. [2].



(a) PBtMeOH process with biomass combustion.



(b) PBtMeOH process with biomass oxy-gasification.



(c) PBtMeOH process with biomass steam-gasification.

Figure 3.9.: Sankey diagrams of the exergy flows for a Power- and Biomass-to-Methanol (PBtMeOH) process with (a) biomass combustion, (b) biomass oxy-gasification, and (c) biomass steam-gasification. The exergy flows in MW are scaled per unit of product. The numbers at the diagram nodes represent the exergy flows of the energy sources and the total exergy flows through the process units.

3.6.2. Power- and Biomass-to-X: Sensitivity analyses

In this subsection, we investigate the effect of key process parameters on the efficiency of PBtX processes with biomass combustion and gasification calculated via the back-of-the-envelope analysis. In particular, we analyze the impact of the efficiency of the electrolysis unit, the efficiency of the power cycle unit, and the composition of the carbon feedstock on the exergy efficiency.

3.6.2.1. Electrolyzer efficiency

The efficiency of the electrolysis unit significantly affects the efficiency of PBtX processes, since this unit is responsible for high exergy losses. Increasing the electrolyzer efficiency from 60 % to 80 % increases the PBtX efficiency of all products by around 10 percentage points (see Table A.4).

As expected, the ranking of the pathways in terms of exergy efficiency does not change when increasing the electrolyzer efficiency. Nonetheless, the gap between the combustion and the gasification pathways is narrower, since combustion-based processes have higher hydrogen demands. Among the different products, methane production benefits the most from electrolyzer efficiency improvements, since it requires the highest number of hydrogen moles per mole of carbon.

Interestingly, the difference in efficiency between the steam-based and oxygen-based gasification processes becomes smaller with higher electrolyzer efficiencies (Table A.4). This is due to the lower exergy losses in the electrolysis unit for hydrogen production in both absolute and relative terms. Therefore, if the electrochemical hydrogen production route is sufficiently efficient, producing additional hydrogen via steam gasification at the price of a higher energy demand for gasification might not be beneficial. However, this situation does not happen with the current state-of-the-art low-temperature water electrolyzers. Furthermore, in case steam was produced by recovering heat from the synthesis unit (not considered here), even higher electrolyzer efficiencies would be needed to make oxygen-based gasification processes more efficient than steam-based ones.

3.6.2.2. Power cycle efficiency

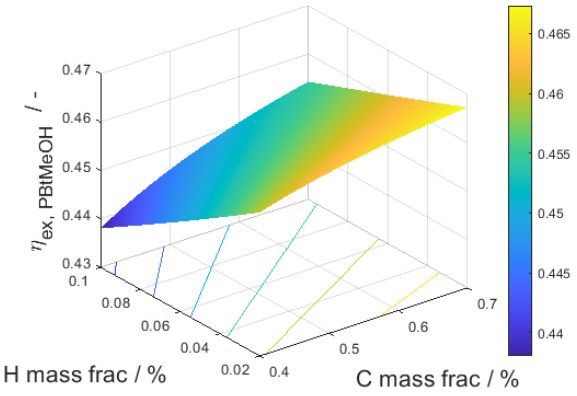
The efficiency of the power cycle unit plays a minor role compared to the efficiency of the electrolyzer: a better conversion of the residual heat into electricity leads to little improvements in the PBtX exergy efficiency (see Table A.5) since the power cycle unit handles a limited amount of energy, and most of the exergy losses has already occurred in the upstream units as shown in Figure 3.9.

Among the different pathways, the efficiency of gasification-based PBtX processes depends less on the power cycle unit efficiency since less heat is supplied to that unit.

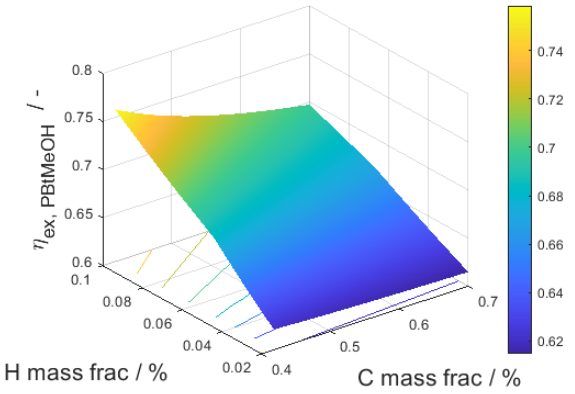
3.6.2.3. Carbon feedstock composition

The composition of the carbon feedstock has a significant impact on the exergy efficiency of PBtX processes, since it affects how much heat is produced or required in the combustion and gasification units and how much hydrogen can be produced via gasification. In Figure 3.10, we show the exergy efficiency of combustion-based and gasification-based PBtMeOH processes, respectively, by varying the carbon and hydrogen mass fractions in

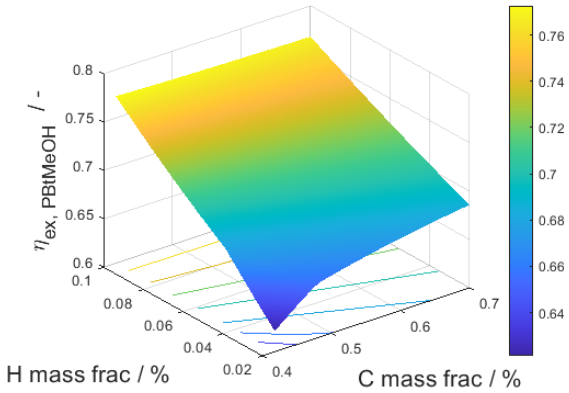
the biomass. Relatively wide ranges ([0.4, 0.7] and [0.02, 0.10] for carbon and hydrogen, respectively) are considered since the sustainable feedstock composition, e.g., biomass, biogas, and wastes, can vary significantly [237, 265].



(a) PBtMeOH with biomass combustion.



(b) PBtMeOH with biomass oxy-gasification.



(c) PBtMeOH with biomass steam-gasification.

Figure 3.10.: Sensitivity analysis of the exergy efficiency of a Power- and Biomass-to-Methanol (PBtMeOH) process with (a) biomass combustion, (b) biomass oxy-gasification, and (c) biomass steam-gasification, with respect to the feedstock composition. The considered mass fractions of S and N are equal to 0.001 and 0.004, respectively (values for woody biomass). In contrast, the mass fractions of C and H are varied, while the oxygen content is calculated by difference. Note: due to the over-stoichiometric presence of oxygen in the biomass at low carbon contents (lower than ca. 0.42), no efficiency could be calculated for the gasification-based processes with the considered model.

The sensitivity analysis shows that gasification-based processes are more efficient, irrespective of the biomass composition. The changes in the exergy efficiency for the combustion-based processes are smaller than the ones for the gasification-based processes when considering the same H and C ranges. Therefore, the choice of a proper biomass feedstock is more important for gasification processes. Furthermore, the analysis carried out with these simple models suggests that the composition of the most suitable feedstock differs for the three considered processes.

For combustion-based processes, high carbon contents in the feedstock increase the

amount of product per mole of biomass as well as the biomass LHV. These two aspects conflict with each other since they contribute to the numerator and denominator of the exergy efficiency, respectively (see Section 3.5). Nevertheless, the exergy efficiency increases with high carbon contents in the feedstock (Figure 3.10 a) since the increase of the produced product plays the major role. In contrast, high hydrogen contents in the feedstock seem not to be worth it, since hydrogen only contributes to the biomass LHV, whose energy content is mostly wasted not being entirely converted into electricity in the power cycle unit. In fact, the reduction of the net electricity demand due to the additional electricity produced in the power cycle unit is smaller than the increase of the energy stored in the biomass per unit of product when increasing the biomass LHV via hydrogen concentration.

For oxygen-based gasification processes, high hydrogen mass fractions increase the exergy efficiency since, according to the model, they increase the amount of H_2 produced per mole of carbon within the gasification unit, thus reducing the hydrogen demand from the electrolysis unit (Figure 3.10 b). In contrast, high carbon concentrations slightly decrease the overall PBtMeOH efficiency since the exothermic reaction of carbon oxidation (Reaction (3.1)) is promoted and the H:C ratio is reduced. Higher exergy efficiencies are achieved when the biomass composition is such that the gasification process is endothermic (Figure A.5) since endothermic processes have lower exergy losses.

For steam-based gasification processes, an increasing concentration of hydrogen and carbon improves the exergy efficiency of the PBtMeOH process (Figure 3.10 c), since it leads to higher hydrogen production in the syngas. In particular, high carbon concentrations reduce the oxygen content in the feedstock and require higher amounts of steam, thus promoting the endothermic reaction of carbon oxidation via steam (Reaction (3.2)). Similarly to the oxygen-based gasification process, higher exergy efficiencies are achieved when the gasification process is endothermic (Figure A.5).

Finally, although sensitivity analyses on feedstock composition provide interesting insights into the variation of the exergy efficiency of PBtX processes, the feedstock composition cannot be chosen arbitrarily. For this reason, the efficiency of PBtX processes has also been calculated for real carbon feedstock compositions, e.g., herbaceous biomass, biogas, and solid waste (the results are reported in Appendix A.6.3). In agreement with the results presented above, gasification-based processes are more efficient than combustion-based processes, irrespective of the feedstock composition. Moreover, different carbon feedstocks are more suitable for gasification-based rather than combustion-based processes.

Finally, it is important to highlight that other practical aspects related to biomass handling and conversion, such as feedstock moisture, sulfur and ash contents (not considered in this analysis), can significantly affect biomass suitability for efficient and direct use in PBtX processes. In fact, an energy-intensive pre-treatment of the carbon feedstock and post-treatment of flue gases may be necessary and could significantly reduce the overall process efficiency.

3.6.3. Practical considerations

The calculated exergy efficiencies via the relatively simple process models provide valuable insights into inherent thermodynamic differences and represent upper thermodynamic limits for the considered PBtX processes (except for the electrolyzer and power cycle, where current practical values were used). In fact, the efficiency of real processes also depends

on other aspects such as ashes and moisture in the carbon feedstock, the energy demand of auxiliaries and separation units, nonidealities in reactors, and imperfect heat integration. Therefore, the efficiency of real processes is lower, and the efficiency gap between the combustion-based and gasification-based PBtX processes might change.

In the following, we critically analyze some practical aspects that may impact the efficiency of PBtX processes.

3.6.3.1. Challenges of biomass as feedstock

As discussed above, biomass is a promising carbon and energy feedstock for the synthesis of valuable and sustainable products. Furthermore, biomass utilization for product synthesis is particularly effective when hydrogen is added, since it generally increases the carbon yield (and the process efficiency depending on the electrolyzer efficiency), as already shown, for instance, for PBtL processes [225, 227].

However, biomass handling requires energy-intensive pre-treatment, e.g., biomass drying and particle size reduction [266, 267], to increase the conversion performance and the quality of the produced syngas [210, 267]. Furthermore, elements like sulfur, chlorine, and potassium can contribute to plant corrosion and slag formation when biomass is converted [268]. Also, ashes and the formed pollutants, e.g., SO_x and NO_x, must be properly removed since they cause fouling and might poison the catalysts of the downstream synthesis units [228].

Finally, biomass is not uniformly distributed, and its availability might be limited in certain areas. Also, biomass transport over long distances is generally not economically viable due to its relatively low energy density. Therefore, the size of the conversion plants is generally relatively small, thus limiting the economy of scale effect. Also, the plant location and biomass supply chain should be optimized simultaneously to improve process viability [269].

3.6.3.2. Combustion processes

The relatively simple model of the (oxy-)combustion process does not differ significantly from real processes since biomass oxidation is generally almost complete if conducted at proper conditions, e.g., good biomass-oxidizer mixing, combustion in stages, and high residence times [268]. While excess oxygen could be used to ensure almost complete char combustion and CO burnout, its presence in the flue gases may hinder the direct feed of the clean and dried CO_2 stream into the synthesis unit since oxygen is poisonous for several catalysts. In that case, an energy-intensive separation process such as a CC unit that separates CO_2 from the flue gas should be considered (see Section 2.3.2). Furthermore, big recycles of the flue gases, mainly composed of CO_2 and H_2O, are needed to control the combustion temperature due to the high adiabatic flame temperature of oxy-combustion.

Combustion-based PBtX processes may require additional conversion units depending on the target product and the catalyst for its synthesis. In fact, several catalysts are developed for CO since it is more active than CO_2, thus meaning that an intermediate RWGS unit for CO_2 reduction would be necessary before feeding the stream into the synthesis unit (Subsection 2.4.3). Nonetheless, catalysts allowing direct hydrogenation of CO_2 have also been developed, e.g., for methanol [196] and kerosene [244, 245] production.

3.6.3.3. Gasification processes

Real gasification processes deviate from the considered model because of the incomplete biomass conversion (lower than 98 % and dependent on the technology and the operating conditions [210]) due to the scarcity of the oxidizing agent. Furthermore, the selectivity to syngas is lower than what is predicted by the stoichiometry and varies based on the feedstock composition and particle size, and the operating conditions, such as temperature, pressure, and oxidant-to-biomass ratio [224, 270]. In fact, relevant amounts of side products, e.g., H_2O, CO_2, CH_4, and tars are formed, and energy-intensive and expensive flue gas cleaning processes might be required to remove impurities [210, 230, 271]. However, their formation can be reduced by using catalysts, e.g., dolomite and alkali catalysts [224, 228, 272], and proper operating conditions [210, 272].

Although herein we investigate the gasification processes with pure oxygen and steam with simple models, these models are still able to capture key trends. In fact, it is experimentally proven that steam-based gasification can produce syngas with higher hydrogen content and energy density [210, 228, 229], at the expense of higher energy inputs.

The energy demand for gasification can be higher than what is estimated by the considered models due to, e.g., high biomass moisture and non-ideal heat integration. In the case the gasifier is operated with an excess of the oxidizing agent, the amount of CO_2 in the syngas could be quite significant since the excess of the oxidizing agent promotes full oxidation of the carbon atoms to CO_2, thus reducing the high-temperature heat demand for gasification.

The presence of CO_2 in the produced syngas does not necessarily represent a problem, since CO_2 can be inert or even converted in the product synthesis process depending on the catalyst. Furthermore, if required, the CO_2 concentration could be reduced via separation processes, e.g., membranes and adsorption processes, and the separated CO_2 recycled into the gasifier to increase the carbon efficiency and reduce emissions.

All the mentioned aspects reduce the efficiency of gasification-based PBtX processes and, thus, the efficiency gap with combustion-based PBtX processes.

3.6.3.4. Economics

In conventional combustion and gasification plants, air is often used as the oxidizing agent, since oxygen has to be separated from the air in dedicated and expensive air separation units. In contrast, PBtX processes already produce oxygen as a side product that can therefore be used within the plant. Moreover, the possibility of using pure oxygen reduces the complexity, size, and cost of the plants, since they can be smaller and additional separation units are not required, thanks to the absence of the inert gases nitrogen and argon.

Comparing the different pathways, gasification-based PBtX processes are expected to have lower production costs than combustion-based PBtX processes. Moreover, despite the higher costs for the biomass conversion unit and syngas cleaning [273], gasification-based processes do not necessarily require intermediate units like the RWGS unit (if most of the CO_2 is separated and recycled into the gasifier or catalysts can convert both CO and CO_2 [274]) and need significantly smaller power cycle and electrolysis units, which are often the major cost drivers of PtX processes.

3.6.4. Power- and Biomass-to-Methanol: Validation with detailed models

As previously discussed, real processes pose additional challenges, such as incomplete reactant conversion, that are not considered in the process unit models described in Section 3.3.

In this subsection, we compare the results obtained via the relatively simple models against the results of a combustion-based and gasification-based PBtMeOH process modeled in detail, i.e., accounting for several nonidealities, including the presence of moisture in the biomass feedstock, non-ideal heat integration, incomplete reactant conversion, side-product formation, and energy demand for auxiliaries (see Appendix A.7 for more details on the Aspen Plus models). Thus, this analysis assesses the suitability of the simpler models in identifying inherent thermodynamic differences between combustion-based and gasification-based PBtX processes, and how much the process efficiency obtained with relatively simple models changes when considering nonidealities. Further, we compare the PBtMeOH processes with respect to the estimated methanol production cost.

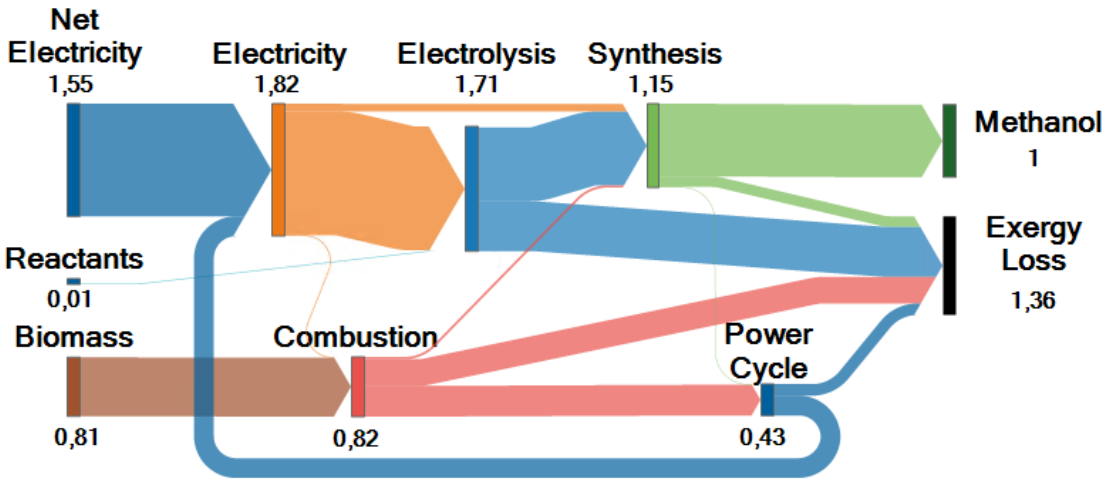
3.6.4.1. Technical results

The process efficiencies obtained with the detailed PBtMeOH models are 42 % and 58 % for the combustion-based and gasification-based processes, respectively. These efficiency values are a few percentage points lower than those calculated with the simpler models (ca. 46 % and 70 %). In particular, the efficiency of the detailed gasification-based process model deviates the most from the simpler one. Nevertheless, the gasification-based PBtMeOH process is significantly more efficient than the combustion-based one. Thus, the simpler process models were already able to capture the key inherent differences between these combustion-based and gasification-based processes.

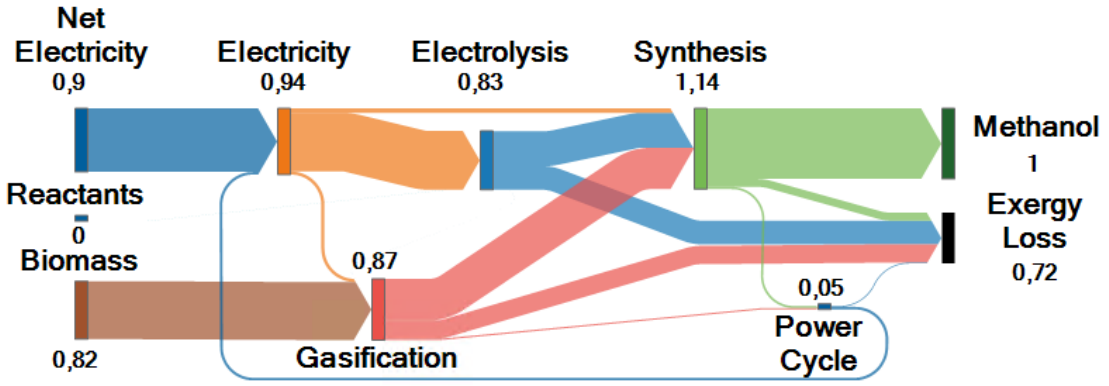
The Sankey diagrams of the exergy flows in Figure 3.11 confirm that the efficiency difference between the combustion-based and gasification-based processes is mainly due to the lower exergy destruction in the electrolysis and biomass conversion units (see Figure 3.9 to compare the Sankey diagrams obtained with the simpler models).

The exergy efficiency of the methanol synthesis process (the "Synthesis" node in Figure 3.11), including product purification via distillation (Appendix A.7), is ca. 85-90 %, thus aligned with previous works [31] and slightly lower than what is estimated with the simpler models. In contrast, the exergy efficiency of the gasifier is noticeably lower than what was estimated with the simpler model (70 % vs. 85 %). This is mainly due to the incomplete biomass conversion, side-product formation, full oxidation of part of the carbon atoms (combustion reaction) to achieve a nearly autothermal gasifier, and energy demand for syngas purification. Nonetheless, the exergy efficiency of the gasifier calculated with the detailed model aligns with the work of Brown et al. (ca. 73 %-77 % [230]). Further, the lower syngas quality and H_2:CO ratio caused by side-product formation also require a higher hydrogen stream from the electrolysis unit, thus increasing the overall exergy losses of the gasification-based PBtMeOH process modeled in detail compared to the ones of the simpler process model.

In summary, the results presented for a PBtMeOH process modeled in detail confirm the key result obtained with the simpler models, i.e., the gasification-based PBtMeOH process is more efficient than the combustion-based one, although the nonidealities of the gasification process significantly reduced the process efficiencies and efficiency gap.



(a) PBtMeOH process with biomass combustion.



(b) PBtMeOH process with biomass gasification.

Figure 3.11.: Sankey diagrams of the exergy flows for a Power- and Biomass-to-Methanol process with (a) biomass combustion and (b) biomass gasification modeled in detail in Aspen Plus. The exergy flows in MW are scaled per unit of product. The numbers at the diagram nodes represent the exergy flows of the energy sources and the total exergy flows through the process units. Note: these Sankey diagrams differ from the ones in Figure 3.9 for the level of detail of the models (complex vs. simple models, respectively).

The same conclusion can be drawn when comparing combustion-based and gasification-based PBtK processes (Subsection 3.6.5). Given these results from the detailed models and the fact that the efficiency difference between the considered combustion-based and gasification-based PBtX processes is significant (Figure 3.8), we expect a similar trend for the other target products.

Although the relatively simple models could identify key trends and inherent thermodynamic differences in the considered PBtX processes, they can be less accurate when strong nonidealities are not properly accounted for, as in the gasifier of the PBtMeOH process. This aspect will be further investigated in Subsection 3.6.5, when comparing different production pathways for kerosene production.

3.6.4.2. Economic results

Similarly to the process efficiency, the estimated levelized cost of methanol (see Equation (A.1)) is lower for the gasification-based PBtMeOH process than for the combustion-based one (refer to Section A.7 for details on the models and on the economic analysis). This difference is due to both Capital Expenditures (CAPEX) and Operating Expenditures (OPEX), as shown in Figure 3.12. Despite the higher cost of the biomass conversion and flue gas purification units, the investment and operating costs for the electrolysis unit are significantly lower, thus making methanol production via the gasification-based PBtMeOH process more economically competitive (ca. 0.71 € kg^{-1} vs. 1.07 € kg^{-1}).

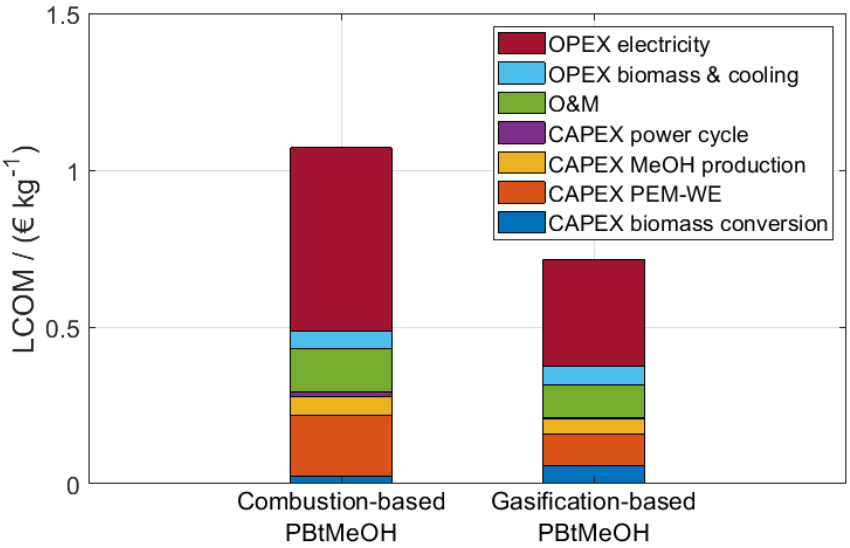


Figure 3.12.: Levelized Cost Of Methanol (LCOM) produced via the combustion-based and gasification-based PBtMeOH pathways. Note that a mixture of oxygen and steam is considered as the gasifying agent as discussed in Section A.7.

3.6.5. Power- and Biomass-to-Kerosene case study

As discussed in the previous subsection, the relatively simple models used for the back-of-the-envelope analysis (Section 3.3) are suitable to identify key trends concerning combustion-based vs. gasification-based PBtX processes. However, their accuracy in representing real processes can suffer from significant process nonidealities, e.g., due to side-product formation. To further investigate the suitability of these models in highly non-ideal processes with multiple reaction steps as well as to evaluate the performance of a novel production pathway, we analyze several PBtK processes (Section 3.4.2) from a technical and economic perspective (see the assumptions in Appendix A.8.4).

3.6.5.1. Technical results

In the following, we analyze the results of the exergy analysis for the simpler models of Power- and Biomass-to-Dodecane processes, where dodecane is considered the representative alkane for the typical kerosene range (C_{8-16}), and for the detailed models of PBtK

processes. Moreover, we first compare combustion-based and gasification-based processes, and then the two considered kerosene production pathways.

Simpler models

As can be noticed in Table 3.3, gasification-based processes are significantly more efficient than combustion-based ones for both production pathways, i.e., FT and MtO pathways (ca. 20 percentage points). Thus, these results confirm the trend described in Section 3.6.1.

Table 3.3.: Exergy efficiency of the combustion-based and gasification-based Power- and Biomass-to-Dodecane processes for the FT and MtO pathways modeled with relatively simple models (values in %). Woody biomass was considered as carbon feedstock [237].

Pathway	$\eta_{ex,\,PBtC_{12}H_{26}}$ (combustion)	$\eta_{ex,\,PBtC_{12}H_{26}}$ (O_2-gasification)	$\eta_{ex,\,PBtC_{12}H_{26}}$ (H_2O-gasification)
FT	42	63	66
MtO	41	61	64

When comparing the two production pathways, the results suggest that dodecane production via the FT pathway is slightly more efficient by 1-2 percentage points. This efficiency difference can be explained by the modeling assumptions of the dodecane synthesis unit (see Section 3.4.2). For instance, after each conversion step (one and four sequential conversion steps for the FT and MtO pathways, respectively), all material streams are assumed at ambient conditions at the process unit interface; therefore, additional compression energy is required (and accounted for) when the downstream operating units are operated at pressures higher than 1 bar. Further, some reaction steps of the MtO pathway, e.g., the methanol synthesis, are operated at higher pressures than the FT synthesis, thus requiring a significantly higher compression energy, which reduces the overall process efficiency.

As the efficiency difference between FT and MtO pathways is relatively small (differently from combustion-based and gasification-based processes) and the models are relatively simple, more detailed models are needed to draw more robust conclusions. In fact, process nonidealities, e.g., reaction selectivity, and heat integration can significantly affect process efficiencies as discussed in Subsection 3.6.3.

Detailed models

Figure 3.13 shows the exergy efficiency of the modeled PBtK processes when considering both kerosene and the whole produced liquid fuel, i.e., including the gasoline and diesel side products, as target products.

The detailed models confirm that gasification-based PBtK processes are significantly more efficient than combustion-based ones (ca. 10 percentage points), irrespective of the kerosene production pathway. This result can be explained by analyzing the exergy flows of the processes (Figure 3.14). Similarly to the PBtMeOH processes (Subsection 3.6.4), gasification-based processes have fewer exergy losses in the biomass conversion unit and require less hydrogen, thus reducing the absolute exergy losses related to the water electrolysis unit. Also, the higher electricity demand of the electrolysis unit is not offset by the higher electricity production in the steam power cycle of the combustion-based PBtK processes.

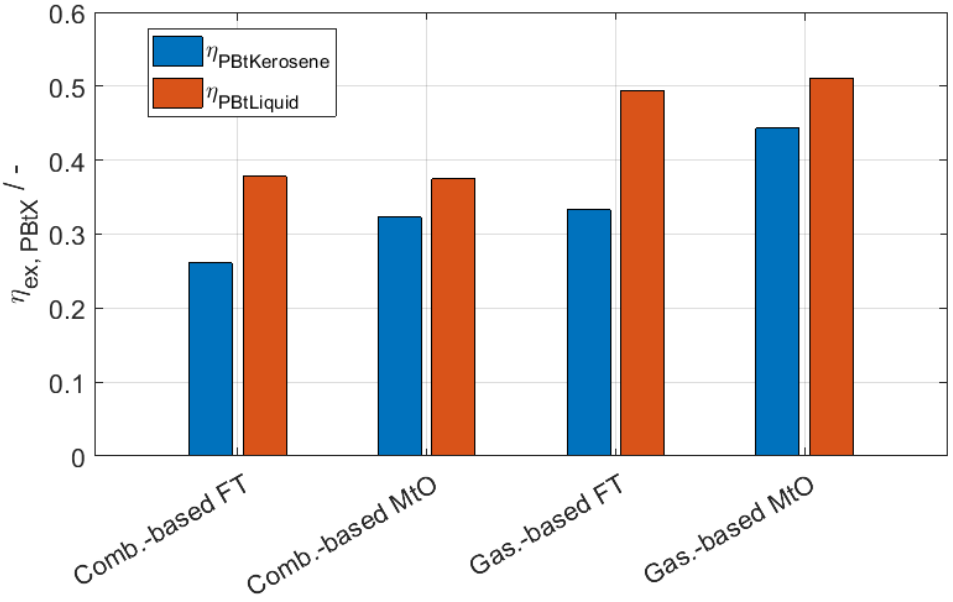
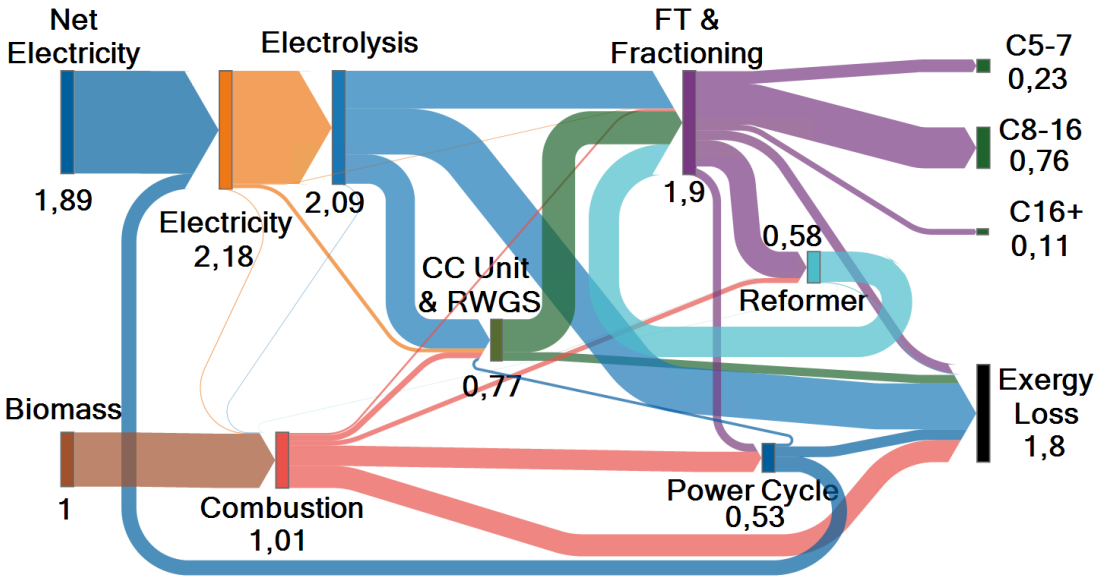


Figure 3.13.: The exergy efficiency of the considered Power- and Biomass-to-Kerosene processes modeled in detail is shown. $\eta_{\mathrm{PBtKerosene}}$ considers only kerosene as a product, while $\eta_{\mathrm{PBtLiquid}}$ includes other fuel fractions, i.e., gasoline and diesel.

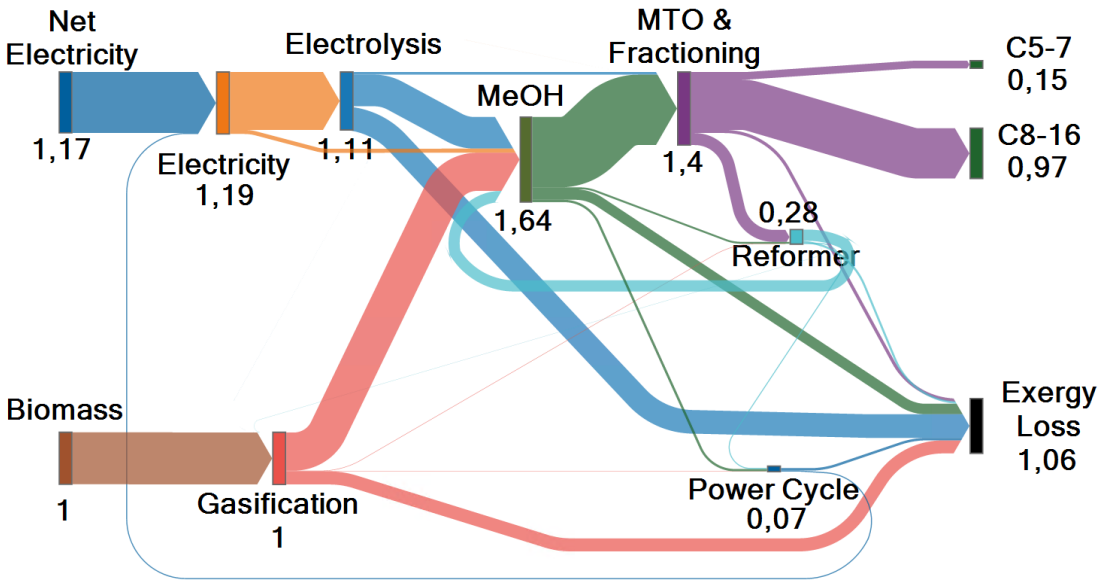
The efficiency values obtained with the simple and detailed models are significantly different (nearly 30 percentage points when comparing gasification-based kerosene production via the FT pathway). If the other liquid fuels, namely gasoline and diesel, are included in the efficiency calculation instead of only kerosene (see orange bars in Figure 3.13), these differences are significantly lower than 20 percentage points for all cases. Also, these efficiency differences are larger than those observed for the PBtMeOH processes (Section 3.6.4). This is mainly due to the significant process nonidealities, e.g., incomplete conversion and side-product formation, and energy demand for auxiliary units.

The two modeled kerosene production pathways, i.e., FT and MtO, have similar liquid fuel productions and similar process efficiencies (see orange bars in Figure 3.13). Nonetheless, in contrast to the relatively simple models, the MtO pathway results in a higher efficiency than the conventional FT pathway when considering the kerosene fraction of the produced liquid fuel (see blue bars in Figure 3.13). This difference can be explained by the higher selectivity to the C_{8-16} hydrocarbon range of the MtO pathway (Figure 3.14), which is also reported in some simulation-based works, e.g., of Bernardi et al. [246] and Bube et al. [248] for PtK processes, and observed in experimental investigations [25]. In contrast, these observations differ from those of Atsonios et al. [247], who, however, modeled a PtK process with a different design, i.e., with several oligomerization reactors and without the recycle of short C-chain olefins.

Further, the kerosene composition differs significantly for the considered production pathways (Table 3.4. In particular, kerosene produced via the FT pathway has a relatively even hydrocarbon distribution compared to kerosene produced via the MtO pathway. The difference in the product distribution can be explained by the modeling assumptions for the production of syncrude: ASF distribution vs. oligomerization with conversion factors that depend on the olefin C-number for the FT and MtO pathways, respectively.



(a) Exergy flows of the combustion-based PBtK process via the FT pathway.



(b) Exergy flows of the gasification-based PBtK process via the MtO pathway.

Figure 3.14.: Exergy flows for the least efficient (combustion-based PBtK process via FT) and the most efficient (gasification-based PBtK process via MtO) PBtK processes are shown on the left and right of the figure, respectively. Note: the exergy flows are scaled with respect to the biomass exergy input, which is the same for the considered case studies.

The results of the detailed models thus show that the relatively simple models considered for the back-of-the-envelope analysis could identify inherent thermodynamic differences between combustion-based and gasification-based PBtK processes, but are not sufficiently accurate for comparing the FT and MtO pathways for dodecane (kerosene) production: the efficiency differences among the pathways are relatively small, thus not very reliable, and could have even led to misleading conclusions. Therefore, some process nonidealities should be considered even in the relatively simple models to improve their representativeness

Table 3.4.: Molar fractions of the hydrocarbons in the kerosene stream for the modeled PBtK processes, clustered with respect to their carbon number.

C-number	Comb.-based FT	Gas.-based FT	Comb.-based MtO	Gas.-based MtO
C_7	0	0	0.01	0.04
C_8	0.12	0.13	0.34	0.34
C_9	0.10	0.11	0.24	0.24
C_{10}	0.13	0.14	0.10	0.10
C_{11}	0.15	0.15	0.06	0.06
C_{12}	0.14	0.13	0.20	0.18
C_{13}	0.13	0.12	0	0
C_{14}	0.12	0.11	0	0
C_{15}	0 09	0.08	0.04	0.04
C_{16}	0.03	0.03	0	0

and provide a more rigorous basis for comparing these kerosene production pathways. In contrast, such models can already suggest the lack of big efficiency differences among the pathways if a wider definition of the target fuel is adopted, i.e., from gasoline to diesel range instead of kerosene range only (compare Table 3.3 and Figure 3.13).

3.6.5.2. Economic results

The estimated levelized cost of kerosene ranges between 2 € kg^{-1} and 4 € kg^{-1} for the considered processes (Figure 3.15). The calculated kerosene production costs do not account for the sale of side products such as crude gasoline, thus representing a worst-case cost scenario.

Similarly to what was shown for the PBtMeOH processes (Subsection 3.6.4), gasification-based PBtK processes have lower kerosene production costs than combustion-based ones (Figure 3.15). The specific cost gap could be lower when operating the combustion unit with a slightly under-stoichiometric oxygen flow rate (not considered here) as modeled for the PBtMeOH process (see Appendix A.7 for additional details): this process would still have a high biomass conversion, but a relatively cheap flue gas cleaning treatment unit and no CC unit.

Kerosene produced via the MtO pathway has a lower production cost than kerosene produced via the FT pathway (Figure 3.15), mainly due to the higher process selectivity. In contrast, Bernardi et al. [246] showed that kerosene production in PtK processes via the FT pathway has a lower production cost. This difference is likely due to the different cost correlations and the design of the MtO and FT pathways. In particular, in the work of Bernardi et al. [245], the latter is based on direct CO_2 hydrogenation over a newly-developed catalyst, which is more selective to shorter C-chain alkanes than the conventional FT synthesis modeled in this work.

The gasification-based PBtK process via the MtO pathway has the lowest production cost (ca. 2 € kg^{-1}) thanks to the lower investment and operating costs for the electrolysis unit, which is the main economic driver (Figure 3.15). Further, this process also has great potential for flexible operation and coupling with renewable power sources, since the electrolysis and methanol synthesis units can be operated highly flexibly differently

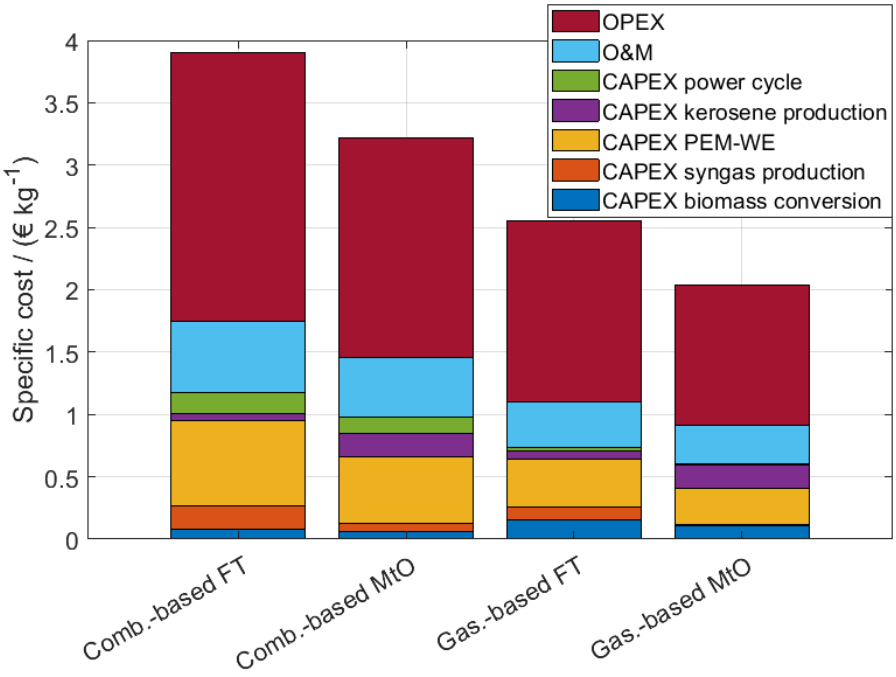


Figure 3.15.: The specific production cost of kerosene for the considered Power- and Biomass-to-Kerosene processes is shown. Note that the sale of side products is hereby not considered.

from high-temperature RWGS (Chapter 2), and methanol can be easily stored as an intermediate. Nevertheless, the MtO pathway has a lower technological maturity than the FT pathway, and the fuel produced via this pathway cannot be used as a drop-in fuel for aviation purposes yet (the approval process is currently ongoing [25]).

The calculated kerosene production costs align with other literature works (ca. 3 € kg^{-1} of e-kerosene in Schmidt et al. [242]; ca. 1.1 € L^{-1} and 1.7 \$ L^{-1} of liquid e-bio-fuels in Habermeyer et al. [227] and Hillestad et al. [225], respectively). Nonetheless, these production costs are not competitive against the current average price of fossil-based kerosene (ca. 1 \$ L^{-1} [275]).

This price gap could be reduced via technological improvements, e.g., of the electrolyzer, and investment and operating cost reductions. For instance, improvements in the electrolyzer efficiency can have a significant impact on kerosene production cost as shown in the sensitivity analysis performed for the most promising PBtK process (Figure 3.16). Similarly, the electricity price plays an important role in the kerosene production cost: the operating costs related to electricity consumption result in ca. 50 % of the overall kerosene production cost when an electricity price of 60 € MWh^{-1} is assumed (Figure 3.15). In the case that the PBtK process is grid-connected, a reduction of the average electricity price can be potentially achieved via DSM. However, flexible operation should be properly evaluated, as it reduces the plant capacity factor, i.e., equivalent operating hours, and requires oversizing the process units to meet production goals (this trade-off will be investigated in Chapters 4 and 5). Further, considering the sale of side products, e.g., oxygen, gasoline, and diesel, carbon certificates, or subsidies could reduce the price gap.

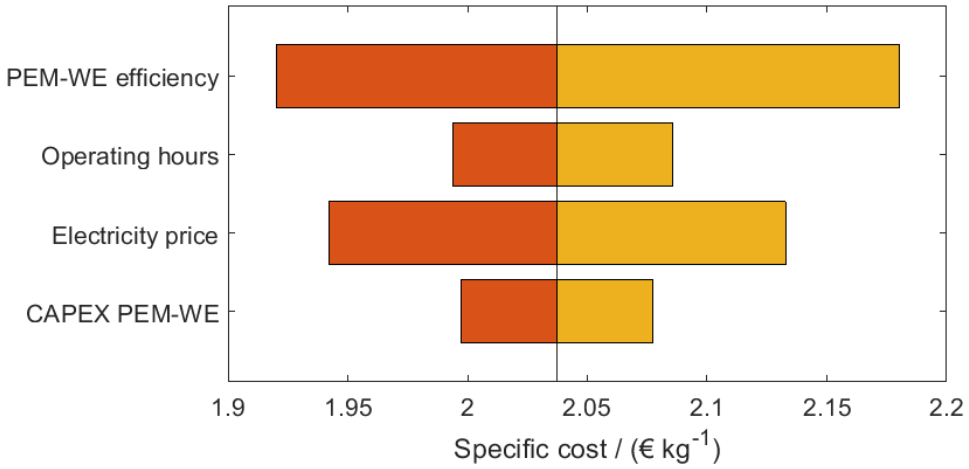


Figure 3.16.: Sensitivity analysis of the specific kerosene production cost for the gasification-based Power- and Biomass-to-Kerosene process via the MtO pathway. A relative variation of ± 10 % of the electrolyzer efficiency, electrolyzer investment cost, and average electricity price is considered. In contrast, a relative variation of ± 5 % is considered for the (equivalent) operating hours as the nominal value is 8000 h. Nonetheless, note that 10 % relative variations are significantly harder to achieve for some parameters, e.g., electrolyzer efficiency, than for others, e.g., electricity price.

3.7. Conclusion

Power- and Biomass-to-X processes could play a significant role in the green transition in the short-to-medium term, since biomass is a sustainable carbon and energy source, and the availability of low-carbon electricity is expected to increase in the next few years in order to meet the environmental targets [276, 277]. In this chapter, we investigated two thermochemical pathways, i.e., combustion and gasification, for utilizing residual biomass into Power-to-X processes. In particular, we compared the corresponding combustion-based and gasification-based PBtX processes via an exergetic analysis for several products "X", i.e., methane, methanol, DME, and dodecane, to identify inherent thermodynamic differences. For this purpose, relatively simple models of the main units of PBtX processes were built.

Gasification-based PBtX processes outperform the combustion-based ones in terms of efficiency for all the considered products (exergy efficiency around 15-20 percentage points higher when considering relatively simple process models), thus revealing that the carbon atoms should not be fully oxidized before the product synthesis. Therefore, the conversion of biomass to CO_2 via combustion for the production of chemicals leads to suboptimal utilization of the biomass potential, which is instead valorized from an exergy perspective in gasification-based processes. There are two main reasons for this higher efficiency: first, the exergy loss is higher for the biomass combustion unit than for the gasification unit because the energy content of biomass is converted into heat rather than stored in the molecular bonds of the produced syngas; second, the gasification pathway significantly reduces the amount of hydrogen to be produced via the electrolysis unit, which is the main contributor to exergy losses in most PtX processes. Moreover, gasification with steam instead of oxygen leads to higher efficiencies, since syngas with a higher H_2:CO ratio can

be produced, thus reducing the amount of hydrogen that the electrolysis unit has to supply even further.

The sensitivity analyses conducted on the electrolyzer efficiency, power cycle efficiency, and carbon feedstock composition, show that the ranking does not change: gasification-based PBtX processes are more efficient than combustion-based ones. The electrolyzer efficiency has a strong influence on the PBtX process efficiency, differently from the efficiency of the power cycle converting the residual heat of reaction. Furthermore, the carbon feedstock composition that results in the highest efficiencies differs among the considered pathways.

Although the results clearly indicate the thermodynamic advantages of gasification-based PBtX processes, the calculated values represent upper efficiency limits of real processes despite the use of empirical efficiency parameters for the electrolysis and power cycle units. Moreover, the considered relatively simple models do not capture several non-ideal aspects, e.g., real reaction conversions, side reactions, and energy demand for product purification, that contribute to reducing the efficiency. For instance, when accounting for several non-idealities in a combustion-based and gasification-based PBtMeOH process, the calculated process efficiencies are lower (from 46 % to 42 % and from 70 % to 58 % for the combustion-based and gasification-based processes, respectively).

While the relatively simple models were suitable for identifying the underlying differences between combustion-based and gasification-based PBtX processes, such models can show their limitations when the real process units significantly deviate from the considered assumptions, e.g., product selectivity. Such limitations were highlighted when comparing two kerosene production pathways, i.e., FT and MtO pathways, in PBtK processes: the efficiency differences among these pathways were too small to confidently draw conclusions. Moreover, the relatively simple models suggest that the production of dodecane, assumed as the representative alkane for the kerosene range, via the FT pathway is slightly more efficient than its production via the MtO pathway, which requires several conversion steps. In contrast, the detailed models show that the MtO pathway is more selective to the kerosene range, thus making this kerosene production pathway more efficient. Nevertheless, it must be mentioned that some of the reaction steps of the MtO pathway were modeled under relatively strong assumptions. Thus, experimental validation as well as the implementation of kinetic models of such steps would be needed to provide a definitive answer.

Finally, while biomass is a promising carbon and energy feedstock for the sustainable production of chemicals, its availability might be limited by temporal and geographical factors. Furthermore, instead of converting biomass thermochemically into CO_2 or syngas, the existing functionalized molecular structures could be (partially) exploited for the production of other valuable chemicals [221]. In contrast, CO_2 captured from either point sources or air (Subsection 2.3) is less subject to availability issues, and can be used directly for the production of bulk e-chemicals. However, the use of CO_2 in PtX processes generally requires higher electricity demands, which result in higher operating costs. Nonetheless, given the abundant availability of CO_2 sources [21], the need to reduce net CO_2 emissions [21], and the significant potential for production cost reduction via DSM related to the high electricity demand, the following chapters focus on PtX processes using CO_2 as the carbon feedstock.

4. Optimization of Power-to-Methanol Processes with Intermediate Storage

In the previous chapter, the use of biomass as a carbon and energy source in Power-to-X processes was explored. However, the production of chemicals and fuels via these Power- and Biomass-to-X processes based on thermochemical biomass conversion can be limited by the availability of biomass, which can also be used for the production of other valuable chemicals, e.g., by exploiting functionalized molecular structures in biochemical processes. In contrast, CO_2 does not suffer from availability issues and can be used directly as carbon feedstock in PtX processes. However, these PtX processes generally have higher specific electricity demands per unit of product and production costs than PBtX processes.

The high electricity demand of PtX processes particularly motivates the investigation of the role of flexible operation and intermediate storage, as well as their interplay, to reduce the production cost of e-chemicals, as mentioned in Chapter 2. In this chapter, we therefore aim to address these key questions for a Power-to-Methanol case study. In particular, we optimize the design of a PtMeOH process while simultaneously optimizing its scheduling as graphically visualized in Figure 4.1.

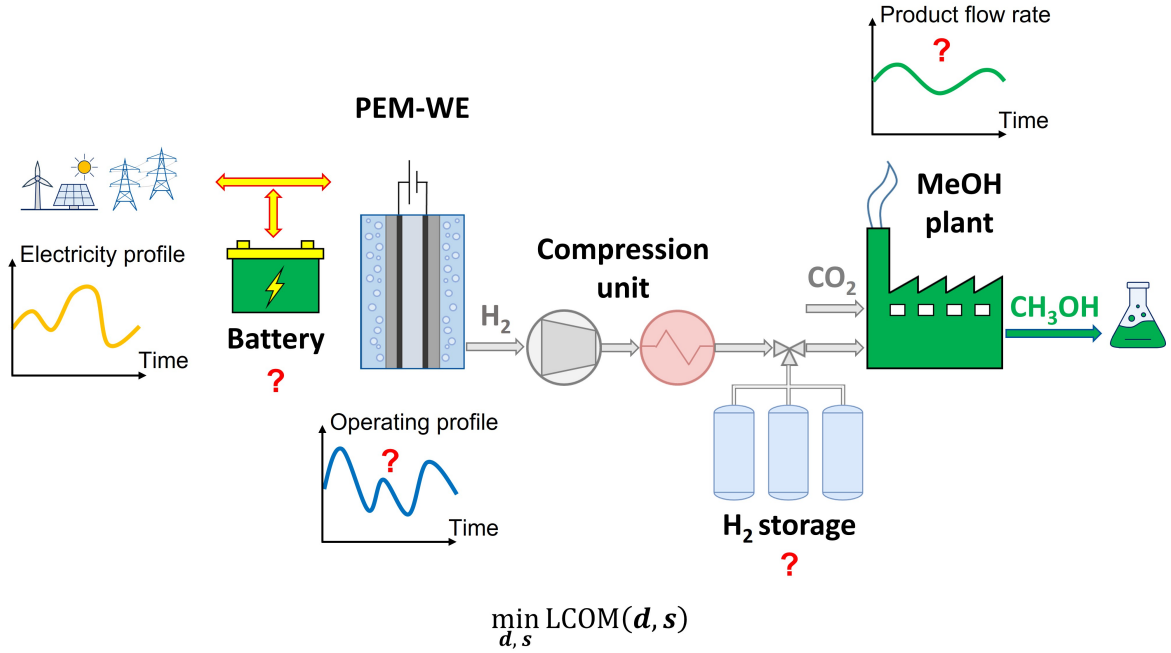


Figure 4.1.: Graphical representation highlighting the focus of Chapter 4, i.e., the investigation of whether flexible operation or intermediate storage are economically beneficial for a Power-to-Methanol process via combined design and scheduling optimization.

4.1. Introduction

Because of the high electricity demand of Power-to-Methanol (and Power-to-X) processes and the high flexibility of methanol plants (Table 2.2), Demand-Side Management [40, 278] is a promising operating strategy to reduce the production cost or to synthesize the product according to the power availability [24]. However, time-variable operation requires oversizing some process units or the whole plant to meet production targets or increase process flexibility margins. Thus, the extent to which the plant is operated flexibly has to be chosen carefully to balance operating and capital costs.

In combination with process unit oversizing, the use of intermediate or product storage has often been proposed to deal with renewables or fluctuating prices in different applications, e.g., biodiesel production [42], chlor-alkali electrolysis [208], and Power-to-Fuel [85, 169] processes. Storage technologies, e.g., batteries and tanks for intermediates, in support of PtMeOH plants could therefore contribute to reducing the production cost of methanol: batteries can decouple electricity production from its utilization, while intermediate hydrogen storage can decouple hydrogen production from its conversion (Figure 2.2).

While batteries and hydrogen storage systems are frequently considered in microgrid [279] and multi-energy system [41] optimization to cope with renewables and variable loads, few works about hydrogen storage and plant capacity optimization are found in the Power-to-Chemical field (Table 4.1). For instance, the interplay between batteries and hydrogen storage has been investigated for Power-to-Ammonia plants: both storage technologies were chosen by the Cplex optimizer for a case study in which the production rate of ammonia was assumed constant [217], while either the hydrogen storage or both storage technologies were chosen depending on the solving method and case study in another work [280]. As regards PtMeOH processes, Chen et al. [45, 281] optimized the design of a plant including hydrogen storage for several scenarios. A more extended process network with multiple components and storage technologies, including hydrogen storage and batteries, was optimized by Svitnič and Sundmacher [46]. However, in these works [45, 46, 281], the model of highly nonlinear components of the PtMeOH plant is linearized, and the integer variables, which allow setting the operating limits of the units, are avoided. These formulations make the optimization problem easier to solve, but affect the accuracy of the results. Furthermore, these works do not investigate the possibility of optimally exploiting electricity price variations in grid-connected PtMeOH plants with storage to minimize the methanol production cost. Therefore, it is unclear whether batteries and hydrogen storage are always beneficial from an economic perspective, especially in grid-connected plants, and if and to what extent the methanol synthesis unit should be operated flexibly even in their presence.

To tackle these questions and address these literature shortcomings, we modeled a PtMeOH plant with both a battery and hydrogen storage in General Algebraic Modeling System (GAMS) based on mass and energy balances and performance models for the units. The resulting Mixed-Integer NonLinear Programming (MINLP) was optimized with the commercial optimizer BARON [282] with respect to both its design (mainly sizing) and scheduling in the so-called Combined Design and Scheduling (CDS) optimization problems. These problems were not simplified, e.g., via linearization and integer variable removal or relaxation, to account for, e.g., economy of scale effects and the operating limits of every process unit. Moreover, we optimized a grid-connected and stand-alone PtMeOH plant for single scheduling scenarios to investigate how the optimal plant design depends on these.

Table 4.1.: Selection of relevant combined design and scheduling optimization works for the main Power-to-X processes with storage.

	Power-to-X process	Grid-connected	Stand-alone	Battery	Hydrogen storage	Other storage technologies	X-process flexibility	Scheduling horizon	Problem formulation
Li et al. [218]	$PtNH_3$	No	Yes	No	Yes	No	Yes	1 day	LP
Schulte Beerbühl et al. [283]	$PtNH_3$	Yes	No	No	Yes	No	Yes	1 year	NLP
Osman et al. [217]	$PtNH_3$	No	Yes	Yes	Yes	Yes	No	1 year	LP
Allman et al. [280, 284]	$PtNH_3$	No	Yes	No	Yes	Yes	Yes	2-day moving horizon for 1 year	MILP
Chen et al. [281]	$PtCH_3OH$	Yes *	Yes	No	Yes	No	No	1 year	NLP
Chen and Yang [45]	$PtCH_3OH$	Yes *	Yes	No	Yes	Yes	Yes	1 year	LP
Svitnič and Sundmacher [46]	$PtCH_3OH$	No	Yes	Yes	Yes	Yes	Yes	Time series aggregation	LP
This work [4]	$PtCH_3OH$	Yes	Yes	Yes	Yes	No	Yes	60 days	MINLP

* Renewable plant as the main energy source; electricity grid as energy backup, but no hourly price variability was considered.

The specific cost of methanol was used as the objective function and as the metric to compare different configurations and case studies.

The remainder of the chapter is structured as follows: in Sections 4.2 and 4.3, the investigated PtMeOH plant and its model are described; Sections 4.4 and 4.5 present the case studies and the formulation of the optimization problems, while in Section 4.6 and 4.7, the optimization results are analyzed and the conclusions are drawn.

4.2. Process description

The investigated PtMeOH process is composed of three key units, i.e., the water electrolyzer, the hydrogen compression unit, and the methanol synthesis plant (Figure 4.1). Additionally, a battery and hydrogen storage are considered to investigate their role. A short description of these units is provided in the following subsections.

4.2.1. Battery

Electricity can be stored electrochemically in batteries in order to be used in following periods. Different battery technologies have been developed for energy storage and automotive purposes [23]. For the current work, we considered a lithium-ion type battery because of the high roundtrip efficiency (around 95 %), high technological readiness level, and the expected cost drop due to large-scale production [23, 285].

4.2.2. PEM water electrolyzer

The water electrolyzer is the key component of the investigated PtMeOH processes. Among the electrolysis technologies, we chose PEM Water Electrolyzers (PEM-WEs), since they have high technological maturity and efficiency, wide operating limits [50], and they are reported to be particularly suitable to follow varying power inputs [48, 49] (Section 2.2).

Furthermore, PEM-WEs can be operated at relatively high pressures. While pressurized electrolyzers require smaller and cheaper downstream compression units, they are less efficient (higher operating costs). The trade-off between higher capital or operating cost depends on the considered boundary conditions, e.g., electricity cost and delivery hydrogen pressure, and is investigated for the considered PtMeOH process.

4.2.3. Hydrogen compression unit

Hydrogen has to be compressed from the pressure at the outlet of the electrolyzer up to the delivery pressure. Although several compression technologies are available, e.g., mechanical and electrochemical compression, only reciprocating and centrifugal hydrogen compressors have reached a high technological maturity on a large scale [286]. We selected centrifugal compressors because of their high reliability and capability of handling high hydrogen flow rates.

The delivery pressure of hydrogen that the compression unit has to reach varies according to the plant configuration. In the absence of hydrogen storage, the delivery pressure

matches the operating pressure of the methanol synthesis unit (set to 75 bar). If intermediate H_2 storage is present, the delivery pressure varies over time depending on the pressure inside the storage.

For the considered case studies, a compression unit without intermediate cooling is sufficient to supply hydrogen at the delivery pressure. The compressed hydrogen is then cooled to 25 °C before being injected into the hydrogen storage or supplied to the methanol synthesis plant.

4.2.4. Hydrogen storage

Hydrogen can be stored either physically, i.e., as liquid or gas, or in some materials via chemical or physical sorption [287]. We chose physical-based storage for the considered application since it is the most mature technology [287].

Liquid hydrogen has a high energy density, thus requiring smaller storage sizes than gaseous hydrogen. However, this storage option requires a dedicated liquefaction plant, which significantly increases the overall plant complexity and cost. In contrast, gaseous hydrogen storage does not need dedicated plants except for a compression unit.

There are two main gaseous storage alternatives, i.e., above-ground in vessels and underground in caverns [287, 288]. The use of pressurized vessels was chosen since it is geographically unconstrained. Among the several types of above-ground hydrogen storage [287, 289], hydrogen vessels of type I [287] are the most suitable for stationary applications for the pressure range of interest (maximum pressure below 200 bar) as they are the cheapest storage solution.

4.2.5. Methanol synthesis plant

Methanol can be produced from carbon dioxide and hydrogen either directly or indirectly (see Section 2.4.2). Given the lower plant complexity and better process efficiency and economic feasibility [174], we considered the direct methanol production route, i.e., CO_2 hydrogenation.

4.3. Process model

The PtMeOH plant with intermediate storage is modeled via mass and energy balances with discrete time dynamics. We assume quasi-stationarity at the operating points for each unit except for storage, thanks to the relatively high ramp rates and fast dynamics of the key process units [23, 33, 49, 144, 290] (also see Table 2.2) compared to the considered time step duration (1 h): the plant is considered in steady state at each time step independently from the operating point at the previous time step. This means that the duration of transients is assumed to be negligible. Also, cost functions are used to estimate capital and operating costs. The overall model is not linearized to capture economic trade-offs, e.g., related to the economy of scale, and obtain more accurate results since some equations are highly nonlinear. Furthermore, integer variables are considered, e.g., to account for the operating limits of the units.

In this section, the main modeling equations of each unit are presented. For the complete model and the GAMS code, we refer to Appendix B.1 and the Supporting Information of Mucci et al. [4], respectively.

4.3.1. Battery

The battery is modeled via the energy balance

$$\mathrm{E_b}(t) = \mathrm{E_b}(t - \Delta t) \cdot (1 - r_{\mathrm{self-disch}}) + P_{\mathrm{in}}(t) \cdot \eta_{\mathrm{ch}} \cdot \Delta t - \frac{P_{\mathrm{out}}(t)}{\eta_{\mathrm{disch}}} \cdot \Delta t,$$

where $\mathrm{E_b}(t)$ is the energy content, $P_{\mathrm{in}}(t)$ the power input from the grid, $P_{\mathrm{out}}(t)$ the power output in DC that can be effectively used, and Δt the discretization time step (refer to Appendix B.1.1 for the implemented operating constraints). The values for the charging (η_{ch}) and discharging (η_{disch}) efficiencies and the self-discharge rate ($r_{\mathrm{self-disch}}$) were considered constant. The hourly self-discharge rate was estimated by considering an energy loss of 0.2 % per day [23]. Other modeling approaches, e.g., efficiencies as a function of the current and of the state of charge of the battery [291], would have improved the accuracy but also increased the complexity of the optimization problem.

The power output of the battery can be supplied to the water electrolyzer ($P_{\mathrm{to-PEM}}(t)$) or to the grid ($P_{\mathrm{to-grid}}(t)$) if converted from DC to AC:

$$P_{\mathrm{out}}(t) = \frac{P_{\mathrm{to-grid}}(t)}{\eta_{\mathrm{DC-AC}}} + P_{\mathrm{to-PEM}}(t).$$

The capital cost of the battery is estimated from its nominal capacity. The specific cost of 310 \$ kWh^{-1} (the average installation cost of utility-scale stationary battery systems in 2020 [285]) is considered and updated to the reference year (2021) via the Chemical Engineering Plant Cost Index (CEPCI) [292]. To investigate how the investment cost for batteries affects the optimal process design, the cost prediction for the year 2030 (180 \$ kWh^{-1} [285]) has also been considered.

4.3.2. PEM water electrolyzer

The water electrolysis unit is composed of several electrolysis modules. The main specifications of the considered electrolyzer module are summarized in Table 4.2. The PEM-WE module is modeled by considering the equations and parameters in Järvinen et al. [293]. Two additional assumptions are made: i) the Faradaic efficiency is equal to one, and ii) the pressure dependency is considered in the Nernst equation only.

Since the equation-based model contains several variables that are unnecessary for the current scope and would slow down the optimizer, we replaced the electrolyzer model with a polynomial fit of its efficiency (based on the LHV, see Appendix B.1.2). The electrolyzer efficiency is then used to calculate the hydrogen mass flow rate, the power, and the cooling demand.

Additional operating costs are considered for the auxiliaries, e.g., the power electronics units and pumps. In particular, the additional energy consumption is assumed equal to the 5 % of the electricity needed to operate the electrolyzer (constant value for the whole operating range of the electrolyzer).

The capital cost of the PEM-WE is calculated by multiplying the nominal power of the electrolyzer by the specific cost in € kW^{-1}, which is calculated with the correlation proposed by Reksten et al. [87]. The maximum power of the electrolyzer could have been used in the correlation for a more conservative cost estimation. In fact, PEM-WEs can be operated at a maximum power significantly higher than the nominal one (up to 150 % h^{-1} [49];

125 % h^{-1} in our case, see Table 4.2), even though for a limited amount of time [49]. However, the value of the nominal power of the electrolysis unit is generally considered in these correlations. To account for civil works and installation costs, we assume a multiplying factor of 1.75, which is within typical installation cost factor ranges [294]. Additionally, a second electrolysis unit is considered to be purchased in the tenth year, since the typical lifetime of PEM-WEs (30-90 kh [50]) is shorter than the typical lifetime of the chemical plant (20-30 years). This choice indirectly accounts for accelerated degradation when the electrolyzer is operated flexibly since the electrolysis unit is substituted in the tenth year, although the number of yearly equivalent operating hours is lower than when it is constantly operated in steady state (8000 h y^{-1}).

Table 4.2.: Main specifications of the considered PEM water electrolyzer module.

	Values
Operating temperature	75 °C
Operating pressure range	20-40 bar
Nominal power per module	2.0 MW
Maximum power per module	2.5 MW

4.3.3. Hydrogen compression unit

A multi-stage centrifugal compressor is considered in the PtMeOH plant. This compression technology has an operating range of around 50 %-100 % [286] if variable rotating speed [295] or variable inlet guide vanes [296] are used. As the other units have a wider operating range, the operation of two compressors in parallel was considered to extend it to 25 %-100 %, although this affects the capital cost of the unit (economy of scale). The use of a low-pressure buffer tank before the compression unit is not considered, although it would have increased the process flexibility further.

The compressor power ($P_{\text{comp}}(t)$) is calculated as follows:

$$P_{\text{comp}}(t) = \dot{m}_{\text{H}_2}(t) \cdot \frac{c_{\text{p}} \cdot T_{\text{in}}}{\eta_{\text{is}} \cdot \eta_{\text{mec}}} \cdot \left(\beta(t)^{\left(\frac{k-1}{k}\right)} - 1 \right),$$

where $\dot{m}_{\text{H}_2}(t)$, c_{p}, and k are the hydrogen mass flow rate, the specific heat at constant pressure, and the heat capacity ratio of hydrogen, respectively, T_{in} the hydrogen temperature at the inlet of the compression unit (assumed equal to 298 K), β the pressure ratio, and η_{is} and η_{mec} the isentropic and mechanical efficiencies. The isentropic efficiency is assumed constant over the operating range and conservatively equal to 0.8 [286, 295]. A validation of the compressor model can be found in Appendix B.1.3.

The pressure ratio is determined by the operating pressure of the electrolyzer and the pressure inside the hydrogen storage, unless a bypass of the hydrogen storage is considered. With a bypass, some compression energy could be saved depending on the electricity price, the operating load of the methanol synthesis plant, and the pressure inside the storage. Nonetheless, this configuration is not considered in this work to reduce the numerical complexity. Also, no hydrogen losses are considered during the compression phase, since they are generally lower than 0.5 % [286].

The compressed hydrogen is then cooled in a single heat exchanger to 298 K. The cooling demand is assumed equal to the power needed for compression. The capital cost of these components is estimated at the maximum flow rate condition by using the cost models proposed by Biegler et al. [294].

4.3.4. Hydrogen storage

The amount of hydrogen available in the vessel ($M_{H_2}(t)$) is calculated with the following mass balance:

$$M_{H_2}(t) = M_{H_2}(t - \Delta t) + \dot{m}_{H_{2,prod}}(t) \cdot \Delta t - \dot{m}_{H_{2,MeOH}}(t) \cdot \Delta t,$$

where $\dot{m}_{H_{2,prod}}(t)$ is the hydrogen flow rate produced by the electrolyzer, and $\dot{m}_{H_{2,MeOH}}(t)$ the hydrogen flow rate consumed in the methanol synthesis plant.

The hydrogen storage is assumed to be isothermal at 298 K, and the pressure inside the storage ($p(t)$) is estimated from the available hydrogen inside the storage by using a linear interpolation of the density (ρ). As the methanol synthesis occurs at a pressure of 75 bar, the minimum pressure of the storage is set to that value. The available hydrogen stored in the vessel at the time step t and its pressure are, therefore, calculated as follows:

$$M_{H_2}(t) = V \cdot \left(\rho_{(p(t))} - \rho_{(75\ bar)}\right) \approx V \cdot 0.073\ \frac{kg}{m^3 bar} \cdot (p(t) - 75\ bar)\,,$$

where V is the volume of the storage. Although multiple hydrogen vessels of limited size would probably be needed in large-scale plants [288], V is considered as a continuous variable.

The capital cost of the storage is estimated by using the specific cost per unit of volume. Further details can be found in Appendix B.2.

4.3.5. Methanol synthesis plant

The methanol synthesis plant is modeled in Aspen Plus ® V11 (see Appendix B.3 for more details). However, such a detailed model cannot be embedded in GAMS and handled by the optimizer. Therefore, the key information about efficiency, mass flow rates, and energy demand is extracted to build a simplified algebraic model of the plant (see parameter values in Table B.11). In particular, the produced methanol mass flow rate depends linearly on the hydrogen flow rate (assumption of constant efficiency for the methanol synthesis plant), while the electricity demand, the cooling demand, and the inlet CO_2 mass flow rate scale linearly with the methanol production rate. The efficiency of the methanol synthesis plant is assumed constant in the operating range since it is not expected to have significant changes when varying the methanol plant load, especially if relatively low ramp rates ($<$ 50 % h^{-1}) are considered [290].

While the H_2 production is simulated by the model of the electrolysis unit (Section 4.3.2), the model of the carbon capture unit for the CO_2 supply is not included in the optimization problem. Therefore, it is assumed that a suitable CO_2 stream can be supplied to the methanol synthesis plant at every time step.

The investment cost of the methanol synthesis plant ($CAPEX_{MeOH}$) is estimated from the investment cost ($CAPEX_{MeOH,\,ref}$) calculated for the reference Aspen Plus model via a

regression function, which is defined as:

$$\mathrm{CAPEX}_{\mathrm{MeOH}} = \mathrm{CAPEX}_{\mathrm{MeOH,\,ref}} \cdot \left(\frac{\dot{\mathrm{m}}_{\mathrm{H_2,MeOH,\,nom}}}{\dot{\mathrm{m}}_{\mathrm{H_2,MeOH,\,nom\,ref}}} \right)^{\mathrm{b}},$$

where b is the regressive exponent (equal to 0.6 for the six-tenths rule), to evaluate the CAPEX for different plant capacities ($\dot{m}_{\mathrm{H_2,MeOH,\,nom}}$). Further details about the cost estimation can be found in Appendix B.4.

4.4. Case studies

The roles of storage and flexibility in the PtMeOH plant were analyzed for two case studies, i.e., grid-connected and stand-alone plants. The latter case can be representative of a plant built in a remote location with high potential for renewable power production that would require high investments for establishing a grid connection.

For both case studies, two-month scenarios were discretized with hourly resolution (1440 time steps) for the scheduling problem. The relatively short time frame is motivated by the size of the optimization problems: the number of variables and constraints scales linearly with the number of time steps unless time series aggregation techniques are used [6, 297, 298] (also see Section 5.3). Although the simplification of the optimization problems, e.g., via linearization and integer relaxation, thus reducing the problem accuracy, would allow considering longer time horizons, no seasonal storage of hydrogen and electricity is expected, as the methanol plant is likely to be operated almost continuously. This means that the stored H_2 and electricity are used in a relatively short term in case the electricity is expensive or the renewable power is not sufficient to produce enough hydrogen via electrolysis for the methanol plant. Nevertheless, this time frame allows considering price and renewable power variations that occur on different time scales, e.g., electricity price variation between working and weekend days for multiple weeks, and the diurnal effects on renewable power generation.

For the grid-connected case study, we assumed that there are no limitations in terms of power availability and that the amount of energy exchanged with the grid does not affect the electricity price. Two electricity price scenarios based on historical day-ahead electricity prices of Germany (the first 60 days of the years 2021 and 2022, bidding zone BZN|DE-LU of Germany [299]) were analyzed. The choice of these relatively extreme scenarios allows for investigating their impact on the optimal process design. No additional taxes or grid fees were considered, although they can play a significant role in energy costs, as for Germany [300]. The scenarios differ significantly in terms of mean value and standard deviation (Figure 4.2), representing a low-mean price scenario with a small standard deviation, and a high-mean price scenario with a high standard deviation. Although producing low carbon footprint e-methanol is desirable, high penetration of renewables in the electricity grid is not a necessary assumption for this work, since we used methanol production cost as the metric: e-methanol can be produced even when grid electricity has high carbon footprints if economically competitive, although this would go against the main motivation of adopting PtX processes. Nevertheless, the considered electricity price profiles are intended to be two possible and very different indications of future electricity price scenarios when the carbon footprint of the electricity will be lower.

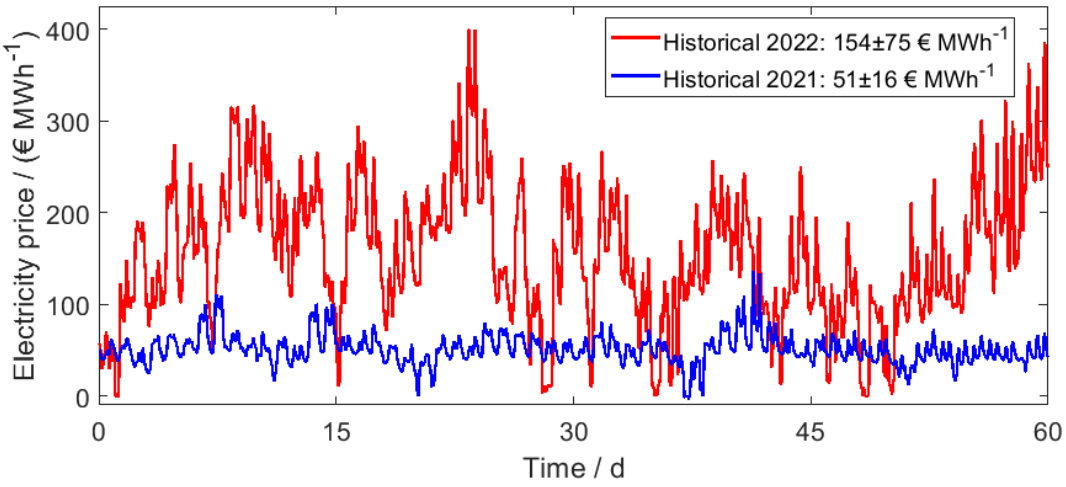


Figure 4.2.: Electricity price scenarios [299].

For the stand-alone case study, the power was assumed to be produced by a dedicated renewable generation park composed of wind and Photovoltaic (PV) plants. The considered power generation profiles (Figure 4.3) do not belong to any specific power plant, but they were taken from German historical data (May-June 2022 and November-December 2022, bidding zone BZN|DE-LU of Germany [299]) and scaled to a typical size for large renewable parks (ca. 125 MW and 110 MW in nominal conditions for wind and PV plants, respectively). The considered profiles were chosen to represent the two extremes, i.e., renewable generation in summer (high PV power generation) and in winter (high wind power generation), since no yearly seasonality could be considered in a single scheduling scenario due to computational issues. Furthermore, the complementarity of wind and PV power generation throughout the year also reduces the production costs [46] and the need for seasonal (hydrogen) storage, thus meaning the estimated size of storage in the two-month scenario might most likely be sufficient. Finally, the renewable power plants present moderate capacity factors over the considered horizons (0.16-0.22). This suggests that higher energy availabilities, e.g., related to more favorable locations or periods, could result in lower methanol production costs.

Additional assumptions were made for the stand-alone case study: i) the renewable power generation profile is known (perfect forecast), ii) the cost of electricity is null since the capital cost of the renewable plants [301] and their O&M expenditures are included in the methanol production cost calculation, iii) the sum of the electricity demand of the whole PtMeOH plant must be less than or equal to the electricity available for each time step; iv) electricity in the battery can also be converted to AC to supply energy to the methanol synthesis plant in case of renewable production shortage; v) the eventual excess of electricity is curtailed.

To investigate the role of storage, four plant configurations were considered, i.e., the PtMeOH plant without storage, with a battery, with H_2 storage, and with both storage technologies (Figure 4.4) in the grid-connected case study.

In contrast, only the PtMeOH plant configuration with both storage technologies was considered in the stand-alone case study, since storage is essential to grant continuous operation of the downstream plant: the battery can supply energy to the plant in case

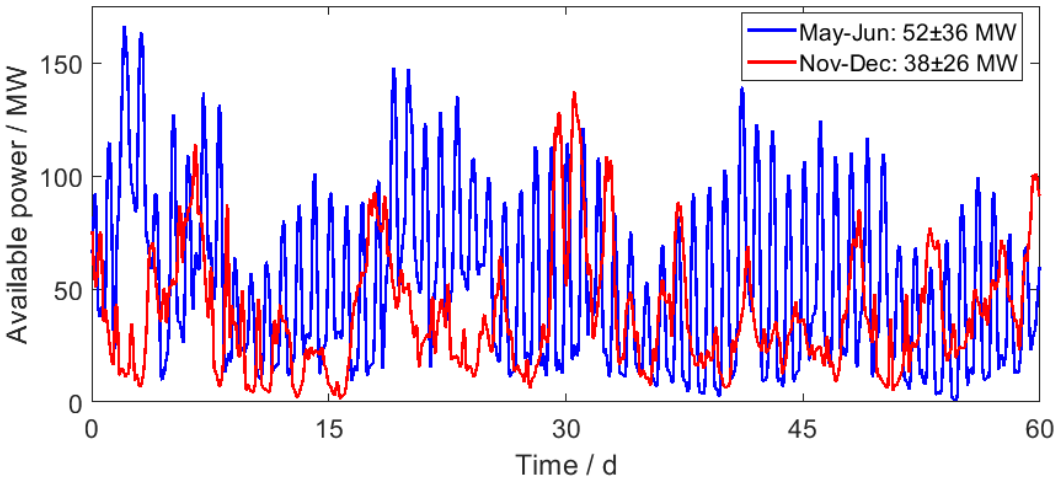


Figure 4.3.: Power availability scenarios [299].

of a temporary electricity generation shortage, while the H_2 storage can supply H_2 to the methanol synthesis plant when the electricity production is not sufficient to run the electrolysis unit.

Further, as the investment cost of some process units is expected to significantly reduce in the near future, the optimization problems were also solved by considering capital cost predictions for the year 2030 ("Scenario 2030"). The assumed values can be found in Appendix B.5.

Finally, the Levelized Cost Of Methanol (LCOM) was used as a metric to compare the configurations for each case study. In particular, the LCOM depends on both design ($\boldsymbol{d} \in \mathbb{R}^{N_{\text{design var}}}$) and scheduling ($\boldsymbol{s} \in \mathbb{R}^{N_{\text{scheduling var}} \times N_{\text{TS}}}$) optimization variables. Accordingly, $N_{\text{design var}}$ is the number of design variables, $N_{\text{scheduling var}}$ the number of distinct scheduling variables, and N_{TS} the number of time steps for each scheduling variable.

The objective function is calculated by assuming a constant methanol sell price over time and a net present value equal to zero at the end of the plant lifetime, and it is defined as

$$\text{LCOM}(\boldsymbol{d}, \boldsymbol{s}) = \frac{\text{CAPEX}_0(\boldsymbol{d}) + \text{CAPEX}_{\text{r, PEM}}(\boldsymbol{d}) \cdot (1+i)^{-10} + \sum_{j=1}^{N_y} (\text{O\&M}_{\text{y}}(\boldsymbol{d}) + \text{OPEX}_{\text{y}}(\boldsymbol{d}, \boldsymbol{s})) \cdot (1+i)^{-j}}{\sum_{j=1}^{N_y} (M_{\text{MeOH, y}}(\boldsymbol{d}, \boldsymbol{s})) \cdot (1+i)^{-j}}, \tag{4.1}$$

where CAPEX_0, $\text{O\&M}_{\text{y}}$, and OPEX_{y} are the initial capital expenditures, the yearly operation and maintenance, and the operating costs of the plant, respectively. N_y is the number of operating years, $M_{\text{MeOH, y}}$ the yearly production of methanol, and i the interest rate. Additionally, a replacement of the electrolysis unit at the end of the tenth year is considered ($\text{CAPEX}_{\text{r, PEM}}$). Neither the salvage value of the plant nor the sale of oxygen is considered to have a conservative estimation of the methanol production cost.

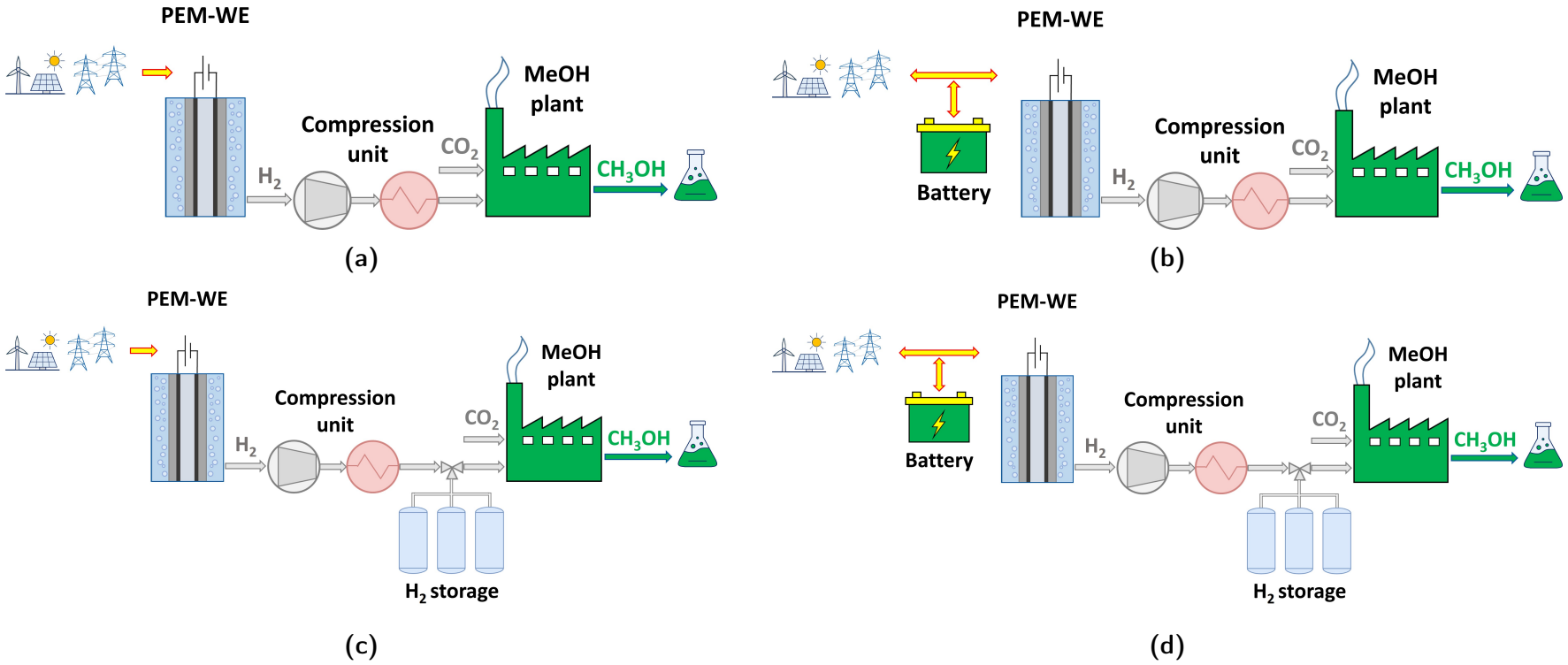


Figure 4.4.: Investigated Power-to-Methanol plant configurations: (a) without any storage, (b) with a battery, (c) with H_2 storage, and (d) with battery and H_2 storage.

The capital cost of the single units was calculated with the cost models described in Section 4.3 as the result of the optimal design. The operating costs were calculated based on the optimal scheduling as well as the methanol production. In fact, no methanol production target was set to avoid limiting the economic savings from scheduling and enable a fair comparison among the configurations (setting a target might, for instance, limit the benefits of storage utilization for the considered bounds). Therefore, methanol production is mainly limited by the ranges of the optimization variables, e.g., the size of the electrolysis unit, or the availability of renewable energy. Nevertheless, a minimum value of 40 kt y^{-1}, half of the maximum methanol production for the considered boundaries, was set for the grid-connected case studies to avoid not meaningful solutions with the assumed cheap future cost of batteries (see "Scenario 2030" in Section 4.6). Further assumptions for the economic evaluations are summarized in Table 4.3.

Table 4.3.: Main assumptions for the economic evaluations.

	Values
Reference year	2021
$ to € conversion factor	0.85
Lifetime of the Power-to-Methanol plant	20 y
Operating weeks per year for the methanol synthesis plant	48 w y^{-1}
Yearly O&M as % of the initial investment cost ($CAPEX_0$)	5 %
Interest rate i	5 %
Cooling cost	1 € MWh^{-1}
CO_2 stream cost	50 € t^{-1} [302]

4.5. Optimization

The Combined Design and Scheduling (CDS) optimization problems were formulated in GAMS 38.2.1 and solved on an Intel Xeon Gold 6226 CPU with 2.7 GHz and 384 GB RAM. These MINLP problems were initialized with a starting solution found after a multi-start local search and then solved with the deterministic global optimizer Branch-And-Reduce Optimization Navigator (BARON), version 22.2.3 [282]. Two stopping criteria were considered for the optimizer, i.e., an optimality gap of 0.01 and the CPU time limit of 12 h. Unfortunately, the relative difference between the upper bound (best feasible solution found) and the lower bound (best possible solution) did not reach the required optimality gap within the computational time limit in most of the optimization problems; thus, overall global optimality cannot be guaranteed. Nevertheless, the upper bound stabilized after a few iterations, thus suggesting that the convergence issues were mainly due to the difficulty of proving global optimality with wide variable bounds (global optima were proven in some of the problems after tightening the variable bounds). In preliminary analyses, we also tested Knitro, ANTIGONE, SCIP, and DICOPT, but their performance in identifying optima was worse than that of BARON.

For all the considered case studies, the LCOM was minimized. In the following subsections, the optimization variables and the main constraints are discussed.

4.5.1. Optimization variables

The considered optimization variables can be divided into two categories: design and scheduling variables. The design variables allow defining the optimal size and capacities of the units, which mainly contribute to the investment cost, while the scheduling variables determine how the units are operated, thus affecting the production rates and the operating costs (Equation (4.1)).

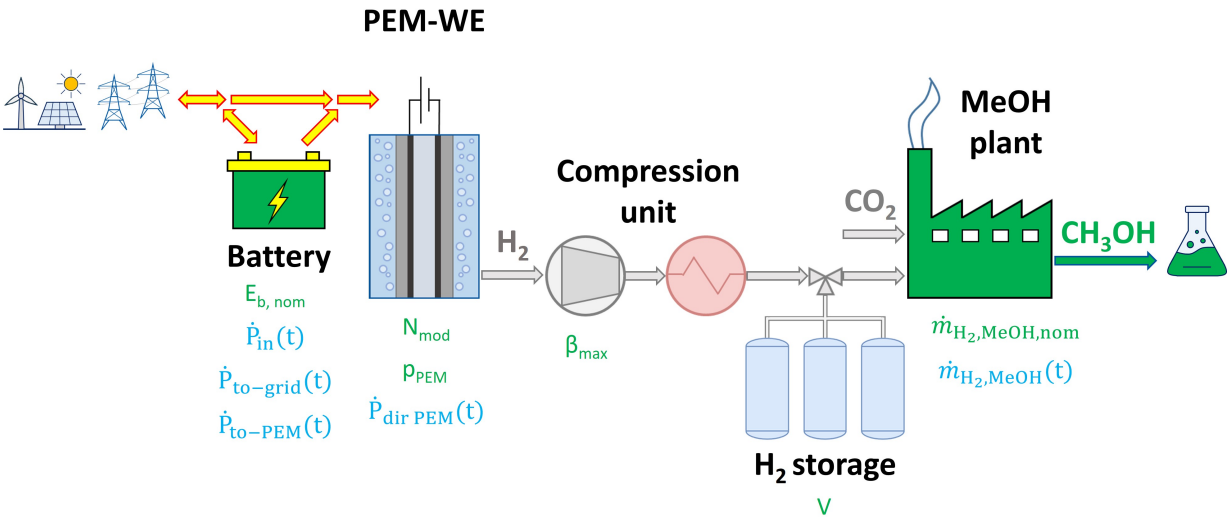


Figure 4.5.: Sketch of the Power-to-Methanol process with intermediate storage (configuration (d)) considered for the CDS problems. The design and scheduling optimization variables are displayed in green and light blue, respectively. Refer to Table 4.4 for more details on the optimization variables.

As regards the plant design, the size of the battery, electrolyzer, compression unit, H_2 storage, and methanol synthesis plant was optimized (Figure 4.5). In particular, the size of the methanol synthesis plant was estimated from the nominal H_2 input stream since a constant hydrogen conversion efficiency was assumed for the methanol plant (see Subsection 4.3.5). This modeling choice reduces the number of variables seen by the optimizer, thus improving the computational performance. The nominal H_2 input stream in the methanol plant can differ from the maximum hydrogen production rate of the electrolysis unit in case there is H_2 storage. Two additional design variables that also have a high impact on the operating phase were considered, i.e., the operating pressure of the electrolysis unit and the maximum pressure ratio of the compressor. The first affects the electrolyzer efficiency as well as the size of the downstream compression unit, while the second determines the maximum pressure that can be achieved in the H_2 storage. The choice of these two design variables aims at capturing the interplay between the size of the compression unit and the H_2 storage.

A maximum size of 100 MW (40 modules) was considered as representative of the electrolyzer module size in the short-term future [84, 87]. The maximum size of the battery and H_2 storage was defined accordingly in order to provide a few hours of storage (around 4 h and 18 h, respectively, when the electrolyzer is operated at 100 MW). The electrolyzer pressure range is typical for PEM-WEs. The maximum pressure ratio of the compressor

unit is limited by technical issues, e.g., discharge temperature [286] and overall efficiency. A summary of the design variables and their bounds can be found in Table 4.4.

As regards the plant scheduling, optimization variables for the battery, the electrolyzer, and the H_2 storage were introduced (Figure 4.5). For the battery, the power input ($P_{\text{in}}(t)$) and the power output ($P_{\text{to-grid}}(t)$ and $P_{\text{to-PEM}}(t)$) were optimized. For the electrolysis unit, the power taken from the grid ($P_{\text{grid}}(t)$) was considered. The operating constraints for the battery and electrolysis unit were enforced via three sets of binary variables. The hydrogen flow rate fed into the methanol synthesis plant ($\dot{m}_{\text{H}_2,\text{MeOH}}(t)$) determines the methanol production rate over time. The bounds of the operational variables for optimization depend on both the design optimization variables and technical constraints and will be discussed in more detail in Section 4.5.2.

Table 4.4 shows the optimization variables for the most general configuration, i.e., the PtMeOH plant with both storage technologies. Though the four investigated configurations (Figure 4.4) could have been optimized via a single superstructure optimization problem by introducing binary variables, enumeration was preferred to limit the complexity of the optimization problem, which already counts 8646 independent variables (6 design and 8640 scheduling variables) for the flexible PtMeOH plant with both storage technologies, and explicitly evaluate the design and production cost differences among them. The optimization problem was modified when considering simpler plant configurations (no storage and no flexibility) to reduce the problem size and improve convergence.

4.5.2. Operation constraints

The operation of the PtMeOH plant depends on the size of the units and on their operational limits.

Batteries have wide operating ranges with respect to their state of charge [23]. A minimum state of charge of 10 % is assumed to prevent deep discharge phenomena (not considered in this work). Some operational constraints on the hourly energy flows are also set. When active, a minimum power flow of 0.5 MW is considered to avoid small energy transfers, which would not be feasible for the power electronics in large plants. The maximum charge and discharge rates are also limited by either the nominal capacity of the battery or the maximum power of the electrolyzer (100 MW). These operating load constraints are enforced through binary variables (also see Section B.1.1).

PEM-WEs also have wide operating limits (0-160 % relative to the nominal load [50]). Nonetheless, we consider an operating range of 25-125 % since the downstream compression unit has a narrower operating range (25-100 % of the H_2 flow rate) and no buffer tank is considered between the electrolyzer and the compressor unit. These operating constraints are also enforced via binary variables.

The H_2 storage located after the compression unit has a 0-100 % operating range, where 0 % corresponds to the pressure inside the storage of 75 bar (no H_2 available for the methanol synthesis in the storage).

The methanol synthesis plant is assumed to always be operating over the considered time horizon within a range of 20-100 % of the nominal load [33]. This choice also allows avoiding the implementation of additional optimization variables for the on-off, start-up and shutdown phases, as well as the introduction of an economic penalty due to the energy and hydrogen consumption during these phases.

Table 4.4.: Design (a) and scheduling (b) variables of the optimization problem for the grid-connected and stand-alone case studies. A brief description of the variable and the considered upper and lower bounds is also provided.

Unit	Symbol	Variable description	Lower bound	Upper bound
Battery	$E_{b,\,nom}$	Energy capacity	5 MWh	400 MWh
PEM-WE	N_{mod}	Number of modules (integer)	10	40
	p_{PEM}	Operating pressure	20 bar	40 bar
H_2 compression	β_{max}	Maximum pressure ratio	1.88	3.50
H_2 storage	V	Volume of the vessel	25 m^3	7500 m^3
MeOH plant	$\dot{m}_{H_{2,MeOH},nom}$	Nominal H_2 flow rate for the methanol synthesis plant	0.4 t h^{-1}	2 t h^{-1}

(a) Design variables.

Unit	Symbol	Variable description	Lower bound	Upper bound
Battery	$P_{in}(t)$	Power input	0.5 MW *	$\min(100\text{ MW}, (0.9 \cdot E_{b,\,nom}/1h))$
	$P_{to-grid}(t)$	Power output, electricity back to the grid (AC)	0.5 MW *	$\min(100\text{ MW}, (0.9 \cdot E_{b,\,nom}/1h))$
	$P_{to-PEM}(t)$	Power output, electricity to the electrolyzer	0.5 MW *	$\min(100\text{ MW}, (0.9 \cdot E_{b,\,nom}/1h))$
PEM-WE	$P_{grid}(t)$	Power directly from the grid/renewable plant	0.5 MW $\cdot N_{mod}$ *	2.5 MW $\cdot N_{mod}$
H_2 storage	$\dot{m}_{H_{2,MeOH}}(t)$	H_2 flow rate from storage to the methanol synthesis plant	$0.2 \cdot \dot{m}_{H_{2,MeOH},nom}$	$\dot{m}_{H_{2,MeOH},nom}$

* 0 MW if the unit is not operating - enforced via binary variables (not shown).

(b) Scheduling variables.

As mentioned in Section 4.5.1, the methanol flow rate is calculated from the hydrogen flow rate fed into the methanol synthesis plant ($\dot{m}_{\mathrm{H_2,MeOH}}(t)$). This hydrogen flow is equal to the hydrogen flow produced by the electrolyzer unless there is the H_2 storage. In this case, the hydrogen flow to the methanol synthesis plant is considered an optimization variable. Furthermore, to investigate the effect of the flexibility of the methanol synthesis plant on its production cost, the following ramp constraint is set:

$$|\dot{m}_{\mathrm{H_2,MeOH}}(t) - \dot{m}_{\mathrm{H_2,MeOH}}(t - \Delta t)| \leq \mathrm{RL} \cdot \dot{m}_{\mathrm{H_2,MeOH,nom}},$$

where RL is the maximum ramp limit expressed in percentage, and $\dot{m}_{\mathrm{H_2,MeOH},nom}$ is the nominal H_2 flow rate fed into the methanol synthesis plant. In case no flexibility is considered, the methanol synthesis plant is operated steadily at the nominal capacity.

Further, different operating ranges and ramp rates for the methanol synthesis and methanol purification units could be considered as in Svitnič et al. [46] and Bai et al. [303], thus improving the model accuracy. However, such model adaptation would have increased the problem complexity due to the additional design and scheduling variables for the purification unit and the intermediate storage for crude methanol and steam, which is used for heat integration between the methanol synthesis reactor and the distillation column reboiler. Furthermore, distillation columns can be operated quite flexibly [46, 144, 304]. Therefore, this option has not been considered in this work.

A summary of the operating limits and of the operational constraints can be found in Tables 4.4 and 4.5. We refer to the GAMS files in the Supporting Information of Mucci et al. [4] for the implementation of all constraints.

Table 4.5.: Summary of the operation ranges of the plant units (minimum-maximum load).

Unit	Operating range
Battery	10-100 %
PEM-WE	25-125 %*
H_2 compression	25-100 %
H_2 storage	0-100 %
Methanol synthesis plant	20-100 %

* Referred to the nominal load.

4.6. Results and discussion

In this section, the optimization results for the two case studies (grid-connected and stand-alone) are shown.

4.6.1. Grid-connected Power-to-Methanol case study

In order to investigate the role of storage, we compared the four plant configurations (Figure 4.4) for both a low-mean low-standard-deviation and a high-mean highly-standard-deviation electricity price scenarios (Figure 4.2). The role of flexibility was investigated by

varying the maximum ramp limit (RL) of the methanol synthesis plant (in % h^{-1} of the nominal load).

4.6.1.1. Low-mean low-standard-deviation electricity price scenario (Historical 2021)

The calculated specific cost of methanol (LCOM) is around 0.9 € kg^{-1}, which is, as expected, higher than typical methanol prices in the spot market (0.5-0.6 € kg^{-1} in Europe [305]). As shown in Table 4.6, the specific cost gets slightly lower (around 1 %) by allowing flexible operation of the methanol synthesis plant.

When allowing flexibility in all the configurations for this electricity scenario (the electrolyzer size is at its upper bound), the optimal size of the methanol synthesis plant does not change. Therefore, the LCOM reduction is due to the savings on the operating costs (OPEX), although the overall methanol production ($M_{\mathrm{MeOH,\,y}}$) is reduced because of the part-load operation (see Equation (4.1)). In fact, if the methanol synthesis plant is operated flexibly, the electrolyzer, the most energy-intensive unit, can be operated at the maximum load when the electricity is cheap, and at a lower load when the electricity is expensive (Figure 4.6). Nevertheless, the capacity factor of the methanol synthesis plant is above 94 % (calculated on the working hours) even when the plant is operated flexibly in the considered scenario.

The process configuration with the lowest LCOM has no storage, thus indicating that the potential operating cost savings due to storage do not repay the related investment costs. This is probably due to the relatively low mean value and standard deviation of the electricity price profile considered for this case study.

As regards the other design variables, the optimal pressure of the electrolyzer reaches the upper bound (Table B.17). Thus, the increased operating costs related to the reduction of the electrolyzer efficiency are lower than the additional capital cost required for a bigger compression unit. Also, the nominal hydrogen flow rate for the methanol synthesis plant is equal to the maximum hydrogen production of the electrolyzer, since decoupling H_2 storage is not used. An optimal design solution close to the upper bounds was expected for electricity price profiles with moderate fluctuations and without restrictions on power availability, since the cost of the plant components benefits from the economy of scale.

Similar conclusions can be drawn when considering lower capital costs for the storage and electrolysis units ("Scenario 2030"). In fact, the relatively small fluctuations in the electricity price profile do not make storage technologies an economically viable solution, even with the reduced future investment costs of the storage units.

Table 4.6.: Optimization results for the grid-connected case study without storage for the low-mean low-standard-deviation electricity price scenario. Refer to Appendix B.6 for the complete results.

Flexibility % h^{-1}	LCOM € kg^{-1}	$M_{\mathrm{MeOH,\,y}}$ kt	CAPEX_0 M€	OPEX_y M€
0	0.91	80.3	133	51
5	0.90	76.2	133	46
10	0.90	75.7	133	46

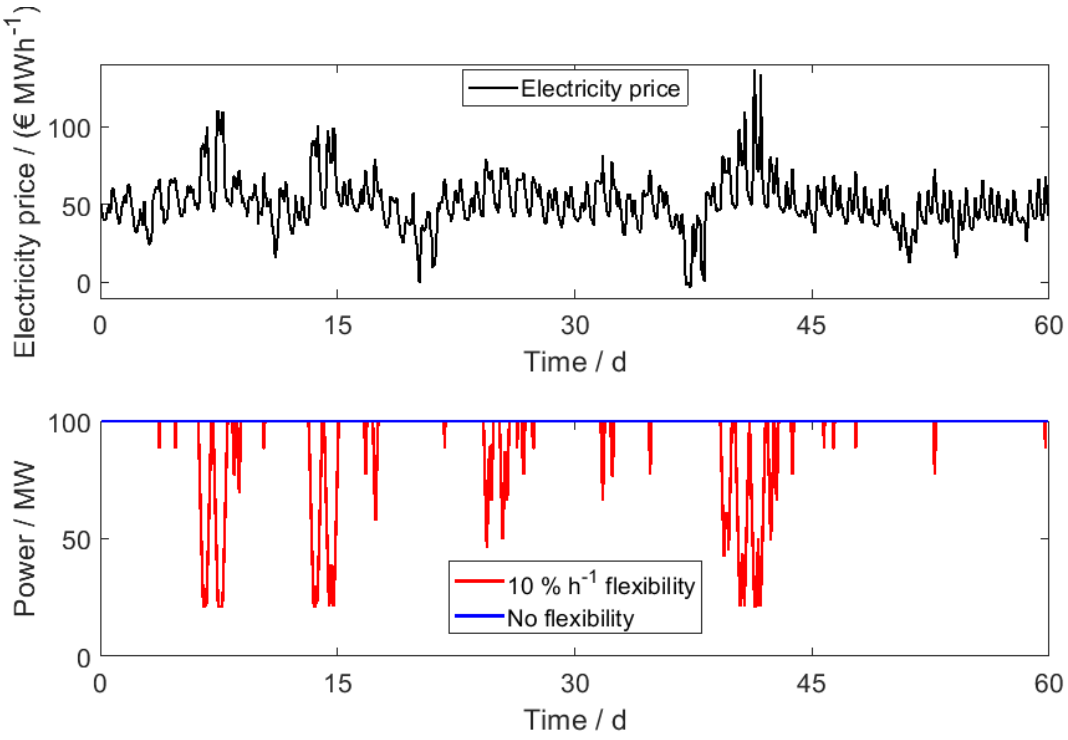


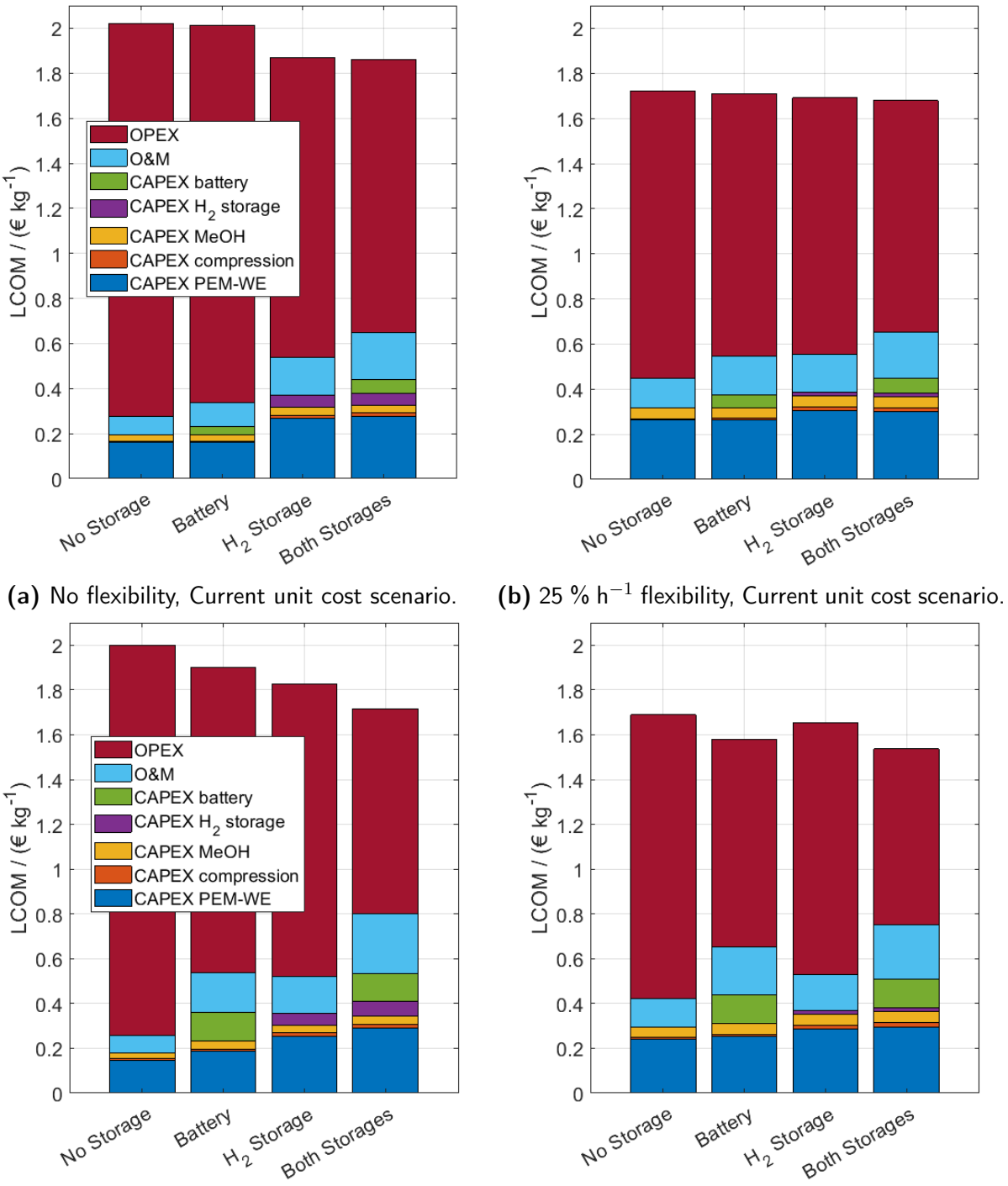
Figure 4.6.: Power of the PEM water electrolyzer for two levels of flexibility of the methanol synthesis plant, i.e., "No flexibility" and "10 % h^{-1} flexibility". The results are shown for the PtMeOH plant without any storage for the low-mean low-standard-deviation electricity price scenario (top part of the figure).

4.6.1.2. High-mean high-standard-deviation electricity price scenario (Historical 2022)

In this scenario, the methanol cost is around two times higher than the low-mean low-standard-deviation electricity price scenario. This shows the strong influence of the electricity price on the final product cost (Figure 4.7 a-d).

Flexible operation significantly (10-15 %) reduces the methanol cost compared to the previous scenario. In particular, there is a steep decrease in the methanol cost from the "No flexibility" and "5 % h^{-1} flexibility" cases (Table 4.7). This result is explained by the fact that a relevant part of the hourly price variations is lower than 5 % (see Appendix B.5) and by the possibility of reducing the production rate of methanol during the highly expensive electricity hours that characterize this scenario. This frequent, though optimal, operation at part loads reduces the methanol synthesis plant capacity factor to around 60 % for all the configurations in this electricity price scenario. Further minor relative cost reductions can be noticed when higher ramp limits are allowed, since the methanol production rate can adapt better to the highly fluctuating electricity price profile.

In this scenario, storage plays a relevant role, regardless of whether the methanol synthesis plant is operated constantly at nominal load or flexibly. The presence of the hydrogen vessel has the highest impact on the methanol cost, since it decouples the production and the consumption of hydrogen and allows downsizing the methanol synthesis plant (7 % to 40 % when operating flexibly and constantly at nominal load, respectively). Thanks to the



(a) No flexibility, Current unit cost scenario.

(b) 25 % h^{-1} flexibility, Current unit cost scenario.

(c) No flexibility, Future unit cost scenario.

(d) 25 % h^{-1} flexibility, Future unit cost scenario.

Figure 4.7.: Relative contribution to the methanol production cost (LCOM) of the investment cost of the units and of the operating costs for the "No flexibility" and "25 % h^{-1} flexibility" cases for four plant configurations, i.e., without any storage, with a battery, with a H_2 vessel, and with both storage for the high-mean high-standard-deviation electricity price scenario. The current and future unit cost scenarios are shown at the top and bottom of the figure, respectively.

Table 4.7.: Optimization results for the grid-connected case study for the high-mean high-standard-deviation electricity price scenario. Only the results of the PtMeOH configurations with (B&V) and without (No B&V) both storage technologies are shown here. Refer to Appendix B.6 for the complete results.

	Flexibility % h^{-1}	LCOM € kg^{-1}	$E_{b,\,nom}$ MWh	V m^3	$M_{MeOH,\,y}$ kt	$CAPEX_0$ M€	$OPEX_y$ M€
No B&V	0	2.02	-	-	80.7	135	141
B&V	0	1.86	115	4730	47.0	196	57
No B&V	5	1.75	-	-	49.5	133	64
B&V	5	1.69	116	1210	42.4	179	43
No B&V	25	1.72	-	-	49.4	133	63
B&V	25	1.68	111	1040	42.9	177	44

H_2 storage, the electrolyzer can be turned off during expensive electricity hours (Figures 4.8 and 4.9), while the downstream plant is still producing methanol. Nevertheless, the optimal storage size gets lower when the methanol plant can be operated flexibly, as already observed in literature [45, 85, 218]. Furthermore, the methanol synthesis plant with H_2 storage has a smoother operational profile than the case without H_2 storage (see the bottom part of Figure 4.9). The battery unit also contributes to reducing the methanol production cost through savings in the operating costs (Figure 4.7): it supports the PtMeOH plant by providing electricity to the electrolyzer and selling electricity back to the grid (Table B.20). Interestingly, more electricity can be sold to the grid during expensive electricity hours if hydrogen storage is present: the hydrogen demand of the methanol plant can still be met while the electricity stored in the battery can be sold instead of supplied to the electrolyzer.

As regards the design of the PtMeOH plant, the electrolyzer size always reaches the upper bound (see Table B.18). The nominal hydrogen flow rate into the methanol plant differs from the maximum amount of hydrogen that can be produced from the electrolyzer (around 1.9 t h^{-1}) only when there is H_2 storage. Interestingly, when there is no H_2 storage and the methanol synthesis plant is operated constantly at nominal load, more efficient production of hydrogen seems to be favored because of the high cost of electricity: the operating pressure is below the upper bound (around 31.5 bar), differently from all the other configurations.

When considering the future unit cost scenario, the methanol production cost is lower (Table B.19). Similarly to the current unit cost scenario, enabling flexible operation reduces the methanol production cost. Also, the PtMeOH plant with both storage technologies is still the best configuration (Figure 4.7 c-d).

Thanks to the reduction of the installation cost of storage, bigger storage units, especially the battery, are chosen by the optimizer (Table B.19). In fact, the battery provides not only electricity to the electrolyzer but also generates high revenues by selling electricity back to the grid during expensive electricity hours (Table B.20), thus significantly reducing the overall operating costs (Figure 4.7 c-d).

As opposed to what is observed for storage sizes, the optimizer selects smaller electrolysis and methanol unit sizes, thereby reducing the related investment cost and their power demand. This allows the battery to supply less electricity to the PtMeOH plant and sell

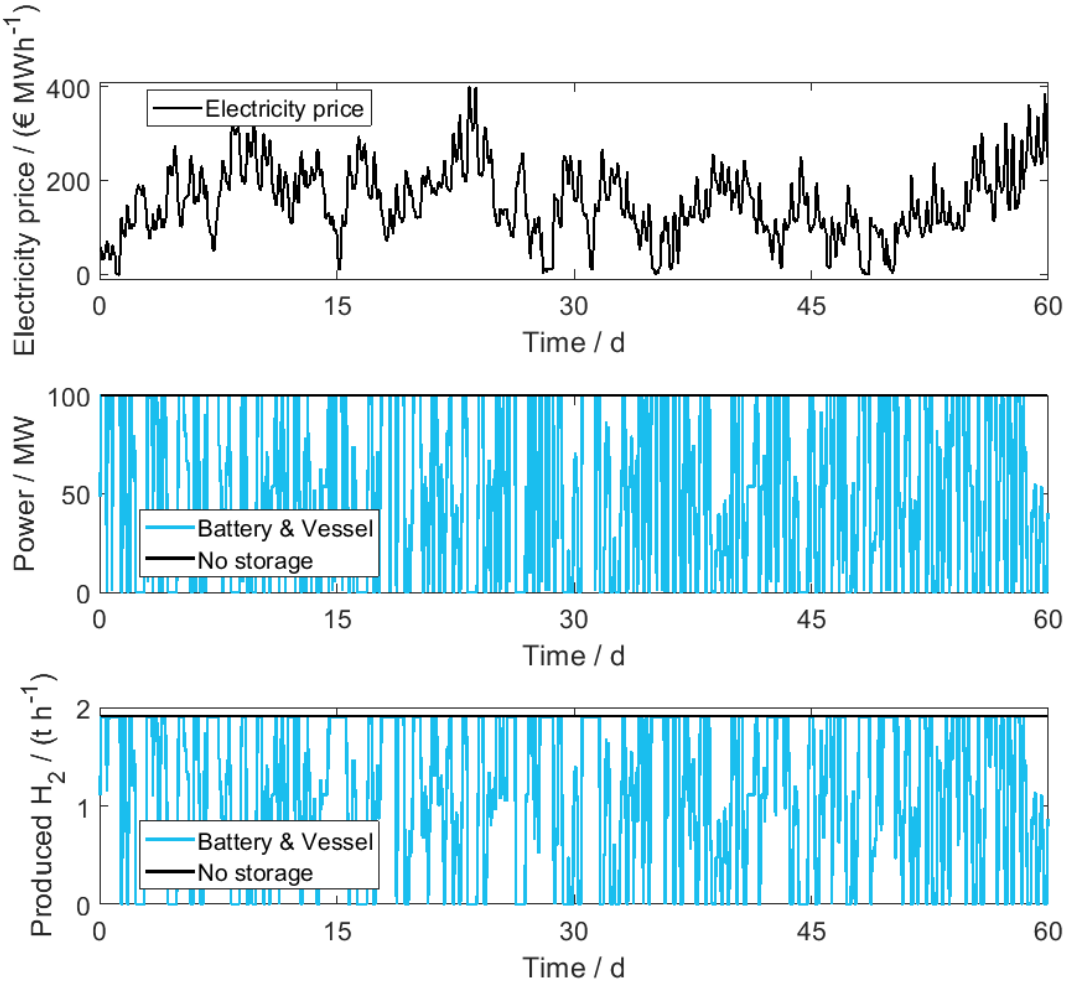


Figure 4.8.: Power of the PEM-WE taken from the grid over time and hydrogen produced by the electrolyzer for the "No flexibility" case. The best ("Battery & Vessel") and worst ("No storage") cases are shown. The electricity cost profile is also shown to interpret the optimal scheduling better. Note: the power profile might not match qualitatively the hydrogen production profile for the "Battery & Vessel" configuration due to the additional power flowing from the battery unit.

more electricity to the grid (remember the charging and discharging rate limits of 100 MW for the battery), generating revenues during expensive electricity hours. This combined effect on CAPEX and OPEX induced by the battery effectively reduces the methanol production cost despite the reduction in the produced methanol. The minimum value for the yearly methanol production (40 kt) is therefore always obtained when batteries are present for the future unit cost scenario (Table B.19).

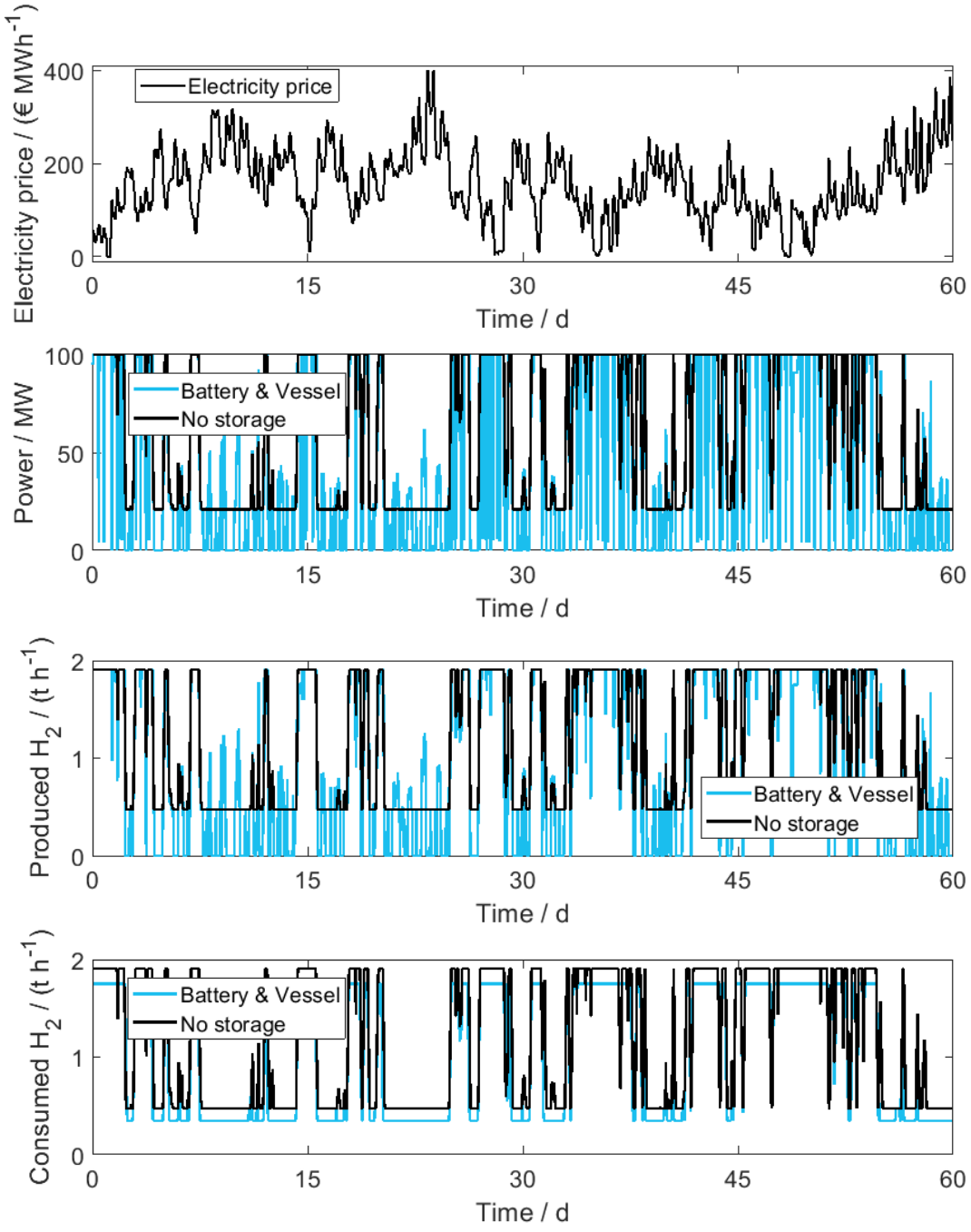


Figure 4.9.: Power of the PEM-WE taken from the grid and H_2 flow rate produced by the electrolyzer and consumed in the methanol synthesis plant for the "25 % h^{-1} flexibility" case. The best ("Battery & Vessel") and worst ("No storage") cases are shown. The electricity cost profile is also shown to interpret the optimal scheduling better. Note: the power profile might not match qualitatively the hydrogen production profile for the "Battery & Vessel" configuration due to the additional power flowing from the battery unit. Also, the hydrogen production profile might not match the hydrogen consumption profile due to the hydrogen flowing from the vessel.

4.6.2. Stand-alone Power-to-Methanol case study

The calculated LCOM for the stand-alone PtMeOH case study ranges between 1.39-1.78 € kg^{-1} and 1.69-2.38 € kg^{-1} for the "May-Jun" and "Nov-Dec" scenario, respectively (Table 4.8). Also in this case study (with both storage technologies), flexible operation of the methanol synthesis plant significantly affects the specific cost of methanol in both scenarios. The steep reduction of the LCOM between the "No flexibility" and "5 % $^{-1}$ flexibility" case is mainly due to the possibility of increasing the consumption of the available electricity and thus the methanol production (see the reduction of the relative contribution of the renewable plants to the methanol production cost in Figure B.4), although the capacity factor of the methanol synthesis plant is around 60 %.

In both scenarios, the utilization factor of the produced electricity rises from around 65-70 % to over 90 % (Figures 4.10 and 4.11), thus reducing the renewable curtailment. High utilization factors reduce the levelized cost of electricity, which significantly affects the methanol production cost. For instance, the levelized cost of electricity for the considered scenarios is ca. 80-100 € MWh^{-1} when process flexibility is enabled, thus partially explaining why the calculated LCOM for the stand-alone case study is higher than the one calculated for the grid-connected case study for the "Historical 2021" scenario, but lower than the one for the "Historical 2022" scenario (also see Figure 4.2). Even higher utilization factors are not economically optimal, since a significantly higher storage capacity would be needed to follow the few power peaks, and its investment would not be repaid. The maximum power that the PtMeOH plant can consume will therefore be lower than the installed capacity of the renewable park, as already observed in other works [45, 51].

Table 4.8.: Optimization values for the stand-alone case study for the considered scenarios (May-Jun and Nov-Dec). Refer to Appendix B.6 for the complete results.

	Flexibility % h^{-1}	LCOM € kg^{-1}	$E_{b,nom}$ MWh	V m^3	N_{mod} -	$\dot{m}_{H_{2,MeOH},nom}$ t h^{-1}	$M_{MeOH,y}$ kt
May-Jun	0	1.78	70	5000	20	0.67	28.3
May-Jun	5	1.40	27	800	33	1.43	37.9
May-Jun	25	1.39	28	510	33	1.43	37.9
Nov-Dec	0	2.38	35	5930	15	0.46	19.5
Nov-Dec	5	1.70	23	940	28	1.22	29.2
Nov-Dec	25	1.69	17	900	26	1.15	28.5

Storage is essential in the stand-alone configuration to grant continuous operation of the methanol synthesis plant in both scenarios, especially in low-power generation hours. H_2 storage always plays a relevant role, though its optimal volume gets lower when allowing increased flexibility: the optimizer selects larger methanol synthesis plant sizes rather than large storage capacities (Table 4.8). In contrast, the battery plays a minor role compared to the H_2 storage for the considered scenarios: the maximum amount of stored energy can satisfy the maximum power demand of the electrolyzer for less than one hour (if flexibility is allowed). Nevertheless, it intensively exchanges power with the system, especially during the production peaks and shortages when the electrolyzer cannot be operated (Figures 4.10 and 4.11) and when the electrolyzer cannot be operated at full capacity (also see Figures B.5 and B.6).

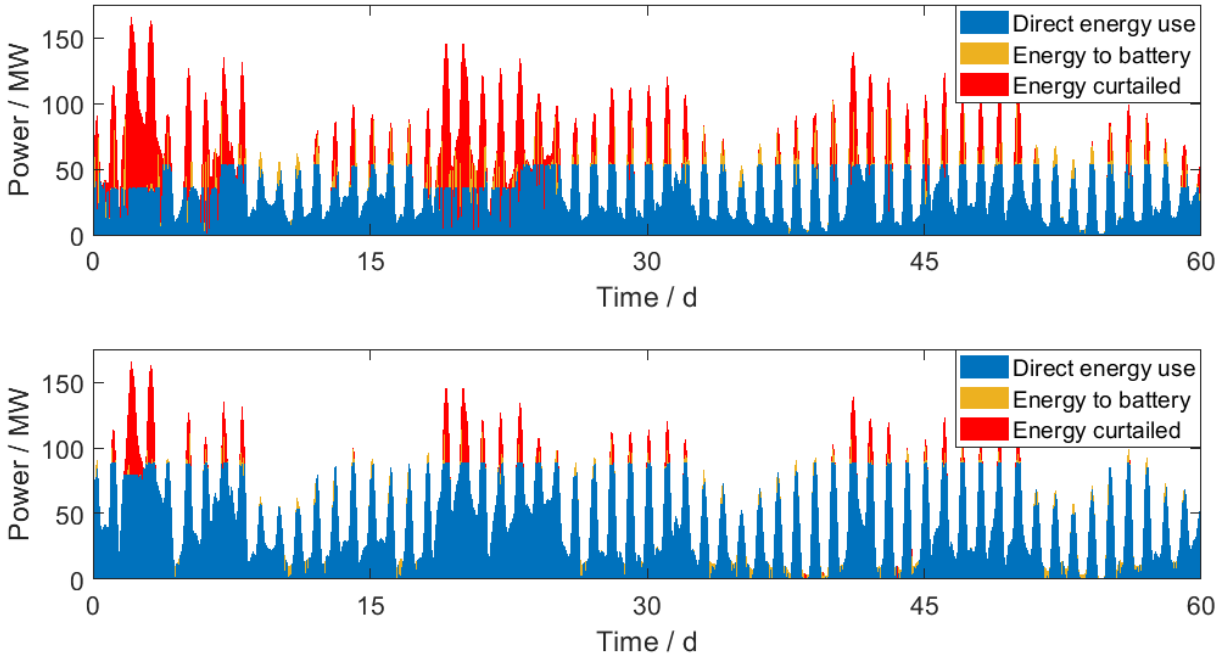


Figure 4.10.: Energy consumption, energy that is stored in the battery in that hour, and energy curtailed for the "No flexibility" (top) and ± "25 % h^{-1} flexibility" (bottom) cases (May-Jun scenario).

When considering the future unit cost scenario, the main difference lies in the significant reduction of the LCOM values (9-11 %). Moreover, the LCOM from a flexible stand-alone PtMeOH plant is significantly lower than the one from a grid-connected plant operated when electricity is expensive, e.g., in the "high-mean high-standard-deviation electricity price scenario".

Differently from the high-mean high-standard-deviation electricity price scenario of the grid-connected case study, the optimal size of both storage technologies does not change significantly between the current and future unit cost scenarios, since the battery cannot act as pure energy storage by performing energy arbitrage. Nevertheless, a bigger battery and a relatively smaller hydrogen storage are selected by the optimizer for the non-flexible methanol plant for the May-June Scenario (Table B.21). This is probably due to the periodic and frequent peaks related to photovoltaic generation (its average capacity factor over the considered horizon is around 0.25).

4.6.3. Discussion

The optimal design of the PtMeOH plant with and without storage in both case studies is highly dependent on the considered scenario. Nevertheless, general trends can be observed.

4.6.3.1. Role of flexibility

Flexible operation of the methanol synthesis process effectively reduces the methanol production cost in PtMeOH plants both with and without storage. This is mainly due to the wide operating range of methanol synthesis plants (20-100 %), which has been shown to play a big role in methanol cost reduction for flexible stand-alone plants [46]. In fact,

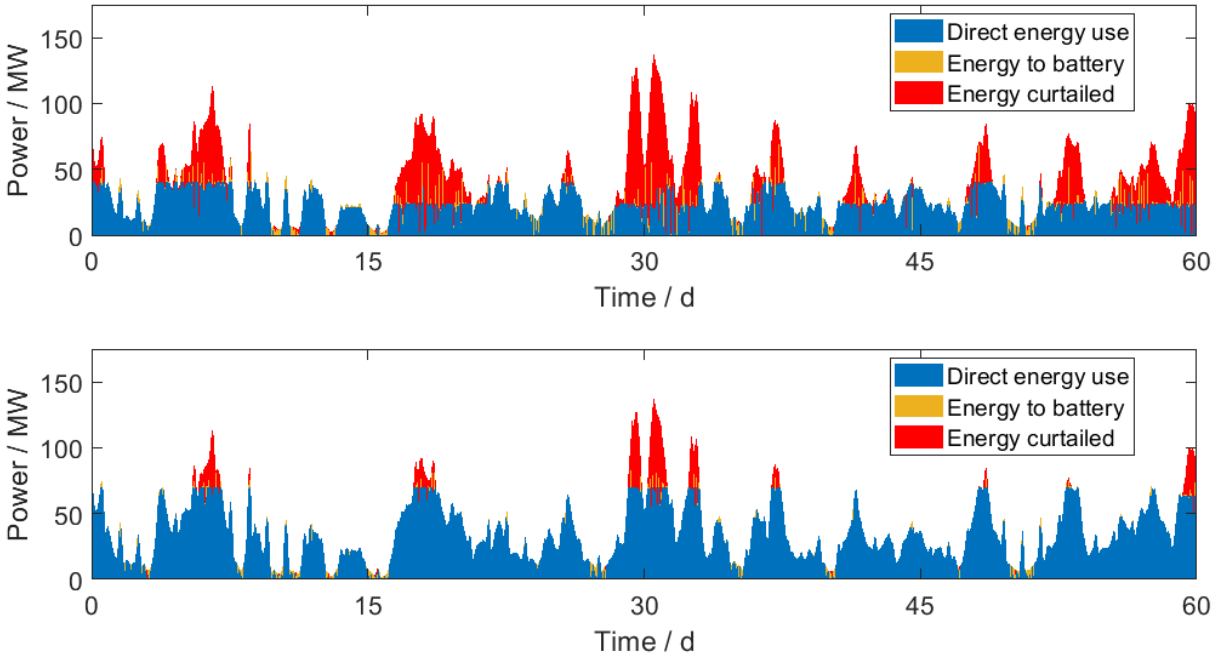


Figure 4.11.: Energy consumption, energy that is stored in the battery in that hour, and energy curtailed for the "No flexibility" (top) and ± "25 % h^{-1} flexibility" (bottom) cases (Nov-Dec scenario)

when the methanol plant is operated flexibly, the benefits obtained in our case studies by varying the ramp rate, e.g., from 10 % h^{-1} to 25 % h^{-1}, are lower than the reported benefits of extending the operating range of the methanol plant, e.g., from 75 %-100 % to 50 %-100 % [46], since the energy consumption can be further reduced when electricity is expensive or there is a renewable generation shortage.

The cost reduction related to the flexibility of the methanol synthesis process for both the grid-connected and stand-alone case studies aligns with other works in literature [45, 51]. However, a quantitative comparison is difficult, as it depends on the considered scenarios and boundaries.

In the grid-connected case study, the reduction of the methanol production during the high-price hours allows reducing the operating costs and, at the same time, the production cost of methanol (value in agreement with the cost range calculated by IRENA, i.e., 0.8-1.6 \$ kg^{-1} [302]). However, the optimal capacity factor of the methanol synthesis plant highly depends on the electricity price scenario (94 % and 60 % for the investigated scenarios with current unit costs).

In the stand-alone case study, flexible operation allows increasing the utilization of the electricity from the renewable park and the produced methanol, thus reducing the production cost. A similar cost reduction between flexible and not flexible stand-alone PtMeOH plants can be found in literature (1.50-1.85 \$ kg^{-1} and 1.89-2.84 \$ kg^{-1} for flexible and not flexible PtMeOH with hydrogen storage [45]). In contrast, the methanol cost reduction due to flexibility obtained by Svitnič and Sundmacher [46] was lower (1.39-1.58 \$ kg^{-1} and 1.46-1.75 \$ kg^{-1} for flexible and not flexible PtMeOH for the renewable availability scenario including both solar and wind generation). However, this might be due to the operational constraints and nonlinearities considered in this work, as well as the more ex-

tended process network considered in their work. In fact, the process network was able to provide relatively low production costs of methanol even when the plant was operated in steady state [46]. The even bigger methanol production cost difference for the future unit cost scenario (0.80-1.03 \$ kg^{-1} in [46] vs. 1.26-2.11 € kg^{-1} in this work) can likely be explained by the different models, boundaries, and cost predictions as well as the considered technologies in the process network. Further reduction of the methanol production cost could be achieved in case some electricity is taken from another source or the plant is interfaced with the grid [45, 281]: electricity can be sold (instead of curtailed) or purchased in case of renewable generation surplus and shortage, respectively, also reducing the need for storage.

The relative improvements in the objective function value decrease by increasing the maximum allowed ramp rate of the methanol synthesis plant. This aspect might be due to the considered time discretization, since electricity price and renewable production may in practice vary on shorter time scales. Nevertheless, flexibilization raises the issue of degradation: it might be worth not performing extremely quick load variations if these degrade some plant components and the related economic savings are small. For instance, the electrolyzers could particularly suffer from degradation due to frequent load changes, start-ups, and shutdowns and have a shorter operational lifetime. However, these phenomena are still not well understood and are difficult to model. An additional oversizing of the electrolyzer to consider the long-term efficiency loss [306] or considering different operating strategies, e.g., avoiding frequent start-ups and shutdowns by introducing a penalty function, could be alternative ways to account for these phenomena and refine the results. The possibility of shutting down the methanol plant (not considered in this work) could also be beneficial [278] in case the economic penalty due to catalyst degradation and start-up/shutdown procedures is not too high, as it might reduce the optimal size and cost of storage.

4.6.3.2. Role of storage

The role of storage depends on the considered boundaries, especially when the plant purchases electricity from the grid. When the electricity is cheap and its profile is not highly fluctuating, as in the historical scenario 2021, the savings in the operating costs thanks to intermediate storage do not repay its investment cost. If the electricity price is higher, as in the historical scenario 2022, storage improves the economic profitability of the plant. Nevertheless, the flexibilization of the methanol synthesis unit has a greater economic benefit compared to adding storage.

For the considered boundary conditions and the current unit cost scenario, the H_2 vessel provides big economic savings. The potential of the H_2 vessel estimated in this optimization problem could even be rather conservative. In fact, a hydrogen bypass could be applied when the hydrogen consumption of the methanol synthesis plant is higher than the produced hydrogen ($\dot{m}_{H_2,\,MeOH}(t) \geq \dot{m}_{H_2,\,prod}(t)$): the produced hydrogen is compressed and directly fed into the methanol synthesis plant together with the already pressurized hydrogen taken from the vessel. The bypass would save electricity in the compression unit, since the produced hydrogen has to be compressed up to the pressure of the synthesis plant (75 bar) instead of the higher pressure inside the vessel. From a post-analysis of the worst case (not flexible PtMeOH plant with H_2 storage for the high-mean high-standard-deviation electricity price scenario), the estimated economic savings of a bypass would be

around 9 % of the operating costs of the compression unit, but less than 0.1 % of the overall yearly operating costs. However, modeling this configuration would have introduced additional variables and complexity to the optimization problem for small improvements. Therefore, it was not considered in this work.

Compared to the vessel, the benefit of batteries on the production cost is lower for the current unit cost scenario and the considered boundary conditions, despite the nearly ideal model. In fact, small capacities are selected by the optimizer. This result was confirmed in recent studies about grid-connected and stand-alone PtMeOH processes with intermediate storage performed by Qi et al. [79] and Bai et al. [303]. In contrast, in the future unit cost scenario, batteries become competitive and can effectively reduce the methanol production cost when the electricity price is highly variable. In any case, batteries play an essential role in stand-alone configurations to supply electricity in case of shortage and damp power generation fluctuations with a time scale lower than one hour (considered time step size). Also, the battery is used for short-term storage (a few hours). For longer storage periods, the H_2 vessel seems to be a better option, since it does not suffer from self-discharge. Nevertheless, the potential of batteries could change when considering other battery types [46] or boundary conditions.

Finally, intermediate storage might play an even more important role when considering shorter time scales and input data, e.g., renewable power generation, from real locations. In fact, the averaging of such input data over wide geographical areas, as done in the considered case studies (see Section 4.4), smoothens profile variations and underestimates the need for storage.

4.6.3.3. Challenges and opportunities for grid-connected Power-to-Methanol plants

In this work, no constraints related to grid congestions were considered in the grid-connected case study, since it would have required the choice of the location of the PtMeOH plant and a dedicated model of the grid [307], which was out of the scope. Nevertheless, its consideration could probably affect the optimization results, since bigger batteries could supply energy to the PtMeOH plant even in case of grid congestions. Similarly, we neglected the additional costs related to electricity taxes and grid balancing, which are location-dependent.

Further, a different optimal design of the PtMeOH plant would probably have been obtained by participating in the intra-day market (in addition to the day-ahead market) and offering ancillary services with both the battery and the water electrolysis units. In fact, the additional savings or revenues related to simultaneously bidding in different electricity markets [308, 309] and offering ancillary services [310] could make storage technologies, especially batteries, more competitive, thus likely affecting the optimal size of the other process units.

4.6.3.4. Scenario-dependency

In this chapter, the role of storage and flexibility was analyzed for a few rather different historical electricity price and renewable generation scenarios. Nevertheless, the considered scenarios and boundaries can significantly affect the optimal design of the PtMeOH plant as well as the production cost. Moreover, while flexible operation was shown to be beneficial

in all scenarios, the need for storage is not consistent throughout the considered scenarios.

Besides solving these optimization problems for other representative scenarios, multiple scenarios could be considered simultaneously in two-stage Stochastic Combined Design and Scheduling (S-CDS) problems to account for scenario uncertainty. The latter approach has been chosen to obtain more robust indications of the optimal design of these processes (see Chapter 5).

4.7. Conclusion

In this chapter, we solved Combined Design and Scheduling optimization problems for a grid-connected and stand-alone Power-to-Methanol process with battery and hydrogen storage to investigate the role of flexibility and the need for intermediate storage. These problems were solved for several electricity price and renewable generation profiles, and unit cost scenarios.

Although the required optimality gap was not reached and overall global optimality cannot be guaranteed, meaning that better optima might exist, the results suggest that flexible operation of all units of the PtMeOH process significantly reduces the production cost of methanol in every case study and scenario. Also, no significant cost reduction was achieved by considering maximum ramp rates higher than 10 % h^{-1} for the considered scenarios and time discretization. This suggests that grid-connected PtMeOH plants do not necessarily require extreme load variations to have significant operating cost savings, as significant hourly price variations (typical for the European day-ahead electricity market before October 2025) occur only on a few occasions. In contrast, higher ramp rates might be beneficial for stand-alone PtMeOH plants to better follow renewable power generation fluctuations if the scheduling is performed with a finer time discretization, which was, however, not considered in this work.

In the grid-connected case study, storage technologies play a relevant role when the electricity profile is highly fluctuating and at a high average price. In this scenario, the PtMeOH configuration with both the battery and the H_2 storage minimizes the methanol production cost. However, among these storage technologies, H_2 storage provides the major economic benefits, since it allows decoupling hydrogen production from its conversion, and thus a downsizing of the methanol synthesis plant.

In the stand-alone case study, storage is widely used regardless of whether the methanol synthesis plant is operated constantly at nominal load or flexibly. Furthermore, intermediate storage might play an even more relevant role when shorter time scales and data from specific renewable power generation plants are considered, since the input data do not undergo temporal and spatial smoothening; these scenarios were, however, not considered in this work.

When considering future (2030) unit cost reductions of the key technologies, i.e., batteries, hydrogen storage, and electrolyzers, batteries were shown to be beneficial in reducing the production cost of methanol in grid-connected plants with highly fluctuating price profiles. In particular, batteries can generate high revenues by selling electricity to the grid during expensive electricity hours, thus repaying their investment and reducing the methanol production cost.

Further, improvements in some unit models could increase the accuracy of the results. For instance, degradation phenomena in the electrolyzer due to flexible operation and an

efficiency map of the methanol synthesis plant at partial loads could be considered. Further, extending the model to include the potentially fluctuating availability of the CO_2 source (or the dynamics of the carbon capture unit), other storage technologies [46], and the participation in the other electricity and ancillary service markets for the optimal design of grid-connected PtMeOH plants could shed light on the full potential of intermediate storage.

Also, longer time series should be considered for the optimal plant design to account for renewable production seasonality, since the optimal designs differ when considering different power generation scenarios. However, some time series aggregation techniques [46, 298] or problem reformulations should be applied to numerically handle these optimization problems.

Finally, although other electricity price and renewable power generation profiles could be investigated, the related optimization results would remain highly dependent on these profiles (which are generally uncertain), and thus difficult to generalize. Such limitations can be partially overcome by considering several scenarios simultaneously in S-CDS optimization problems. The formulation and solution of this type of optimization problems are presented in the following chapter for a grid-connected PtMeOH case study with intermediate storage.

5. Stochastic Optimization of Power-to-Methanol Processes with Intermediate Storage

In the previous chapter, the role of flexible operation and intermediate storage was investigated for a Power-to-Methanol process and for several cases, being two important options to reduce production costs and thus improve the viability of PtX processes, as also highlighted in Chapter 2. While the benefits of flexible operation of the methanol process were consistent in reducing the production cost for all the considered cases, the benefits of intermediate storage were scenario-dependent.

In this chapter, we tackle this uncertainty related to scenario realization by solving Stochastic Combined Design and Scheduling optimization problems for a grid-connected Power-to-Methanol process, as graphically visualized in Figure 5.1. In particular, we first analyze the sensitivity of the production cost to optimal process design and scheduling, focusing on flexible operation and the need for intermediate storage. Then, we investigate some approaches to tackle the numerical complexity of these S-CDS optimization problems.

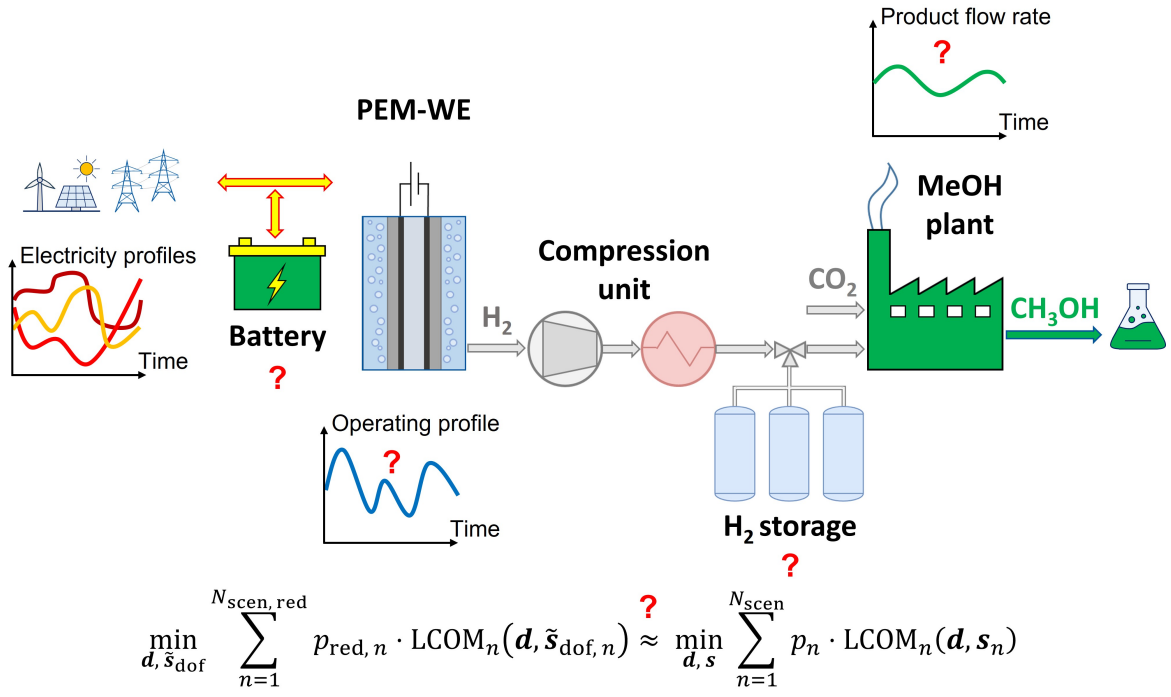


Figure 5.1.: Graphical representation highlighting the focus of Chapter 5, i.e., the optimization of the design and scheduling of a Power-to-Methanol process with intermediate storage under scenario uncertainty as well as numerical approaches to reduce the numerical complexity of such optimization problems.

5.1. Introduction

As shown, for instance, in the previous chapters, the cost of hydrogen-based chemicals and fuels produced via Power-to-X processes is generally dominated by high operating costs. Under time-varying electricity prices, their production cost can be minimized by optimizing the design of PtX processes, including both design variables and unit sizing, while considering process scheduling so that the process units are optimally designed and (over-)sized while meeting the production goals.

Most works modeling such energy-intensive processes and optimizing their design simultaneously with their scheduling consider single specific electricity price or renewable power generation profiles, e.g., in the case of Power-to-Ammonia [280, 283], Power-to-Gas [44, 51], and Power-to-Methanol [4, 45, 46]. However, the use of different profiles makes the results of these works difficult to compare with each other and generalize. While the use of standardized electricity profiles built from historical data for scheduling problems [311] can overcome the first issue, the challenge of accurately capturing the uncertainty related to scenario realization remains.

An approach to account for such uncertainty is formulating the deterministic equivalent of risk-neutral Stochastic Combined Design and Scheduling (S-CDS) optimization problems [22, 312–315]. In these two-stage stochastic programming problems, the uncertainty is generally addressed by simultaneously considering several scheduling scenarios, which are generally obtained or generated from historical profiles under the assumption that they properly represent the underlying distribution and that similar profiles can occur in the future (this assumption becomes weaker in case of major changes due to, e.g., increasing renewable penetration and international crises). However, these problems can become extremely challenging to solve within reasonable CPU times depending on factors such as the model type, e.g., LP vs. MINLP, number of scheduling scenarios, and length and time discretization of the scheduling horizons.

To tackle the numerical complexity directly on the solver side, several optimization strategies based on either black-box optimizers, e.g., a genetic algorithm to identify first-stage variables [316], sample average approximation performed within the solver [317], or decomposition approaches to exploit the problem structure have been proposed, mainly for stochastic LPs and MILPs [312, 314, 318]. For instance, L-shaped methods based on generalized Benders decomposition iteratively identify first-stage variables in a master problem, which are then fixed to solve a stochastic scheduling problem that is used to introduce feasibility and optimality cuts into the master problem [312, 314, 319]. Lagrangean or scenario decomposition [312, 314, 318] is also used to generate simpler (non-stochastic) independent two-stage subproblems, which embed penalty terms into the objective function to enforce the equality of the first-stage variables across the subproblems through the iterations. Further, beyond improving the above-mentioned optimization strategies, e.g., introducing stronger Benders cuts [320, 321], dedicated branching strategies [322, 323] have also been proposed.

For cases where these optimization strategies still cannot solve two-stage problems or are not implemented in conventional solvers, several tailored optimization algorithms have been proposed, especially for energy system applications. For instance, Liu et al. [324] proposed a decomposition algorithm based on optimality cuts for two-stage stochastic programming problems reformulated as large-scale multi-period MINLPs by applying a sampling and integration technique. Heo et al. [325] proposed a decomposition algorithm for

CDS problems that first identifies a design candidate with a simplified model and then tests the design candidate's performance by solving an optimal scheduling problem with a linearized model. Further, Baumgärtner et al. [326] proposed RiSES^4, an algorithm for CDS problems based on time series aggregation, whose time resolution is iteratively increased until the desired optimality gap is reached. RiSES^4 [326] was later extended to account for nonlinearities (RiNSES^4 [327]). However, some of these tailored approaches [325, 327], which can be applied in stochastic problems, can generate infeasible design candidates for the original problem due to linearization [327].

To tackle the high numerical complexity of such problems without the need for tailored optimization algorithms, the models are often simplified, e.g., by removing model nonlinearities or integer variables [328], by reformulating them as scheduling-informed design problems [280], and by discretizing the original time series for multi-period optimization [329, 330]. In addition, typical or representative scheduling periods can be identified via scenario clustering [47, 297], and the time series can be aggregated [297, 331, 332] to reduce the size of the original optimization problems.

Given the importance of tackling the high numerical complexity of S-CDS problems, in this chapter, we first investigate and compare several S-CDS problem approximations for optimizing a grid-connected Power-to-Methanol process with intermediate storage based on the model presented in Chapter 4. Moreover, we investigate the effect of optimal design and optimal scheduling, as well as the role of flexible operation and intermediate storage, on the objective function (Section 5.2). Then, we investigate some numerical complexity reduction approaches that combine scenario clustering with reducing the degrees of freedom related to the scheduling variables (Section 5.3). Finally, the conclusions are drawn in Section 5.4.

5.2. Production cost sensitivity to optimal process design vs. scheduling

As mentioned above, S-CDS problems often suffer from numerical intractability. As an alternative to model linearization or scenario clustering, S-CDS problems can be approximated by optimizing the process design considering steady-state operation of some or all process units, or optimizing the process scheduling for fixed process designs. Nonetheless, it remains unclear whether these approximations of S-CDS problems are sufficiently accurate for stochastic optimization of PtX processes. Moreover, the literature has not considered whether optimal process design versus optimal process scheduling is more important for reducing production costs when accounting for the uncertainty of scenario realization.

Further, the impact of process design variables on the production cost in PtX processes is generally unknown, particularly when several scheduling scenarios are considered. In fact, several process designs can potentially lead to similar objective function values, i.e., with a difference below the optimality tolerance. This situation can occur, for instance, when the objective function is weakly sensitive to certain design variables [333] or because of the economic trade-offs captured by the objective function when optimized under uncertainty [313, 334, 335].

To answer these questions, in this section, we compare the results of a grid-connected Power-to-Methanol process with intermediate storage for which i) the process design is

optimized under uncertainty when enabling flexible operation for different process units, and *ii*) the process scheduling is optimized under uncertainty for several process designs. Further, the latter allows exploring the design space by calculating the objective function related to several candidate process designs. This choice also enables the statistical analysis of the optimization results to identify general trends between the process design variables and the methanol production cost.

5.2.1. Methodology

To investigate how sensitive grid-connected PtMeOH processes are to optimal design and scheduling when several scenarios are considered, we formulate and solve the deterministic equivalent of the corresponding two-stage stochastic programming problems.

In the following, the optimization problems, the statistical analysis, as well as their implementation are described.

5.2.1.1. Stochastic programming

In the considered S-CDS problems (OP 5.1), the PtMeOH process is optimized while accounting for the uncertainty related to the electricity price scenario realization. Note that the input scenario set for the considered S-CDS problems is assumed to be composed of samples that represent the uncertainty distribution sufficiently well. Further, the full sequence of N_{TS} values within each scenario n is assumed to be known (assumption of perfect information on the scenario time series) and is collected in a vector $\boldsymbol{c}_n \in \mathbb{R}^{N_{\mathrm{TS}}}$. For simplicity, for the most general cases, we assume uniform probability across scenarios, i.e., each scenario n has a probability $p_n = 1/N_{\mathrm{scen}}$, where N_{scen} is the number of scenarios.

For each scenario n, the levelized cost of methanol LCOM_n accounts for both investment and operating costs (see Equation (4.1)). The weighted sum of the scenario objective functions (LCOM_n) is minimized subject to equality (h_n) and inequality (g_n) constraints:

$$
\begin{aligned}
&\min_{\boldsymbol{d},\, \boldsymbol{s}} \left(\sum_{n=1}^{N_{\mathrm{scen}}} p_n \cdot \mathrm{LCOM}_n(\boldsymbol{d},\, \boldsymbol{s}_n(\boldsymbol{c}_n)) \right) \\
&\quad s.t. \\
&\qquad h_n(\boldsymbol{d},\, \boldsymbol{s}_n(\boldsymbol{c}_n)) = 0 \qquad\qquad n = 1, ..., N_{\mathrm{scen}} \\
&\qquad g_n(\boldsymbol{d},\, \boldsymbol{s}_n(\boldsymbol{c}_n)) \leq 0 \qquad\qquad n = 1, ..., N_{\mathrm{scen}},
\end{aligned}
\tag{OP 5.1}
$$

where $\boldsymbol{d} \in \mathbb{R}^{N_{\text{design var}}}$ are the first-stage variables (design) and $\boldsymbol{s} \in \mathbb{R}^{N_{\mathrm{scen}} \times N_{\text{scheduling var}} \times N_{\mathrm{TS}}}$ the accumulated second-stage variables (scheduling). Accordingly, $N_{\text{design var}}$ is the number of design variables and $N_{\text{scheduling var}}$ the number of distinct scheduling variables for each scenario instance.

The considered PtMeOH model is a MINLP due to the presence of integer decision variables as well as nonlinearities in the process unit efficiencies and cost correlations (Section 5.2.3). This model is particularly challenging to solve when used in S-CDS problems, especially for long and finely discretized scheduling horizons and high scenario numbers.

Depending on the considered case study (Section 5.2.3), the original S-CDS problem (OP 5.1) is simplified. For instance, when only the process design is optimized, steady-state operation for the scheduling variables $\boldsymbol{s}_n$ is assumed. This reduces the complexity of

the original S-CDS problem significantly, since the number of optimization variables does not scale with N_{TS}. When only the stochastic scheduling is optimized, the process design is fixed. This reduces the problem complexity and also allows solving every instance of the stochastic problem independently.

To benchmark these results, we solve both the original and a reduced S-CDS problem. The reduced S-CDS problem is obtained by applying a complexity reduction technique that combines feature-based scenario clustering and selective Degrees of Freedom (DoF) reduction (see Section 5.3 for additional details). To sufficiently represent the original scenario space, we consider 15 scenario clusters, i.e., ca. 30 % of the original scenario space. Further, after fixing the design obtained in the reduced S-CDS problem, we solve a stochastic scheduling problem, being interested in the objective function in the original scenario and DoF spaces. As the objective function value of the original S-CDS problem is worse than the one obtained through the reduced S-CDS problem (the optimizer could not find the global optimum or a better local optimum within the considered computational time limit due to the significantly higher numerical complexity), we do not report these results.

5.2.1.2. Statistical analysis

To analyze the complex relationship among the process design variables and the objective function, we carry out a statistical analysis based on the results obtained by solving stochastic scheduling problems for several process designs. In particular, the process designs have been identified via Latin Hypercube Sampling (LHS), a frequently used sampling approach that allows covering the design space with a relatively low number of samples [336]. For these samples, the correlation analysis is performed by calculating distance correlation coefficients [337], which can capture nonlinear correlation trends for single variables and their combinations.

The correlation direction is estimated via the sign of the Spearman coefficient between single design variables and the objective function. Nonetheless, given the nonlinear, not-strictly-monotonic relationship between the design variables and the objective function, the correlation coefficients and directions represent an average trend over the considered design variable range rather than an absolute indication.

5.2.1.3. Implementation

The above-described two-stage stochastic programming problems were implemented and solved in Matlab and GAMS: a Matlab script calls GAMS to solve the implemented deterministic equivalent of the two-stage stochastic programming problems with BARON 23.6.22 [282] to global optimality. Moreover, the data processing, scenario clustering, DoF reduction, and data exchange file generation are performed in Matlab before solving the optimization problems in GAMS. Also, the stochastic scheduling problems are solved in parallel by splitting the problem into four smaller subproblems to reduce the numerical complexity; the optimization results of the subproblems are combined afterward.

A relative optimality tolerance and a CPU time limit were set to 2 % and 6 h, respectively, for most optimization runs. Global optimality was achieved for most optimal design and optimal scheduling problems within this CPU time. In contrast, global optimality was not achieved for the reduced S-CDS optimization problem despite setting a higher CPU time

limit (12 h). For the cases where global optimality was not achieved within the CPU time limit, the locally optimal solution found by BARON was considered.

The statistical analysis is also performed in Matlab.

5.2.2. Process description and model

The considered PtMeOH process is analogous to the process described in Section 4.2. In particular, it is composed of five units, namely, a battery, a PEM water electrolysis unit, a mechanical hydrogen compression unit, a pressurized hydrogen vessel for hydrogen storage, and a methanol synthesis plant (Figure 4.5).

As already described in Section 4.3, the process model is an MINLP to account for the operating limits and nonlinearities of the process unit efficiency and energy demand, as well as the cost correlations. Also, the model is quasi-steady state, i.e., modeled in discrete time, due to the relatively fast dynamics of the key process units [1, 49, 144] compared to the considered time step (1 h). Further, we assume a maximum hourly ramp rate of 10 % for the methanol synthesis plant, which is lower than typical capabilities [144], since moderate flexibility already provides most of the economic benefits (Section 4.6).

Concerning the design, the nominal sizes of the battery, PEM-WE, compression unit, hydrogen storage, and methanol synthesis plant, which is defined in terms of the nominal hydrogen flow rate, are optimized (see Table 5.1). Note that, in this chapter, the pressure of the PEM-WE is not a design variable but is set to 40 bar, differently from the model in Section 4.5, as it was almost always at its upper bound (Section 4.6). These considered design variables directly affect the investment costs of each process unit and enable investigation of trade-offs between process unit oversizing and intermediate storage needs. Concerning the scheduling, the power flows in the battery and PEM-WE as well as the hydrogen outlet flow rate from the hydrogen storage are optimized.

The LCOM for each scenario n is defined as in Equation (4.1). However, unlike Section 4.5, where the yearly methanol production rate ($M_{\mathrm{MeOH,\,y}}$) was the result of the optimal process scheduling, a yearly production target of 50 kt is considered to enable the comparison among the case studies (Section 5.2.3). By considering a methanol production target, the denominator of the objective function does not depend on any optimization variables. The production target is enforced via an inequality constraint to reduce the numerical complexity via relaxation. This simplification is possible since we assume that as much power as needed can always be taken from the grid.

Finally, a few modifications to the PtMeOH model used in Chapter 4 were made to reduce the number of intermediate variables and update the unit investment costs with respect to inflation to the year 2023 (see Appendix C.1 for additional details).

5.2.3. Case studies

To investigate how sensitive the LCOM of grid-connected PtMeOH processes is to optimal design or scheduling when accounting for uncertainty of scenario realization, we investigated several case studies, which correspond to different levels of approximation of the original S-CDS problem (OP 5.1).

For all case studies, the input scenario space for the S-CDS problems was obtained by slicing a one-year input time series of day-ahead electricity prices for Germany from 2023 [299],

Table 5.1.: Design variables of the optimization problem for the grid-connected case study with their upper and lower bounds. Note that the optimization problem feasibility is always ensured under the considered variable bounds and modeling assumptions.

Unit	Variable	Symbol	Lower bound	Upper bound
Battery	Battery	$E_{b,\,nom}$	5 MWh	150 MWh
PEM-WE	Modules	N_{mod}	25	35
H_2 compression	Pressure ratio	β_{max}	1.88	3.50
H_2 storage	Volume	V	50 m^3	1000 m^3
MeOH plant	H_2 flow	$\dot{m}_{H_2,MeOH,nom}$	1.18 t h^{-1}	1.60 t h^{-1}

thus being consistent with the considered economic data. In particular, 52 weekly scenarios (consecutive weeks) with hourly resolution were extracted from the input time series. No taxes or grid fees were added to the considered day-ahead electricity price profiles, although they can significantly affect the electricity costs, as for Germany [300].

The chosen time horizon (one week) enables evaluating storage utilization benefits, as this time horizon captures significant profile variations, e.g., between working days and weekends for the electricity price, and assessing whether investing in large-capacity storage instead of small-capacity storage is beneficial. Although even longer time horizons could provide more insights, we did not consider them because we target a methanol process with a nearly continuous demand throughout the year, e.g., to serve a downstream process. Additionally, they would have increased numerical complexity and weakened the assumption of perfect knowledge of scenario time step sequences, since long-term profile predictions suffer from poor reliability.

The considered case studies are described below and are also summarized in Table 5.2:

- ***Random designs and optimal scheduling - Flexible: No unit***: 100 process designs are generated via LHS within the design variable bounds (see Table 5.1) to explore the solution space, thus evaluating their performance and then identifying good process design patterns. These process designs are then fixed in the optimization problems, thus defining the operating constraints and investment cost of the process units. For these process designs, the scheduling of the process units is optimized to meet the yearly methanol production target (50 kt) for each scenario instance. However, for each scenario instance, steady-state operation for the PEM-WE and methanol synthesis units is assumed within the scheduling horizon. In this simplified case that does not allow any flexible operation, the generated design values of the battery, compression unit, and the hydrogen storage are discarded: the hydrogen compression unit is sized to reach 75 bar (the operating pressure of the methanol production plant), and the battery and hydrogen storage are removed from the model, since they cannot be properly exploited given the enforced operating strategy.

- ***Random designs and optimal scheduling - Flexible: Battery***: For the 100 generated process designs, the scheduling of the process units is optimized assuming steady-state operation only for the PEM-WE and methanol synthesis units. In contrast, the battery can be operated flexibly. While the battery size is now determined as part of the generated random designs, the design values for the compression unit

and the hydrogen storage are discarded, as in the previous case: the hydrogen compression unit is sized to reach 75 bar and the hydrogen storage is removed from the model, since it cannot be exploited given the enforced operating strategy.

- ***Random designs and optimal scheduling - Flexible: Battery & PEM-WE***: For the 100 generated process designs, the scheduling of the process units is optimized assuming steady-state operation of only the methanol synthesis unit, thus meaning the battery and the electrolyzer can be operated flexibly.
- ***Random designs and optimal scheduling - Flexible: Battery, PEM-WE, & MeOH***: For the 100 process designs generated via LHS, all process units can be operated flexibly, and their scheduling is optimized.
- ***Optimal design and scheduling - Flexible: No unit***: The PtMeOH process design is optimized while simultaneously optimizing the process scheduling. Therefore, the process design is decided by the optimizer and is not preliminarily fixed. For this case study, steady-state operation of the PEM-WE and methanol synthesis units is considered. No battery and intermediate hydrogen storage are considered.
- ***Optimal design and scheduling - Flexible: Battery***: The PtMeOH process design is optimized while considering steady-state operation only of the PEM-WE and methanol synthesis units and no intermediate hydrogen storage. The battery can be operated flexibly, and its scheduling is optimized.
- ***Optimal design and scheduling - Flexible: Battery & PEM-WE***: The PtMeOH process design is optimized while considering steady-state operation only of the methanol synthesis unit. In contrast, the other process units can be operated flexibly, and their scheduling is optimized.
- ***Optimal design and scheduling - Flexible: Battery, PEM-WE, & MeOH***: Both the design and scheduling of all process units are optimized. Moreover, all process units can be operated flexibly. To ensure numerical tractability, we solve an approximated version of the original S-CDS problem (OP 5.1) by applying feature-based scenario clustering considering the first four central moments (15 scenario clusters) and selective DoF reduction (see Subsection 5.3.2 for more details on this approach). The resulting process design is then fixed in the original S-CDS problem to solve a stochastic scheduling problem in the original scenario and DoF spaces, so that the objective function value can be compared with those from the other case studies.

Table 5.2.: Summary of the case studies investigated for the stochastic optimization of a grid-connected Power-to-Methanol process with intermediate storage. Note that, when the process design is not optimized, a generated process design is fixed and only optimal stochastic scheduling is performed.

	Design optimization	Scheduling optimization		
		Battery	PEM-WE	MeOH
Random designs and optimal scheduling - Flexible: No unit	No*	-	Steady state	Steady state
Random designs and optimal scheduling - Flexible: Battery	No**	Flexible	Steady state	Steady state
Random designs and optimal scheduling - Flexible: Battery & PEM-WE	No	Flexible	Flexible	Steady state
Random designs and optimal scheduling - Flexible: Battery, PEM-WE, & MeOH	No	Flexible	Flexible	Flexible
Optimal design and scheduling - Flexible: No unit	Yes*	-	Steady state	Steady state
Optimal design and scheduling - Flexible: Battery	Yes**	Flexible	Steady state	Steady state
Optimal design and scheduling - Flexible: Battery & PEM-WE	Yes	Flexible	Flexible	Steady state
Optimal design and scheduling - Flexible: Battery, PEM-WE, & MeOH	Yes	Flexible	Flexible	Flexible

* Neither battery nor intermediate hydrogen storage are considered.
** No intermediate hydrogen storage is considered.

5.2.4. Results and discussion

In the following, we first evaluate how optimal design and scheduling affect the methanol production cost. The relationship between the considered designs and the objective function is then analyzed to identify data correlation and the sensitivity of the objective function to the design variables.

5.2.4.1. Optimal design vs. scheduling

The LCOMs obtained for the 100 randomly generated designs show different values and data distributions depending on which units can be operated flexibly when scheduling is optimized (Figure 5.2). In particular, the average LCOM values decrease and the data distribution skewness increases when the hydrogen storage is used and the key process units, i.e., electrolysis and methanol synthesis units, are operated flexibly.

When assuming steady-state operation of all (or some) process units for the 100 random designs, the LCOM ranges are quite wide: 1.46-1.52 € kg^{-1}, 1.46-1.54 € kg^{-1}, and 1.44-1.54 € kg^{-1} (three violin plots on the left in Figure 5.2, respectively). As expected, these results indicate that optimal design plays a significant role in reducing the production cost (black, green, and cyan markers in Figure 5.2).

When the electrolysis and methanol synthesis units are operated in steady state, the results suggest that battery storage is not economically viable (compare the two violin plots on the left in Figure 5.2). In fact, the savings in the operating expenditures due to the battery are not sufficient to repay the investment expenditures under the considered economic assumptions.

When the electrolysis unit is operated flexibly differently from the methanol synthesis plant (and hydrogen storage is present), the data distribution is skewed towards lower LCOM values (compare the violin plots in the middle in Figure 5.2). This suggests that the use of hydrogen storage combined with the flexible operation of the PEM-WE unit reduces, on average, the methanol production cost. This is again confirmed by comparing the LCOMs obtained via optimal design: LCOM of 1.42 € kg^{-1} instead of 1.46 € kg^{-1} thanks to the possibility of exploiting price fluctuations to reduce the hydrogen production cost, and thus the LCOM.

When flexible operation of the methanol synthesis unit is enabled, the LCOMs are on average ca. 4 % lower (compare the two violin plots on the right in Figure 5.2). The LCOM reduction is due to the savings in the operating expenditures, which range between -1 % and -12 % for the considered process designs (also see Figure C.1), thus confirming the importance of flexible operation. Also, the LCOM range obtained when optimizing the scheduling for the same generated process designs is slightly lower than for the case with no methanol process flexibility: 1.40-1.47 € kg^{-1} vs. 1.44-1.54 € kg^{-1} (compare the two violin plots on the right in Figure 5.2). Further, the LCOM data distribution is more skewed towards low LCOMs, thus meaning that several process design combinations lead to similar objective function values, as also mentioned in previous works [313, 334, 335] (this aspect will be investigated in more detail in Subsection 5.2.4.2). These results show that the enhanced process flexibility related to the methanol process operation helps mitigate economic losses caused by poor process design choices. Nonetheless, the relatively wide LCOM range highlights that making sufficiently good process design choices matters even when methanol process flexibility is enabled.

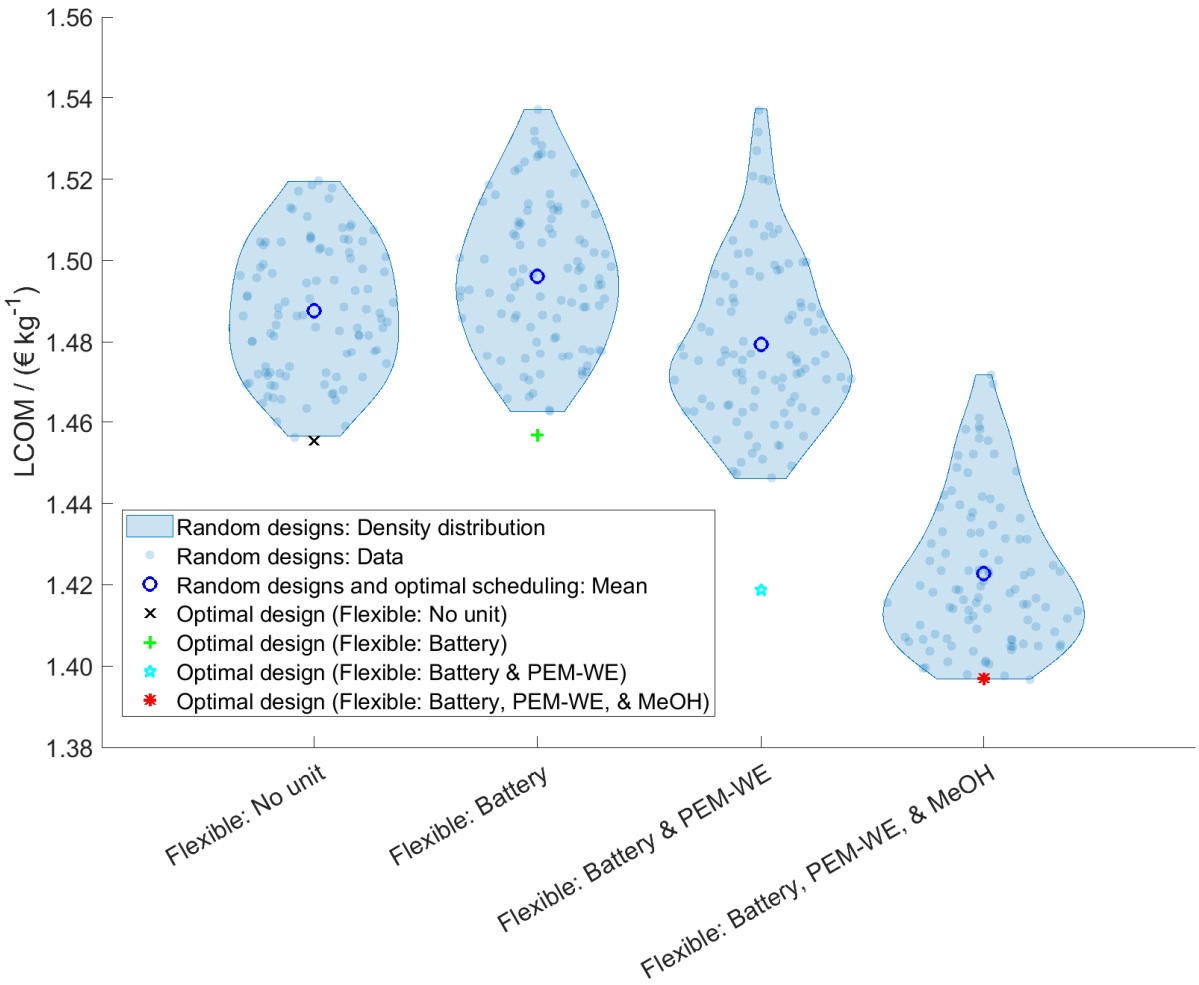


Figure 5.2.: Violin plots displaying the levelized cost of methanol (LCOM) data points and their density distribution for the 100 randomly generated designs. Note that the density distribution is displayed only within the obtained LCOM ranges. The LCOMs for the "Flexible: No unit" case are calculated by assuming no battery and hydrogen storage and steady-state operation for the electrolysis and methanol synthesis units; the LCOMs for the "Flexible: Battery" case are calculated by assuming no hydrogen storage and steady-state operation for the electrolysis and methanol synthesis units; the LCOMs for the "Flexible: Battery & PEM-WE" case are calculated by considering flexible operation for the battery and the electrolysis unit and steady-state operation for the methanol synthesis unit; the LCOMs for the "Flexible: Battery, PEM-WE, & MeOH" case are calculated by assuming flexible operation of all process units. Additionally, the LCOMs of the Power-to-Methanol processes optimized with respect to the design (black, green, cyan, and red markers) are displayed; these values are not displayed in all violin plots since they were obtained for different process configurations, namely storage technologies.

Further, the best LCOM obtained for a randomly generated process design when allowing methanol process flexibility is better than the LCOM obtained by optimizing the PtMeOH design while considering steady-state operation of the methanol synthesis unit, thus highlighting that these processes should be operated flexibly. Moreover, the average of the LCOMs in the violin plot on the right is quite close to the cyan marker that indicates the LCOM of the PtMeOH with the process design optimized when assuming

steady-state operation of the methanol synthesis unit (Figure 5.2). This suggests that optimal scheduling (when allowing flexible operation and assuming perfect information on the scenario time series) is, on average, more important than optimal design (when assuming steady-state operation of the process units) in PtMeOH processes. This is most likely due to the high share of the operating costs on the LCOM in PtX processes (see, for instance, Figure 4.7).

5.2.4.2. Data correlation analysis

As several process designs can lead to similar objective functions, we analyze the optimization results to identify patterns among these variables. In particular, we investigate the impact of the process design variables on the LCOM.

For this analysis, we consider the results obtained by optimizing the (stochastic) scheduling for the 100 generated process designs, while allowing flexible operation of all process units (violin plot on the right of Figure 5.2). The considered data set is suitable for this correlation analysis since the design variables, i.e., the only input that is varied in the solved stochastic scheduling problems, show weak-to-no cross-correlation because of the LHS (Figure C.2). The correlation analysis between the process design variables and the objective function is conducted by examining the design variables first independently and then together.

Correlation between single design variables and objective function

In analyzing the distance correlation coefficients (Table 5.3), either weak or moderate negative correlation with the LCOM emerges across the considered design variable ranges. In particular, the sizes of the electrolysis and methanol production units exhibit the strongest effect on the methanol production cost. While intermediate storage can also contribute positively to LCOM reduction, its impact remains relatively minor compared to oversizing the electrolysis and methanol production units under the considered economic assumptions.

Table 5.3.: Signed distance correlation coefficients between the design variables and the objective function. The distance correlation coefficient ranges from 0 (independent) to 1 (strongly dependent). The correlation direction indicated via the sign is estimated from the Spearman coefficient. Note that, given the nonlinear relationship between the design variables and the objective function, the displayed metrics represent only average trends over the considered design variable ranges.

Variable	Distance correlation	Sign
Battery	0.191	-
Modules	0.405	-
Pressure ratio	0.199	-
Volume	0.199	-
H_2 flow	0.417	-

These general trends are confirmed by analyzing the objective function values (LCOMs) plotted against the single design variables (Figure 5.3). The LCOM is quite sensitive to the electrolyzer module number and the nominal hydrogen flow rate supplied to the

methanol synthesis unit. In contrast, a less sensitive behavior is experienced for the other design variables, since low and high objective function values are obtained for all design variable ranges. However, the process performance with those design variables depends on the combination of the others. A relatively low sensitivity to certain key design variables was already shown in other processes, for instance, a pressurized oxy-coal combustion process [333].

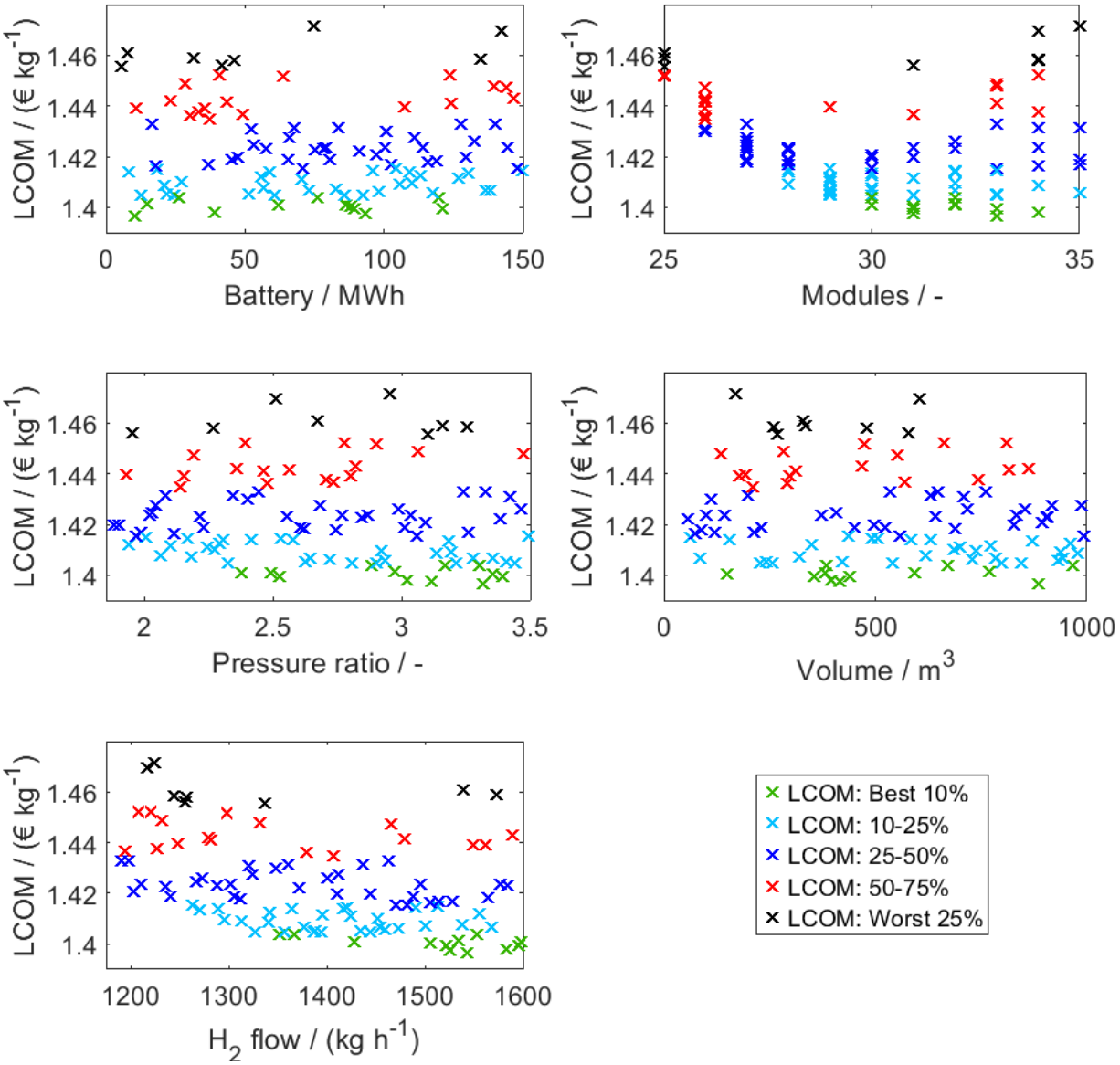


Figure 5.3.: Objective function (LCOM) value obtained when optimizing the scheduling of all process units for the 100 randomly generated process designs plotted against the design values. The color of the crosses is based on the LCOM value.

The low sensitivity to certain design variables was further explored by fixing the sizes of the electrolysis and methanol synthesis units equal to the ones of the random design leading to the lowest objective function. In this case, the LCOM is nearly insensitive to battery and hydrogen storage sizes (Figure 5.4), its variation being lower than the optimization tolerance for wide variable ranges. Similar results were obtained for different maximum

pressure ratios for the compression unit (Figure C.3). These results are in contrast with the findings in Section 4.6 where the grid-connected PtMeOH process was optimized for a single highly fluctuating profile ("Historical 2022"). This is most likely due to the fact that several (highly and mildly fluctuating) scenarios are simultaneously considered, and that the high flexibility of the electrolysis and methanol plants can largely offset the lack or presence of storage when stochastic scheduling is optimized. Nonetheless, solving S-CDS optimization remains necessary because the results of this case study cannot be generalized, and the relationship between design variable values and LCOM is not known across the entire solution space.

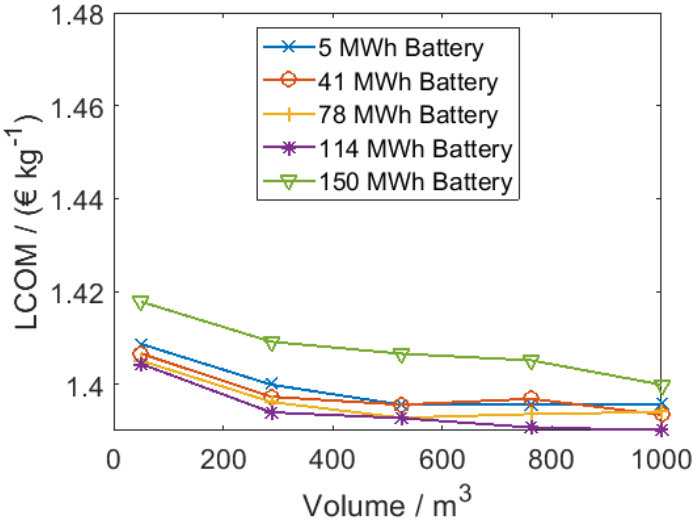


Figure 5.4.: Sensitivity analysis of the objective function (LCOM) calculated by optimizing the stochastic scheduling for fixed process designs. In particular, the storage sizes were varied, while the electrolysis modules, maximum pressure ratio of the compression unit, and nominal hydrogen flow rate supplied to the methanol synthesis plant were set equal to 33, 3.5, and 1.54 t h^{-1}, respectively. For these sizes of the electrolysis and methanol synthesis units, the storage sizes only have a minor impact on the LCOM.

Correlation between multiple design variables and objective function

Identifying clear patterns between combinations of design variables is, in general, more complicated, especially because of the problem nonlinearities and the fact that the objective function does not always have a monotonic behavior with respect to the process design variables in the considered variable ranges (Figure 5.3). For instance, large hydrogen storage volumes can be either economically favorable or unfavorable based on the other design variable values. Nonetheless, a few trends can be extracted.

Increasing the number of modules of the electrolysis unit helps reduce the levelized cost of methanol (Figure 5.5). However, excessively oversized electrolysis units, e.g., with 35 modules, can again lead to high LCOMs, most likely because of the high investment costs and the set yearly methanol production constraint (50 kt). Further, installing battery or hydrogen storage of any size is beneficial when the electrolyzer is moderately oversized to enable a flexibility margin (Figure 5.5, top row). Similarly, relatively large storage capacities are preferred when the methanol synthesis unit is oversized. Also, an oversized

methanol synthesis unit should be combined with an oversized electrolysis plant to increase the flexibilization potential further.

For the other design variable combinations, there is no clear trend. For instance, the relationship between the H_2 storage volume and the pressure ratio of the compression unit, which determines how much hydrogen can be stored within the volume, is unclear. Similarly, whether and when having both storage technologies is beneficial depends on the other design variables.

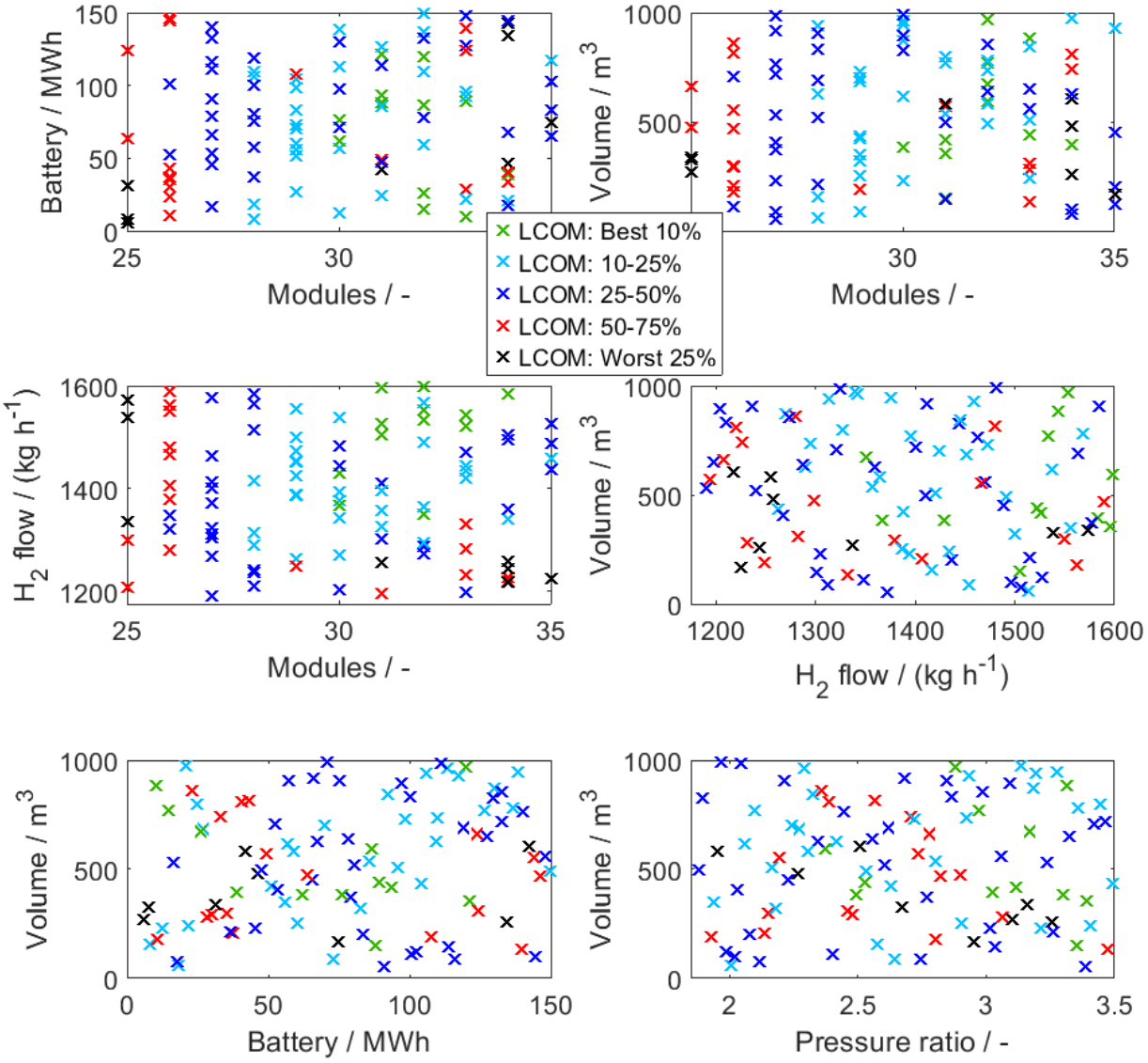


Figure 5.5.: Comparison of key couples of the 100 randomly generated design variables colored according to the objective function value (LCOM) obtained when allowing scheduling of all process units. The color of the crosses is based on the LCOM value.

5.3. Numerical complexity reduction approaches

As previously shown, enabling flexible operation of all process units allows reducing the methanol production cost (Figure 5.2). Further, the spread of the LCOMs values when solving optimal stochastic scheduling problems for randomly generated process designs within reasonable variable bounds indicates that having a good process design matters. Moreover, the lack of clear trends for all design variables when exploring the design space (Figure 5.5) highlights the need for optimizing design and scheduling simultaneously. However, these S-CDS optimization problems suffer from numerical intractability, unless they are simplified.

The fact that the LCOM in the original scenario and DoF spaces (red marker in Figure 5.2) is close to the best objective function value obtained via stochastic scheduling for random designs (the difference is below the optimization tolerance as can be noticed in Figure 5.2) might suggest that developing strategies to solve S-CDS optimization problems, even for this case study, is not necessary. However, random design generation does not account for any information about the relationship between the process design and the objective function of the S-CDS problem itself. Therefore, the number of stochastic scheduling optimization problems that need to be solved before identifying a good process design is not known in advance, thus potentially requiring extremely high computational costs.

In this section, we therefore investigate some numerical approaches that aim at reducing the size of S-CDS optimization problems by combining feature-based scenario clustering with selective DoF reduction.

5.3.1. Literature background

As discussed in the introduction (Section 5.1), S-CDS optimization problems can be approximated to reduce their size, thus improving their numerical tractability. For instance, typical or representative periods can be identified as time slices, e.g., via heuristics and scenario clustering approaches [297], or generated, e.g., via k-means [297], to represent the original scenario space with fewer scenarios, thus effectively reducing the size of the original stochastic programming problem (OP 5.1). Analogously, the number of optimization variables related to the time steps of each scenario can be reduced via time series aggregation methods such as downsampling and segmentation [297, 331]. However, such methods do not generally retain time step chronology information, essential for systems with storage, unless the time-related DoFs are mapped [338] or additional variables and constraints are introduced to account for inter-period storage levels [297, 326].

Scenario clustering [297] could potentially be performed inside the solver to capture the interplay between the scenario time series and the stochastic programming problem [339]. More commonly though, scenarios are clustered outside the solver and *ex-ante*, i.e., before solving the optimization problems. Several outside-the-solver scenario clustering approaches based on heuristics [329, 330, 340–342], brute force [343], hierarchy [332, 342, 344–346], correlation loss [347], or different distance definitions such as the forward selection and backward reduction approaches [313, 348–351], k-means and k-medoids [332, 344–346], have been proposed to simplify optimization problems. An overview of the main clustering approaches proposed in literature can be found in Figure 5.6.

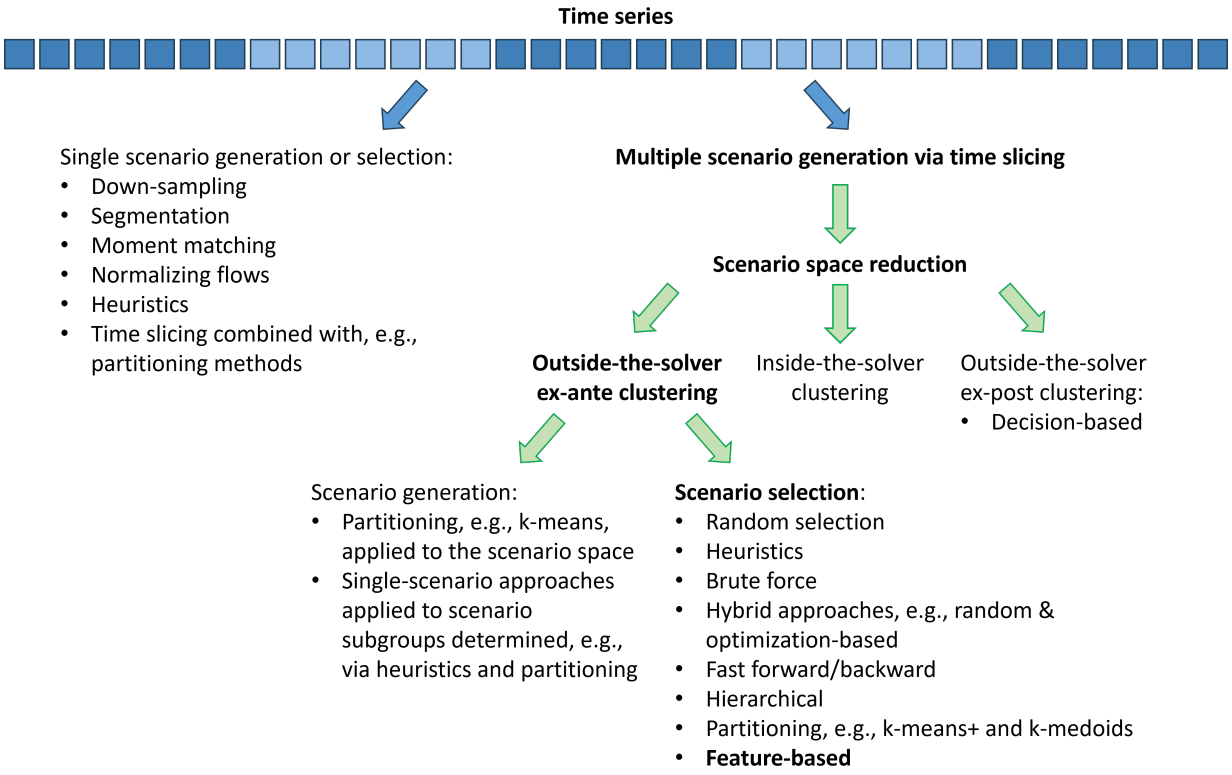


Figure 5.6.: Overview of the main approaches for either single scenario or reduced scenario space generation from an input time series, which is displayed in blue. The main clustering approach investigated within this work is displayed in bold. Note that, in contrast to *generated* scenarios, *selected* scenarios are data slices that belong to the input time series.

Some of these scenario clustering approaches have been compared for different applications, e.g., for a risk-averse stochastic problem of a generalized continuous process [352], generation expansion planning [342, 353], stochastic unit commitment [351, 354], energy supply systems [332, 345, 355, 356], an electricity storage [344] and a gas turbine power generation problem [344]. However, based on the results of the above-mentioned works, no clustering approach consistently performs best, as its performance most likely depends on the problem itself.

The above-mentioned clustering approaches generally consider the time series of the original scenario space to determine a pre-defined number of representative scenarios. As an alternative, a set of features extracted from each scenario can be used as input space for the so-called feature-based clustering [357]. The sets of features are like scenario fingerprints and are used to identify the corresponding scenarios once clustering is performed. For example, the most relevant eigenvalues of the scenario time series extracted via Principal Component Analysis (PCA) could be used as features for clustering [353, 358]. Also, interpretable features such as central moments, e.g., mean and standard deviation, can be considered for clustering. Alternatively, information from preliminary optimization runs can be used as features to account for the interplay between the input scenarios and the model itself [346, 358–360]. However, this type of *ex-post* feature-based clustering, also called decision-based clustering, requires high computational resources compared to other *ex-ante* clustering approaches [360] and does not always outperform them [358].

Although feature-based scenario clustering can filter some noise from the scenario time series, namely, underlying data patterns that are not necessary for two-stage stochastic programming problems, it is rarely applied. Further, which features should be considered to generate the scenario fingerprints for clustering is unclear. We therefore address these literature shortcomings by applying feature-based scenario clustering to reduce the numerical complexity of S-CDS optimization problems for a PtMeOH case study. Furthermore, we investigate the use of both interpretable and non-directly interpretable features, i.e., central moments and principal components from PCA, respectively, for scenario clustering, and compare feature-based clustering against k-means and k-medoids applied directly to the time series, i.e., the state-of-the-art clustering approaches.

Also, we combine feature-based scenario clustering with DoF reduction for the scheduling variables to reduce the number of optimization variables further. In particular, for each instance of the S-CDS optimization problem, we linearly map the scheduling variables from the original to the reduced time domain before solving the S-CDS problem. This allows maintaining time step chronology memory and ensures scheduling feasibility even in the presence of storage. Further, we evaluate how applying DoF reduction *selectively* to the scheduling variables affects the optimal solution.

5.3.2. Methodology

In the deterministic equivalent of S-CDS problems (see for instance OP 5.1), the weighted sum of the scenario objective functions Obj_n over the N_{scen} scenarios $\boldsymbol{c}_n \in \mathbb{R}^{N_{\mathrm{TS}}}$ is minimized with respect to first-stage or design ($\boldsymbol{d} \in \mathbb{R}^{N_{\mathrm{design\,var}}}$) variables and second-stage or scheduling ($\boldsymbol{s}_n \in \mathbb{R}^{N_{\mathrm{scheduling\,var}} \times N_{\mathrm{TS}}}$) variables.

To solve these challenging computationally S-CDS problems with high numbers of scenarios and relatively long time horizons, i.e., with high N_{scen} and N_{TS}, we combine two strategies: 1) the reduction of the scenario space via clustering and 2) the reduction of the DoFs related to the scheduling variables.

5.3.2.1. Scenario clustering

The underlying assumption of scenario clustering is that the optimizer chooses similar process designs for scenarios with similar characteristics. Thus, the scenarios can be grouped into $N_{\mathrm{scen,\,red}}$ clusters according to their similarities. Then, a representative scenario $\boldsymbol{c}_n \in \mathbb{R}^{N_{\mathrm{TS}}}$ for each cluster n is selected (or generated), and its probability $p_{\mathrm{red},n}$ evaluated based on the cluster size: $\boldsymbol{c} \in \mathbb{R}^{N_{\mathrm{scen,\,red}} \times N_{\mathrm{TS}}}$ and $\boldsymbol{p}_{\mathrm{red}} \in \mathbb{R}^{N_{\mathrm{scen,\,red}}}$, i.e., the matrix and the vector with all representative scenarios and their probabilities, respectively, are the input of the two-stage stochastic programming problem (OP 5.2):

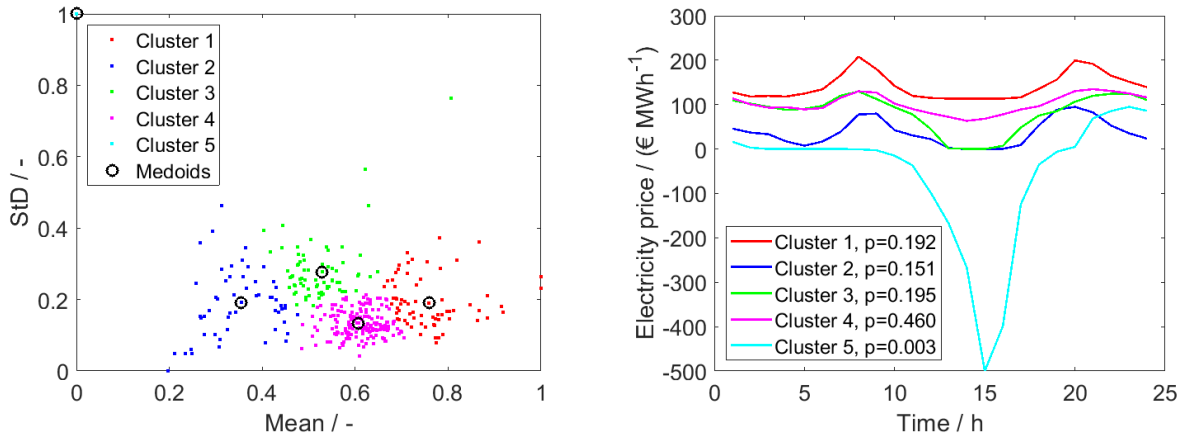
$$
\begin{aligned}
&\min_{\boldsymbol{d},\,\boldsymbol{s}} \left(\sum_{n=1}^{N_{\mathrm{scen,\,red}}} p_{\mathrm{red},n} \cdot \mathrm{Obj}_n(\boldsymbol{d},\, \boldsymbol{s}_n(\boldsymbol{c}_n)) \right) \\
&s.t. \\
&\qquad h_n(\boldsymbol{d},\, \boldsymbol{s}_n(\boldsymbol{c}_n)) = 0 \qquad\qquad n = 1, ..., N_{\mathrm{scen,\,red}} \\
&\qquad g_n(\boldsymbol{d},\, \boldsymbol{s}_n(\boldsymbol{c}_n)) \leq 0 \qquad\qquad n = 1, ..., N_{\mathrm{scen,\,red}},
\end{aligned}
\tag{OP 5.2}
$$

where $\boldsymbol{d} \in \mathbb{R}^{N_{\mathrm{design\,var}}}$ and $\boldsymbol{s} \in \mathbb{R}^{N_{\mathrm{scen,\,red}} \times N_{\mathrm{scheduling\,var}} \times N_{\mathrm{TS}}}$.

To identify the cluster centers and their probability via feature-based clustering, N_{Feature} features are first extracted from the scenarios to generate an input matrix $B \in \mathbb{R}^{N_{\text{Feature}} \times N_{\text{scen}}}$. Then, k-medoids clustering is used to identify the sub-matrices of B, i.e., the clusters, and the cluster centers, which are columns belonging to the sub-matrices of B. The cluster centers, i.e., the scenario features, are used as fingerprints to identify the corresponding scenarios, which represent the input for OP 5.2 (see the example in Figure 5.7 where mean and standard deviation are used as features).

For feature-based scenario clustering, we considered several features: the first four central moments, i.e., mean, standard deviation, skewness, and kurtosis; the mean of the absolute change between consecutive time steps, which can be a significant indicator for storage technologies; and the principal components determined via PCA. Further, the combination of some of these features was also considered. Other features could be considered for scenario clustering, e.g., features belonging to the spectral domain [361]. Nevertheless, we opted for features that are either directly interpretable, such as the mean, or can be obtained via established data analysis methods, e.g., PCA.

Finally, we benchmarked feature-based clustering against k-medoids and k-means applied directly to the time series of the scenarios, which are the state-of-the-art clustering approaches. For an overview of the considered clustering approaches, refer to Appendix C.3.



(a) Feature-based clusters. **(b)** Scenario cluster profiles.

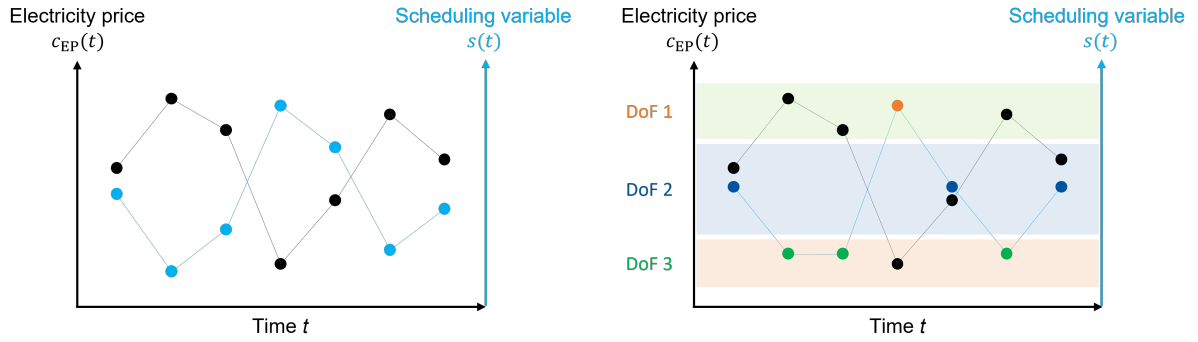
Figure 5.7.: Example of feature-based scenario clustering via k-medoids with respect to mean and standard deviation of day-ahead electricity prices for Germany in the year 2023 [299]. In Figure (a), the normalized mean and standard deviation (StD) are shown, where each dot corresponds to a scenario derived from a 24 h time slice of day-ahead electricity prices, as well as the five clusters and cluster medoids. In Figure (b), the day-ahead electricity prices corresponding to the cluster medoids, which represent the reduced scenario space, are shown as well as their probability.

5.3.2.2. Degrees of freedom reduction

The underlying assumption of DoF reduction applied to scheduling variables is that the optimizer chooses similar scheduling variable values for similar values of the time-dependent input, e.g., the electricity price. Thus, the input time series can be clustered based on its

values, and each scheduling variable is then assigned one DoF for each of these clusters only, instead of one for each of the N_{TS} time steps.

DoF reduction is performed by linearly mapping the scheduling variables from the original time domain to the reduced time domain, thus decreasing the effective number of time steps as done, for instance, in Schäfer et al. [338] (see an exemplary sketch in Figure 5.8). Moreover, this approach maintains memory of the chronological order of time steps and ensures optimal scheduling feasibility in the original time domain, even when storage is present, since the model equality and inequality constraints related to storage can be kept in the original time domain. However, it does impose a restriction compared to the original optimization problem, as it enforces patterns between scheduling variables that can lead to suboptimal (although feasible) solutions of the original problem (Figure 5.8).



(a) No DoF reduction. **(b)** With DoF reduction.

Figure 5.8.: Exemplary sketch of DoF reduction that conserves time step chronology. In Figure (a), where no DoF reduction is performed, the scheduling variable $s(t)$ can have a different value at every time step. In Figure (b), the input time series values, i.e., the electricity prices $c_{\mathrm{EP}}(t)$, were assigned to three groups (indicated with the shaded areas), and the scheduling variable $s(t)$ are constrained to have the same value for each time step in which the input values belong to the same group. However, the value of the scheduling variable for each group can be optimized. Thus, there are three DoFs in this example.
Note: The groups in the input time series value range and the corresponding scheduling variable value are displayed in the same color.

The described DoF reduction via linear mapping can be applied to all scheduling optimization variables. This option significantly reduces the number of optimization variables but, as mentioned above, might affect the optimization results, especially when the scheduling variables do not have a strong dependency on the input time series used for the linear mapping. This case can occur when intermediate decoupling storage is present, since DoF reduction does not account for the intermediate storage level, thus underestimating its utilization potential when performing scheduling. In this work, we therefore also evaluate the option of applying DoF reduction *selectively* to some scheduling variables, thus excluding the remaining ones from the linear mapping.

The optimization problem in the reduced scenario and DoF spaces can be represented as in OP 5.3:

$$\begin{aligned}
\min_{\boldsymbol{d},\ \tilde{\boldsymbol{s}}_{\mathrm{dof}}} \quad & \left(\sum_{n=1}^{N_{\mathrm{scen,\,red}}} p_{\mathrm{red},n} \cdot \mathrm{Obj}_n(\boldsymbol{d},\, \boldsymbol{s}_n(\boldsymbol{c}_n)) \right) \\
s.t. \quad & \\
& \boldsymbol{s}_n(\boldsymbol{c}_n) = A_{\mathrm{dof},n} \cdot \tilde{\boldsymbol{s}}_{\mathrm{dof},n}(\boldsymbol{c}_n) && n = 1, ..., N_{\mathrm{scen,\,red}} \\
& h_n(\boldsymbol{d},\, \boldsymbol{s}_n(\boldsymbol{c}_n)) = 0 && n = 1, ..., N_{\mathrm{scen,\,red}} \\
& g_n(\boldsymbol{d},\, \boldsymbol{s}_n(\boldsymbol{c}_n)) \leq 0 && n = 1, ..., N_{\mathrm{scen,\,red}},
\end{aligned} \tag{OP 5.3}$$

where $\boldsymbol{d} \in \mathbb{R}^{N_{\mathrm{design\,var}}}$, $\boldsymbol{s} \in \mathbb{R}^{N_{\mathrm{scen,\,red}} \times N_{\mathrm{scheduling\,var}} \times N_{\mathrm{TS}}}$, $\tilde{\boldsymbol{s}}_{\mathrm{dof}} \in \mathbb{R}^{N_{\mathrm{scen,\,red}} \times N_{\mathrm{scheduling\,var}} \times N_{\mathrm{dof,\,sched}}}$, and $N_{\mathrm{dof,\,sched}}$ is the number of DoFs per scheduling variable, which is chosen to be much smaller than N_{TS}. The scheduling variables $\boldsymbol{s}_n$ are linearly mapped to the scheduling variables in the reduced DoF space $\tilde{\mathbf{s}}_{\mathrm{dof},n}$ via the matrix $A_{\mathrm{dof},n}$. Note that the linear mapping of the scheduling variables is applied only to some of the $N_{\mathrm{scheduling\,var}}$ distinct scheduling variables when DoF reduction is performed selectively.

After implementing and testing several equivalent model formulations to embed DoF reduction (see Appendix C.4), we opted for a reduced-space formulation [362]. In this way, we not only reduce the number of DoFs via the linear mapping as equality constraints but also explicitly eliminate $\boldsymbol{s}_n$ via this mapping. This approach reduces the number of variables and constraints in the optimization problem, and thus its size. This can potentially reduce the computational time for solving large optimization problems.

DoF reduction is applied to the scheduling variables of each scenario cluster c_n independently. To determine the linear mapping matrix A_{dof}, we apply k-medoids to the normalized input scenario time series. Further, we tested two approaches for generating the linear mapping matrix A_{dof}: using k-medoids including and excluding the extreme values of the input time series. In the latter case, we assigned two DoFs to the lowest and highest values of the original time series, and then created $N_{\mathrm{dof,\,sched}} - 2$ clusters via k-medoids with the remaining values of the input time series. This choice is motivated by the fact that a few extreme hours can significantly affect the representativeness of the reduced time series [47, 332, 335, 363] and a special handling of those might be beneficial.

Finally, although the best number of DoFs could be determined while optimizing, e.g., by applying wavelet grid adaptation [338, 364, 365], we chose the number of DoFs after preliminary analyses to avoid introducing an iterative loop with two-stage stochastic programming problems to solve.

5.3.2.3. Implementation

Analogously to Subsection 5.2.1.3, the above-described complexity reduction approaches and the two-stage stochastic programming problems were implemented and solved in Matlab and GAMS. In particular, data processing, scenario clustering, and DoF reduction were performed in Matlab *ex-ante*, while the deterministic equivalent of the S-CDS problems was implemented in GAMS and solved with the global optimizer BARON 23.6.22 [282].

The information about the scenario clusters and the linear mapping matrix was passed from Matlab to GAMS through GAMS data exchange files (.gdx files) and Excel data sheets. Further, GAMS was called directly from Matlab to solve the optimization problems,

thus making it possible to embed the optimization problems in iterative loops, e.g., for a sensitivity analysis with respect to the number of scenario clusters. A CPU time limit of 4 h and 12 h was imposed for the optimization runs with a daily and weekly scheduling horizon, respectively.

The code is made available in the Supporting Information of Mucci and Bongartz [6] for the implementation details.

5.3.3. Case study

The above-described numerical complexity reduction approaches were applied to the S-CDS optimization of a grid-connected PtMeOH process with intermediate storage. The same process model, i.e., a quasi-steady-state MINLP model, and optimization variables as described in Subsection 5.2.2 were considered.

The input scenario space for the S-CDS problems was obtained by slicing a one-year input time series of day-ahead electricity prices for Germany from 2023 [299], thus being consistent with the considered economic data. In particular, daily and weekly scenarios with hourly resolution were extracted from the input time series. For weekly scenarios, 359 profiles composed of seven consecutive days were obtained by slicing the yearly time series and shifting the starting day. This choice increases the possibilities of the scenario clustering algorithm to determine representative profiles, since the scenarios do not necessarily start on the same day of the week.

When considering daily scenarios, the scheduling variables were kept in the original time domain ($N_{\mathrm{dof,\,sched}}$ equal to N_{TS}), thus avoiding suboptimal solutions of the original problem, since it could be handled numerically. Furthermore, this allows isolating the effect of the scenario clustering approach and $N_{\mathrm{scen,\,red}}$ on the objective function. In contrast, when considering weekly scenarios, DoF reduction for the scheduling variables was performed to reduce the numerical complexity. In particular, we applied k-medoids clustering to the electricity price scenarios of the reduced scenario space to determine the linear mapping matrix.

For a similar analysis based on a stand-alone PtMeOH case study, we refer to Mucci and Bongartz [6].

5.3.4. Results and discussion

In Subsections 5.3.4.1 and 5.3.4.2, we compare the clustering approaches for daily and weekly scenarios, respectively. Moreover, the latter investigates the effect of applying DoF reduction selectively to some scheduling variables. Finally, the results are discussed in Subsection 5.3.4.3.

5.3.4.1. Daily scenarios: Effect of clustering approaches and number of scenario clusters

In Figure 5.9, we compare the considered feature-based scenario clustering approaches (Table C.3) for a different number of daily scenario clusters ($N_{\mathrm{scen,\,red}}$) with hourly resolution for the grid-connected PtMeOH process. $N_{\mathrm{scen,\,red}}$ is varied since the number of scenario clusters needed to represent the original scenario space properly is not known in advance.

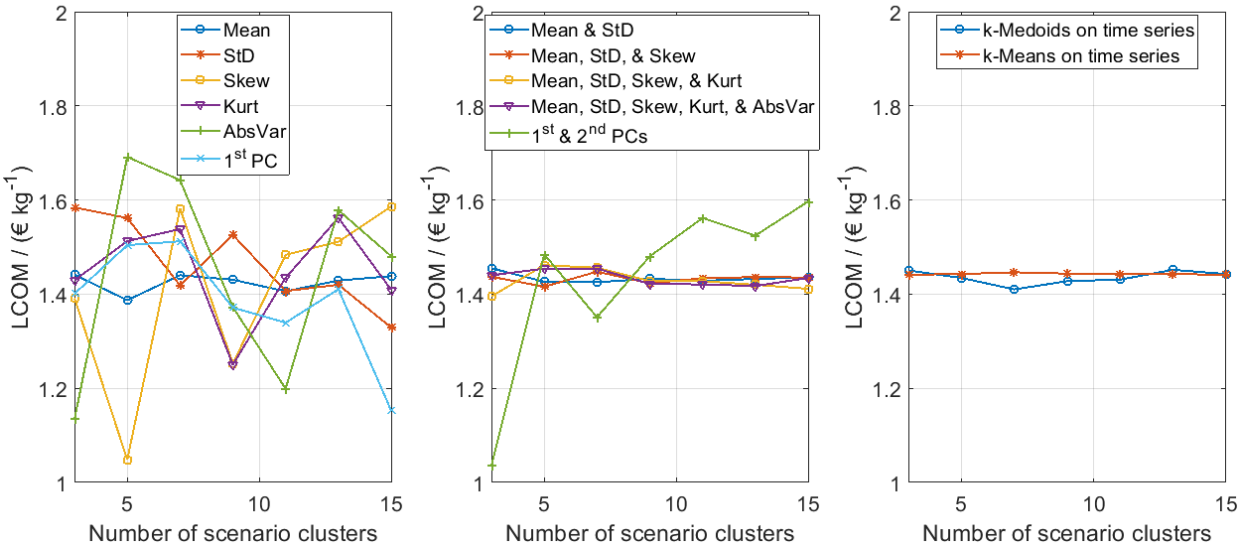


Figure 5.9.: Levelized cost of methanol (LCOM) for the grid-connected case study for different numbers of daily scenario clusters and clustering approaches. Left: Single-feature clustering via k-medoids based on mean, standard deviation (StD), skewness (Skew), kurtosis (Kurt), the mean of the absolute variation between consecutive time steps (AbsVar), and principal components (PCs). Middle: Multi-feature clustering via k-medoids based on the previously mentioned features. Right: k-medoids and k-means applied to the original time series.

When the scenarios are clustered based on a single feature, the objective function varies quite significantly with respect to the number of scenario clusters. This means that single-feature scenario clustering is not able to identify representative scenario subsets and probabilities for low $N_{\text{scen, red}}$. Among the considered features, the mean value of the scenario time series provides an objective function that is the least dependent on $N_{\text{scen, red}}$. This result suggests that the mean is the most relevant feature to estimate the methanol production cost. This outcome was expected since the average electricity price directly affects the operating costs.

When several features are simultaneously considered for scenario clustering, the objective function remains nearly constant with respect to $N_{\text{scen, red}}$, thus meaning that a few clusters, e.g., nine (< 3 % of the original scenario space), is sufficient to estimate the LCOM for the considered case study. Further, multi-feature clustering always outperforms single-feature clustering, since the objective function is less dependent on $N_{\text{scen, red}}$; thus, the latter has not been considered when investigating longer time horizons in Subsection 5.3.4.2.

No major differences can be noticed between the multi-feature clustering approaches, except for the one using the first two principal components extracted from the original scenario time series. Thus, the most relevant eigenvalues calculated from the input time series seem to be less important than other features, e.g., the central moments, to estimate the methanol production cost with low $N_{\text{scen, red}}$.

When the input time series are directly clustered (k-means and k-medoids approaches), the objective function value is nearly independent with respect to the scenario cluster number, similarly to the results obtained with multi-feature clustering. Moreover, these objective function values are similar to the ones obtained with multi-feature clustering.

For the sake of completeness, we report the results of the optimal design variables as well as the results of the same analysis conducted for the stand-alone case study, which has similar outcomes, in Section 3 of Supporting Information of Mucci and Bongartz [6].

5.3.4.2. Weekly scenarios

Differently from the S-CDS problems solved for daily scenarios (Subsection 5.3.4.1), DoF reduction is applied to reduce the optimization problem sizes related to the longer time horizon considered in this subsection, i.e., a week. Therefore, this subsection first investigates selective DoF reduction as a trade-off between numerical complexity and solution accuracy, and then compares the clustering approaches for different numbers of scenario clusters.

5.3.4.2.1 Degrees of freedom reduction

In the following, we present the results of DoF reduction for the grid-connected PtMeOH case study with three weekly scenarios identified via k-medoids applied on the original time series. This clustering approach was chosen after preliminary optimization runs (see Subsection 5.3.4.1). Nonetheless, note that the chosen clustering approach marginally affects the choice of the number of DoFs, since the same input profiles are considered for all cases.

The results in Table 5.4 show that reducing the DoF number $N_{\mathrm{dof,\,sched}}$ from 168, i.e., the number of time steps N_{TS}, to 12 is already sufficient to approximate the objective function (error below 2 % compared to the problem solved in the original time domain). However, the optimal design differs when DoF reduction is applied. In particular, the case where DoF reduction is applied to all scheduling variables leads to an optimal solution with no storage (design variables for storage at the lower bound).

Concerning the possibility of assigning DoF selectively to the scheduling variables, Table 5.4 shows that the objective function and optimal design values differ for the same number of DoFs (more significant differences are experienced for the stand-alone case study [6], which is hereby not reported). In particular, the fewer scheduling variables are mapped through DoF reduction, the lower the objective function and the closer the optimal design to the design of the benchmark case, i.e., without DoF reduction. This is mainly because the mapping introduces a strong correlation between scheduling variables. However, this correlation might not hold when the scheduling variables do not directly depend on the input time series used for clustering, i.e., the electricity price profile, and there is intermediate storage. In fact, the linear mapping is performed without including any information on the storage level, which might affect the optimal process design.

For this case, mapping the power of the electrolyzer and the hydrogen supplied to the methanol synthesis plant ($\dot{m}_{\mathrm{H_2,MeOH}}(t)$) leads to an optimal scheduling in which the produced hydrogen is converted directly into methanol instead of being partially stored in the hydrogen storage. Moreover, when excluding the scheduling variable $\dot{m}_{\mathrm{H_2,MeOH}}(t)$ from the linear mapping, the optimization problem has more optimization variables (3907 vs. 2971 for $N_{\mathrm{dof,\,sched}} = 12$), but its solution shows the need for hydrogen storage and the objective function is improved (Table 5.4). The difference in process operation due to the hydrogen storage can be noticed in Figure 5.10, e.g., in the different PEM-WE power demand, and by analogy the hydrogen production, and the hydrogen flow into the methanol synthesis plant.

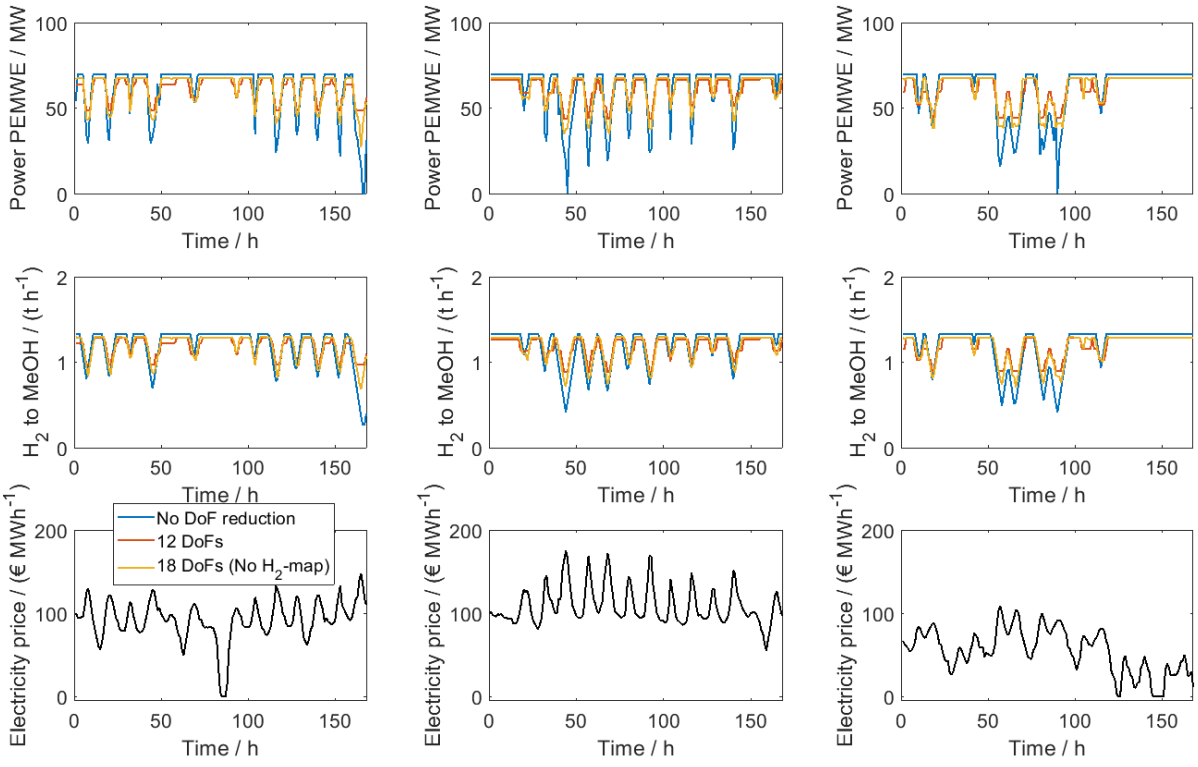
Table 5.4.: Comparison of the objective function and the design variable values for different DoF reduction approaches applied to a two-stage stochastic programming problem of a grid-connected PtMeOH process with intermediate storage. Three weekly electricity price scenario clusters of 168 h each are considered. The number of model variables as well as the NL_{code}, a GAMS indicator of the complexity for handling model nonlinearities, are also displayed. The results were extracted after 6 h CPU time. No global optimality was achieved.

$N_{\mathrm{dof,\,sched}}$	Mapped scheduling variables	Specific cost of MeOH	$\mathrm{En_{batt}}$	V	N_{mod}	β_{max}	$\dot{m}_{\mathrm{H_{2,MeOH},nom}}$	Model variables	$\mathrm{NL_{code}}$
-		€ $\mathrm{kg^{-1}}$	MWh	$\mathrm{m^3}$	-	-	t $\mathrm{h^{-1}}$	-	-
168	None	1.46	5*	240	28	2.65	1.33	8587	31 822
12	All variables	1.46	5*	50*	27	1.88*	1.29	2971	11 698
12	All variables except for $\dot{m}_{\mathrm{H_{2,MeOH}}}(t)$	1.46	5*	120	27	2.18	1.30	3907	11 698
12**	All variables except for $\dot{m}_{\mathrm{H_{2,MeOH}}}(t)$	1.46	5	120	27	2.20	1.30	3907	11 698
18	All variables except for $\dot{m}_{\mathrm{H_{2,MeOH}}}(t)$	1.46	5*	120	27	2.18	1.30	4087	12 472
18**	All variables except for $\dot{m}_{\mathrm{H_{2,MeOH}}}(t)$	1.46	5*	120	27	2.19	1.29	4087	12 472

* At bound.
** The extremes have a dedicated DoF.

The scheduling variables of the battery could also be excluded from the linear mapping. However, this option has not been investigated here, since the operation of batteries directly depends on the electricity prices used for defining the linear mapping matrix A_{dof}. Further, the optimizer often chooses small-size batteries, thus not playing a big role in the process economics under the considered economic assumptions.

Concerning the different ways of assigning DoFs, Table 5.4 shows that assigning DoFs to the extreme values of the input time series to generate the linear mapping leads to similar results concerning both the objective function and process design. In contrast, this approach was not beneficial for the stand-alone PtMeOH case study [6] (the results are hereby not reported). As there is no noticeable difference between the two approaches for the grid-connected PtMeOH case study and the original weekly time series have several peaks and valleys that could potentially be clustered within the same DoF, we opted for clustering the input time series with $N_{\mathrm{dof,\,sched}} = 18$ without handling the extremes differently for generating the results shown in Subsection 5.3.4.2. Furthermore, thanks to the implemented reduced-space formulation [362], a significant reduction of the problem size is achieved, e.g., ca. 50 % model variable reduction for the case in Table 5.4.



(a) Scenario cluster 1. **(b)** Scenario cluster 2. **(c)** Scenario cluster 3.

Figure 5.10.: Optimal solution of the S-CDS problem for a grid-connected PtMeOH process when considering three weekly scenario clusters and different DoF reduction strategies (the three solid lines in the two upper graphs). In particular, the blue line represents the case where no DoF reduction is applied, the red line the case where DoF reduction is applied to all relevant scheduling variables and 12 DoFs are considered, and the yellow line the case where DoF reduction with 18 DoFs is applied to all relevant scheduling variables besides $\dot{m}_{\mathrm{H_{2,MeOH}}}(t)$.

5.3.4.2.2 Effect of clustering approaches and number of scenario clusters

In the following, we compare the optimization results of the S-CDS problems solved with different scenario clustering approaches for different weekly scenario cluster numbers while applying selective DoF reduction. In particular, we evaluate the effect of clustering on the objective function and design variables.

To evaluate whether the clustering approaches can identify representative scenario subsets and weights and estimate the objective function value of the full S-CDS problem, which itself is computationally intractable, we solved a relaxed S-CDS problem for the full scenario space without DoF reduction using the local optimizer SNOPT 7.7.7 (see Appendix C.5 for details on the model).

Objective function

In Figure 5.11, we show how the objective function evaluated on the reduced scenario space varies with respect to the number of scenario clusters for different clustering approaches.

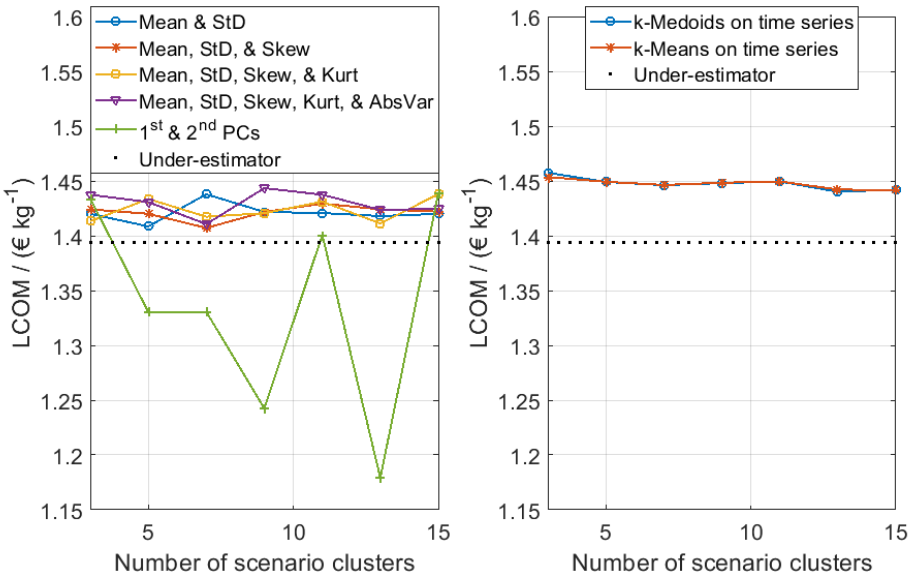


Figure 5.11.: Levelized cost of methanol for the grid-connected case study for different numbers of weekly scenario clusters and clustering approaches ($N_{\mathrm{dof,\,sched}} = 18$). Left: Multi-feature clustering via k-medoids based on mean, standard deviation (StD), skewness (Skew), kurtosis (Kurt), the mean of the absolute variation between consecutive time steps (AbsVar), and principal components (PCs). Right: k-medoids and k-means clustering applied to the original scenario time series. The black dotted line represents the under-estimator of the original S-CDS problem.

When multiple interpretable features, namely central moments, are considered for clustering, the LCOM is almost independent of the number of clusters in the considered range, thus meaning that a limited number of representative scenarios, e.g., five (ca. 2 % of the original scenario space), is sufficient to estimate the objective function value for this case study. In contrast, the objective function shows a strong dependency on $N_{\mathrm{scen,\,red}}$ when multi-feature clustering is performed with the first two principal components of the scenarios. In this case, the objective function varies significantly even with relatively high

$N_{\text{scen, red}}$ (this behavior was already observed for daily scenarios as shown in Figure 5.9). Moreover, the objective function value is on average significantly lower than the one obtained for the other clustering approaches, thus meaning that this clustering approach does not identify suitable scenario subsets and probabilities to estimate the objective function for the considered case study and $N_{\text{scen, red}}$ range.

The LCOM obtained with scenarios clustered via k-medoids and k-means applied to the input time series shows the least dependent behavior with respect to $N_{\text{scen, red}}$ among all the clustering approaches. Nevertheless, the LCOMs obtained via multi-feature clustering are similar to these, thus suggesting that feature-based clustering can identify representative scenario subsets and scenario probabilities. Furthermore, the LCOMs obtained via multi-feature clustering are closer to the LCOM obtained by solving the relaxed S-CDS problem, thus being closer to the best estimation available of the objective function of the original S-CDS problem (Figure 5.11).

Design variables

Despite an objective function that is nearly independent of $N_{\text{scen, red}}$, the design variables still exhibit mild variations when increasing the number of scenario clusters for all clustering approaches (see, for instance, the hydrogen flow rate to the methanol synthesis plant in Figure 5.12). This behavior was already observed, for instance, by Teichgraeber et al. [47]

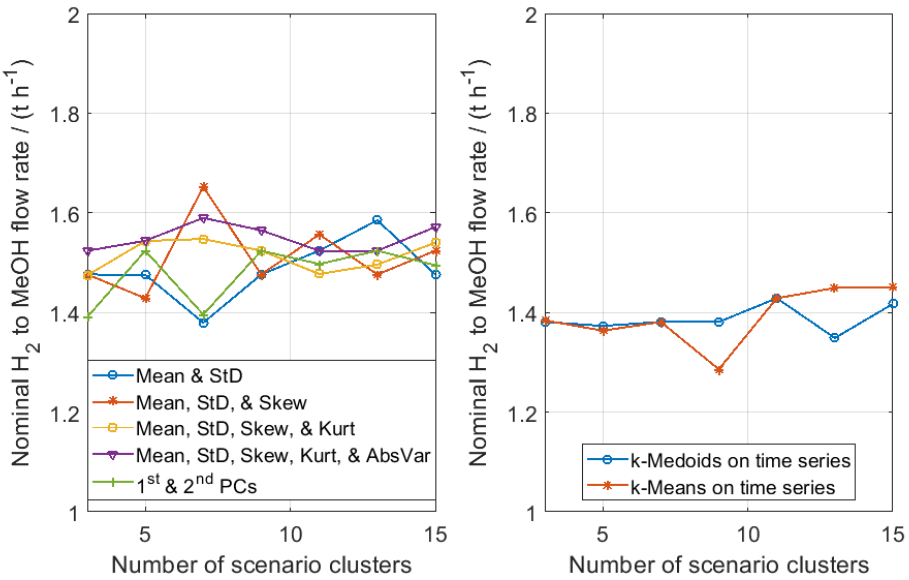


Figure 5.12.: Hydrogen flow rate to the methanol plant for the grid-connected case study for different numbers of weekly scenario clusters and clustering approaches ($N_{\text{dof, sched}} = 18$). Left: Multi-feature clustering via k-medoids based on mean, standard deviation (StD), skewness (Skew), kurtosis (Kurt), the mean of the absolute variation between consecutive time steps (AbsVar), and principal components (PCs). Right: k-medoids and k-means clustering applied to the original scenario time series.

and can be due to several reasons: approximations due to scenario clustering and DoF reduction; the lack of global convergence; and the fact that several plant designs can have similar objective function values as discussed in Section 5.2. The latter can be confirmed by

fixing the process designs obtained by solving the reduced S-CDS problems and then solving stochastic scheduling problems in the original scenario and DoF spaces (Figure 5.13).

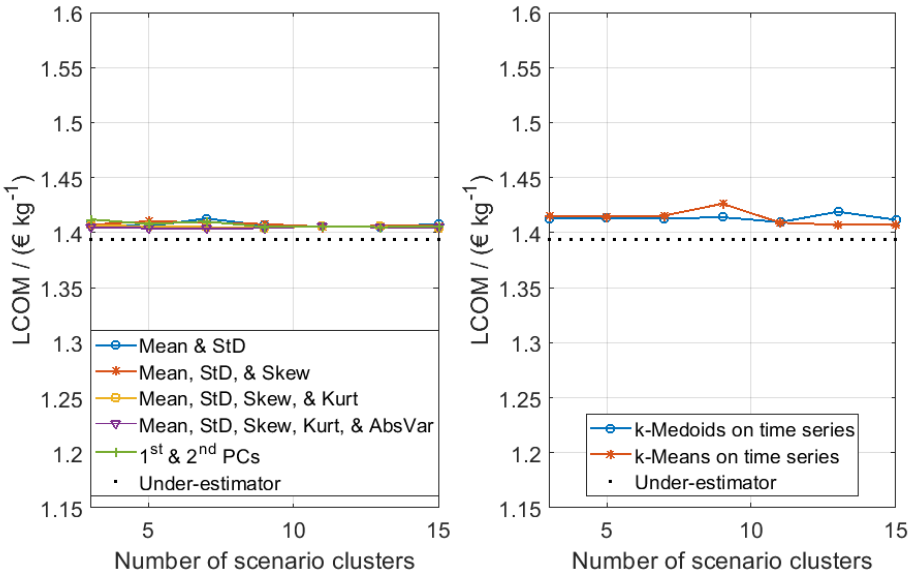


Figure 5.13.: Levelized cost of methanol for the grid-connected PtMeOH case study calculated by solving stochastic scheduling problems in the original scenario and DoF spaces for the process designs identified by solving reduced stochastic combined design and scheduling problems (LCOMs displayed in Figure 5.11) for different numbers of weekly scenario clusters and different clustering approaches. Left: Multi-feature clustering via k-medoids based on mean, standard deviation (StD), skewness (Skew), kurtosis (Kurt), the mean of the absolute variation between consecutive time steps (AbsVar), and principal components (PCs). Right: k-medoids and k-means clustering applied to the original scenario time series. The black dotted line represents the under-estimator of the original S-CDS problem. Note that the same y-axis scale as in Figure 5.11 is used.

The variations of the design variables with respect to $N_{\text{scen, red}}$ are generally lower when multi-feature clustering instead of k-medoids and k-means applied directly to the input time series is performed and a sufficiently high number of clusters is considered (see, for instance, Figure 5.14). Furthermore, these variables are, on average, less dependent on $N_{\text{scen, red}}$ for relatively low $N_{\text{scen, red}}$ values, e.g., nine. Also, their values are quite similar across the different multi-feature clustering approaches. Moreover, the process designs identified via multi-feature clustering (and selective DoF reduction) perform on average slightly better in the original scenario and DoF spaces for the considered case study (Figure 5.13). This suggests that the proposed methodology generates reduced S-CDS problems that preserve the key characteristics of the original S-CDS problem, thus allowing identifying promising design candidates.

Similarly to what was observed for a daily time horizon (Subsection 5.3.4.1), no multi-feature clustering approach clearly outperforms the others in identifying process designs in the reduced scenario space. Nevertheless, considering higher central moments, e.g., up to kurtosis, for clustering leads on average to relatively similar results within the considered $N_{\text{scen, red}}$ range. Interestingly, multi-feature clustering based on principal components allows

identifying process designs that are quite independent of $N_{\text{scen, red}}$ despite the significant variation of the objective function.

For the sake of completeness, the results of the sensitivity analysis for the remaining design variables are reported in Section 4.1 of Supporting Information of Mucci and Bongartz [6].

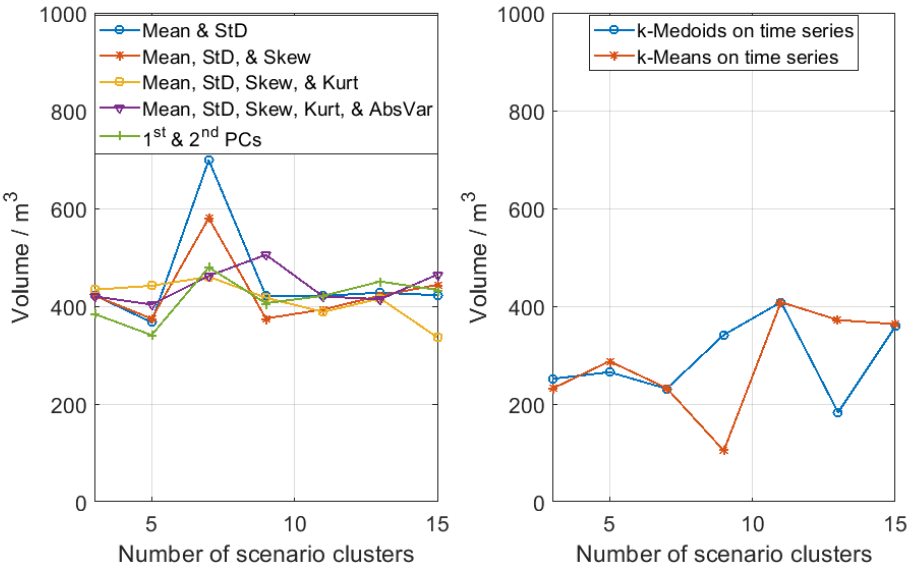


Figure 5.14.: Hydrogen storage volume for the grid-connected case study for different numbers of weekly scenario clusters and clustering approaches ($N_{\text{dof, sched}} = 18$). Left: Multi-feature clustering via k-medoids based on mean, standard deviation (StD), skewness (Skew), kurtosis (Kurt), the mean of the absolute variation between consecutive time steps (AbsVar), and principal components (PCs). Right: k-medoids and k-means clustering applied to the original scenario time series.

5.3.4.3. Discussion

Complexity reduction method applicability and performance

The investigated methodology, which combines feature-based scenario clustering with DoF reduction, has been applied to a PtMeOH process with intermediate storage modeled as a MINLP. Nonetheless, it can also be applied to solve S-CDS optimization for other processes, e.g., other PtX processes and energy systems, and model types, e.g., MILPs. In fact, the considered numerical complexity reduction techniques are applied *ex-ante*: scenario clustering and the linear mapping for DoF reduction are performed without any prior knowledge about the process and model type, unless DoF reduction is applied selectively. For the latter case, considering information about the process is beneficial to select which scheduling variables should be linearly mapped.

Despite the general applicability of this methodology, its computational performance against other complexity reduction techniques might depend on the considered process and model type as well as solver, and it should therefore be evaluated on a case-by-case basis. In fact, even for the same process model, the computational benefits of using scenario

clustering and DoF reduction are not always clear and consistent, although they reduce the overall number of optimization variables.

For the considered case study, scenario clustering allows solving approximations of the original S-CDS optimization problem, for which BARON could not identify a feasible solution solvable within reasonable computational times. Moreover, the computational time needed by BARON to identify a feasible solution tends to increase when the number of scenario clusters increases and no DoF reduction is applied (around 500 s, 2 000 s, and 40 000 s for the grid-connected PtMeOH case study with 3, 15, and 50 scenario clusters, respectively). However, it increases not monotonically when DoF reduction is applied (around 500 s, ca. 20 000 s, and 10 000 s for the grid-connected PtMeOH case study with 3, 15, and 50 scenario clusters, respectively). Further, the use of DoF reduction does not always lead to improved computational performance compared to considering the original time domain for the same number of scenario clusters. Finally, its performance seems to also depend on the considered solvers, e.g., BARON vs. ANTIGONE, which have different algorithms to identify feasible solutions and calculate model relaxations, and have been shown to react differently to reduced space formulations of optimization problems [366].

Clustering approaches: objective function vs. design variables

As shown for the grid-connected PtMeOH case study, feature-based scenario clustering can identify representative scenario subsets and probabilities to reduce the complexity of S-CDS problems: the objective function of the S-CDS problem in the reduced scenario and DoF spaces becomes almost independent from the number of scenario clusters already when considering a relatively low $N_{\text{scen, red}}$ (see for instance Subsection 5.3.4.2). In particular, considering the first four central moments provides, on average, the best results among the investigated multi-feature clustering approaches for the grid-connected case study (a similar conclusion can be drawn for the stand-alone PtMeOH case study, hereby not reported).

Further, multi-feature clustering performs similarly or sometimes better than state-of-the-art clustering approaches, e.g., k-means applied directly to the time series. However, the best clustering approach is often problem-dependent [332, 358]. Thus, multi-feature clustering should be tested for other case studies and time horizons to draw more robust conclusions.

In contrast to the objective function, the process design variables still exhibit a quite strong dependency on the number of scenario clusters even at high $N_{\text{scen, red}}$. Nonetheless, these process designs, especially the designs identified via multi-feature clustering, perform well in the original scenario and DoF spaces as shown for the grid-connected PtMeOH case study (Figure 5.13). One potential reason is that the objective function captures the trade-off between investment and operating costs and several process designs can lead to similar values [313, 335, 367] (also see Section 5.2).

Process design and operation implications

For the considered economic assumptions (Appendix C.1) and irrespective of the clustering approach, all optimal process designs include oversizing the electrolysis and methanol synthesis units as well as the presence of hydrogen storage. This confirms that PtMeOH processes should be designed to enable flexibility, as also discussed in Section 5.2.

The extent of oversizing varies depending on the scenario clustering approach (ca. 20 %-30 % and ca. 15 %-30 % for the electrolysis and methanol synthesis units, respectively). Such relatively wide ranges can be due to the selection of representative scenario sets, the

approximations related to DoF reduction, and the fact that different process designs can perform similarly well with respect to the objective function.

The optimal designs have bigger electrolysis and methanol synthesis units, as well as hydrogen storage (Figure 5.14), when multi-feature instead of k-medoids and k-means clustering approaches are considered. These process designs perform slightly better when solving stochastic scheduling problems in the original scenario and DoF spaces, as shown in Figure 5.13 for the grid-connected PtMeOH process. These design choices were expected when scenarios are clustered via k-means, since it tends to smoothen the scenario profiles [297, 332] (also see Figure C.4). In contrast, they were not necessarily expected for k-medoids clustering since it generally selects scenarios with more profile variations [332].

In all results, the optimal maximum pressure ratio of the compression unit is close to the upper bound to store as much hydrogen as possible within the volume (Figure C.7) so that electricity price and renewable power generation fluctuations can be better exploited to reduce the methanol production cost.

Under the considered economic assumptions (Appendix C.1), the optimization results suggest that battery storage is not economically beneficial for the grid-connected case study (value close to the lower bound in Figure C.5). Nonetheless, the battery might play a major role at time scales shorter than the considered time discretization (1 h) and with the expected drop in their investment costs as already shown in Section 4.6. Further, the need for batteries might change in the case aging models for both the battery and electrolysis units are considered (not investigated in this work).

Scenario horizon duration and input data

The scenario horizon duration can affect optimal storage size and its utilization. Nonetheless, the optimal storage size calculated for a daily and weekly time horizon does not differ significantly for the grid-connected case study optimized after applying the investigated numerical complexity reduction approaches. This result suggests that, for the considered PtMeOH process and input scenario space, hydrogen storage is used to deal with electricity price variations occurring within a few hours rather than to store large quantities of hydrogen. Nonetheless, these assumptions should be confirmed by investigating longer time horizons.

Further, solving risk-neutral S-CDS problems for other input scenario data, e.g., considering several years [342, 345], could potentially increase the confidence in the obtained optimal process designs. However, the input scenario sets, which are often generated from historical data, remain uncertain, since there is no guarantee that the considered scenarios will actually occur in the future, especially if major policy and structural changes occur. In the latter case, solving risk-averse or robust S-CDS problems as well as including profile forecasts in the scenario sets could be beneficial.

5.4. Conclusion

In this chapter, Stochastic Combined Design and Scheduling optimization problems were solved for a grid-connected PtMeOH process with intermediate storage under electricity price scenario uncertainty. Given the generally high numerical complexity of these problems, we investigated the effectiveness and accuracy of several approximation approaches that aim at improving their numerical tractability. In particular, we first investigated the effect of optimizing the design, the scheduling (enabling different levels of process flexibility), and their combination on methanol production cost, and then analyzed the effectiveness of scenario clustering combined with DoF reduction.

By solving stochastic scheduling optimization problems with perfect information on the scenario time series for randomly generated designs, we showed that a significant reduction in methanol production cost can be achieved by enabling flexible operation, especially of the methanol synthesis unit. Moreover, optimizing the scheduling when enabling flexible operation of all process units seems to be, on average, more important than optimizing the design when assuming steady-state operation of the electrolysis and methanol synthesis units. This is because process flexibility can mitigate economic losses due to poor design choices.

The operating strategy of the methanol synthesis process affects the optimal process design. Nevertheless, very different process designs lead to similar objective function values. Moreover, the objective function seems to be quite insensitive to certain design variables, e.g., storage capacity, for wide variable ranges under the considered economic assumptions, thanks to the high flexibility enabled by the other process units. Also, no clear patterns in well-performing process designs were found via statistical analysis, besides the fact that oversizing the water electrolysis and methanol synthesis units seems the most relevant design choice. These results therefore highlight the need to optimize the design and scheduling simultaneously.

For the cases where the numerical complexity cannot be handled within reasonable computational times, we investigated the potential of combining feature-based scenario clustering with selective DoF reduction to generate representative S-CDS problems. Furthermore, we assessed the performance of different sets of features (both interpretable and non-directly interpretable features like central moments and principal components, respectively) for clustering purposes.

For a daily horizon, we found that the mean of the scenario profiles is the most relevant single feature for identifying representative scenario subsets and estimating the objective function. Nonetheless, single-feature scenario clustering is always outperformed by multi-feature scenario clustering, in the sense that the latter can approximate the optimal objective value well with fewer clusters.

For a weekly horizon, we found that multi-feature clustering based on the first four central moments performs similarly or sometimes better than state-of-the-art clustering approaches, e.g., k-means, with respect to the objective function. In particular, the objective function exhibits a behavior that is almost independent of the scenario cluster number already with a small number of clusters (less than 10 % of the original scenario space).

As opposed to the objective function, the optimal design variables still exhibit a relatively strong dependency on the scenario cluster number, although the variations are lower when clustering based on several central moments, e.g., up to kurtosis. This might be due to the fact that several process designs can lead to similar levelized costs of methanol, since this

objective function captures the trade-off between investment and operating costs, as shown for the grid-connected PtMeOH case study by solving stochastic scheduling problems for fixed process designs. Further, the process designs identified via feature-based clustering for relatively low scenario cluster numbers perform slightly better in the original scenario and DoF spaces than those obtained via k-medoids and k-means applied directly to the scenario time series. This suggests that the generated reduced S-CDS problems represent the original S-CDS problem sufficiently well. Therefore, these problems could potentially be embedded in an optimal design algorithm: the reduced S-CDS problems are solved to identify suitable candidate designs that are then assessed in the original scenario and DoF spaces by solving stochastic scheduling problems.

Further, for the weekly horizon, we applied a DoF reduction approach tailored for scheduling variables that maintains the time step chronology memory to reduce the numerical complexity further. We found that DoF reduction should be applied selectively only to some scheduling variables, since the variable mapping introduces a strong correlation that can affect the optimal process design.

Future work on the considered S-CDS problems might include relaxing the assumption of perfect information on the scenario time series to investigate its effect on the optimal stochastic process design. Further, as several process designs lead to similar methanol production costs, identifying an optimal design space instead of a single optimal design could provide valuable insights. Approaches like modeling-to-generate-alternatives [368] could be applied to obtain optimal design variable ranges, which could be particularly valuable when commercial process unit sizes are modular or standardized.

Despite the potential and effectiveness of the investigated numerical complexity reduction approach, the best clustering approach is generally problem-dependent [332, 358]. Therefore, feature-based clustering should be tested for other time horizons, input scenario sets, problem formulations, and case studies. Nonetheless, using scenario features that directly affect the operating costs has the potential to perform well in other grid-connected energy-intensive applications. Further, other features, e.g., belonging to the frequency domain and accounting for the peak and valley positions of the profiles, may also be worth investigating.

Finally, while scenario clustering allowed identifying representative S-CDS problems that are solvable within reasonable times, the use of selective DoF reduction was not always numerically beneficial for the considered case studies, although it significantly reduces the number of optimization variables. This aspect could be affected by the numerical solver and the optimization problem numerics. Therefore, the computational improvements related to this approach should be further investigated.

6. Conclusion and Outlook

Hydrogen-based Power-to-X processes have significant defossilization potential for the industrial, transport, and energy sectors if the predictions of wide availability of low-carbon electricity to achieve the environmental goals are met [21]. However, the currently high investment and operating costs of PtX processes do not make the sustainable products "X" economically competitive against fossil-based ones.

To improve the understanding of such processes and contribute to bridging this price gap, this dissertation focused on the design, modeling, and optimization of some key hydrogen-based PtX processes. In particular, we modeled and compared different pathways for integrating biomass into PtX processes, since biomass has the potential to improve their economic viability thanks to its valuable energy input. Further, we investigated via optimization the need for flexible operation and intermediate storage, as well as their interplay, as viable options to reduce production costs.

In the following paragraphs, the key conclusions are summarized, and some future research directions are suggested.

Conclusion

The literature-based analysis conducted on some key Power-to-X process units shows that the low-temperature water electrolysis, carbon capture, and hydrogen conversion units are suitable for flexible operation to a certain extent, depending on the process technologies and configurations (Chapter 2). This enables the possibility of PtX processes to deal with fluctuating power inputs resulting from either process scheduling or power availability, thus potentially improving their economic competitiveness. Nonetheless, these PtX processes might require intermediate storage when operated flexibly if it is economically beneficial and if certain process units are less responsive than others (Table 2.2) or undergo accelerated degradation under highly fluctuating power inputs.

Further, process integration concerning both material and heat streams can increase the process efficiency and potentially reduce production costs. Nonetheless, highly integrated processes might make flexible operation more challenging. Therefore, the design of these flexible PtX processes, including the extent of material and heat integration, should be optimized considering information about their operation.

The use of alternative sustainable feedstocks, such as residual biomass, instead of CO_2 can also improve the economic competitiveness of hydrogen-based PtX processes, thus potentially paving the way for their swift industrial realization. In fact, unlike CO_2, biomass contains not only carbon atoms but also a valuable energy input. If biomass is properly exploited, the resulting Power- and Biomass-to-X processes have higher yields than BtX processes, and lower electrolysis unit sizes as well as net electricity inputs than PtX processes, which both significantly affect production costs [39, 225].

To this end, we investigated two pathways for integrating biomass into PtX processes (Chapter 3). In particular, we compared combustion-based vs. gasification-based PBtX processes via an exergy analysis performed by using relatively simple steady-state models.

These models are sufficiently accurate to highlight the key inherent thermodynamic differences between the processes, clearly showing the advantages of gasification-based processes over combustion-based ones. For instance, the full oxidation of the carbon atoms in the biomass to CO_2, typical of combustion-based processes, generates high exergy losses, since the biomass energy content is converted into heat instead of being stored in the molecular bonds, e.g., of CO and H_2. Additionally, gasification-based processes require a significantly lower amount of hydrogen produced via water electrolyzers, which are generally the main contributors to exergy losses in PtX and PBtX processes. These key differences were confirmed for two processes modeled in detail, i.e., a Power- and Biomass-to-Methanol and a Power- and Biomass-to-Kerosene process. For these processes, we also showed that the significant reduction of the electrolysis unit size and the electricity demand in gasification-based processes leads to lower production costs.

Further, we evaluated the effectiveness of these relatively simple models in comparing two promising pathways, i.e., Fischer-Tropsch and Methanol-to-Olefins pathways, for the production of Sustainable Aviation Fuels, specifically synthetic kerosene (Chapter 3). For this comparison, the considered relatively simple models show some limitations, as they are not sufficiently representative of real processes, which present significant nonidealities. Moreover, the relatively simple models suggest a similar performance of the two pathways in producing dodecane (hydrocarbon assumed as representative of the kerosene range). In contrast, the detailed models suggest that the MtO pathway is more selective, efficient, and cost-effective in producing kerosene-like fuel than the FT pathway. Therefore, this example highlights that simple models, often used in a process screening phase, should be sufficiently representative, e.g., including key nonidealities, to avoid excluding promising process pathways that might be better than others when modeled in detail.

As opposed to biomass, CO_2 does not suffer from availability issues [38], thus representing a promising feedstock for large-scale implementation of PtX processes. We therefore considered this feedstock for investigating flexible process operation and intermediate storage as options to reduce the production cost of one of the most produced platform chemicals, i.e., methanol. For this purpose, we built quasi-steady-state models of a grid-connected and stand-alone Power-to-Methanol process with intermediate storage, namely battery and hydrogen storage, and then solved Combined Design and Scheduling optimization problems seeking trade-offs between investment and operating costs (Chapter 4).

Concerning flexible operation, the optimization results show that the flexible operation of all process units always reduces the methanol production cost. Moreover, the effectiveness of flexible operation in reducing methanol production cost is higher for highly fluctuating input profiles. Interestingly, moderate flexibility of the methanol synthesis unit, e.g., assuming a maximum ramp rate of 10 % h^{-1}, already provides most of the economic savings in grid-connected PtMeOH plants. This can be due to the considered models, scenarios, and time discretization (hourly time steps). Also, this result suggests that extreme load variations are not necessary to achieve significant operating savings if hourly price variations, which were typical for the European day-ahead electricity market before October 2025, are considered. In contrast, higher maximum ramp rates of the methanol synthesis unit might be beneficial for stand-alone PtMeOH plants to better follow renewable power generation fluctuations on shorter time scales. However, this option has not been investigated in this work.

Concerning intermediate storage, its need and optimal size strongly depend on the considered scheduling scenarios and economic assumptions. For instance, when electricity

price profiles have relatively high average values and fluctuations, intermediate storage, especially hydrogen storage, reduces the methanol production cost irrespective of the operation strategy of the methanol synthesis unit (steady state vs. flexible). In contrast, when electricity price profiles have relatively low average values and fluctuations, the investment cost for storage is not repaid by the savings in the operating costs. Further, the results suggest that using hydrogen storage reduces the methanol production cost more than using batteries under current economic assumptions. Nonetheless, batteries could play a major role if shorter time scales are considered and their investment cost drops.

To partially overcome the above-described limitations related to designing a process with respect to a single scheduling scenario, we also solved Stochastic Combined Design and Scheduling optimization problems for a grid-connected PtMeOH process with intermediate storage accounting for uncertainty of scenario realization (Chapter 5). As these problems often suffer from numerical intractability, we implemented and solved several S-CDS optimization problem approximations, e.g., optimizing the process design and the scheduling when enabling different levels of process flexibility.

The results show that optimal process scheduling performed with perfect information on the scenario time series and enabling flexible operation of all process units is, on average across the randomly generated designs, more important than optimal process design performed by assuming steady-state operation of the methanol synthesis unit. This is due to two main reasons: 1) process flexibility allows mitigating potential economic losses due to poor design choices, and 2) several process designs (with oversized electrolysis and methanol synthesis units) lead to very similar and relatively low methanol production costs when process flexibility is enabled and the scheduling is optimized. Nonetheless, proper design choices matter, since the stochastic scheduling problems solved for the randomly generated designs still exhibit a relatively wide methanol production cost range. Further, these results indirectly indicate the importance of having reliable electricity price forecasts for process scheduling to ensure relatively low operating costs once the plant is built.

While process flexibilization was proven to reduce production costs even under scenario uncertainty, no clear indication concerning the need for intermediate storage was obtained under the considered economic assumptions and time scales: the methanol production cost is relatively insensitive to the size of the battery and hydrogen storage, especially when both the electrolysis and methanol synthesis units are oversized. Moreover, the economic benefit of intermediate storage also depends on the size of the other process units. However, no clear well-performing process design patterns were identified, thus highlighting the need to optimize design and scheduling simultaneously.

We then investigated a numerical complexity reduction approach for S-CDS optimization problems that combine feature-based scenario clustering and selective degrees of freedom reduction (Chapter 5). The results show that considering several central moments, e.g., up to kurtosis, as features for scenario clustering allows identifying suitable scenario subsets and probabilities. Also, DoF reduction should be applied selectively to the scheduling variables to avoid introducing patterns among the scheduling variables that might not hold true. Further, for the considered grid-connected PtMeOH case study, the resulting reduced S-CDS problems were sufficiently representative of the original S-CDS problem: they could identify process designs that performed well in the original scenario and DoF spaces, often outperforming the ones identified via reduced S-CDS problems obtained via state-of-the-art clustering approaches such as k-means and k-medoids applied directly to the scenario time series. Finally, while scenario clustering effectively improves the numerical tractability, the

use of selective DoF reduction in a reduced-space formulation [362] does not always lead to computational improvements despite significantly reducing the number of optimization variables and the size of the optimization problems.

Outlook

Although the understanding and the key technologies of hydrogen-based PtX processes have improved over the past few years, several aspects still need to be addressed to make these processes competitive against fossil-based alternatives and accelerate their industrial realization. In fact, only a few PtX processes have so far reached the commercial scale, e.g., the PtMeOH processes by Carbon Recycling International [143] and BSE Engineering [144].

A more extensive implementation of PtX processes is required to reduce their investment costs, especially of the electrolyzers, and thus production costs, and meet the environmental targets. Also, the experience gained through their operation, as well as the continuous development of the key process units, is essential to improve these PtX processes further and reduce the cost gap with conventional production processes. For instance, data on degradation under flexible operation could be used to improve materials, e.g., catalysts, and process configurations, as well as refine process models and develop optimization-driven operating strategies to mitigate such phenomena.

As discussed also in this dissertation, PtX processes should be designed considering information on how they will be operated. In fact, certain process design decisions that lead to a process efficiency gain might reduce the flexibility range and response time, thus affecting the overall economics. For instance, extensive heat integration improves process efficiency, but could affect the process responsivity; therefore, its viability should be properly evaluated with dynamic models. Further, large-scale flexible PtX processes could employ different electrolyzer types: some electrolyzers could be designed for steady-state operation to cover a base hydrogen demand of the downstream process, whereas others could be designed for enhanced flexibility (and lower investment costs) to exploit electricity price fluctuations.

In this dissertation, we also showed that relatively simple models can often provide key insights into the processes and help screen process configurations before modeling them in more detail. However, given the importance of flexible operation of energy-intensive processes to reduce production costs, accounting for the potential for flexible operation in the process screening could reduce the risk of discarding process configurations that, for instance, are less efficient at the design point but have wide flexibility ranges and good off-design performance.

Concerning the investigated PBtX processes, we showed that the Methanol-to-Olefins pathway seems to be particularly promising for producing fuel in the kerosene range as well as for flexible operation (methanol can be easily stored as an intermediate, thus decoupling hydrogen from kerosene production). However, further work is required to improve the models of some key process steps, such as the oligomerization unit, and validate them with experimental data, which are often limited in the open literature. Additionally, beyond optimizing the flowsheet to reduce the kerosene production cost of the considered configuration, other process configurations could be investigated, e.g., with a dedicated ethylene oligomerization reactor to overcome its generally low conversion over acidic catalysts [236]. Further, the fuel upgrading section could be extended to assess the effort and costs required to meet the specifications for drop-in aviation (and automotive) fuels. Nonetheless, the Methanol-to-Olefins pathway should be officially approved before this

synthetic kerosene can actually be used for civil aviation purposes (the approval process is ongoing at the time of writing).

Concerning the PtMeOH process considered for CDS optimization, the level of detail of the models used could be improved, e.g., embedding operating maps for the compression and methanol synthesis units based on the operating load and accounting for degradation. Further, the models could be extended to account for the carbon capture unit as well as fluctuations related to the carbon source availability. Also, investigating scenarios with longer horizons could be particularly interesting to capture how the seasonality of renewable production affects the optimal design of stand-alone PtMeOH processes.

Further, for the grid-connected PtMeOH case study and scenarios considered in Chapter 4, moderate flexibility of the methanol synthesis unit could provide most of the economic savings when optimizing the process scheduling considering hourly discretized electricity price profiles from the European day-ahead electricity market. However, the day-ahead electricity trading has recently switched from hourly to 15-minute intervals in most European countries [369]. Therefore, CDS optimization problems should be solved for electricity scenarios with finer time discretization to assess whether some conclusions, e.g., on the maximum ramp rate or need for batteries, still stand. For this purpose, dynamic models for some process units might be required to account for transients, as the quasi-steady-state assumption becomes weaker. Further, the possibility of bidding simultaneously in other electricity markets, e.g., the intra-day market, or of offering ancillary services could be explored to reduce the production costs of PtX processes further. Finally, the effect of having independent, but cooperative entities for the PtMeOH plant, storage facilities, and renewable power generation plants, on the optimal process design and objective function could be investigated.

Concerning the optimization of PtMeOH processes under scenario uncertainty, we have shown that several process designs can lead to similar objectives when scheduling is optimized with perfect information on the scenario time steps. Following from this observation, two key extensions of this work could be foreseen: 1) assessing how the optimal process design is affected when the process scheduling is optimized with no perfect information on the scenario set and time series, and 2) identifying an optimal process design space instead of a single optimal process design. Moreover, the identification of a design space could be particularly valuable as it allows checking whether commercially available modular process units (with a similar investment cost compared to the cost used in the optimization problems) can be employed instead of custom process units without significantly affecting the production costs.

Concerning the investigated numerical complexity approaches for S-CDS problems (Section 5.3), i.e., feature-based scenario clustering and selective DoF reduction, further work could explore the use of different features, as well as their application to other case studies. Also, as the reduced S-CDS problems could approximate the original S-CDS problem quite well and identify promising process designs for the considered case study, they could potentially be embedded in an optimal design algorithm: the reduced S-CDS problems can be solved to identify candidate process designs that are then assessed by solving a stochastic scheduling problem in the original scenario and DoF spaces. Nonetheless, the effectiveness of these approaches, especially DoF reduction, should be further investigated, e.g., with different solvers and case studies. In fact, the investigated numerical complexity approaches were not always leading to improved computational performance despite the significantly smaller size of the optimization problems.

Declaration of use of generative AI and AI-assisted technologies

During the preparation of some chapters of this dissertation, I used generative AI tools, namely ChatGPT and RWTHgpt. In particular, they were used in the thesis' Summary, Chapters 1, 5, and 6, and Appendices A and C in order to improve the readability and language of the text.

The text, code, and images in this thesis are my own (unless otherwise specified).

Generative AI tools have only been used in accordance with the guidelines of RWTH Aachen University and KU Leuven.

After using these tools, I have reviewed and edited the content as needed, and I take full responsibility for the content of this dissertation.

Appendix A.

Additional Information to Chapter 3

A.1. Molar balances

In Table A.1, the reactions considered in each process unit for the back-of-the-envelope analysis are collected. As regards the synthesis units, multiple reactions are listed according to the inlet stream (CO_2 – H_2 or CO – H_2 mixture) and the target product, i.e., alkane (C_nH_{2n+2}) and alcohol or ether ($C_nH_{2n+2}O$).

From the reaction stoichiometry, it can be noticed that gasification-based processes require a significantly lower amount of hydrogen than combustion-based ones (compare "Synthesis unit" in Table A.1). This difference has a major impact on the overall electricity demand of the PBtX processes as well as on their efficiency, as shown in Section 3.6.

Table A.1.: Complete set of reactions for the considered process units.

Combustion unit		
$C_xH_yO_zN_wS_t + \left(x + \frac{y}{4} + t - \frac{z}{2}\right) O_2$	$\rightarrow$	$xCO_2 + \frac{y}{2}H_2O + \frac{w}{2}N_2 + tSO_2$
Oxy-gasification unit		
$C_xH_yO_zN_wS_t + \left(\frac{x}{2} + t - \frac{z}{2}\right) O_2$	$\rightarrow$	$xCO + \frac{y}{2}H_2 + \frac{w}{2}N_2 + tSO_2$
Steam-gasification unit		
$C_xH_yO_zN_wS_t + (x + 2t - z)\, H_2O$	$\rightarrow$	$xCO + \left(\frac{y}{2} + x + 2t - z\right) H_2 + \frac{w}{2}N_2 + tSO_2$
Electrolysis unit		
H_2O	$\rightarrow$	$H_2 + \frac{1}{2}\, O_2$
Synthesis unit with a CO_2 – H_2 mixture		
n CO_2 + (3n + 1) H_2	$\rightarrow$	C_nH_{2n+2} + 2n H_2O
n CO_2 + 3n H_2	$\rightarrow$	$C_nH_{2n+2}O$ + (2n - 1) H_2O
Synthesis unit with a CO – H_2 mixture		
n CO + (2n + 1) H_2	$\rightarrow$	C_nH_{2n+2} + n H_2O
n CO + 2n H_2	$\rightarrow$	$C_nH_{2n+2}O$ + (n - 1) H_2O

We refer to Figures S1-S4 in the Supporting Information of Mucci et al. [2] for the visualization of the molar flow rates for the considered PBtX processes when woody biomass is used as carbon feedstock.

A.2. Energy balances

The steady-state energy balances are written for each process unit by neglecting the kinetic and potential energy contributions, and heat losses. Except for the power cycle and the synthesis unit, no work exchange for either compression or expansion is considered.

The material streams at the interfaces of each unit are assumed at ambient conditions (T_0=298 K, P_0=1 bar). Also, we assume ideal heat integration between the inlet and outlet streams (Figure A.1), thus making the whole reaction heat available at the typical reaction temperature of all process units, except for the biomass combustion one. In the latter case, the reactants are heated up to the typical reaction temperature through the energy release of the oxidation reactions, and the product stream supplies heat to the power cycle, while cooling down to ambient temperature. This unit model better represents a real combustion unit and avoids overestimating the exergy flow (Subsection A.4.1).

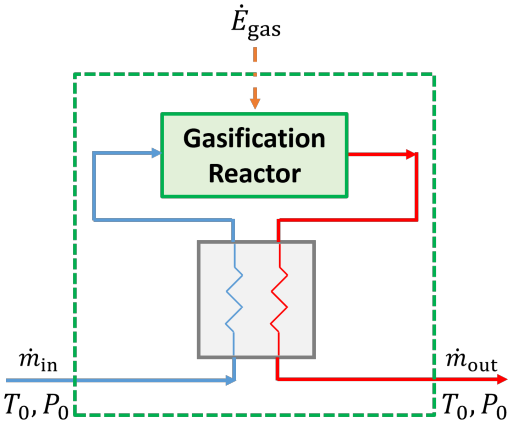


Figure A.1.: Heat integration for the (endothermic) gasification unit, contained in the dashed green line, is shown. Similar heat integration was considered for the electrolysis and synthesis units.

The assumption of perfect heat integration is acceptable for oxygen-based gasification since the streams have similar heat capacities, and for steam gasification if an additional heat source is considered to generate steam, as done in this work. For water electrolysis, the heat capacity of the inlet and outlet streams differ significantly when considering ideal reaction conversion (no excess of water as opposed to what occurs in real applications). However, the energy needed to preheat the inlet stream is significantly lower ($< 1\%$) than the energy needed to drive the electrolysis; therefore, this energy demand is neglected. For the synthesis unit, the change of phase of some products and by-products during the cooling makes heat integration technically (and thermodynamically) challenging. This aspect is considered in the exergy balance (Subsection A.4.3).

Finally, no energy demand for product separation is considered. This assumption is acceptable when separating a gaseous product from water, while it is weaker for liquid products like methanol. Nevertheless, the separation process is analogous in the combustion-based and gasification-based processes, apart from the product concentration (higher in the gasification-based process). This means that these processes can still be compared to each other concerning the exergy efficiency, but the calculated values represent upper limits.

A.3. Modeling assumption overview

Table A.2.: Overview of the key technical assumptions for the model of the PBtX process units.

Unit	Molar balance	Energy balance
Combustion	- dry ash-free biomass feedstock - ideal reaction conversion (100 %) - stoichiometric oxidant-to-fuel ratio - no side product formation - see Table A.1 for reactions	- no energy demand for biomass pretreatment - operating temperature: 1000 °C - cold product gas recycle for combustion temperature control - combustion heat is provided to the power cycle - no heat losses - no energy demand for flue gas cleaning and CO_2 separation
Gasification	- dry ash-free biomass feedstock - ideal reaction conversion (100 %) - stoichiometric oxidant-to-fuel ratio - no side product formation - see Table A.1 for reactions	- no energy demand for biomass pretreatment - operating temperature: 900 °C - perfect heat integration between reactants and products - if endothermic (typical operating condition), electric heating is considered - if exothermic, it is modeled as the combustion unit except for the operating temperature - no heat losses - no energy demand for flue gas cleaning and CO-H_2 separation
Electrolysis	- ideal reaction conversion (100 %) - see Table A.1 for reactions	- operating temperature: 60 °C - perfect heat integration between reactants and products - energy efficiency: 60 % - low-temperature heat is not recovered
Synthesis	- ideal reaction conversion (100 %) - stoichiometric feed stream - no side product formation - see Table A.1 for reactions	- product-dependent product synthesis temperature and pressure - energy demand for reactant compression is considered - perfect heat integration between reactants and products - low-temperature heat from the synthesis reactor is provided to the power cycle - no energy demand for product separation
Power cycle		- power cycle efficiency for low-temperature heat: 30 % - power cycle efficiency for high-temperature heat: 40 %

A.4. Exergy analysis

In the following, we provide additional information about how the exergy related to heat flows and material streams is calculated.

A.4.1. Exergy related to heat flows

For the back-of-the-envelope analysis, the calculation of the exergy related to heat flows ($\dot{\varepsilon}_{\mathrm{q}}$) is tailored to the models of the process units. In the following, details on the exergy calculation are provided for each unit.

The exergy flow is calculated under the assumption of ideal gases as follows:

$$\dot{\varepsilon}_{\mathrm{q}} = \dot{Q} \cdot \left(1 - \frac{T_0}{T_{\mathrm{m}}}\right),$$

where $\dot{Q}$ is the available heat, and T_0 and T_{m} are the ambient and thermodynamic mean temperatures.

For the combustion unit, the exhaust gases are cooled from the combustion temperature to the ambient temperature. Thus, T_{m} is equal to the logarithmic mean between these two temperatures. For the endothermic gasification unit, the exergy related to the heat transfer is assumed equal to the energy demand for gasification (it is assumed to be provided via electricity). In contrast, for the exothermic gasification unit, the whole enthalpy of reaction is considered available and exchanged at the typical reaction temperature (T_{m}). This implies the assumption of heat integration within the unit (Figure A.1) as mentioned in Appendix A.2. The exergy related to the heat transfer of the electrolysis unit is calculated similarly to the exothermic gasification unit.

For the synthesis unit, the above-mentioned approximations would not be acceptable since the product stream changes phase partially or totally while cooling. Considering the whole enthalpy of reaction available at the reaction temperature would significantly overestimate the exergy value, since the phase transition occurs at a temperature lower than the synthesis temperature. Therefore, the exergy associated with this heat transfer was calculated as the sum of three contributions, i.e., the exergy change for heating the reactants ($\dot{\varepsilon}_{\mathrm{q,\,heating}}$), the exergy related to the heat transfer at the reaction temperature ($\dot{\varepsilon}_{\mathrm{q,\,reactor}}$), and the exergy change for cooling the products ($\dot{\varepsilon}_{\mathrm{q,\,cooling}}$):

$$\dot{\varepsilon}_{\mathrm{q}} = \dot{\varepsilon}_{\mathrm{q,\,cooling}} + \dot{\varepsilon}_{\mathrm{q,\,reactor}} - \dot{\varepsilon}_{\mathrm{q,\,heating}}.$$

$\dot{\varepsilon}_{\mathrm{q,\,heating}}$ and $\dot{\varepsilon}_{\mathrm{q,\,cooling}}$ are calculated as the difference of the physical exergy at the ambient and synthesis temperatures, while $\dot{\varepsilon}_{\mathrm{q,\,reactor}}$ is calculated as in the gasification unit by considering the real amount of heat available at the reaction temperature. This data is obtained from the Aspen Plus database.

In the case the electricity generated via the power cycle, which is calculated by multiplying the reaction heat by the power cycle efficiency, is higher than the available exergy associated with the heat flows, the generated electricity is assumed equal to the available thermal exergy stream.

For the detailed PBtMeOH and PBtK models, the exergy related to heat flows, except for the heat flow from the electrolysis unit, is calculated by considering the variation of stream physical exergy (see Appendix A.4.2).

A.4.2. Molar physical exergy

For the detailed PBtMeOH and PBtK models, the physical exergy contribution (e_{ph}) is calculated by taking enthalpy (h) and entropy (s) values from Aspen Plus as shown below:

$$e_{\mathrm{ph}} = (h - h_0) - T_0 \cdot (s - s_0)\,.$$

A.4.3. Molar chemical exergy

The chemical exergy of the material streams is calculated with respect to a reference environment [370]. For the molecules in the reference environment, the molar chemical exergy for a pure component k ($e_{\mathrm{ch},k}$) can be calculated with the following equation:

$$e_{\mathrm{ch},k} = \frac{RT_0}{\mathrm{MW}_k} \cdot \ln\left(\frac{P_0}{P_{0,k}}\right).$$

For other substances such as fuels, the molar chemical exergy value is often found in tables [370] or calculated as a function of the LHV:

$$e_{\mathrm{ch},k} = \phi_k \cdot \mathrm{LHV}_k \cdot \mathrm{MW}_k.$$

As the molar chemical exergy values are known for all the considered gaseous and liquid fuels (Table A.3), the factor ϕ is used for biomass and mixtures of liquid hydrocarbons (assumed equal to 1.15, the lowest value in the range suggested by Kotas [370], and 1.06, respectively).

Table A.3.: Considered molar chemical exergy and LHV at 25 °C and 1 bar.

	e_{ch}* kJ mol^{-1}	LHV** MJ kg^{-1}
H_2O(l)	3.1	-
O_2	4.0	-
CO_2	20.1	-
H_2	238.5	120.0
CO	275.4	10.1
CH_4	836.5	50.0
CH_3OH	722.6***	19.9
CH_3OCH_3	1426.4	28.8
$C_{12}H_{26}$	8059.3	44.1
C_4H_8	2668.9	19.8
$C_{12}H_{24}$	7902.0***	44.0

* Kotas [370] unless specified.
** Aspen Plus database.
*** Calculated from the formation reaction.

The molar exergy of mixtures can be calculated as follows:

$$e_{\mathrm{ch}} = \sum_{k=1}^{N} x_k \cdot e_{\mathrm{ch},k} + RT_0 \sum_{k=1}^{N} x_k \cdot \ln(x_k).$$

However, the second term is neglected since it has a significantly lower value compared to the contribution of the sum of the molar exergy of the components (< 1 % for a 1:1 H_2O-CH_3OH mixture). Similarly, the minimum exergy demand for separation of the components of the mixture, which can be calculated via the above-mentioned equation, is neglected.

A.5. Additional results of the back-of-the-envelope analysis

In the following subsections, additional results about the energy and exergy analysis are presented.

A.5.1. Energy analysis

The energy efficiency of the considered PBtX processes is shown in Figure A.2. The ranking among the considered PBtX pathways with respect to the energy efficiency is analogous to the one shown for the exergy efficiency (Figure 3.8). However, the energy and exergy efficiency values slightly differ due to the different ways of calculating the energy and exergy content of the reactants and products.

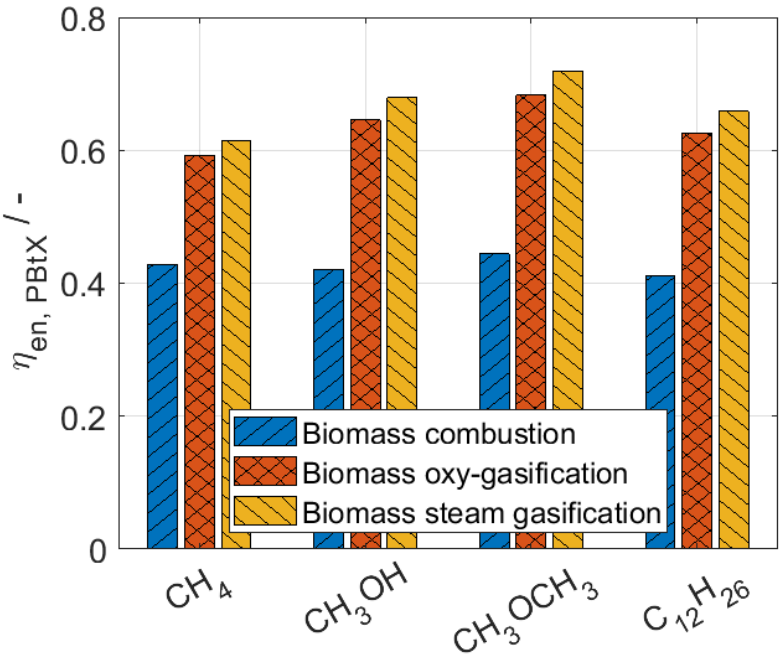
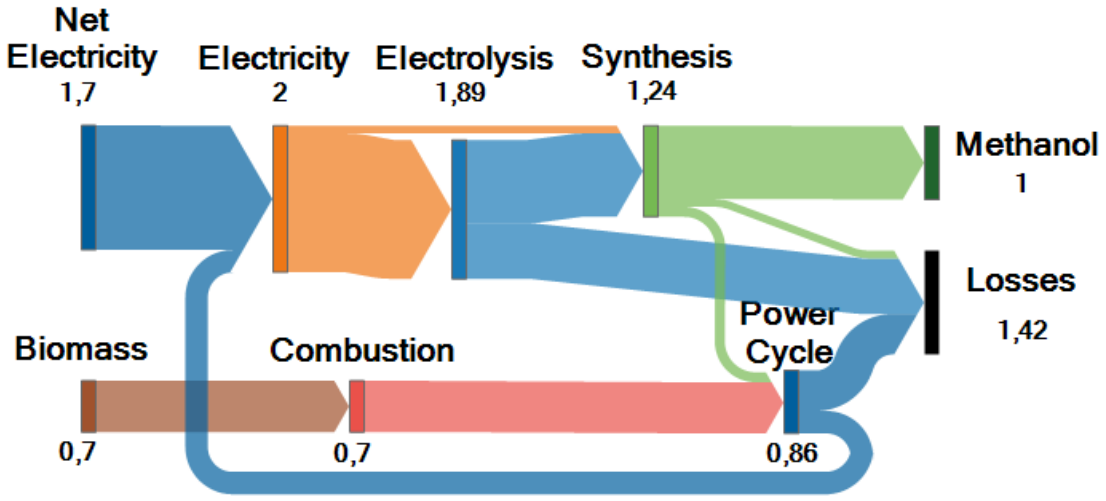
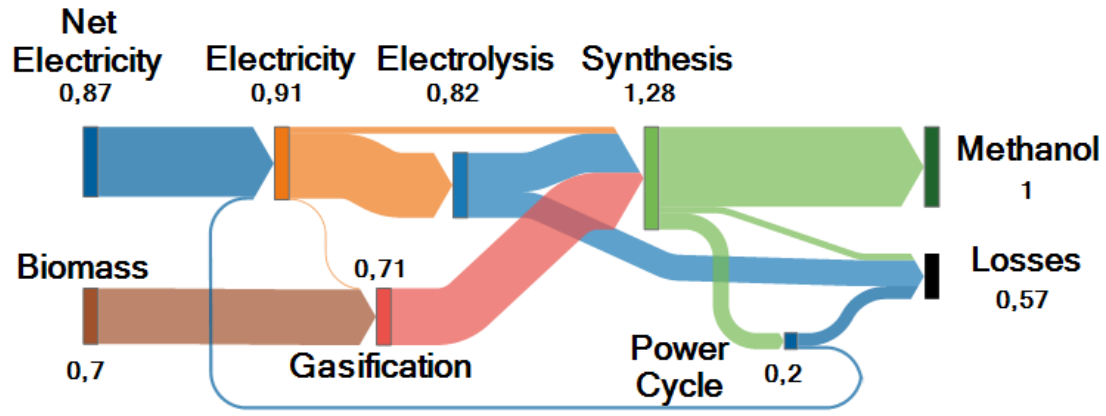


Figure A.2.: Energy efficiency of Power- and Biomass-to-X processes with biomass combustion and gasification for different products "X". Woody biomass is considered as carbon feedstock [237].

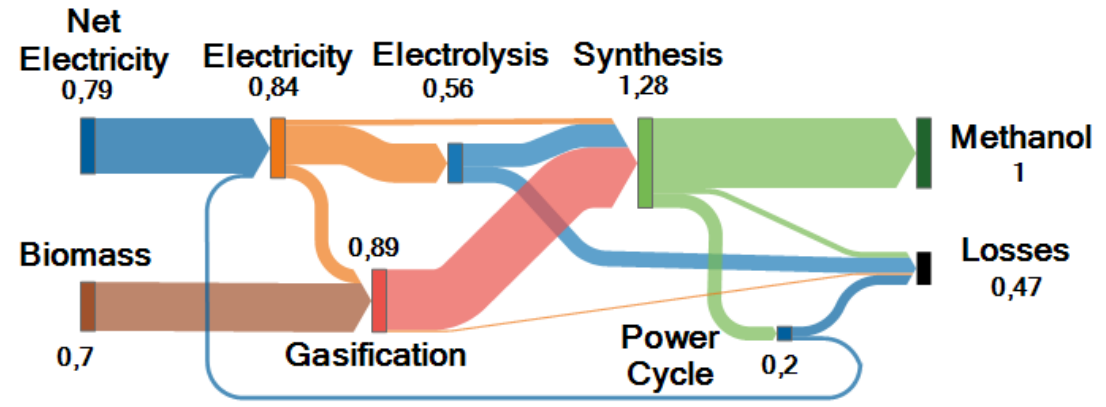
Figure A.3 shows the Sankey diagrams of the energy flows for the considered PBtMeOH process when woody biomass is used as carbon feedstock. We refer to the Supporting Information of Mucci et al. [2] for the other products.



(a) PBtMeOH process with biomass combustion.



(b) PBtMeOH process with biomass oxy-gasification.



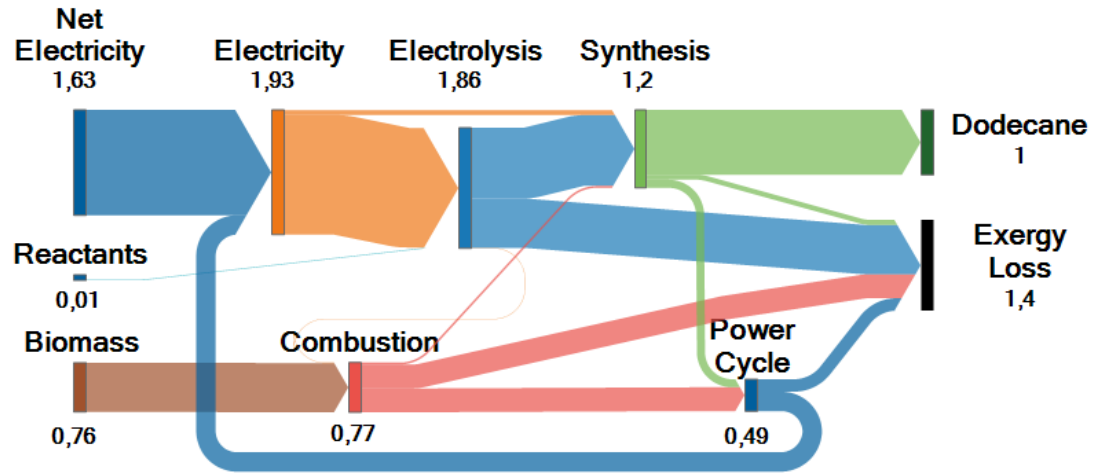
(c) PBtMeOH process with biomass steam-gasification.

Figure A.3.: Sankey diagrams of the energy flows for the Power- and Biomass-to-Methanol (PBtMeOH) process with (a) biomass combustion, (b) biomass oxy-gasification, and (c) biomass steam-gasification. The energy flows in MW are scaled per unit of product and are based on the LHV of the components. The numbers at the diagram nodes represent the energy flows of the energy sources and the total energy flows through the process units.

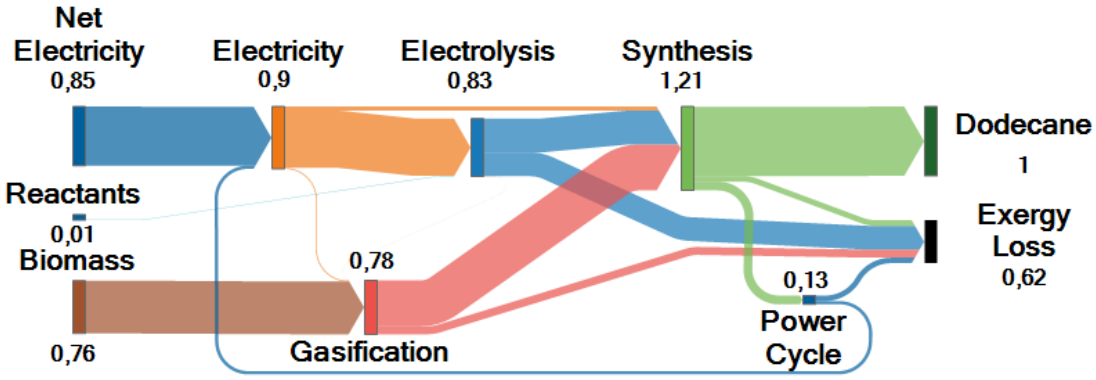
As shown in Figure A.3, the electrolysis and power cycle units are the main contributors to the energy losses, which are hereby intended as the amount of energy that is not stored in the process unit product. Further, the biomass conversion units have high energy efficiency in contrast to what was shown via the exergy analysis (see Section 3.6). This result can be explained by the fact that the energy analysis does not consider the quality of the energy flows differently from the exergy analysis. In fact, the biomass conversion units significantly contribute to energy quality degradation (despite their high energy efficiency); in contrast, the power cycle units play a minor role in energy quality degradation since their energy input already has a relatively low quality.

A.5.2. Exergy analysis

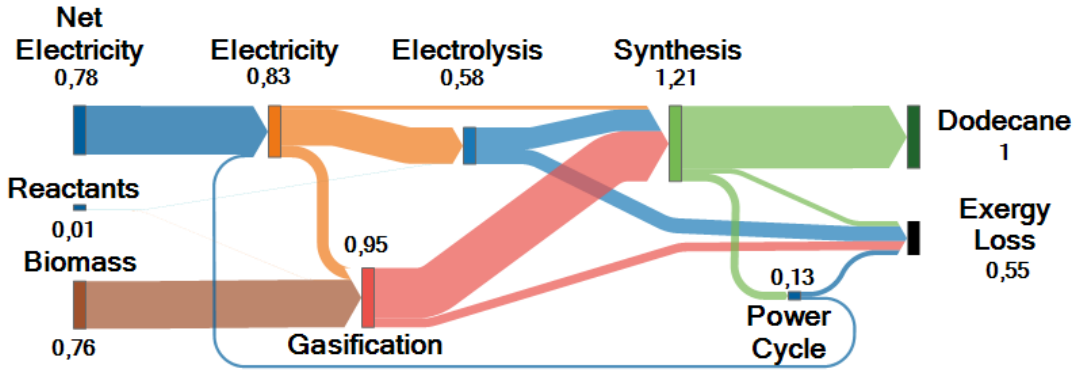
The Sankey diagrams of the exergy flows for dodecane production are shown in Figure A.4. We refer to the Supporting Information of Mucci et al. [2] for the products methane and DME.



(a) Power- and Biomass-to-Dodecane process with biomass combustion.



(b) Power- and Biomass-to-Dodecane process with biomass oxy-gasification.



(c) Power- and Biomass-to-Dodecane process with biomass steam-gasification.

Figure A.4.: Sankey diagrams of the exergy flows for the Power- and Biomass-to-Dodecane process with (a) biomass combustion, (b) biomass oxy-gasification, and (c) biomass steam-gasification. The exergy flows in MW are scaled per unit of product. The numbers at the diagram nodes represent the exergy flows of the energy sources and the total exergy flows through the process units.

A.6. Additional results of the sensitivity analyses

In this section, additional results concerning the conducted sensitivity analyses are presented.

A.6.1. Electrolyzer efficiency

The effect of the efficiency of the electrolyzer on the overall PBtX efficiency ($\eta_{\mathrm{ex,\,PBtX}}$) is shown in Table A.4. Note that an electrolyzer efficiency of 60 % was considered for generating the results in Subsection 3.6.1.

Table A.4.: Exergy efficiency of the Power- and Biomass-to-X processes with biomass combustion and gasification for the considered products (values in %). Sensitivity analysis with respect to the electrolyzer efficiency (based on the LHV). Woody biomass was considered as carbon feedstock [237].

Product	Electrolyzer efficiency	$\eta_{\mathrm{ex,\,PBtX}}$ (combustion)	$\eta_{\mathrm{ex,\,PBtX}}$ (O_2-gasification)	$\eta_{\mathrm{ex,\,PBtX}}$ (H_2O-gasification)
CH_4	60	43	59	61
CH_4	80	54	70	71
CH_3OH	60	46	68	72
CH_3OH	80	56	78	79
CH_3OCH_3	60	46	69	72
CH_3OCH_3	80	57	78	79
$C_{12}H_{26}$	60	42	63	66
$C_{12}H_{26}$	80	52	72	73

A.6.2. Power cycle efficiency

The results of the sensitivity analysis with respect to the efficiency of the power cycle unit are shown in Table A.5. In particular, three cases are evaluated:

- The "30 % & 20 %" case, where 30 % and 20 % of the high and low-temperature heat are converted into electricity, respectively.
- The "40 % & 30 %" case (base case), where 40 % and 30 % of the high- and low-temperature heat are converted into electricity, respectively.
- The "Carnot" case, where the maximum amount of electricity is produced from the residual high-temperature and medium-temperature heat without any exergy loss. A Carnot efficiency ranging from 47 % to 56 % is considered depending on the heat source temperature. Heat recovery from the electrolysis unit is also considered differently from all the other cases. The corresponding Carnot efficiency is ca. 12 %.

Table A.5.: Exergy efficiency of the Power- and Biomass-to-X processes with biomass combustion and gasification for the considered products (values in %). Sensitivity analysis with respect to the power cycle efficiency. Woody biomass was considered as carbon feedstock [237].

Product	Power cycle efficiency	$\eta_{ex,\,PBtX}$ (combustion)	$\eta_{ex,\,PBtX}$ (O_2-gasification)	$\eta_{ex,\,PBtX}$ (H_2O-gasification)
CH_4	30 % & 20 %	42	58	60
CH_4	40 % & 30 %	43	59	61
CH_4	Carnot	48	63	65
CH_3OH	30 % & 20 %	44	67	71
CH_3OH	40 % & 30 %	46	68	72
CH_3OH	Carnot	50	70	74
CH_3OCH_3	30 % & 20 %	44	68	71
CH_3OCH_3	40 % & 30 %	46	69	72
CH_3OCH_3	Carnot	50	72	75
$C_{12}H_{26}$	30 % & 20 %	41	62	65
$C_{12}H_{26}$	40 % & 30 %	42	63	66
$C_{12}H_{26}$	Carnot	47	66	69

A.6.3. Carbon feedstock composition

In the following paragraphs, we present the results of the sensitivity analysis concerning the carbon feedstock composition. In particular, we first analyze key efficiency trends by varying the biomass carbon and hydrogen composition, and then evaluate the process efficiencies for real feedstock compositions.

"Artificial" carbon feedstocks

Figure A.5 shows the variation of the energy demand for gasification with respect to the feedstock composition. Steam-based gasification has a significantly higher energy demand for gasification, as already discussed in Subsection 3.3.1.3. Also, the exergy efficiency of the gasification-based PBtMeOH process is higher when the gasification process is endothermic, despite the higher energy input (recall Figure 3.10).

The energy demand for gasification ($\dot{E}_{gas}$) estimated with the relatively simple models can differ from the one of real gasification processes due to nonidealities and practical operating conditions, e.g., residual moisture in biomass feedstocks, the oxidizing agent supplied in excess, and lack of perfect heat integration between the reactant and product streams. For instance, the energy demand for gasification increases significantly when assuming no heat integration within the gasification unit since the reactant stream has to be heated up to the reaction temperature (compare Figures A.5 and A.6). This additional energy demand reduces the efficiency of gasification-based PBtX processes. Nevertheless, the efficiency is higher than combustion-based processes. Furthermore, the efficiency reduction between the gasification-based PBtX processes with and without heat integration would be even higher in the case of gasification with air as gasifying agent due to the large amount of inert gases, e.g., nitrogen, that has to be heated.

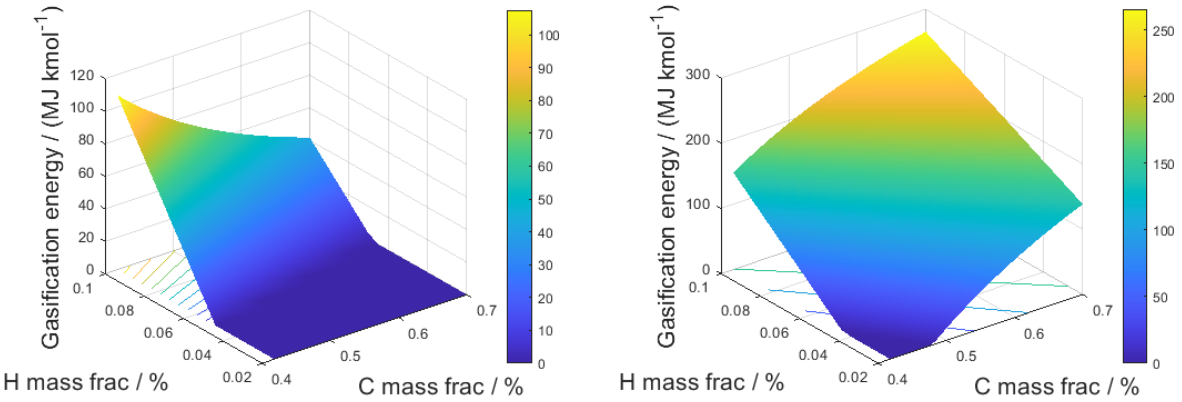


Figure A.5.: Sensitivity analysis of the heat demand for gasification of the Power- and Biomass-to-Methanol process with respect to the feedstock composition using oxygen (left) and steam (right) as gasifying agents. The considered mass fractions of S and N are equal to 0.001 and 0.004, respectively (values for woody biomass). In contrast, the mass fractions of C and H are varied, while the oxygen content is calculated by difference. When the energy demand for gasification is equal to 0, the gasification process is exothermic.

"Real" carbon feedstocks

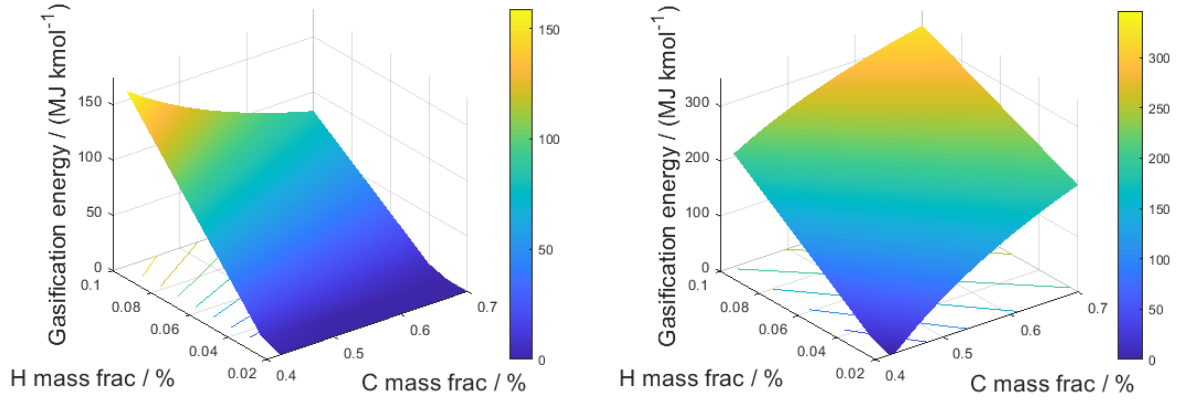
In these paragraphs, we investigate several carbon feedstocks, ranging from biomass and biogas to municipal solid waste (Table A.6), under the assumptions of dry and ash-free feedstocks. The LHV of the feedstocks is calculated according to the correlations proposed by Sheng and Azevedo [238] and Boumanchar et al. [265] for the biomass-related and waste-related feedstocks, respectively. The LHV of biogas is instead calculated by assuming a molar composition of 60 % CH_4 and 40 % CO_2. Finally, the considered ϕ factors for the chemical exergy calculation (see Appendix A.4.3) are 1.15 and 1.02 for biomass-related and biogas feedstocks, respectively [370]. The ϕ factor of waste-related feedstock is assumed equal to the ϕ factor of biomass (1.15).

Table A.6.: Ash-free dry composition of the carbon feedstock in wt.% (ultimate analysis).

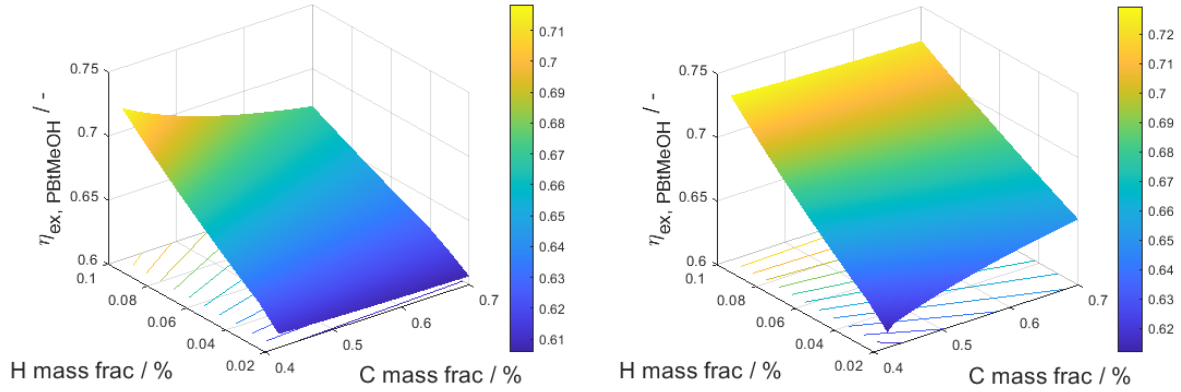
	x_C	x_O	x_H	x_N	x_S	Source
Woody biomass (mean)	52.1	41.2	6.2	0.4	0.1*	[237]
Herbaceous and agricultural biomass (mean)	49.9	42.6	6.2	1.2	0.1*	[237]
Mixture of biomass (mean)	52.9	39.6	6.2	1.0	0.3*	[237]
Marine macroalgae	43.2	45.8	6.2	2.2	2.6	[237]
Biogas (60-40 %mol. CH_4-CO_2)	44.2	47.0	8.8	0	0	-
Paper (mean)	43.4	50.2	5.9	0.4	0.1*	[265]
Plastics and rubber (mean)	71.9	17.7	9.2	0.8	0.4*	[265]
Solid waste incinerator (mean)	29.7	65.5	3.8	0.7	0.3*	[265]

* Adapted or rounded.

As already observed in the sensitivity analysis of the carbon feedstock (Section 3.6.2.3), the exergy efficiency of gasification-based processes is more affected by the carbon feedstock



(a) Heat demand for gasification of the gasification-based PBtMeOH processes using oxygen (left) and steam (right) as gasifying agents when no heat integration is considered in the gasification unit.



(b) Exergy efficiency of the gasification-based PBtMeOH processes using oxygen (left) and steam (right) as gasifying agents when no heat integration is considered in the gasification unit.

Figure A.6.: Sensitivity analysis of the heat demand for gasification of the Power- and Biomass-to-Methanol process with respect to the feedstock composition in the case heat integration within the gasification unit is not performed (Figure (a)). The considered mass fractions of S and N are equal to 0.001 and 0.004, respectively (values for woody biomass). In contrast, the mass fractions of C and H are varied, while the oxygen content is calculated by difference. When the energy demand for gasification is equal to 0, the gasification process is exothermic. The process exergy efficiency is shown in Figure (b) to ease interpretation.

composition than the exergy efficiency of combustion-based processes (Table A.7). Also, the effect of feedstock variations on the process efficiency is higher when the H:C ratio of the product is low. Nevertheless, gasification-based PBtX processes are always more efficient under the model assumptions, irrespective of the feedstock composition.

Among the considered feedstocks, biogas results being the best alternative. This is mainly due to the significantly lower ϕ factor compared to biomass. However, the direct comparison with the other feedstocks is not completely fair, since biogas is obtained from biomass via anaerobic digestion, and this conversion process is not included in the efficiency calculation. Nevertheless, its use would also have advantages in real plants since the pre-processing of the biogenic feedstock avoids ashes and pollutants in its conversion process

Table A.7.: Exergy efficiency of the Power- and Biomass-to-X processes with biomass combustion and gasification for the considered products (values in %). Sensitivity analysis with respect to the feedstock composition (Table A.6).

Product	Feedstock	$\eta_{ex,\,PBtX}$ (combustion)	$\eta_{ex,\,PBtX}$ (O_2-gasification)	$\eta_{ex,\,PBtX}$ (H_2O-gasification)
CH_4	Woody biomass	43	59	61
CH_4	Herbaceous and agricultural biomass	43	59	61
CH_4	Mixture of biomass	43	59	61
CH_4	Marine macroalgae	43	60	61
CH_4	Biogas	44 #	65 *#	66 *#
CH_4	Paper	44	60	60
CH_4	Plastics and rubber	42	57	63
CH_4	Solid waste incinerator	44	§	§
CH_3OH	Woody biomass	46	68	72
CH_3OH	Herbaceous and agricultural biomass	45	69	72
CH_3OH	Mixture of biomass	46	68	72
CH_3OH	Marine macroalgae	45	70	72
CH_3OH	Biogas	47	79 *	81 *
CH_3OH	Paper	46	70	71
CH_3OH	Plastics and rubber	44	66	75
CH_3OH	Solid waste incinerator	47	§	§
CH_3OCH_3	Woody biomass	46	69	72
CH_3OCH_3	Herbaceous and agricultural biomass	46	69	72
CH_3OCH_3	Mixture of biomass	46	68	72
CH_3OCH_3	Marine macroalgae	45	70	72
CH_3OCH_3	Biogas	47	79 *	81 *
CH_3OCH_3	Paper	46	70	71
CH_3OCH_3	Plastics and rubber	44	66	76
CH_3OCH_3	Solid waste incinerator	47	§	§
$C_{12}H_{26}$	Woody biomass	42	63	66
$C_{12}H_{26}$	Herbaceous and agricultural biomass	42	63	66
$C_{12}H_{26}$	Mixture of biomass	42	63	66
$C_{12}H_{26}$	Marine macroalgae	42	64	66
$C_{12}H_{26}$	Biogas	44	73 *	74 *
$C_{12}H_{26}$	Paper	43	64	65
$C_{12}H_{26}$	Plastics and rubber	41	61	69
$C_{12}H_{26}$	Solid waste incinerator	44	§	§

Biogas upgrading would be more efficient for the production of methane.
* Biogas is reformed instead of gasified.
§ Too high oxygen content for the considered model of gasification.

to valuable chemicals: biogas combustion or reforming instead of biomass combustion or gasification can be used to produce either CO_2 or syngas, thus reducing the effort for solid handling in the conversion process.

Apart from biogas, marine macroalgae are the most promising biomass-related feedstock for gasification with respect to the calculated exergy efficiencies. However, the high concentration of sulfur might be problematic in real applications. Paper waste and plastics and rubber waste are the most efficient waste-related feedstocks for oxygen-based and steam-based gasification. However, the gasification of waste, especially plastic waste, does not have a high technological readiness level yet [371].

Finally, as already mentioned in Section 3.6.3, other practical aspects related to biomass handling and conversion could make these feedstocks not suitable for efficient or direct use in PBtX processes.

A.7. Detailed model of the Power- and Biomass-to-Methanol processes

In the following, the PBtMeOH processes modeled in Aspen Plus ® V11 are described. The thermodynamic models NRTL and PSRK are used for low-pressure and high-pressure process units, respectively.

A.7.1. Combustion-based Power- and Biomass-to-Methanol process

A woody biomass stream (composition in Table 3.1) with 10 wt.% moisture is considered as biogenic feedstock for the PBtMeOH process.

As shown in the simplified process flow diagram in Figure A.7, biomass is preheated to ca. 175 °C by recycling part of the hot flue gases (ca. 85 %) before being combusted with a stoichiometric amount of oxygen produced by the electrolyzer. The large flue gas recycle allows maintaining the outlet temperature of the biomass oxy-combustor [372] (modeled with an RGibbs reactor) at ca. 1000 °C. The choice of recycling flue gas rather than feeding excess oxygen (or air) eliminates the need for a carbon capture unit since the flue gas stream is mainly composed of H_2O and CO_2.

A quite pure CO_2 stream can be obtained from the flue gas via water condensation (Figure A.7). The other side products of the combustion unit (mainly ashes and SO_x if the combustion occurs at proper operating conditions) are considered to be fully removed in the flue gas treatment section. In particular, ashes are removed via a cyclone and a bag filter [373] (a pressure loss of ca. 0.1 bar is accounted for), while the sulfur compounds are removed in situ, e.g., by using limestone in the fluidized bed and via wet scrubbing [373], which can achieve high removal efficiencies [374]. These units are modeled in Aspen Plus with a separator block. In contrast, the formation of NO_x is neglected since the concentration of N_2 in the combustion chamber is low (oxy-combustion) and the combustion temperature is relatively low [373]. Thus, the considered model of the flue gas cleaning treatment represents one of the most favorable cases. Additional flue gas cleaning steps, as well as the corresponding energy demand, would be needed if the impurity concentrations exceed the tolerance threshold of the catalyst of the downstream conversion process.

The heat from the flue gases with a temperature higher than 100 °C is recovered and converted into electricity in a power cycle with an efficiency of 40 % (as in Subsection 3.3.4). In contrast, the residual heat that is removed to condense the water in the flue gases is considered wasted.

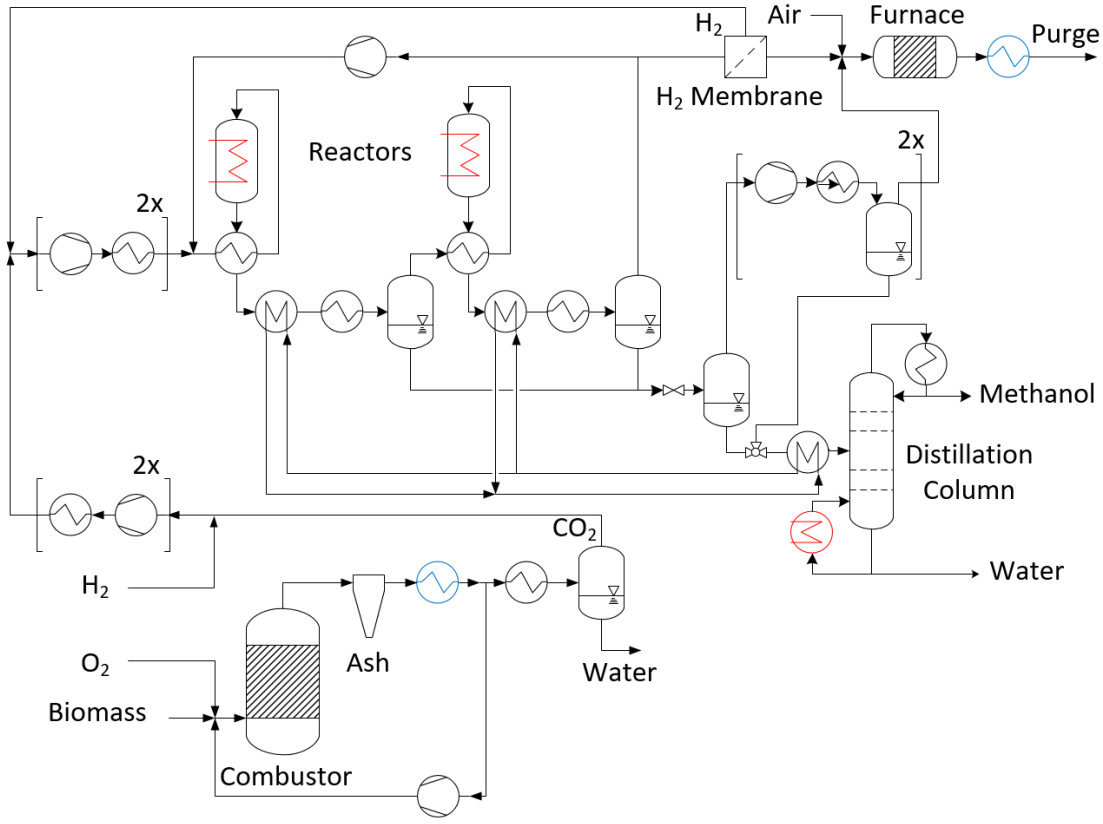


Figure A.7.: Simplified process flow diagram of the modeled combustion-based Power- and Biomass-to-Methanol process. Note: the electrolysis unit and the power cycle are not represented in the sketch since they were not modeled in Aspen Plus. Also, heat integration between the methanol synthesis reactors and the reboiler of the distillation column is not explicitly shown in the sketch for simplicity (the corresponding heat exchangers are marked in red). The heat exchangers in the biomass conversion and furnace units, where heat is removed and supplied to the power cycle, are marked in blue to ease identification.

The CO_2 stream from the biomass conversion unit is then mixed with a stoichiometric stream of hydrogen produced in a water electrolyzer with an efficiency of 60 % (as in Subsection 3.3.2). The CO_2-H_2 mixture is pressurized to 75 bar and preheated via heat integration before being supplied to the methanol production section.

The methanol synthesis is modeled by using two water-cooled RPLUG reactors operated at ca. 250 °C with intermediate removal of the product (crude methanol) from the unreacted gases via condensation in a flash unit (Figure A.7). The operating pressure of the reactor unit is around 75 bar, and a 1 bar pressure drop was assumed for each reactor. A commercial catalyst $Cu/ZnO/Al_2O_3$ is considered for the implemented reactor kinetic model Langmuir-Hinshelwood-Hougen-Watson (LHHW) [196, 375]. The choice of having two reactors is motivated by the low conversion per pass. The intermediate removal of products via condensation helps shift the chemical equilibrium.

After the second reactor, the unreacted gases are separated from crude methanol, the mixture of water and methanol, via condensation and partially (98 %) recycled back to the methanol synthesis unit. The remaining high-pressure stream of unreacted gases is fed into a membrane unit (modeled via a shortcut model) to recover ca. 90 % of hydrogen, which is then recycled into the synthesis unit.

Crude methanol is then purified via distillation (RADFRAC unit) to meet the desired purity specification, i.e., 99.5 wt.%. Heat for the reboiler can be supplied via heat integration. In particular, the surplus heat of the methanol reactor and the heat from the purge stream combustion are sufficient to satisfy its thermal demand under the considered modeling assumptions. The heat integration between the methanol reactors and the distillation column is not explicitly shown in the flowsheet in Figure A.7, though it is considered for the calculation of the heat and cooling demands. The remaining heat from the methanol synthesis reactors is recovered and converted into electricity in a power cycle with an efficiency of 30 % (as in Subsection 3.3.4).

The low-pressure stream resulting from the methanol purification unit is compressed to recover additional methanol, which is supplied to the distillation column (Figure A.7).

The remaining low-pressure and high-pressure gaseous streams are then combusted with air in a furnace, and the resulting heat is recovered and supplied to the power cycle (Figure A.7).

A.7.2. Gasification-based Power- and Biomass-to-Methanol process

Analogously to the combustion-based PBtMeOH process, a woody biomass stream with 10 wt.% moisture is considered as biogenic feedstock.

Oxygen from the electrolysis unit is the main gasifying agent for the biomass conversion unit. Nevertheless, a mixed oxygen-steam biomass gasifier is modeled with an RGibbs reactor since a significant amount of water is present in the biomass stream. In the gasification model, a biomass conversion factor of 95 % [210] is considered to account for incomplete biomass conversion due to the scarcity of the oxidizing agent.

To reduce the heat demand for operating the gasifier at ca. 900 °C, the feed stream is preheated to ca. 450 °C via internal heat integration (Figure A.8). The gasifier is operated in an auto-thermal configuration [210, 267], thus meaning that the heat demand for gasification is satisfied by supplying oxygen in excess compared to the stoichiometric amount (see Table A.1): on the one hand, the need for an external high-temperature heat source is avoided; on the other hand, the combustion reaction is promoted and CO_2 is produced. Alternatively to the auto-thermal gasifier configuration, electricity heating or biomass and purge stream combustion could have been considered to satisfy the energy demand, perhaps also improving the economic competitiveness of the gasification-based process. However, investigating different heating options was out of the scope of this work.

To improve the syngas quality, part of the CO_2 is removed from the produced syngas via a PSA unit simulated with a shortcut model based on Santos et al. [255] (Figure A.8). The separated CO_2-rich stream is then recycled into the gasifier to decrease the carbon losses of the process and the need for fresh gasifying agent. Similarly to the combustion unit model, the removal of the side products (ashes and sulfur-based compounds) is modeled by using a separator block. The formation of tars and the energy demand for their separation

and cracking have not been included in the model since their concentration can be quite low when gasification occurs under proper operating conditions and in the presence of a catalyst. Thus, the modeled flue gas cleaning treatment of the gasification unit represents one of the most favorable cases.

The H_2:C ratio of syngas is then adjusted by adding green hydrogen produced in a water electrolyzer. The resulting stream is then pressurized and converted into methanol in a process designed similarly to the methanol synthesis unit described above for the combustion-based PBtMeOH process (Figure A.8).

Analogously to the model of the combustion-based PBtMeOH process, heat from the methanol synthesis reactors is supplied to the reboiler of the methanol purification unit. Further, the residual heat from the methanol synthesis unit, the gasification unit, and the furnace is recovered and converted into electricity in a power cycle unit.

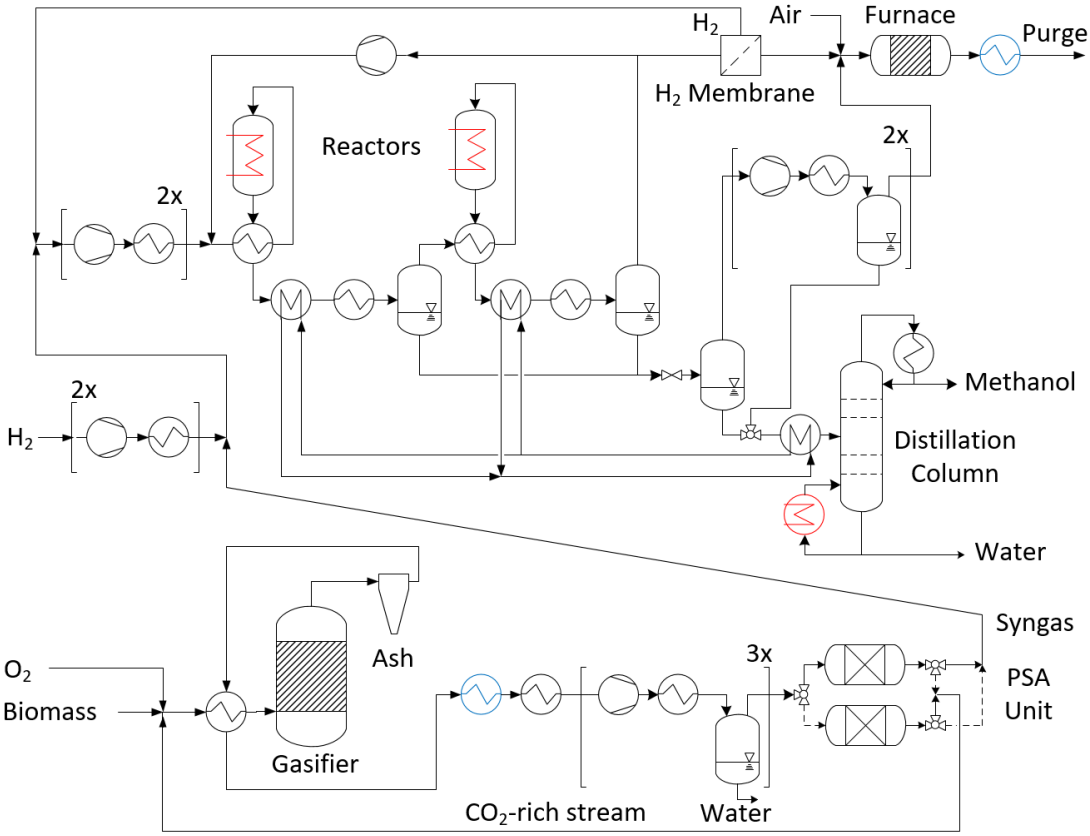


Figure A.8.: Simplified process flow diagram of the modeled gasification-based Power- and Biomass-to-Methanol process. Note: the electrolysis unit and the power cycle are not represented in the sketch since they were not modeled in Aspen Plus. Also, heat integration between the methanol synthesis reactors and the reboiler of the distillation column is not explicitly shown in the sketch for simplicity (the corresponding heat exchangers are marked in red). The heat exchangers in the biomass conversion and furnace units, where heat is removed and supplied to the power cycle, are marked in blue to ease identification.

A.7.3. Techno-economic analysis assumptions

The levelized cost of methanol (LCOM) for the modeled PBtMeOH processes is calculated as follows

$$\mathrm{LCOM} = \frac{\mathrm{CAPEX}_0 + \mathrm{CAPEX}_{\mathrm{r,\,PEM}} \cdot (1+i)^{-10} + \sum_{j=1}^{N_y} (\mathrm{O\&M_y} + \mathrm{OPEX_y}) \cdot (1+i)^{-j}}{\sum_{j=1}^{N_y} (M_{\mathrm{MeOH,\,y}}) \cdot (1+i)^{-j}}, \tag{A.1}$$

where CAPEX_0, $\mathrm{O\&M_y}$, and $\mathrm{OPEX_y}$ are the initial investment cost, the yearly operation and maintenance, and operating costs, respectively, $M_{\mathrm{MeOH,\,y}}$ the yearly methanol production, N_y the plant lifetime, and i the interest rate. The replacement of the electrolysis unit ($\mathrm{CAPEX}_{\mathrm{r,\,PEM}}$) in the tenth year is also considered. No salvage value of the plant is considered to have a conservative estimation of the methanol production cost.

The investment cost of the main equipment is estimated based on the correlations recommended by Biegler et al. [294] and updated to the reference year (2021) via the CEPCI. More specific cost correlations are used for the biomass conversion unit [273], power cycle unit [273], methanol synthesis reactors [174], and water electrolysis unit [87]. For the latter unit, the correlation for the PEM technology was considered [87], and the resulting specific investment cost was multiplied by 1.75 to account for civil works and installation costs: the calculated specific investment cost is around 1.10-1.20 M€ MW^{-1} for the considered electrolysis plant sizes, and aligns with installation costs estimated in other works, e.g., by Hemauer et al. [86]. Utility and biomass prices also align with other literature works. Additional assumptions of the economic analysis are collected in Table A.8.

Table A.8.: Main assumptions for the economic analysis.

	Values
Reference year	2021
$ to € conversion factor	0.85
Plant lifetime	20 y
Yearly operating hours	8000
Yearly O&M as % of the initial investment cost (CAPEX_0)	5 %
Interest rate	5 %
Electricity price	60 € MWh^{-1}
Cooling price	0.1 € MWh^{-1}
Biomass price (dry basis)	70 € t^{-1}

A.8. Detailed model of the Power- and Biomass-to-Kerosene processes

In the following subsections, we provide additional details of the built models for some key units of PBtK processes.

A.8.1. RWGS unit

In the combustion-based PBtK via the FT pathway (Figure 3.5 a), the CO_2 stream obtained via the CC unit is reduced to CO via hydrogenation in a catalytic RWGS unit.

The produced syngas needs to satisfy a few specifications, e.g., a delivery pressure of ca. 25 bar, a H_2:CO ratio higher than 1.5, and a relatively low CO_2 concentration (being CO_2 generally inert in the conventional FT synthesis) for a good conversion in the subsequent FT synthesis unit.

While the (equimolar) RWGS reaction is, in theory, not affected by pressure according to Le Chatelier's principle, the Sabatier reaction for methane production, which is unwanted, is affected by pressure (see Section 2.4.3.1). Further, supplying H_2 in excess in the RWGS unit, e.g., up to meet the syngas ratio requirements, promotes CO_2 conversion, but also methanation.

The modeled catalytic RWGS unit for the combustion-based PBtK via the FT pathway is designed based on the key findings of Stollenwerk [12], who investigated the above-mentioned trade-offs by optimizing a syngas production unit as a black-box: the syngas production unit modeled in Aspen Plus was optimized as a black box via the genetic algorithm available in Matlab with respect to an economic objective function, i.e., the syngas production cost. Further optimization of the RWGS unit for the PBtK process flowsheet was not performed, since clear design indications were already provided from these optimization results [12]. Also, we did not optimize the entire PBtK process flowsheets because of the high numerical instability of the Aspen Plus simulations, primarily due to the large model size and the presence of large recycles.

The modeled syngas production unit accounts for two RWGS reactors with intermediate water removal, an LHHW kinetics including the methanation reaction for the RWGS reactors [376], and a membrane separation unit for CO_2 separation [377] and recycle are considered to improve the syngas quality and reduce carbon losses. Further, a high-pressure H_2 stream bypassing the RWGS reactors is considered to reach the desired syngas ratio. A sketch representing the implemented model for syngas production is shown in Figure A.9.

Moderate RWGS reaction pressures (ca. 2-3 bar) and high reaction temperatures (ca. 800 °C, the upper limit for the considered kinetic model [376]) are chosen based on Stollenwerk's optimization results [12], since they promote CO_2 conversion and suppress methanation. Also, operating the RWGS reactors at moderate pressures reduces the overall electricity demand and costs for the compressors: this design choice reduces the compression ratio for the reactants and increases the compression ratio for the produced syngas, which has a lower flow rate thanks to water removal. Similar results were obtained by Adelung et al. [201] when investigating via sensitivity analyses the impact of the RWGS operating parameters in FT-based PtL processes with an equilibrium-based RWGS reactor model.

Further, a nearly stoichiometric H_2:CO_2 ratio at the RWGS unit inlet is considered,

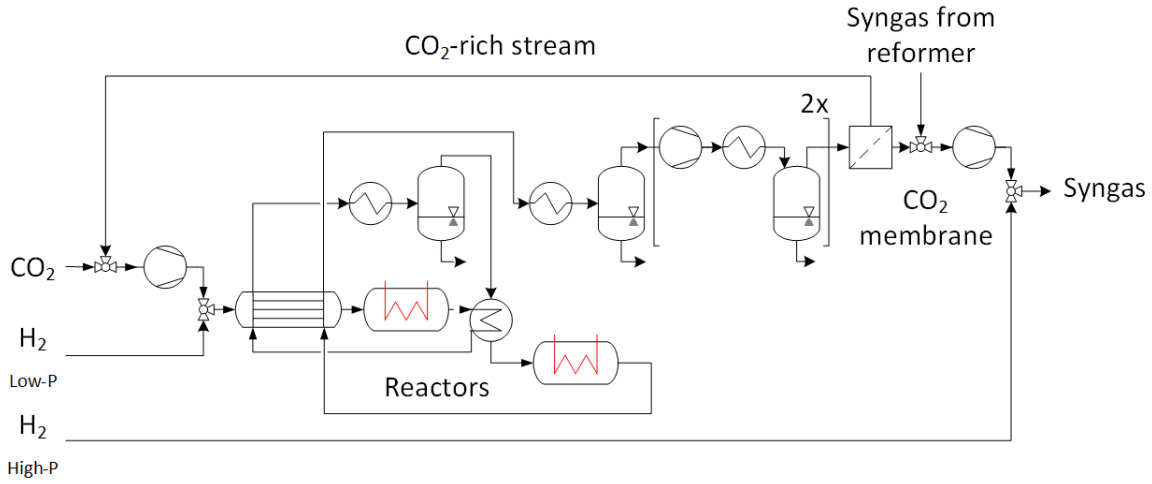


Figure A.9.: Sketch of the considered syngas production unit model. The two endothermic RWGS reactors are marked in red. Heat is supplied by the flue gas (not shown here).

since it inhibits methanation without excessively affecting CO_2 conversion. Moreover, the addition of an already pressurized H_2 stream into the syngas stream to tune the H_2:CO ratio allows reducing the costs for syngas compression, despite the efficiency penalty in the water electrolyzer itself.

A.8.2. Fischer-Tropsch unit

The kinetic model for the FT synthesis is implemented in Aspen Plus via a Fortran routine based on the work of Habermeyer et al. [227].

The implemented model predicts the formation of both alkanes and alkenes. The formation of methane and ethene is modeled differently to match the experimental results in Todic et al. [234], i.e., higher methane production and lower ethene production [235]. In the following, the general expression of the reaction rates r considered in the FT synthesis model is given:

$$r_{\mathrm{CH_4}} = k_{5M} \cdot K_7^{0.5} \cdot p_{\mathrm{H_2}}^{1.5} \cdot \alpha_1 \cdot [S]$$

$$r_{\mathrm{C_2H_4}} = k_{6E,0} \cdot e^{2c} \sqrt{K_7 \cdot p_{\mathrm{H_2}}} \cdot \alpha_1 \cdot \alpha_2 \cdot [S]$$

$$r_{\mathrm{C_nH_{2n+2}}} = k_{5M} \cdot K_7^{0.5} \cdot p_{\mathrm{H_2}}^{1.5} \cdot \prod_{i=3}^{n} \alpha_i \cdot [S] \quad for\ n \geq 2$$

$$r_{\mathrm{C_nH_{2n}}} = k_{6E,0} \cdot e^{2c} \sqrt{K_7 \cdot p_{\mathrm{H_2}}} \cdot \alpha_1 \cdot \alpha_2 \cdot \prod_{i=3}^{n} \alpha_i \cdot [S] \quad for\ n \geq 3,$$

where k_j are the kinetic terms based on Arrhenius, $p_{\mathrm{H_2}}$ the partial pressure of hydrogen, [S] the fraction of vacant sites, which in turn depends on the operating pressure, temperature, and C-chain growth probability factors (α_i). Moreover, the C-chain growth probability factors depend on the operating conditions, i.e., temperature, pressure, and composition. We refer to the publications of Habermeyer et al. [227] and Todic et al. [234] for further details on the kinetic and reactor models.

A.8.3. Olefin oligomerization unit

The oligomerization of short C-chain olefins is generally heterogeneously catalyzed and takes place over acidic zeolite catalysts [25].

When pure olefins are oligomerized, the product distribution generally presents some spikes in correspondence to olefins with carbon numbers that are a multiple of the carbon number of the oligomerized olefins, thus following the Reaction (3.4) stoichiometry (see for instance the product distribution of propene oligomerization in Monama et al. [261]). Olefins with intermediate carbon numbers are also formed, but with lower concentrations, and they are often due to secondary reactions, e.g., asymmetric cracking of unstable longer C-chain olefins [261].

When olefin mixtures are oligomerized, the olefin conversion and product distribution depend on the input stream composition, catalyst, and operating conditions. For instance, ethene is poorly converted in the gaseous phase over acidic catalysts in typical oligomerization operating conditions (high temperature and pressures) differently from longer C-chain olefins [260]. Also, high temperatures promote the formation of shorter C-chain olefins since long C-chain olefins tend to be less stable and crack [261, 263].

The product distribution of oligomerization of olefin mixtures is intuitively expected to be more even. For this reason, it has been sometimes modeled through the smooth ASF distribution [248, 250]. However, a non-smooth olefin distribution can still be obtained due to the composition of the olefin mixture and the conversion of the individual olefins over the catalyst at the considered reaction conditions.

In the absence of experimental data for the oligomerization of the considered olefin mixture, we could not check whether the modified ASF distribution could accurately represent the product distribution, and eventually estimate the ASF chain-growth factor. We therefore modeled the oligomerization of the olefin mixture as a process in which the short C-chain olefins are oligomerized in parallel, i.e., without affecting the conversion of the other olefins, and the resulting products are mixed. To this end, we considered the molar conversion factors of the olefins from experiments conducted at relatively similar operating conditions over similar catalysts.

For ethene oligomerization, we considered the experimental results by Dutta et al. [260] performed at 300 °C and 1 bar over the acidic catalyst HZSM-5. In these operating conditions, around 14 wt.% of ethene is converted into longer C-chain olefins. Furthermore, we assumed that the produced longer C-chain hydrocarbons are alkenes and that olefin cracking occurs to form olefins that have a C-number that is not a multiple of two (see Table A.9). Also, it is important to mention that the considered conversion factors represent most likely a conservative estimation. In fact, the experiments were carried out at a pressure that is significantly lower than the one considered for the oligomerization reactor (40 bar).

For propene and hexene oligomerization, we considered the experimental results by Monama et al. [261] performed at 220 °C and 40 bar over the acidic catalyst D-HZSM-5. A conversion of propene of ca. 85 % is considered and a wide range of long-chain olefins is produced. The formation of olefins with a C-number higher than 13 was neglected in the lack of data. In contrast, only the hexene dimerization was considered in the lack of detailed information about the other reaction products.

For butene oligomerization, we considered the experimental results by Díaz et al. [262] performed at 225 °C and 30 bar over the acidic catalyst HZSM-5. In these operating

conditions, around 37 % of butene is converted into longer C-chain olefins. As the product distribution is only available in an aggregated form, e.g., merging C_5 to C_7 olefins, we assumed an even probability for the corresponding formation reactions. Furthermore, the olefins with a C-number higher than 13 were lumped into $C_{12}H_{24}$ in the lack of data.

For pentene oligomerization, we considered the experimental results by Cowley [263] at 225 °C and 2 bar over the acidic catalyst HZSM-5. Similarly to butene oligomerization, we assumed an even probability for the formation of olefins, e.g., C_2H_4 and C_8H_{16}, via secondary or cracking reactions. Furthermore, the formation of olefins with a C-number higher than 11 (besides $C_{15}H_{30}$) was not modeled in the lack of data.

Finally, the oligomerization of olefins with a C-chain longer than six was not considered since they are not produced in the methanol-to-olefins reactor and are almost entirely removed from the product stream before being recycled into the oligomerization reactor.

The reactions and molar conversion factors implemented in the oligomerization reactor are summarized in Table A.9.

A.8.4. Techno-economic analysis assumptions

The considered PBtK processes are modeled assuming a biomass flow rate of 10 t h^{-1} on a dry basis (around 50 MW based on LHV). The investment and operating costs for biomass pre-treatment, e.g., partial drying and particle size reduction, are not considered in the techno-economic analysis. The size of the other components, e.g., the electrolyzer, is defined according to the modeling assumptions and the considered pathway.

For the economic analysis, the CAPEX of the main equipment modules, e.g., compressors and heat exchangers, is estimated with the cost models proposed by Biegler et al. [294]. In contrast, the technology-specific values or correlations are considered for the biomass conversion units [273], the CC unit [124], PEM-WE [87], PSA unit [378], and the FT reactor [227]. Further, the steam power cycle unit cost is estimated from the individual components via the correlations in Biegler et al. [294], while the ORC is costed by assuming a typical specific cost value (2.75 M€ MW^{-1} [213]). The correlations are updated to 2021 as the reference year. A replacement for the electrolysis unit in the 10^{th} year is also considered. Further assumptions are collected in Table A.8.

Table A.9.: Considered oligomerization reactions and corresponding molar conversion factors of the pure olefins used in Aspen Plus.

Reaction			Conversion factor
2 C_2H_4	→	C_4H_8	0.108
3 C_2H_4	→	2 C_3H_6	0.017
5 C_2H_4	→	2 C_5H_{10}	0.012
3 C_2H_4	→	C_6H_{12}	0.003
3 C_3H_6	→	C_9H_{18}	0.284
2 C_3H_6	→	C_6H_{12}	0.135
8 C_3H_6	→	3 C_8H_{16}	0.124
7 C_3H_6	→	3 C_7H_{14}	0.084
10 C_3H_6	→	3 $C_{10}H_{20}$	0.080
11 C_3H_6	→	3 $C_{11}H_{22}$	0.079
4 C_3H_6	→	$C_{12}H_{24}$	0.027
5 C_3H_6	→	3 C_5H_{10}	0.024
4 C_3H_6	→	3 C_4H_8	0.008
13 C_3H_6	→	3 $C_{13}H_{26}$	0.007
2 C_4H_8	→	C_8H_{16}	0.171
3 C_4H_8	→	$C_{12}H_{24}$	0.166
4 C_4H_8	→	C_5H_{10} + $C_{11}H_{22}$	0.010
4 C_4H_8	→	C_6H_{12} + $C_{10}H_{20}$	0.010
4 C_4H_8	→	C_7H_{14} + C_9H_{18}	0.010
3 C_4H_8	→	4 C_3H_6	0.001
3 C_5H_{10}	→	$C_{15}H_{30}$	0.365
2 C_5H_{10}	→	$C_{10}H_{20}$	0.220
2 C_5H_{10}	→	C_2H_4 + C_8H_{16}	0.063
2 C_5H_{10}	→	C_3H_6 + C_7H_{14}	0.063
2 C_5H_{10}	→	C_4H_8 + C_6H_{12}	0.063
2 C_6H_{12}	→	$C_{12}H_{24}$	0.135

Appendix B.

Additional Information to Chapter 4

B.1. Power-to-Methanol process model

In the following, we provide the modeling equations of the PtMeOH process with intermediate storage, the constraints, and the objective function used in the CDS optimization problems solved in Chapter 4. Some equations are reformulated in an equivalent form to ease comprehension.

All the variables are defined as positive except for the hourly operating cost (OPEX(t)) since the energy stored in the battery can be sold to the grid ($P_{\text{to-grid}}(t)$) and make its value negative. Refer to the GAMS code in the Supporting Information of Mucci et al. [4] for the model implementation.

B.1.1. Battery

The energy content of the battery and the output power flow are modeled with the following equations (for the nomenclature of the variables and parameters, refer to Tables B.1 and B.2):

$$\mathrm{E_b}(t) = \mathrm{E_b}(t-\Delta t)\cdot(1-r_{\text{self-disch}}) + P_{\text{in}}(t)\cdot\eta_{\text{ch}}\cdot\Delta t - \frac{P_{\text{out}}(t)}{\eta_{\text{disch}}}\cdot\Delta t$$

$$P_{\text{out}}(t) = \frac{P_{\text{to-grid}}(t)}{\eta_{\text{DC-AC}}} + P_{\text{to-PEM}}(t).$$

The following constraints allow defining operational limits for the energy content of the battery ($\mathrm{E_b}(t)$), the inlet power flow ($\mathrm{P_{in}}(t)$), and the outlet power flow ($\mathrm{P_{out}}(t)$).

$$\mathrm{E_b}(t) \geq e_{\text{b, min \%}}\cdot\mathrm{E_{b,\,nom}}$$

$$\mathrm{E_b}(t) \leq \mathrm{E_{b,\,nom}}$$

$$\mathrm{E_b}(t=0) = 0.15\cdot\mathrm{E_{b,\,nom}}$$

$$\mathrm{E_b}(t=1440) = 0.15\cdot\mathrm{E_{b,\,nom}}$$

$$\mathrm{P_{in}}(t) \leq P_{\text{in max, b}}$$

$$\mathrm{P_{in}}(t) \geq P_{\text{in min, b}}\cdot x_{\text{b, in}}(t)$$

$$\mathrm{P_{in}}(t) \leq \frac{(1-e_{\text{b, min \%}})\cdot\mathrm{E_{b,\,nom}}}{\Delta t}\cdot x_{\text{b, in}}(t)$$

$$\mathrm{P}_{\mathrm{out}}(t) \leq P_{\mathrm{out\,max,\,b}}$$

$$\mathrm{P}_{\mathrm{out}}(t) \geq P_{\mathrm{out\,min,\,b}} \cdot x_{\mathrm{b,\,out}}(t)$$

$$\mathrm{P}_{\mathrm{out}}(t) \leq \frac{(1 - e_{\mathrm{b,\,min\,\%}}) \cdot \mathrm{E}_{\mathrm{b,\,nom}}}{\Delta t} \cdot x_{\mathrm{b,\,out}}(t)$$

$$x_{\mathrm{b,\,in}}(t) + x_{\mathrm{b,\,out}}(t) \leq 1$$

Table B.1.: Variables of the model of the battery.

Symbol	Description
$\mathrm{E}_{\mathrm{b}}(t)$	Energy content of the battery
$P_{\mathrm{in}}(t)$	Power input of the battery
$P_{\mathrm{out}}(t)$	Power output of the battery
$P_{\mathrm{to-grid}}(t)$	Power output: electricity back to the grid
$P_{\mathrm{to-PEM}}$	Power output: electricity to the PEM water electrolyzer
$\mathrm{E}_{\mathrm{b,\,nom}}$	Nominal energy capacity of the battery
$x_{\mathrm{b,\,in}}(t)$	Binary variable to decide when the battery is charged
$x_{\mathrm{b,\,ou}}(t)$	Binary variable to decide when the battery is discharged

Table B.2.: Parameters of the model of the battery.

Symbol	Description	Value	Unit
Δt	Time step size	1	h
η_{ch}	Efficiency of the charging phase	0.99	-
$P_{\mathrm{in\,min,\,b}}$	Minimum limit for the power input of the battery	0.5	MW
$P_{\mathrm{in\,max,\,b}}$	Maximum limit for the power input of the battery	100	MW
$r_{\mathrm{self-disch}}$	Self discharge rate	≈ 1	-
η_{disch}	Efficiency of the discharging phase	0.96	-
$P_{\mathrm{out\,min,\,b}}$	Minimum limit for the power output of the battery	0.5	MW
$P_{\mathrm{out\,max,\,b}}$	Maximum limit for the power output of the battery	100	MW
$\eta_{\mathrm{DC-AC}}$	Efficiency of the DC-AC conversion	0.99	-
$e_{\mathrm{b,\,min\,\%}}$	Minimum energy content of the battery	10	%

B.1.2. PEM water electrolyzer

The PEM water electrolyzer is modeled with the following equations (for the nomenclature of the variables and parameters, refer to Tables B.3 and B.4):

$$P_{\mathrm{PEM}}(t) = P_{\mathrm{grid}}(t) + P_{\mathrm{to-PEM}}(t)$$

$$P_{\mathrm{mod}}(t) = \frac{P_{\mathrm{PEM}}(t)}{N_{\mathrm{mod}}}$$

$$\eta_{\mathrm{PEM}}(t) = a_{00} + a_{10} \cdot P_{\mathrm{mod}}(t) + a_{20} \cdot P_{\mathrm{mod}}(t)^2 + a_{01} \cdot p_{\mathrm{PEM}}$$

$$\dot{m}_{\mathrm{H_2,\,prod}}(t) = \frac{P_{\mathrm{PEM}}(t) \cdot \eta_{\mathrm{PEM}}(t)}{\mathrm{LHV}_{\mathrm{H_2}}}.$$

As shown above, the implemented efficiency law of the PEM water electrolyzer (η_{PEM}) is a function of the electrolysis module power P_{mod} and the operating pressure p_{PEM}. Moreover, the values of the parameters were obtained by fitting the results of the electrolyzer model in the power and pressure ranges of 0.2-2.5 MW and 20-40 bar (R^2=0.999), respectively. A graphical representation of the PEM-WE efficiency is shown in Figure B.1.

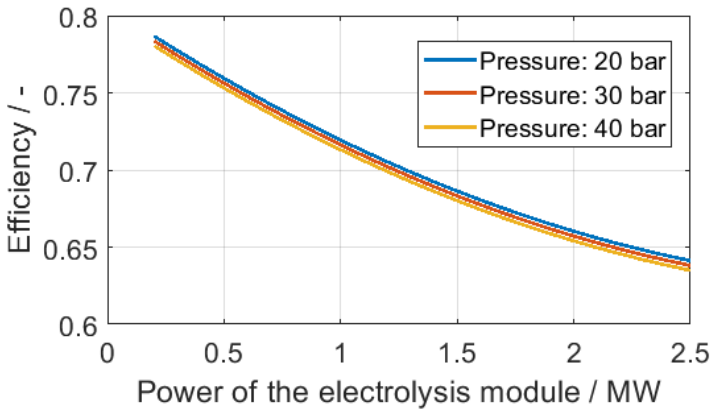


Figure B.1.: Electrolyzer efficiency with respect to the power of an electrolysis module for three pressures.

The limits to the operating power of the PEM water electrolyzer ($P_{\mathrm{PEM}}(t)$) are defined below:

$$P_{\mathrm{PEM}}(t) \geq x_{\mathrm{on-off}}(t) \cdot N_{\mathrm{mod}} \cdot P_{\mathrm{min,\,module}}$$

$$P_{\mathrm{PEM}}(t) \leq x_{\mathrm{on-off}}(t) \cdot N_{\mathrm{mod}} \cdot P_{\mathrm{max,\,module}}.$$

A nominal electrolyzer efficiency ($\eta_{\mathrm{PEM,\,nom}}$) and a maximum hydrogen flow rate value ($\dot{m}_{\mathrm{H_{2,prod\,max}}}$) are calculated as follows (the maximum hydrogen flow rate value is used for costing the compression unit):

$$\eta_{\mathrm{PEM,\,nom}} = a_{00} + a_{10} \cdot P_{\mathrm{max,\,module}} + a_{20} \cdot P^2_{\mathrm{max,\,module}} + a_{01} \cdot p_{\mathrm{PEM}}$$

$$\dot{m}_{\mathrm{H_{2,prod\,max}}} = \frac{N_{\mathrm{mod}} \cdot P_{\mathrm{max,\,module}} \cdot \eta_{\mathrm{PEM,\,nom}}}{\mathrm{LHV}_{\mathrm{H_2}}}.$$

Table B.3.: Variables of the model of the PEM water electrolyzer.

Symbol	Description
$P_{\mathrm{PEM}}(t)$	Power of the PEM water electrolyzer
$P_{\mathrm{grid}}(t)$	Power of the electrolyzer taken from the grid
$P_{\mathrm{mod}}(t)$	Power of an electrolyzer module
N_{mod}	Number of modules
$\eta_{\mathrm{PEM}}(t)$	Efficiency of the electrolyzer
p_{PEM}	Pressure of the electrolyzer
$\dot{m}_{\mathrm{H_2,\,prod}}(t)$	Hydrogen flow rate
$x_{\mathrm{on-off}}(t)$	Binary variable to activate or deactivate the electrolyzer
$\eta_{\mathrm{PEM,\,nom}}$	Nominal efficiency of the electrolyzer
$\dot{m}_{\mathrm{H_{2,prod\,max}}}$	Maximum hydrogen flow rate (to size the compression unit)

Table B.4.: Parameters of the model of the PEM water electrolyzer.

Symbol	Description	Value	Unit
a_{00}	Parameter of the efficiency law	0.813	-
a_{10}	Parameter of the efficiency law	$-1.010 \cdot 10^{-01}$	MW^{-1}
a_{20}	Parameter of the efficiency law	$+1.397 \cdot 10^{-02}$	MW^{-2}
a_{01}	Parameter of the efficiency law	$-3.118 \cdot 10^{-04}$	bar^{-1}
$\mathrm{LHV_{H_2}}$	LHV of hydrogen	120	$\mathrm{MJ\ kg}^{-1}$
$P_{\mathrm{min,\,module}}$	Minimum power of the electrolyzer per module	0.5	MW
$P_{\mathrm{max,\,module}}$	Maximum power of the electrolyzer per module	2.5	MW

B.1.3. Hydrogen compression unit

The power demand of the compressor ($P_{\mathrm{comp}}(t)$) is calculated as follows:

$$P_{\mathrm{comp}}(t) = \dot{m}_{\mathrm{H_2,\,prod}}(t) \cdot \frac{c_{\mathrm{p}} \cdot T_{\mathrm{in}}}{\eta_{\mathrm{is}} \cdot \eta_{\mathrm{mec}}} \cdot \left(\beta(t)^{\left(\frac{k-1}{k}\right)} - 1\right),$$

where the pressure ratio ($\beta(t)$) is a function of the pressure inside the hydrogen storage (equal to 75 bar in case there is no hydrogen storage) and the pressure of the water electrolyzer, as shown below:

$$\beta(t) = \frac{p_{\mathrm{vessel}}(t)}{p_{\mathrm{PEM}}}.$$

The pressure ratio of the compressor is limited due to technical issues:

$$\beta(t) \leq \beta_{\mathrm{max}}.$$

The nominal power of the compressor unit is also calculated to estimate the cost:

$$P_{\mathrm{comp,\,max}} = \dot{m}_{\mathrm{H_{2,prod\,max}}} \cdot \frac{c_{\mathrm{p}} \cdot T_{\mathrm{in}}}{\eta_{\mathrm{is}} \cdot \eta_{\mathrm{mec}}} \cdot \left(\beta_{\mathrm{max}}^{\left(\frac{k-1}{k}\right)} - 1\right).$$

Refer to Tables B.5 and B.6 for the nomenclature of the variables and parameters. The parameters c_p and k for hydrogen were estimated by using the Aspen Plus database (Peng-Robinson property method). An Aspen Plus model of a compression unit was used to benchmark the electricity demand of the modeled compressor. In particular, for a hydrogen inlet stream of 1900 kg h^{-1} at 40 bar for different pressure ratios (β), the power consumption error is lower than 1 % (see Table B.7).

Table B.5.: Variables of the model of the compression unit.

Symbol	Description
$P_\mathrm{comp}(t)$	Power of the compressor
$\beta(t)$	Pressure ratio of the compressor
$p_\mathrm{vessel}(t)$	Pressure inside the hydrogen storage
β_max	Maximum pressure ratio of the compressor
$P_\mathrm{comp,\,max}$	Maximum power of the compressor
$\dot{m}_{\mathrm{H_2,prod\,max}}$	Maximum hydrogen flow rate

Table B.6.: Parameters of the model of the compression unit.

Symbol	Description	Value	Unit
c_p	Specific heat at constant pressure of hydrogen	14.6	kJ $\mathrm{kg}^{-1}\mathrm{K}^{-1}$
k	Heat capacity ratio of hydrogen	1.41	-
T_in	Inlet temperature of hydrogen	298	K
η_is	Isentropic efficiency of the compressor	0.8	-
η_mec	Mechanical efficiency of the compressor	0.9	-

Table B.7.: Compressor model validation.

β	Model	Aspen Plus data
-	kW	kW
2.0	710	710
2.5	970	973
3.0	1196	1202
3.5	1397	1406

B.1.4. Hydrogen storage

The hydrogen storage is modeled with the following equations (for the nomenclature of the variables and parameters, refer to Tables B.8 and B.9):

$$M_{\mathrm{H_2}}(t) = M_{\mathrm{H_2}}(t-\Delta t) + \dot{m}_{\mathrm{H_2,prod}}(t)\cdot\Delta t - \dot{m}_{\mathrm{H_2,MeOH}}(t)\cdot\Delta t$$

$$M_{\mathrm{H_2}}(t) = V\cdot a_\mathrm{vessel}\cdot(p_\mathrm{vessel}(t) - p_\mathrm{vessel,\,min})$$

An initial value for the available hydrogen inside the hydrogen storage at the timestep $t = 0$ and a pressure limit for the storage are also set:

$$M_{\mathrm{H_2}}(t = 0) = 1\,\mathrm{kg}$$

$$p_{\mathrm{vessel}}(t) \leq p_{\mathrm{vessel,\,max}}.$$

Table B.8.: Variables of the model of the hydrogen storage.

Symbol	Description
$M_{\mathrm{H_2}}(t)$	Hydrogen mass available in the storage
$\dot{m}_{\mathrm{H_2,\,prod}}(t)$	Hydrogen flow rate produced by the electrolyzer
$\dot{m}_{\mathrm{H_{2,MeOH}}}(t)$	Hydrogen flow rate that goes into the methanol plant
V	Volume of the hydrogen storage
$p_{\mathrm{vessel}}(t)$	Pressure inside the hydrogen storage

Table B.9.: Parameters of the model of the hydrogen storage.

Symbol	Description	Value	Unit
Δt	Time step size	1	h
a_{vessel}	Hydrogen vessel constant	0.073	kg m^{-3}bar^{-1}
$p_{\mathrm{vessel,\,min}}$	Minimum pressure inside the hydrogen storage	75	bar
$p_{\mathrm{vessel,\,max}}$	Maximum pressure inside the hydrogen storage	140	bar

B.1.5. Methanol synthesis plant

The methanol plant is modeled with the following equations (for the nomenclature of the variables and parameters, refer to Tables B.10 and B.11):

$$\dot{m}_{\mathrm{MeOH}}(t) = a_{\mathrm{MeOH}} \cdot \dot{m}_{\mathrm{H_{2,MeOH}}}(t)$$

$$P_{\mathrm{MeOH}}(t) = a_{\mathrm{P,\,MeOH}} \cdot \dot{m}_{\mathrm{MeOH}}(t)$$

$$\dot{Q}_{\mathrm{MeOH}}(t) = a_{\mathrm{Q,\,MeOH}} \cdot \dot{m}_{\mathrm{MeOH}}(t)$$

$$\dot{m}_{\mathrm{CO_{2,MeOH}}}(t) = a_{\mathrm{CO_2,\,MeOH}} \cdot \dot{m}_{\mathrm{MeOH}}(t)$$

The operating limits of the methanol plants are set with the following inequality constraints:

$$\dot{m}_{\mathrm{H_{2,MeOH}}}(t) \leq \dot{m}_{\mathrm{H_{2,MeOH,\,nom}}}$$

$$\dot{m}_{\mathrm{H_{2,MeOH}}}(t) \geq L_{\mathrm{min,\,MeOH}} \cdot \dot{m}_{\mathrm{H_{2,MeOH,\,nom}}}.$$

A ramp limit (RL) for the methanol plant is also included to investigate the effect of its flexibility:

$$|\dot{m}_{\mathrm{H_{2,MeOH}}}(t) - \dot{m}_{\mathrm{H_{2,MeOH}}}(t - \Delta t)| \leq \mathrm{RL} \cdot \dot{m}_{\mathrm{H_{2,MeOH,\,nom}}}.$$

The yearly methanol production is calculated as the result of the scheduling in the considered time horizon (1440 hourly time steps), which is then scaled for the number of yearly operating hours:

$$M_{\mathrm{MeOH,\,y}} = \sum_{t=1}^{1440} \dot{m}_{\mathrm{MeOH}}(t) \cdot \frac{8000\,\mathrm{h}}{1440\,\mathrm{h}}.$$

A constraint on the minimum yearly production of methanol is also set for the future unit cost scenario:

$$M_{\mathrm{MeOH,\,y}} \geq 40\,\mathrm{kt}.$$

Table B.10.: Variables of the model of the methanol plant.

Symbol	Description
$\dot{m}_{\mathrm{MeOH}}(t)$	Methanol mass flow rate
$\dot{m}_{\mathrm{H_{2,MeOH}}}(t)$	Hydrogen flow rate that goes into the methanol plant
$P_{\mathrm{MeOH}}(t)$	Power demand of the methanol plant
$\dot{Q}_{\mathrm{MeOH}}(t)$	Cooling demand of the methanol plant
$\dot{m}_{\mathrm{CO_{2,MeOH}}}(t)$	CO_2 demand of the methanol plant
$\dot{m}_{\mathrm{H_{2,MeOH,\,nom}}}$	Nominal hydrogen flow rate that goes into the methanol plant
$M_{\mathrm{MeOH,\,y}}$	Yearly methanol production

Table B.11.: Parameters of the model of the methanol plant.

Symbol	Description	Value	Unit
a_{MeOH}	Methanol to hydrogen mass conversion factor	5.23	-
$a_{\mathrm{P,\,MeOH}}$	Specific power demand consumption	$1.85 \cdot 10^{-4}$	MWh kg^{-1}
$a_{\mathrm{Q,\,MeOH}}$	Specific cooling demand consumption	$1.38 \cdot 10^{-3}$	MWh kg^{-1}
$a_{\mathrm{CO_2,\,MeOH}}$	CO_2 to methanol mass conversion factor	1.55	-
$L_{\mathrm{min,\,MeOH}}$	Minimum load of the methanol plant	0.2	-
RL	Ramp limit for the methanol plant	0-0.25	-

B.1.6. Cost models

The capital cost of the units for the year 2021 is calculated as follows (for the nomenclature of the variables and parameters, refer to Tables B.12 and B.13):

The initial investment cost ($\mathrm{CAPEX_0}$) is calculated as the sum of the investment cost of the single process units:

$$\mathrm{CAPEX_0} = \mathrm{CAPEX_B} + \mathrm{CAPEX_{PEM}} + \mathrm{CAPEX_{Comp}} + \mathrm{CAPEX_{Volume}} + \mathrm{CAPEX_{MeOH}}.$$

The hourly operating costs ($\mathrm{OPEX}(t)$) are calculated as the sum of the expenditures for the electricity demand, cooling demand, and raw materials (CO_2):

$$\mathrm{CAPEX_B} = C_b \cdot \mathrm{E_{b,\,nom}}$$

$$\mathrm{Cost_{PEM,\,spec}} = \left(C_{\mathrm{PEM},1} + C_{\mathrm{PEM},2} \cdot \left(N_{\mathrm{mod}} \cdot P_{\mathrm{nom,\,module\,in\,kW}}\right)^{-0.38}\right) \cdot \left(\tfrac{2021}{2020}\right)^{-158.9} \cdot 1.75$$

$$\mathrm{CAPEX_{PEM}} = \mathrm{Cost_{PEM,\,spec}} \cdot N_{\mathrm{mod}} \cdot P_{\mathrm{nom,\,module\,in\,kW}}$$

$$\mathrm{CAPEX_{Comp}} = 2 \cdot C_{\mathrm{comp},1} \cdot \left(C_{\mathrm{comp},2} \cdot \tfrac{P_{\mathrm{comp,\,max}}}{2}\right)^{0.77} + C_{\mathrm{HE},1} \cdot \left(C_{\mathrm{HE},2} \cdot P_{\mathrm{comp,\,max}}\right)^{0.65}$$

$$\mathrm{CAPEX_{Volume}} = C_{\mathrm{Volume}} \cdot V$$

$$\mathrm{CAPEX_{MeOH}} = \mathrm{CAPEX_{MeOH,\,ref}} \cdot \left(\tfrac{\dot{m}_{\mathrm{H_2,MeOH,\,nom}}}{\dot{m}_{\mathrm{H_2,MeOH,\,nom\,ref}}}\right)^{0.6}.$$

$$\begin{aligned}\mathrm{OPEX}(t) = {} & \left(P_{\mathrm{in}}(t) - P_{\mathrm{to-grid}}(t) + P_{\mathrm{grid}}(t) + C_{\mathrm{PEM-aux}} \cdot P_{\mathrm{PEM}}(t) + P_{\mathrm{comp}}(t) + P_{\mathrm{MeOH}}(t)\right) \cdot C_{\mathrm{el}}(t) \\ & + \left(\left(P_{\mathrm{PEM}}(t) - \dot{m}_{\mathrm{H_{2,prod}}}(t) \cdot \mathrm{HHV_{H_2}}\right) + P_{\mathrm{comp}}(t) + \dot{Q}_{\mathrm{MeOH}}(t)\right) \cdot C_{\mathrm{Q}} \\ & + \dot{m}_{\mathrm{CO_{2,MeOH}}}(t) \cdot C_{\mathrm{CO_2}}\end{aligned}$$

.

The yearly operating costs are then calculated as the result of the scheduling in the considered time horizon:

$$\mathrm{OPEX_y} = \sum_{t=1}^{1440} \mathrm{OPEX}(t) \cdot \frac{8000\,\mathrm{h}}{1440\,\mathrm{h}}$$

The total cost of the plant, including investment, operating, and O&M costs, is calculated as:

$$\mathrm{COST_{tot}} = \mathrm{CAPEX_0} + \mathrm{CAPEX_{r,\,PEM}} \cdot (1+i)^{-10} + (\mathrm{OPEX_y} + \mathrm{O\&M_y}) \cdot F_{\mathrm{act}},$$

where $\mathrm{CAPEX_{r,\,PEM}}$ is the cost for replacement of the PEM water electrolysis unit and is equal to $\mathrm{CAPEX_{PEM}}$, while F_{act} is defined as follows:

$$F_{\mathrm{act}} = \sum_{y=1}^{20} \frac{1}{(1+i)^y}.$$

The objective function, the specific cost of methanol (LCOM), is calculated as the ratio of the total cost and the methanol production during the lifetime of the plant:

$$\mathrm{LCOM} = \frac{\mathrm{COST_{tot}}}{M_{\mathrm{MeOH,\,y}} \cdot F_{\mathrm{act}}}.$$

Table B.12.: Variables of the cost models.

Symbol	Description
$\mathrm{CAPEX_B}$	Investment cost of the battery
$\mathrm{E_{b,\,nom}}$	Nominal energy capacity of the battery
$\mathrm{Cost_{PEM,\,spec}}$	Specific cost of the PEM water electrolyzer per unit of power
N_{mod}	Number of modules
$\mathrm{CAPEX_{PEM}}$	Investment cost of the PEM water electrolyzer
$\mathrm{CAPEX_{r,\,PEM}}$	Replacement cost of the PEM water electrolyzer
$\mathrm{CAPEX_{Comp}}$	Investment cost of the compression unit
$P_{\mathrm{comp,\,max}}$	Maximum power of the compressor
$\mathrm{CAPEX_{Volume}}$	Investment cost of the hydrogen storage
V	Volume of the hydrogen storage
$\mathrm{CAPEX_{MeOH}}$	Investment cost of the methanol plant
$\dot{m}_{\mathrm{MeOH}}(t)$	Methanol mass flow rate
$\mathrm{CAPEX_0}$	Initial investment cost
$\mathrm{OPEX}(t)$	Hourly operating costs
$P_{\mathrm{in}}(t)$	Power input of the battery
$P_{\mathrm{to-grid}}(t)$	Power provided back to the grid
$P_{\mathrm{PEM}}(t)$	Power of the PEM water electrolyzer
$P_{\mathrm{comp}}(t)$	Power of the compressor
$P_{\mathrm{MeOH}}(t)$	Power demand of the methanol plant
$\dot{m}_{\mathrm{H_2,\,prod}}(t)$	Hydrogen flow rate produced by the electrolyzer
$\dot{Q}_{\mathrm{MeOH}}(t)$	Cooling demand of the methanol plant
$\dot{m}_{\mathrm{CO_{2,MeOH}}}(t)$	CO_2 demand of the methanol plant
$\mathrm{OPEX_y}$	Yearly operating costs
$\mathrm{COST_{tot}}$	Total cost of the Power-to-Methanol plant
$\mathrm{O\&M_y}$	Yearly O&M expenditures (assumed equal to 5 % of $\mathrm{CAPEX_0}$)
LCOM	Levelized cost of methanol
$M_{\mathrm{MeOH,\,y}}$	Yearly methanol production

Table B.13.: Parameters of the cost models.

Symbol	Description	Value	Unit
C_b	Specific cost of battery	368 [285]	$\$_{2021}$ kWh^{-1}
$C_{\mathrm{PEM,1}}$	Electrolyzer cost constant	582.9 [87]	€ kW^{-1}
$C_{\mathrm{PEM,2}}$	Electrolyzer cost constant	9458.2 [87]	€ kW$^{-0.62}$
$P_{\mathrm{nom,\,module\,in\,kW}}$	Nominal power of the electrolyzer per module	2000	kW
$C_{\mathrm{comp,1}}$	Cost parameter for the compressors	0.81 [294]	M$\$_{2021}$
$C_{\mathrm{comp,2}}$	Cost parameter for the compressors	0.013 [294]	kW^{-1}
$C_{\mathrm{HE,1}}$	Cost parameter for the heat exchanger	0.30 [294]	M$\$_{2021}$
$C_{\mathrm{HE,2}}$	Cost parameter for the heat exchanger	6.73 [294]	kW^{-1}
C_{Volume}	Specific cost of hydrogen storage	7800*	$\$_{2021}$ m^{-3}
$\mathrm{CAPEX}_{\mathrm{MeOH,\,ref}}$	Investment cost of the reference methanol plant	27.8**	M€
$\dot{m}_{\mathrm{H_2,MeOH,\,nom}}$	Nominal methanol flow rate of the reference methanol plant	9.9**	t h^{-1}
$C_{\mathrm{PEM-aux}}$	Percentage of the power needed for the auxiliaries of the PEM water electrolyzer	0.05	-
$\mathrm{HHV}_{\mathrm{H_2}}$	HHV of hydrogen	142	MJ kg^{-1}
$C_{\mathrm{el}}(t)$	Electricity price	[299]	€ MWh^{-1}
C_{Q}	Cooling cost	1	€ MWh^{-1}
$C_{\mathrm{CO_2}}$	Specific cost of CO_2	50 [302]	€ t^{-1}
F_{act}	Actualization factor	12.46	-
i	Interest rate	5	%

* See Section B.2.
** See Section B.4.

B.2. Hydrogen storage cost

The considered hydrogen storage cost is 500 \$ kg^{-1}, which corresponds to the target cost for 160 bar stationary gaseous hydrogen tanks for the year 2020 [379]. This value was converted from the specific cost for unit of hydrogen mass into the specific cost for unit of volume and updated from year 2007 to year 2021 as follows:

$$\mathrm{CAPEX_{volume}} = 500\ \frac{\$}{\mathrm{kg}} \cdot 0.073\ \frac{\mathrm{kg}}{\mathrm{m^3 bar}} \cdot (160\ \mathrm{bar} - 1\ \mathrm{bar}) \cdot \mathrm{UF},$$

where $0.073\ \frac{\mathrm{kg}}{\mathrm{m^3 bar}} \cdot (160\ \mathrm{bar} - 1\ \mathrm{bar})$ determines the available hydrogen mass content per unit of volume, and UF is the update factor equal to 1.35. The calculated cost is around 7800 \$ m^{-3}. Lower specific costs for vessels might be possible in scenarios with higher production volumes [379] and considering a lower maximum pressure inside the vessel, which reduces the wall thickness, thus the material cost.

B.3. Methanol synthesis plant

The reference methanol synthesis plant was modeled in Aspen Plus ® V11 (Figure B.2) similarly to what is described in Appendix A.7.

The methanol synthesis occurs in a two-stage multi-tubular reactor operated at ca. 245 °C and 75 bar with intermediate product removal. After the second stage of the reactor, the unreacted gases are separated from crude methanol, the mixture of water and methanol, via condensation and partially (98 %) recycled back to the reactor. Also, a membrane separation process [377] was considered to partially (90 %) recover H_2 from the purge stream.

Crude methanol is then purified via distillation to meet the desired purity specification, i.e., 99.85 wt.% (AA grade methanol). Heat for the reboiler can be supplied via heat integration. No net heat demand is required.

Table B.14 summarizes the key information about the methanol synthesis plant that was used as the reference for the technical and economic analysis.

Table B.14.: Main data of the reference methanol synthesis plant.

	Values
H_2 mass flow rate	1.9 t h^{-1}
CO_2 mass flow rate	15.4 t h^{-1}
CH_3OH mass flow rate	9.9 t h^{-1}
Overall electricity demand	1.8 MW
Overall cooling demand	13.8 MW
First law efficiency	84.3 %

B.4. Methanol synthesis plant cost

The CAPEX of the main equipment units of the methanol synthesis plant (Figure B.2), i.e., compressors, reactor, heat exchangers, flashes, and distillation column, was estimated by using the cost models proposed by Biegler et al. [294] based on the well-established Guthrie's method [380]. The cost of the membrane was estimated according to Ramírez-Santos et al.'s model [377].

The estimated CAPEX of the reference methanol synthesis plant with a yearly production of 0.08 Mt is 27.8 M€ (350 € $(t/y)^{-1}$). This value is within the typical range for large-scale methanol synthesis plants (200-700 \$ $(t/y)^{-1}$ [381]), which means that the capital cost is probably underestimated. On a similar production capacity (0.06 Mt y^{-1}), the estimated investment cost of a small-scale methanol synthesis plant in Texas was around 40 M\$ [381]. The difference might be due to the uncertainty of the cost models and the different boundary conditions (the steam methane reforming and hydrogen compression units are also included in the plant in Texas). The estimated investment cost is in line with an e-methanol plant in Norway (yearly production of 0.1 Mt and a capital cost of 200 M\$ [302]) if the cost of the electrolysis unit and its replacement after 10 years are considered.

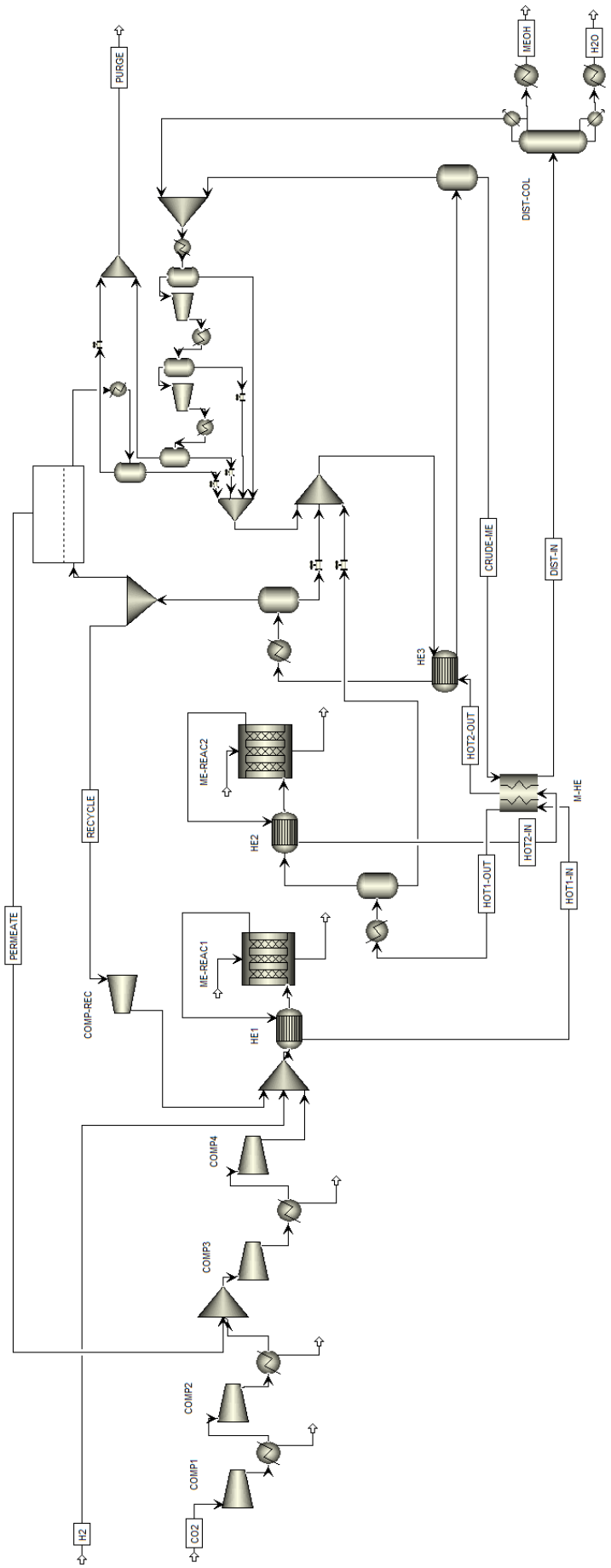


Figure B.2.: Methanol synthesis plant model in Aspen Plus ® V11.

B.5. Scenarios

In this section, additional details about the electricity price, renewable availability, and unit cost scenarios are shown.

Electricity price and renewable availability scenarios

Table B.15 shows that a relevant part of the hourly variations of the electricity price and renewable power availability profiles (relative to the mean value over the considered scheduling scenario) are lower than 5 % (Figures 4.2 and 4.3). This explains why moderate flexibility of the methanol synthesis plant (in % h^{-1}) is already highly beneficial from an economic perspective. However, a linear correlation between the variability of the scenarios and the flexibility of the methanol synthesis plant cannot be established, as other factors, e.g., storage utilization, operating constraints, and chosen objective function, play a role.

Table B.15.: Percentage of the hourly electricity price or renewable power availability variations between consecutive hours lower than 5 %, 10 %, and 25 % for the considered scenarios. The relative hourly variations were calculated with respect to the average value over the considered scenario, i.e., 51 € MWh^{-1}, 154 € MWh^{-1}, 52 MW, and 39 MW for the "Historical 2021", "Historical 2022", "May-Jun", and "Nov-Dec" scenarios, respectively.

	Electricity price scenarios		Power availability scenarios	
Hourly variations	Historical 2021	Historical 2022	May-Jun	Nov-Dec
$\leq$ 5 %	48 %	42 %	36 %	52 %
$\leq$ 10 %	72 %	63 %	50 %	75 %
$\leq$ 25 %	96 %	93 %	80 %	97 %

Cost scenarios

To investigate the effect of the capital cost of the units on the optimal solution, future unit cost predictions were considered. In particular, the CDS optimization problems were solved by assuming capital cost predictions for the year 2030 (Scenario 2030) and considering the same electricity price and renewable availability profiles. A reduction in the investment cost of the battery, electrolyzer, hydrogen storage, PV and wind power plants was considered (see Table B.16). In contrast, the investment cost for the compression and methanol synthesis units was not varied since no significant learning rate is expected.

Table B.16.: Assumed capital cost values of the key units for the base case and future unit cost scenarios (values referred to the year 2021).

	Base case (2021)	Scenario 2030
Battery	368 \$ kWh^{-1} [285]	214 \$ kWh^{-1} [285]
Electrolyzer	Correlation* [87]	Correlation* [87]
Hydrogen storage	7800 \$ m^{-3} [379]	7020 \$ m^{-3} [379]
PV	857 \$ kW^{-1} [301]	690** \$ kW^{-1} [276]
Wind onshore	1325 \$ kW^{-1} [301]	1260** \$ kW^{-1} [277]

* It depends on the installation year.
** Average value of the extremes of the predicted range.

B.6. Optimization results

In this section, additional optimization results are provided.

B.6.1. Grid-connected Power-to-Methanol case study

The optimal design variables and the key performance metrics for the electricity price (Figure 4.2) and unit cost scenarios of the grid-connected case study are shown in Tables B.17, B.18, and B.19. For the "low-mean low-standard-deviation electricity price scenario", the optimization results for the future unit cost scenario are not shown since they slightly differ from the ones shown in Table B.17: the production cost of methanol is slightly lower (0.88-0.89 € kg^{-1}) due to the reduction of the investment cost for the electrolysis unit.

Figure B.3 shows how the battery and the hydrogen storage are optimally operated in the "high-mean high-standard-deviation electricity price scenario" (the produced and consumed hydrogen flow rates are also shown to ease the interpretation of the operation of the hydrogen storage). As expected, the energy stored in the battery and the hydrogen in the vessel are consumed within a few days, thus confirming that the chosen time frame for scheduling (2 months) is suitable. While the use of the battery is similar between the "No flexibility" and "25 % h^{-1} flexibility" cases both qualitatively (Figure B.3) and quantitatively (Table B.20), major differences can be noticed in the H_2 storage. The amount of hydrogen stored inside the vessel is significantly lower when the methanol synthesis plant is operated flexibly. Nonetheless, a similar qualitative behavior can be noticed in the pressure profile (dependent on both the amount of hydrogen and the storage volume). The differences can be explained by the different optimal operating strategies.

Table B.17.: Optimization results for the grid-connected case study for the low-price low-variable electricity price scenario for the 4 plant configurations, i.e., with both storage (B&V), with the hydrogen vessel (V), with battery (B), and without any storage (No B&V).

	Flexibility % h^{-1}	LCOM € kg^{-1}	$E_{b,nom}$ MWh	V m^3	N_{mod} -	p_{PEM} bar	β_{max} -	$\dot{m}_{H_2,MeOH,nom}$ t h^{-1}	$M_{MeOH,y}$ kt	$CAPEX_0$ M€	$OPEX_y$ M€
No B&V	0	0.91	-	-	40*	40*	1.88*	1.91	80.3	133	51
B	0	0.91	5*	-	40*	40*	1.88*	1.91	80.3	134	51
V	0	0.91	-	25*	40*	40*	1.88*	1.91	80.3	133	51
B&V	0	0.91	5*	25*	40*	40*	1.88*	1.91	80.3	135	51
No B&V	5	0.90	-	-	40*	40*	1.88*	1.91	76.2	133	46
B	5	0.91	5*	-	40*	40*	1.88*	1.91	76.3	134	46
V	5	0.90	-	25*	40*	40*	1.88*	1.91	76.2	133	46
B&V	5	0.90	5*	25*	40*	40*	1.88*	1.91	76.3	135	46
No B&V	10	0.90	-	-	40*	40*	1.88*	1.91	75.7	133	46
B	10	0.90	5*	-	40*	40*	1.88*	1.91	75.7	134	46
V	10	0.90	-	25*	40*	40*	1.88*	1.91	75.7	133	46
B&V	10	0.90	5*	25*	40*	40*	1.88*	1.91	75.7	135	46

* At bound.

Table B.18.: Optimization results for the grid-connected case study for the high-price high-variable electricity price scenario for the 4 plant configurations, i.e., with both storage (B&V), with the hydrogen vessel (V), with battery (B), and without any storage (No B&V).

	Flexibility % h^{-1}	LCOM € kg^{-1}	$E_{b,\,nom}$ MWh	V m^3	N_{mod} -	p_{PEM} bar	β_{max} -	$\dot{m}_{H_2,MeOH,nom}$ t h^{-1}	$M_{MeOH,\,y}$ kt	$CAPEX_0$ M€	$OPEX_y$ M€
No B&V	0	2.02	-	-	40*	31.5	2.38	1.91	80.7	135	141
B	0	2.01	116	-	40*	31.6	2.38	1.91	80.7	171	135
V	0	1.88	-	4940	40*	40*	3.5*	1.15	48.5	162	65
B&V	0	1.86	115	4730	40*	40*	3.5*	1.11	47.0	196	57
No B&V	5	1.75	-	-	40*	40*	1.88*	1.91	49.5	133	64
B	5	1.74	115	-	40*	40*	1.88*	1.91	49.2	169	59
V	5	1.70	-	1320	40*	40*	3.5*	1.74	42.7	144	49
B&V	5	1.69	116	1210	40*	40*	3.5*	1.74	42.9	180	44
No B&V	10	1.73	-	-	40*	40*	1.88*	1.91	49.5	133	64
B	10	1.72	111	-	40*	40*	1.88*	1.91	49.3	168	58
V	10	1.69	-	1250	40*	40*	3.5*	1.74	42.7	144	49
B&V	10	1.68	116	1130	40*	40*	3.5*	1.74	42.4	179	43
No B&V	25	1.72	-	-	40*	40*	1.88*	1.91	49.4	133	63
B	25	1.71	115	-	40*	40*	1.88*	1.91	49.3	169	57
V	25	1.69	-	1100	40*	40*	3.5*	1.74	42.7	143	49
B&V	25	1.68	111	1040	40*	40*	3.5*	1.75	42.9	177	44

* At bound.

Table B.19.: Optimization results for the grid-connected case study for the high-price high-variable electricity price scenario with the reduced investment costs (Scenario 2030) for the 4 plant configurations, i.e., with both storage (B&V), with the hydrogen vessel (V), with battery (B), and without any storage (No B&V).

	Flexibility $\%\ h^{-1}$	LCOM € kg^{-1}	$E_{b,\,nom}$ MWh	V m^3	N_{mod} -	p_{PEM} bar	β_{max} -	$\dot{m}_{H_{2,MeOH},nom}$ t h^{-1}	$M_{MeOH,\,y}$ kt	$CAPEX_0$ M€	$OPEX_y$ M€
No B&V	0	2.00	-	-	40*	31.7	2.36	1.91	80.6	126	140
B	0	1.90	347	-	25	37.5	2.00	0.95	40.0	143	54
V	0	1.83	-	5430	40*	40*	1.88*	1.11	46.8	153	61
B&V	0	1.72	347	5470	39	40*	1.88*	0.95	40.0	212	37
No B&V	5	1.72	-	-	40*	40*	1.88*	1.91	48.7	124	63
B	5	1.62	347	-	33	40*	1.88*	1.57	40.0	168	39
V	5	1.66	-	1450	40*	40*	1.88*	1.70	41.6	135	47
B&V	5	1.54	347	1460	40*	40*	1.88*	1.65	40.0	195	32
No B&V	10	1.70	-	-	40*	40*	1.88*	1.91	48.8	124	62
B	10	1.60	347	-	33	40*	1.88*	1.57	40.0	168	38
V	10	1.65	-	1300	40*	40*	1.88*	1.71	41.5	134	47
B&V	10	1.54	347	1350	40*	40*	1.88*	1.60	40.0	197	31
No B&V	25	1.69	-	-	40*	40*	1.88*	1.91	48.8	124	62
B	25	1.59	347	-	34	40*	1.88*	1.62	40.0	171	37
V	25	1.65	-	1250	40*	40*	1.88*	1.74	41.9	134	47
B&V	25	1.54	347	1280	40*	40*	1.88*	1.65	40.0	197	31

* At bound.

Table B.20.: Optimization results for the grid-connected case study for the high-price high-variable electricity price scenario for the plant configurations with battery, i.e., with battery (B) and with both storage (B&V) for the current (a) and future (b) unit cost scenario: Utilization of the energy stored in the battery. Note: the tabled yearly revenue obtained by selling the electricity to the grid does not account for the purchase of the electricity.

	Flexibility % h^{-1}	Yearly energy to PEM-WE GWh	Yearly energy to the grid GWh	Yearly revenue for the electricity sell M€
B	0	83.1	0.1	0
B&V	0	26.9	54.3	11.9
B	25	49.3	34.6	8.2
B&V	25	31.1	49.8	11.5

(a) Current unit cost scenario.

	Flexibility % h^{-1}	Yearly energy to PEM-WE GWh	Yearly energy to the grid GWh	Yearly revenue for the electricity sell M€
B	0	95.3	88.8	17.6
B&V	0	33.0	150.7	32.2
B	25	72.1	110.2	25.0
B&V	25	48.5	134.9	30.6

(b) Future unit cost scenario.

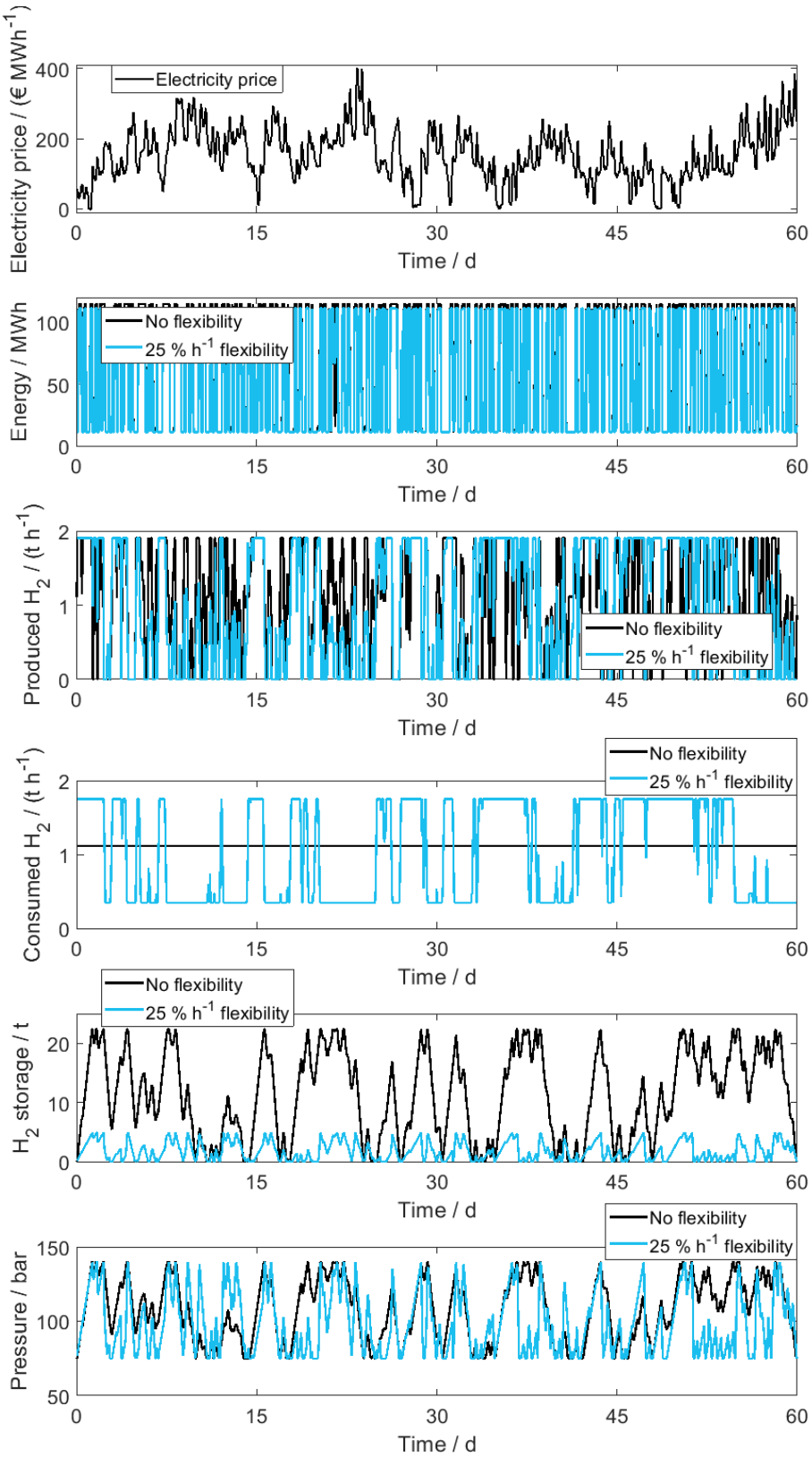


Figure B.3.: Energy content of the battery, H_2 produced by the electrolyzer, H_2 consumed in the methanol plant, and H_2 content and pressure inside the H_2 vessel for the "No flexibility" and "25 % h^{-1} flexibility" cases for the current unit cost scenario. Only the results of the "Battery & Vessel" configuration are shown. The electricity cost profile is also shown to interpret the optimal scheduling better. Note: the energy profiles of the battery for the "No flexibility" and "25 % h^{-1} flexibility" cases are similar, thus they can hardly be distinguished in the picture.

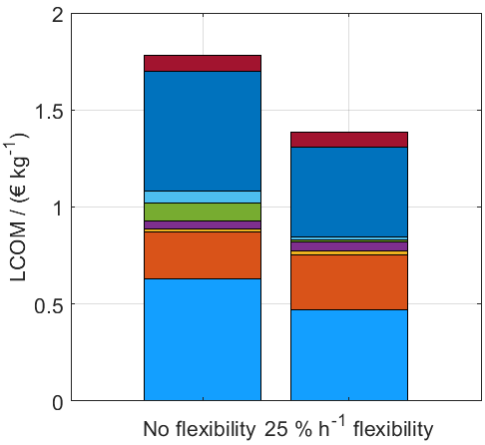
B.6.2. Stand-alone Power-to-Methanol case study

The contribution of the process units to the methanol production cost, the optimal design variables, and the key performance metrics for the two power availability scenarios of the stand-alone case study are shown in Figure B.4 and Table B.21. Despite considering two extremely different power generation scenarios, i.e., a winter generation profile dominated by wind production and a summer generation profile with high peaks due to PV generation, the optimal design of the PtMeOH plants does not have extreme differences. This might be due to the similar size of the photovoltaic and wind power plants and to the complementarity effect of renewables, which affects the need for storage and the costs [46, 281].

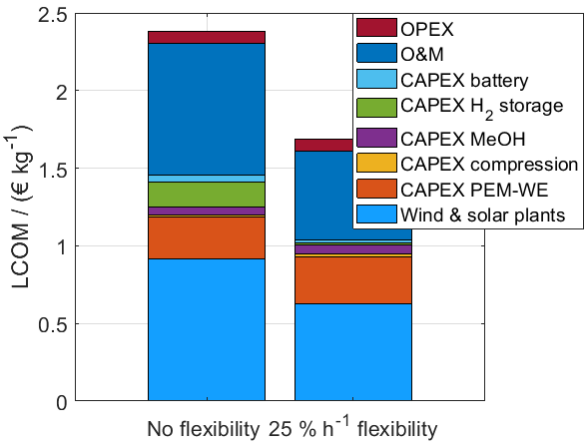
Figures B.5 and B.6 show how the battery and the H_2 storage are optimally operated for the considered scenarios. Both storage technologies are operated on a daily basis to cope with the high power peaks due to the PV generation during the May-Jun scenario (Figure B.5) when flexibility of the methanol synthesis plant is allowed. In fact, the possibility of varying the methanol production rate in periods of renewable production shortage reduces the need for high amounts of stored hydrogen and long-term storage. A similar operation can be noticed for the Nov-Dec scenario (Figure B.6). The main difference lies in the longer duration of the hold phase of both storage technologies, and it is probably due to the scenario, which is characterized by a relevant wind power generation that has different characteristic times from PV generation. Nevertheless, these hold phases last a few days at most since the methanol synthesis plant is assumed to be always operating over the scenario duration.

The duration of the hold phase of storage suggests that shorter time frames could have been considered for scheduling. Nevertheless, even longer time frames would allow for taking into account the seasonality of power generation in the design phase. This aspect is particularly evident from the design differences when considering two power generation profiles of the same renewable park in two periods of the year (Table B.21). In fact, the optimal design of the PtMeOH plant for the Nov-Dec scenario leads to a higher production cost of methanol when the plant is optimally operated in the May-Jun scenario (1.43 € kg^{-1} instead of 1.39 € kg^{-1}). Nevertheless, the relative difference between the methanol production cost for the two power generation scenarios is probably lower than the level of uncertainty of the model, thus meaning that considering a 2-month scenario for scheduling in the design phase already provides good indications of suitable plant designs. However, this might not be true when the ratio between the installed capacity of wind power and photovoltaic plants is quite different. In such cases, long-term hydrogen storage could be needed.

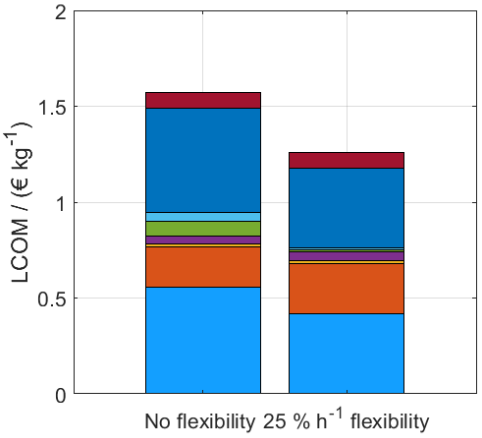
Finally, Table B.21 shows that moderate flexibility of the methanol plant already increases the consumption of the generated renewable energy (P_{renew} in the table), thus reducing the renewable curtailment: a ramp rate of 5 % h^{-1} already increases the renewable energy utilization from 66 %-72 % to 93 %-94 %. In the Nov-Dec scenario with a maximum ramp rate of the methanol plant of 25 % h^{-1} for the current unit cost scenario, a slight increase of the renewable curtailment (93 % instead of 95 %) can be noticed compared to the case with 5 % h^{-1} as ramp rate. This result can be explained by the lower sizes of the electrolysis and methanol synthesis units.



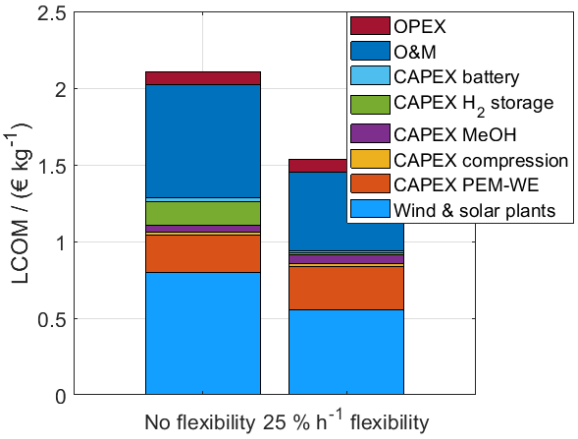
(a) May-Jun, Current unit cost scenario.



(b) Nov-Dec, Current unit cost scenario.



(c) May-Jun, Future unit cost scenario.



(d) Nov-Dec, Future unit cost scenario.

Figure B.4.: Relative contribution to the methanol production cost (LCOM) of the investment cost of the units and of the operating costs for the "No flexibility" and "25 % h^{-1} flexibility" cases for the "May-Jun" and "Nov-Dec" scenarios. The current and future unit cost scenarios are shown at the top and bottom of the figure, respectively. Note: the high share of O&M in the methanol production cost is due to the fact that the O&M expenditures of the renewable generation park are included.

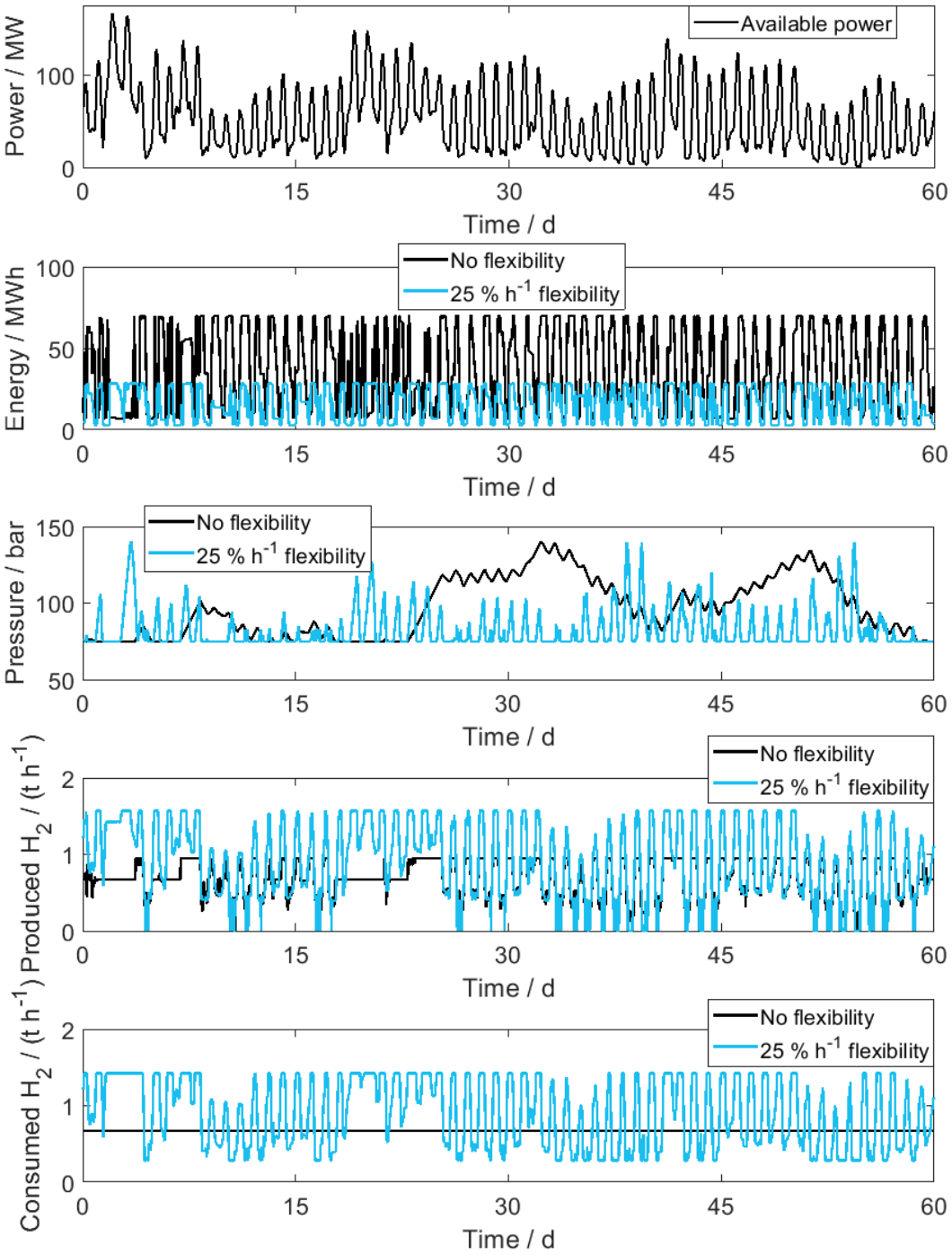


Figure B.5.: Energy content of the battery, H_2 pressure inside the H_2 vessel, H_2 produced by the electrolyzer, and H_2 converted in the methanol plant for the "No flexibility" and "25 % h^{-1} flexibility" cases for the current unit cost scenario. The power availability profile (May-Jun scenario) is also shown to interpret the optimal scheduling better.

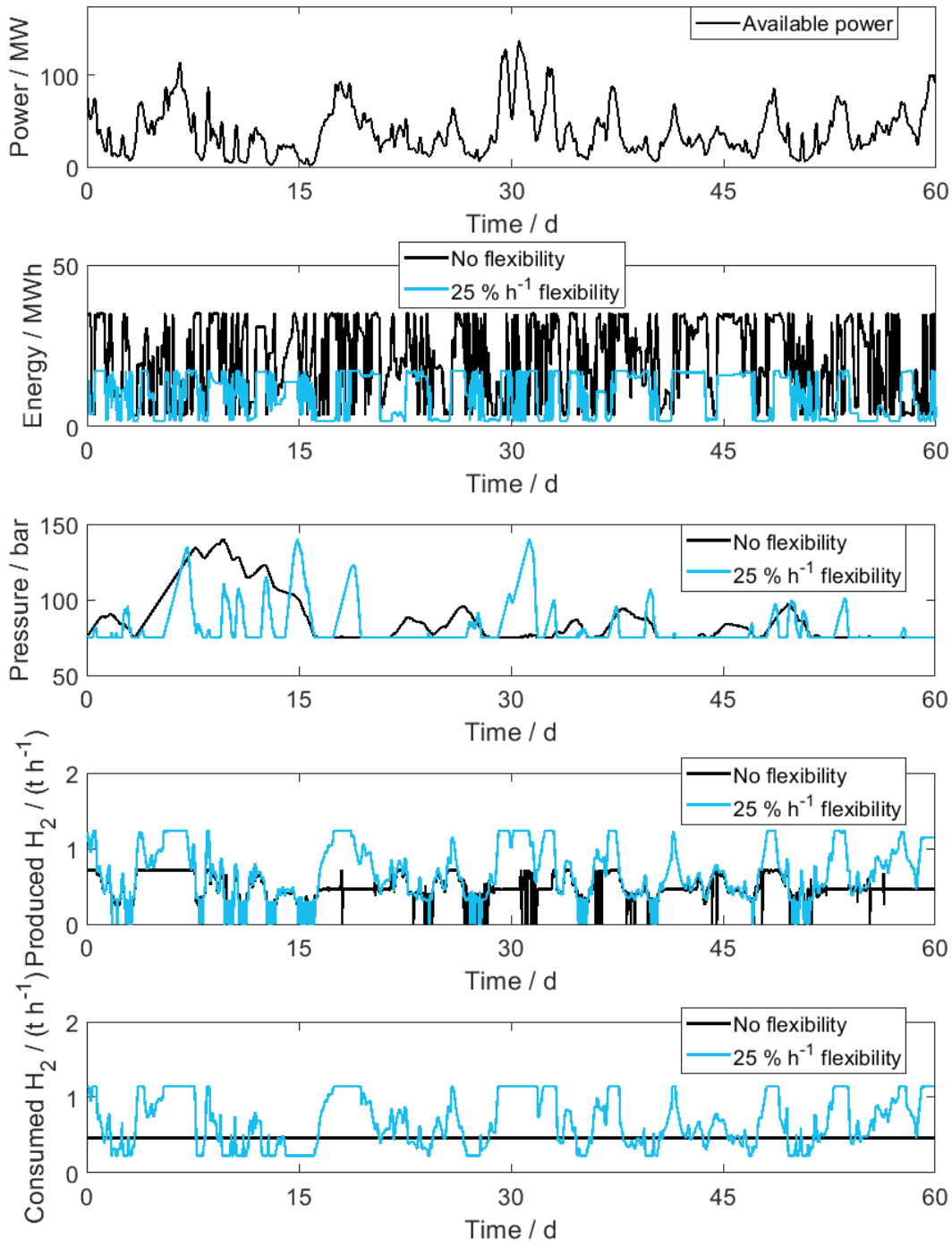


Figure B.6.: Energy content of the battery, H_2 pressure inside the H_2 vessel, H_2 produced by the electrolyzer, and H_2 converted in the methanol plant for the "No flexibility" and "25 % h^{-1} flexibility" cases for the current unit cost scenario. The power availability profile (Nov-Dec scenario) is also shown to interpret the optimal scheduling better.

Table B.21.: Optimization results for the stand-alone case study for the considered renewable power availability scenarios (May-Jun and Nov-Dec) for both current (a) and future (b) unit cost scenarios.

	Flexibility	LCOM	$E_{b,nom}$	V	N_{mod}	p_{PEM}	β_{max}	$\dot{m}_{H_{2,MeOH},nom}$	$M_{MeOH,y}$	$CAPEX_0$	$OPEX_y$	P_{renew}
	% h^{-1}	€ kg^{-1}	MWh	m^3	-	bar	-	t h^{-1}	kt	M€	M€	%
May-Jun	0	1.78	70	5000	20	40*	3.5*	0.67	28.3	350	2	71 %
May-Jun	5	1.40	27	800	33	40*	3.5*	1.43	37.9	350	3	93 %
May-Jun	25	1.39	28	510	33	40*	3.5*	1.43	37.9	349	3	93 %
Nov-Dec	0	2.38	35	5930	15	40*	3.5*	0.46	19.5	329	2	66 %
Nov-Dec	5	1.70	23	940	28	40*	3.5*	1.22	29.2	335	2	95 %
Nov-Dec	25	1.69	17	840	26	40*	3.5*	1.15	28.5	327	2	93 %

(a) Current unit cost scenario.

	Flexibility	LCOM	$E_{b,nom}$	V	N_{mod}	p_{PEM}	β_{max}	$\dot{m}_{H_{2,MeOH},nom}$	$M_{MeOH,y}$	$CAPEX_0$	$OPEX_y$	P_{renew}
	% h^{-1}	€ kg^{-1}	MWh	m^3	-	bar	-	t h^{-1}	kt	M€	M€	%
May-Jun	0	1.57	100	4500	20	40*	3.5*	0.68	28.8	312	2	72 %
May-Jun	5	1.27	30	810	33	40*	3.5*	1.45	38.0	317	3	93 %
May-Jun	25	1.26	37	500	33	40*	3.5*	1.45	38.1	316	3	93 %
Nov-Dec	0	2.10	36	6300	16	40*	3.5*	0.48	20.0	298	2	69 %
Nov-Dec	5	1.53	22	820	27	40*	3.5*	1.19	28.9	298	2	94 %
Nov-Dec	25	1.53	16	880	27	40*	3.5*	1.18	28.8	298	2	94 %

* At bound.

(b) Future unit cost scenario.

Appendix C.

Additional Information to Chapter 5

C.1. Power-to-Methanol process with intermediate storage: Cost estimation

The investment cost of the process units is calculated according to the correlations in Biegler et al. [294] and technology-specific literature values as described in Section 4.3. However, a correction for inflation to the year 2023 (instead of 2021) via the CEPCI [292] was considered.

A summary of the considered specific investment costs can be found in Table C.1, while the main assumptions of the economic analysis are summarized in Table C.2.

Table C.1.: Considered values for the investment costs for the process units. The costs are referred to the year 2023.

	Values
Battery	0.31 M€ MWh^{-1} [382]
PEM water electrolyzer*	1.21-1.27 M€ MW^{-1} [87]
Hydrogen storage	8.8 k€ m^{-3} [379]
Methanol synthesis plant**	31.3 M€ [4]

* Size-dependent correlation; it includes a 1.75 factor for the auxiliaries.
** Reference plant with a yearly production of 0.08 Mt.

Table C.2.: Main assumptions for the economic evaluation.

	Values
Reference year	2023
$ to € conversion factor	0.924
Plant lifetime	20 y
Operating weeks per year for the methanol synthesis plant	48 w y^{-1}
Yearly O&M as % of the initial investment cost ($CAPEX_0$)	5 %
Interest rate i	5 %
Cooling cost	0.1 € MWh^{-1}
CO_2 stream cost	50 € t^{-1}

C.2. Additional results

C.2.1. Optimal design vs. scheduling: Design variables

Figure C.1 shows the design variable values for the most important case studies, i.e., "Flexible: Battery & PEM-WE" and "Flexible: Battery, PEM-WE, & MeOH" (Section 5.2.3).

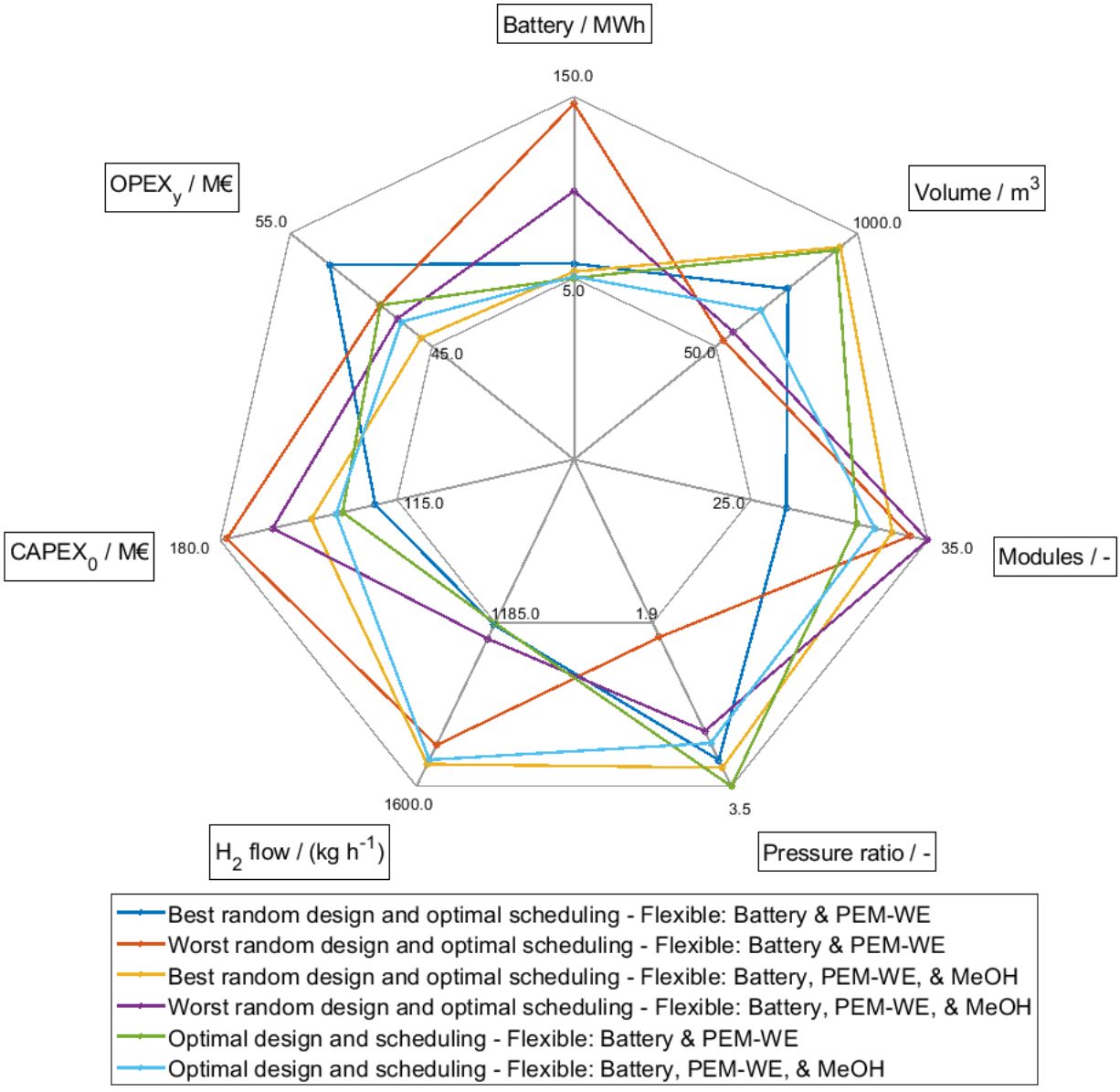


Figure C.1.: Comparison of the design variables, initial investment costs (CAPEX), and the average of the yearly operating costs over the electricity price scenarios ($OPEX_y$) for the cases with random designs and optimal designs when the scheduling is optimized considering "Flexible: Battery & PEM-WE" and "Flexible: Battery, PEM-WE, & MeOH". Note that we hereby report only the random designs that lead to the best and worst LCOMs displayed in Figure 5.2.

The (random) process designs leading to the best LCOMs when the methanol synthesis unit is operated in either steady state or flexibly differ; the same applies for the designs

leading to the worst LCOMs. This suggests that the operation mode of the downstream hydrogen conversion process can significantly affect the performance of a certain process design. For instance, the process design leading to the worst LCOM when the methanol process is operated in steady state has a relatively high nominal hydrogen flow rate that can be supplied to the methanol plant, which cannot actually be exploited. In contrast, the process design leading to the best LCOM when flexible operation of the methanol process is allowed has an even higher nominal hydrogen flow rate to increase the process flexibility margin.

Further, when the methanol process is operated in steady state, a moderate oversizing of the electrolysis unit combined with some hydrogen storage is economically beneficial. In combination with these design choices, oversizing the methanol production unit is also economically favorable when allowing methanol process flexibility: it leads to higher investment costs, but also to lower yearly operating costs (compare yellow and green lines in Figure C.1).

C.2.2. Additional data analysis

C.2.2.1. Cross-correlation among design variables

The correlation among the design variables is shown in Figure C.2. The variable cross-correlation coefficients show weak-to-no correlation, thus meaning that the considered data

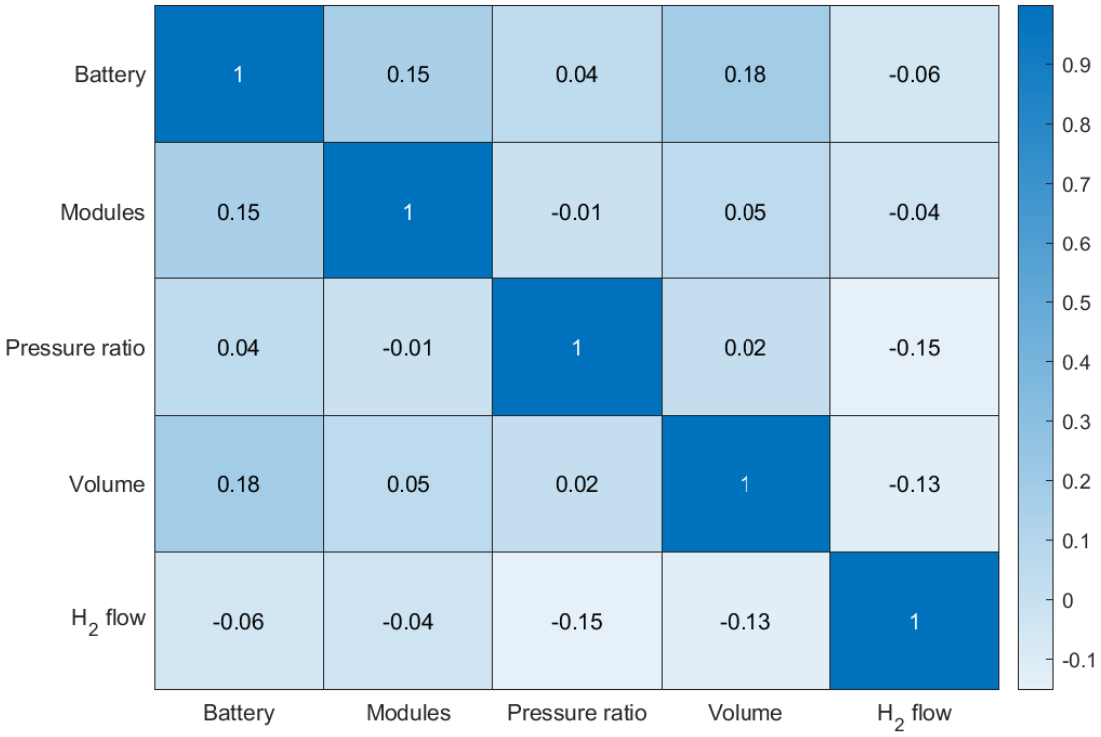


Figure C.2.: Correlation coefficients among the 100 design variable combinations generated via Latin Hypercube Sampling.

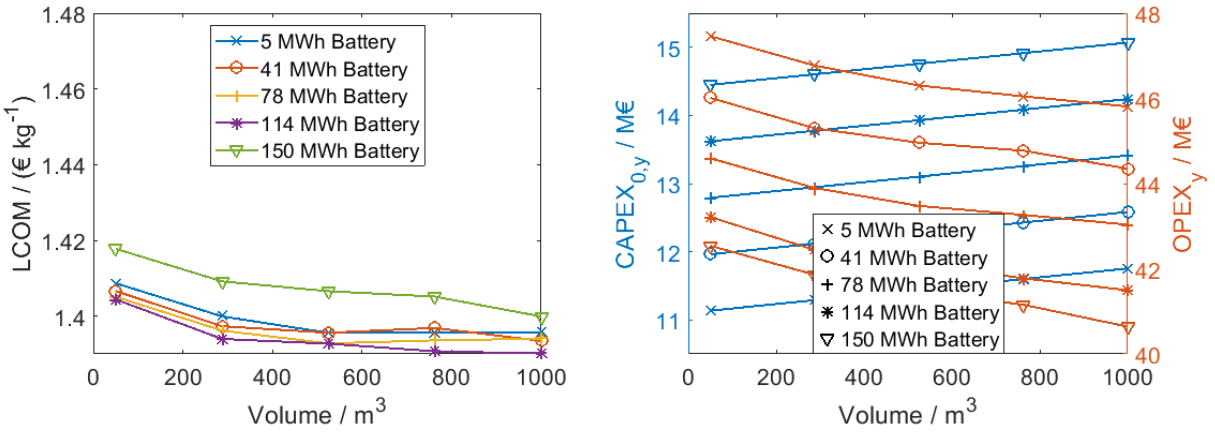
is statistically relevant for the correlation analysis between the design variables and the objective function.

C.2.2.2. Sensitivity to process design

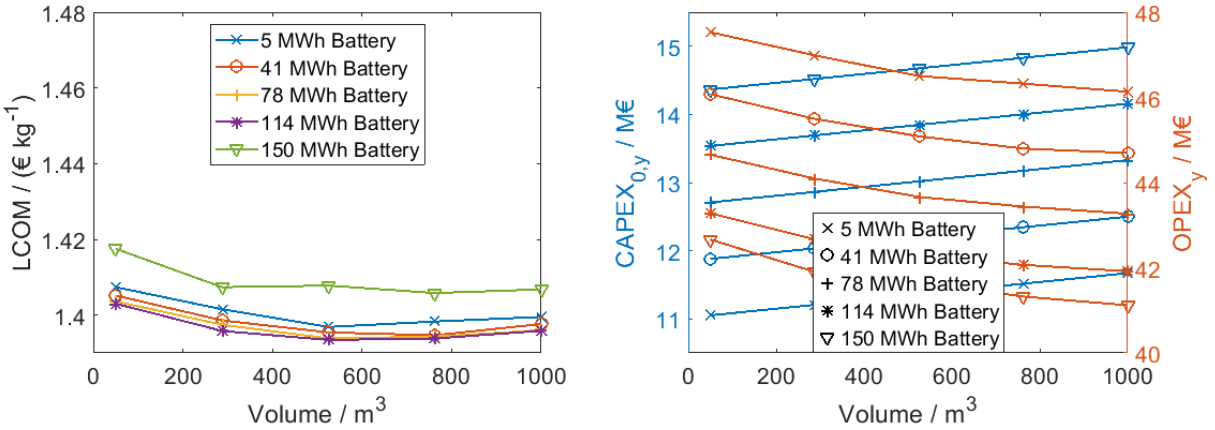
To better analyze the relationship between the design variables and the objective function as well as its sensitivity to the considered design variable values, we fixed the electrolyzer and methanol synthesis unit sizes (best values from the stochastic scheduling case shown in Figure C.1) and optimized the stochastic scheduling for different combinations of the remaining design variables.

The results in Figure C.3 show that the objective function does not exhibit significant variations (generally below 1 %) for a wide range of the storage sizes, despite being the electrolyzer and methanol plant sized for a different process configuration. The process thus shows a relatively low sensitivity to these design variables under the considered economic assumptions most likely because of three concurrent reasons: 1) the considered objective function captures the trade-off between investment and operating costs (Figure C.3), 2) several electricity price scenarios are simultaneously considered in S-CDS problems, meaning that a process design change can favorably affect costs in some scenarios and unfavorably in other ones, leading to marginal changes in the objective function, and 3) the high operating flexibility of the key process units that can offset most of the benefits or losses related to size changes of the other process units.

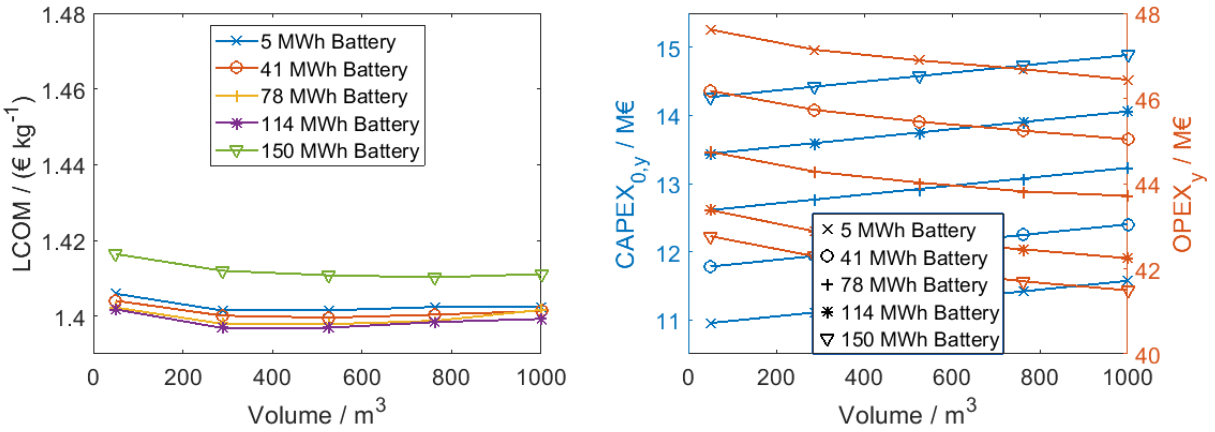
Interestingly, the case with a nominal battery capacity of 150 MWh always represents an outlier in Figure C.3 (LCOM higher than for the case of 114 MWh). This is probably due to the operating constraints that limit the minimum energy content in the battery and the maximum power exchange within one hour (100 MW). Also, exploiting the available H_2 storage by increasing the pressure ratio of the compression unit seems to be beneficial for the considered electrolysis and methanol plant size combination. This might be due to the cost correlation of the hydrogen storage, which is not pressure-dependent.



(a) Maximum pressure ratio of the compression unit equal to 3.5.



(b) Maximum pressure ratio of the compression unit equal to 3.0.



(c) Maximum pressure ratio of the compression unit equal to 2.5.

Figure C.3.: Sensitivity analysis of the objective function (LCOM) calculated by solving a stochastic scheduling problem, initial investment costs ($CAPEX_0$) annualized over the plant lifetime, and the average of the yearly operating costs over the electricity price scenarios ($OPEX_y$) for fixed process designs. In particular, the battery storage and hydrogen storage sizes as well as the maximum pressure ratio of the compression unit are varied. In contrast, the electrolyzer and methanol plant sizes are kept equal to the ones of the best process design found in the preliminary analysis, i.e., 33 electrolysis modules and 1.54 t h^{-1} of nominal hydrogen flow rate supplied to the methanol synthesis unit (see Figure C.1).

C.3. Considered scenario clustering approaches

In Table C.3, the considered scenario clustering approaches are listed. In particular, the scenario clustering approaches 1-6 apply k-medoids to single features, e.g., mean, extracted from the electricity price scenarios. The scenario clustering approaches 7-11 apply k-medoids to a matrix B where several features are combined. In contrast, the scenario clustering approaches 12 and 13 apply k-medoids and k-means directly to the original scenario time series.

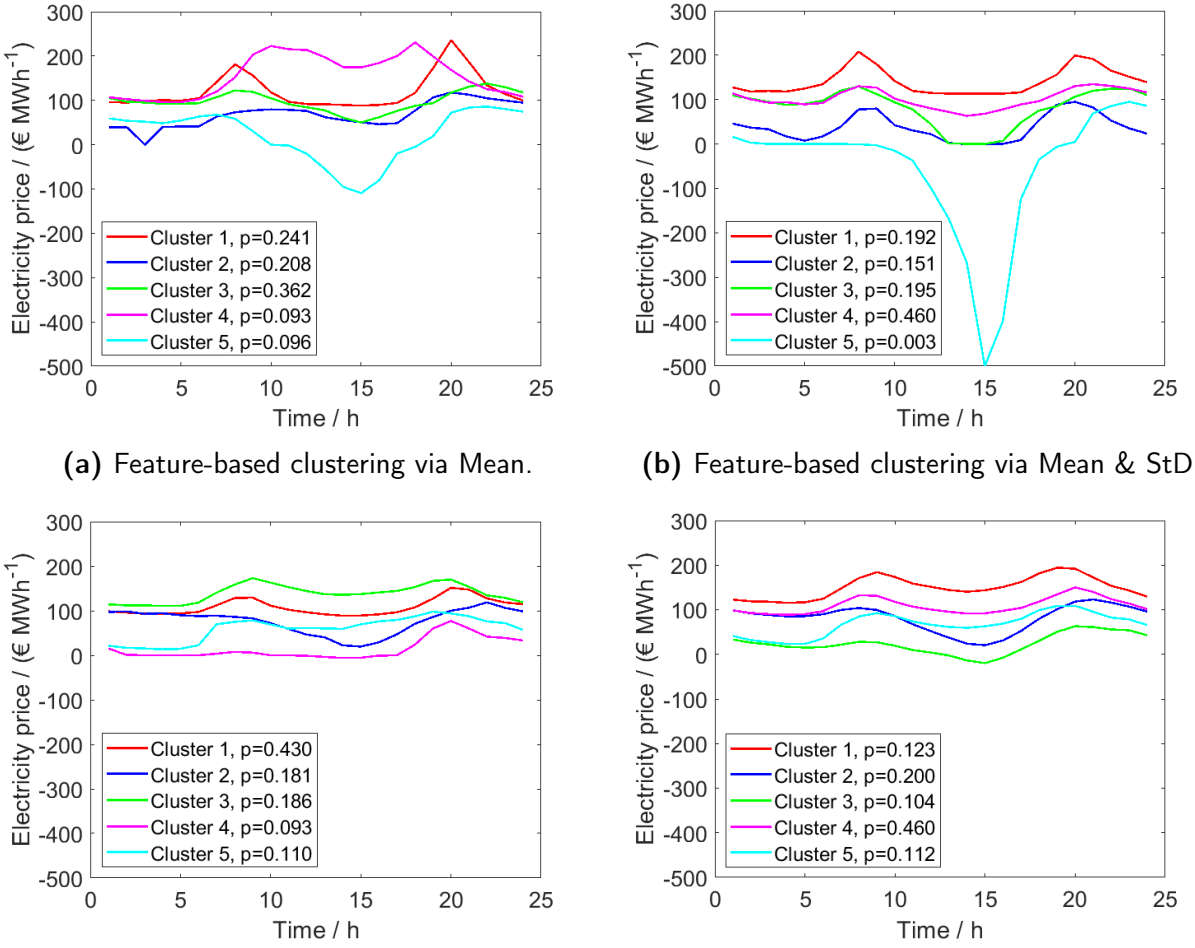
Additional information on the size of the matrix B seen by the k-medoids and k-means clustering approaches, as well as the corresponding cluster centers c, is provided in Table C.3. Note that all cluster centers obtained via k-medoids belong to B, thus meaning that the scenarios corresponding to the centers belong to the original space, differently from cluster centers obtained via k-means.

Table C.3.: Summary of the scenario clustering approaches for a single stochastic variable. Note that B is the matrix seen by the k-medoids method, C is the matrix with the cluster medoids and centroids, N_{TS}, N_{scen}, and $N_{\mathrm{scen,\,red}}$ are the number of time steps per scenario, the number of scenarios, and the number of scenario clusters, respectively. Note that, for feature-based scenario clustering (approaches 1–11), the cluster medoids are used to identify the corresponding (time-dependent) scenarios.

#	Approach	Matrix B	Matrix C
1	k-Medoids: Mean	$B \in \mathbb{R}^{1 \times N_{\mathrm{scen}}}$	$C \in \mathbb{R}^{1 \times N_{\mathrm{scen,\,red}}}$
2	k-Medoids: Standard deviation (StD)	$B \in \mathbb{R}^{1 \times N_{\mathrm{scen}}}$	$C \in \mathbb{R}^{1 \times N_{\mathrm{scen,\,red}}}$
3	k-Medoids: Skewness	$B \in \mathbb{R}^{1 \times N_{\mathrm{scen}}}$	$C \in \mathbb{R}^{1 \times N_{\mathrm{scen,\,red}}}$
4	k-Medoids: Kurtosis	$B \in \mathbb{R}^{1 \times N_{\mathrm{scen}}}$	$C \in \mathbb{R}^{1 \times N_{\mathrm{scen,\,red}}}$
5	k-Medoids: Mean absolute difference*	$B \in \mathbb{R}^{1 \times N_{\mathrm{scen}}}$	$C \in \mathbb{R}^{1 \times N_{\mathrm{scen,\,red}}}$
6	k-Medoids: 1st principal component	$B \in \mathbb{R}^{1 \times N_{\mathrm{scen}}}$	$C \in \mathbb{R}^{1 \times N_{\mathrm{scen,\,red}}}$
7	k-Medoids: Mean & StD	$B \in \mathbb{R}^{2 \times N_{\mathrm{scen}}}$	$C \in \mathbb{R}^{2 \times N_{\mathrm{scen,\,red}}}$
8	k-Medoids: Mean, StD, & Skewness	$B \in \mathbb{R}^{3 \times N_{\mathrm{scen}}}$	$C \in \mathbb{R}^{3 \times N_{\mathrm{scen,\,red}}}$
9	k-Medoids: Mean, StD, Skewness, & Kurtosis	$B \in \mathbb{R}^{4 \times N_{\mathrm{scen}}}$	$C \in \mathbb{R}^{4 \times N_{\mathrm{scen,\,red}}}$
10	k-Medoids: Mean, StD, Skewness, Kurtosis, & Mean Absolute Difference*	$B \in \mathbb{R}^{5 \times N_{\mathrm{scen}}}$	$C \in \mathbb{R}^{5 \times N_{\mathrm{scen,\,red}}}$
11	k-Medoids: 1st & 2nd principal components	$B \in \mathbb{R}^{2 \times N_{\mathrm{scen}}}$	$C \in \mathbb{R}^{2 \times N_{\mathrm{scen,\,red}}}$
12	k-Medoids: full time series	$B \in \mathbb{R}^{N_{\mathrm{TS}} \times N_{\mathrm{scen}}}$	$C \in \mathbb{R}^{N_{\mathrm{TS}} \times N_{\mathrm{scen,\,red}}}$
13	k-Means: full time series	$B \in \mathbb{R}^{N_{\mathrm{TS}} \times N_{\mathrm{scen}}}$	$C \in \mathbb{R}^{N_{\mathrm{TS}} \times N_{\mathrm{scen,\,red}}}$

* Mean absolute difference $= \sum_{t=2}^{N_{\mathrm{TS}}} \frac{|x(t)-x(t-1)|}{N_{\mathrm{TS}}-1}$.

Considering different features for clustering leads to different scenario cluster centers and probabilities (see, for instance, Figure C.4, where the cluster centers of four exemplary clustering approaches are shown).



(a) Feature-based clustering via Mean.

(b) Feature-based clustering via Mean & StD.

(c) k-medoids.

(d) k-means.

Figure C.4.: Daily electricity price profiles and their probability resulting from the clustering of day-ahead electricity prices for Germany in the year 2023 [299]. Figures (a) and (b) show the profiles obtained via feature-based clustering via mean and mean & standard deviation (StD), respectively. Figures (c) and (d) show the profiles obtained by directly clustering the original scenario time series via k-medoids and k-means applied to the original time series, respectively.

C.4. Reformulation of the optimization problem with DoF reduction

As shown in Section 5.3.2, the number of DoFs of the scheduling variables for each scenario can be reduced while maintaining memory of the time step chronology via a linear mapping matrix A_{dof}.

Three equivalent formulations of the optimization problem have been implemented and compared with respect to their numerical complexity. For the sake of simplicity, no selective DoF reduction has been considered when presenting the following formulations. Also, the dependency of the scheduling variables $\boldsymbol{s}_n$ on the input scenario $\boldsymbol{c}_n$ is hereby not displayed.

The first formulation (OP C.1) introduces additional scheduling variables $\tilde{\boldsymbol{s}}_{\mathrm{dof},n}$ as well as N_{TS} equality constraints for each scheduling variable, where N_{TS} is the number of time steps of each scenario. This formulation has the advantage that the original optimization

model is not modified, but additional variables and equalities are added, which overall reduce the number of DoFs. In fact, all equality and inequality constraints of the model are in the original time domain.

$$\begin{aligned}
&\min_{\boldsymbol{d},\, \tilde{\boldsymbol{s}}_{\text{dof}}} \left(\sum_{n=1}^{N_{\text{scen, red}}} p_{\text{red},n} \cdot \text{Obj}_n(\boldsymbol{d}, \boldsymbol{s}_n) \right) \\
&s.t. \\
&\quad \boldsymbol{s}_n = A_{\text{dof},\,n} \cdot \tilde{\boldsymbol{s}}_{\text{dof},\,n} && n = 1, ..., N_{\text{scen, red}} \\
&\quad h_n(\boldsymbol{d},\, \boldsymbol{s}_n) = 0 && n = 1, ..., N_{\text{scen, red}} \\
&\quad g_n(\boldsymbol{d},\, \boldsymbol{s}_n) \leq 0 && n = 1, ..., N_{\text{scen, red}},
\end{aligned} \tag{OP C.1}$$

where $\boldsymbol{d} \in \mathbb{R}^{N_{\text{design var}}}$, $\boldsymbol{s} \in \mathbb{R}^{N_{\text{scen, red}} \times N_{\text{scheduling var}} \times N_{\text{TS}}}$, $\tilde{\boldsymbol{s}}_{\text{dof}} \in \mathbb{R}^{N_{\text{scheduling var}} \times N_{\text{scen, red}} \times N_{\text{dof, sched}}}$, and $N_{\text{dof, sched}}$ is the number of DoFs per scheduling variable.

The second formulation (OP C.2) does not introduce additional variables, but requires equality constraints of higher complexity since every scheduling variable $\boldsymbol{s}_n$ is defined as a linear combination of all scheduling variables in the original time domain.

$$\begin{aligned}
&\min_{\boldsymbol{d},\, \boldsymbol{s}} \left(\sum_{n=1}^{N_{\text{scen, red}}} p_{\text{red},n} \cdot \text{Obj}_n(\boldsymbol{d}, \boldsymbol{s}_n) \right) \\
&s.t. \\
&\quad \boldsymbol{s}_n = A_{\text{dof},\,n} \cdot D_{\text{dof},\,n} \cdot \boldsymbol{s}_n && n = 1, ..., N_{\text{scen, red}} \\
&\quad h_n(\boldsymbol{d}, \boldsymbol{s}_n) = 0 && n = 1, ..., N_{\text{scen, red}} \\
&\quad g_n(\boldsymbol{d}, \boldsymbol{s}_n) \leq 0 && n = 1, ..., N_{\text{scen, red}},
\end{aligned} \tag{OP C.2}$$

where $\boldsymbol{d} \in \mathbb{R}^{N_{\text{design var}}}$ and $\boldsymbol{s} \in \mathbb{R}^{N_{\text{scen, red}} \times N_{\text{scheduling var}} \times N_{\text{TS}}}$.

The equality constraints for this formulation are obtained by rearranging the equation system that linearly maps the scheduling variables of the original time domain to the scheduling variables in the reduced DoF domain ($\boldsymbol{s}_n = A_{\text{dof},\,n} \cdot \tilde{\boldsymbol{s}}_{\text{dof},\,n}$). First, $\tilde{\boldsymbol{s}}_{\text{dof},n}$ is obtained via product with matrices:

$$(A_{\text{dof},n}^T \cdot A_{\text{dof},n})^{-1} \cdot A_{\text{dof},n}^T \cdot \boldsymbol{s}_n = (A_{\text{dof},n}^T \cdot A_{\text{dof},n})^{-1} \cdot (A_{\text{dof},n}^T \cdot A_{\text{dof},n}) \cdot \tilde{\boldsymbol{s}}_{\text{dof},n} = \tilde{\boldsymbol{s}}_{\text{dof},n}.$$

Then, the obtained $\tilde{\boldsymbol{s}}_{\text{dof},n}$ expression is substituted in the original linear mapping problem with $D_{\text{dof},n} := (A_{\text{dof},n}^T \cdot A_{\text{dof},n})^{-1} \cdot A_{\text{dof},n}^T$.

Finally, the third problem formulation (OP C.3), i.e., the reduced space formulation [362], requires modifying the model equations written in the original time domain via direct substitution of the scheduling variables in the reduced time domain via the equality constraints.

$$\begin{aligned}
&\min_{\boldsymbol{d},\ \tilde{\boldsymbol{s}}_{\text{dof}}} \left(\sum_{n=1}^{N_{\text{scen, red}}} p_{\text{red},n} \cdot \text{Obj}_n(\boldsymbol{d}, A_{\text{dof},\,n} \cdot \tilde{\boldsymbol{s}}_{\text{dof},\,n}) \right) \\
&s.t. \\
&\quad h_n(\boldsymbol{d}, A_{\text{dof},\,n} \cdot \tilde{\boldsymbol{s}}_{\text{dof},\,n}) = 0 && n = 1, ..., N_{\text{scen, red}} \\
&\quad g_n(\boldsymbol{d}, A_{\text{dof},\,n} \cdot \tilde{\boldsymbol{s}}_{\text{dof},\,n}) \leq 0 && n = 1, ..., N_{\text{scen, red}},
\end{aligned} \tag{OP C.3}$$

where $\boldsymbol{d} \in \mathbb{R}^{N_{\text{design var}}}$ and $\tilde{\boldsymbol{s}}_{\text{dof}} \in \mathbb{R}^{N_{\text{scen, red}} \times N_{\text{scheduling var}} \times N_{\text{dof, sched}}}$.

To compare the formulations, we show in Table C.4 the model statistics of a S-CDS problem for a grid-connected Power-to-Methanol case study with three scenarios and $N_{\text{dof, sched}} = 18$. The first two formulations increase the number of variables and equations compared to the model without DoF reduction. Note that GAMS does not distinguish between degrees of freedom and variables that are determined by equality constraints. Moreover, there is no reduction of the instructions needed to handle model nonlinearities (NL_{code} value), which is an indicator of the model complexity. Thus, no significant computational improvement can be expected. In contrast, the reduced space formulation effectively reduces the number of variables and the size of the optimization problem as well as the NL_{code}, thus being potentially more computationally efficient. Nonetheless, the computational benefits of applying DoF reduction depend on the solver and problem numerics.

The reduced space formulation for DoF reduction was considered in the main paper.

Table C.4.: Model statistics of the considered optimization problem formulations, i.e., the grid-connected case study without DoF reduction, and the three optimization problem formulations.

$N_{\text{dof, sched}}$	DoF reduction	Equations	Continuous variables	Integer variables	NL_{code}
168	-	11603	8083	1513	31822
18	With additional variables (OP C.1)	14123	8353	1513	31822
18	Without additional variables (OP C.2)	14073	8083	1513	31822
18	Reduced space (OP C.3)	5753	3133	163	12472

C.5. Process model for objective function under-estimation

In order to obtain a lower bound of the objective function of the original S-CDS problem, i.e., in the original scenario space and DoF space, and thus estimate the accuracy of the considered clustering approaches, the original problem considered in Section 5.3 has been simplified. In particular, the operating limits of the units have been relaxed, i.e., all units can be operated from 0 % to 100 % of their operating range (all binary variables have been removed). Also, the design optimization variable N_{modules} has been relaxed to a continuous variable to modify the problem formulation from MINLP to NLP. Furthermore, the complexity of the main nonlinearities resulting from the problem formulations, i.e., the electrolyzer efficiency law, the power calculation of the compression unit, and the cost correlation for the PEM-WE and methanol units, was reduced via linearization at the first order to ensure the under-estimation of the objective function.

Note that, while this relaxed optimization problem can provide an optimistic estimate of the objective function of the original problem, it cannot provide reliable optimal designs and scheduling, since the relaxation of the integer variables and operating constraints can lead to unfeasible process designs and scheduling in the original problem.

C.6. Weekly scenarios: Effect of clustering approaches and number of scenario clusters

In this section, additional results of the S-CDS optimization problems for the grid-connected PtMeOH process with intermediate storage solved for a weekly time horizon are shown. In particular, the results of the sensitivity analysis with respect to the number of scenario clusters for the battery storage, the number of electrolysis modules, and the maximum pressure ratio of the compression unit are shown in Figures C.5, C.6, and C.7, respectively.

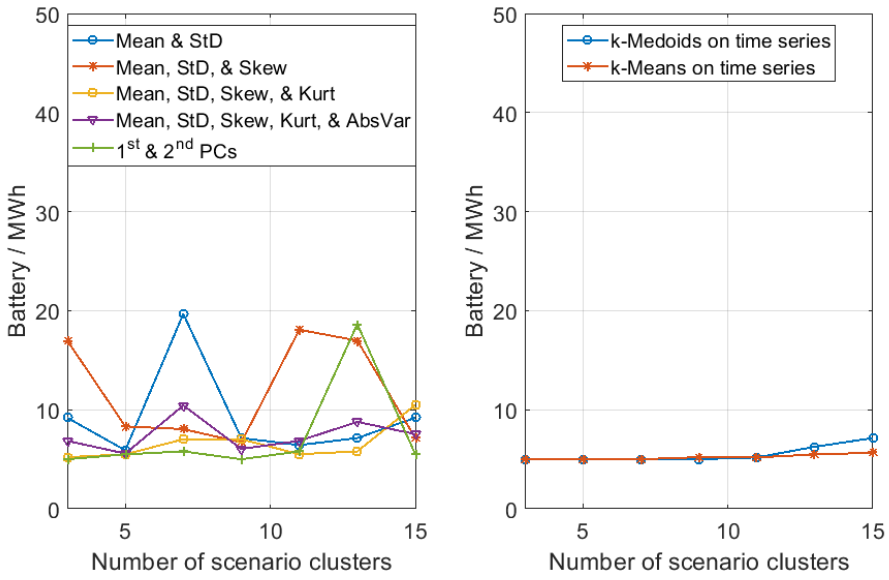


Figure C.5.: Battery capacity for the grid-connected PtMeOH case study for different numbers of weekly scenario clusters and clustering approaches ($N_{\mathrm{dof,\,sched}} = 18$). Left: Multi-feature clustering via k-medoids based on mean, standard deviation (StD), skewness (Skew), kurtosis (Kurt), the mean of the absolute variation between consecutive time steps (AbsVar), and principal components (PCs). Right: k-medoids and k-means clustering applied to the original scenario time series.

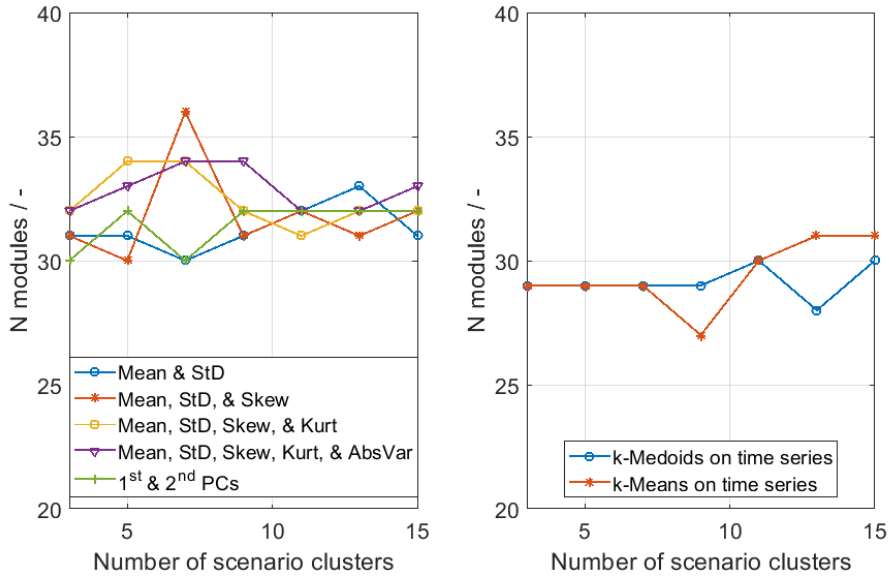


Figure C.6.: PEM water electrolyzer modules for the grid-connected PtMeOH case study for different numbers of weekly scenario clusters and clustering approaches ($N_{\mathrm{dof,\,sched}} = 18$). Left: Multi-feature clustering via k-medoids based on mean, standard deviation (StD), skewness (Skew), kurtosis (Kurt), the mean of the absolute variation between consecutive time steps (AbsVar), and principal components (PCs). Right: k-medoids and k-means clustering applied to the original scenario time series.

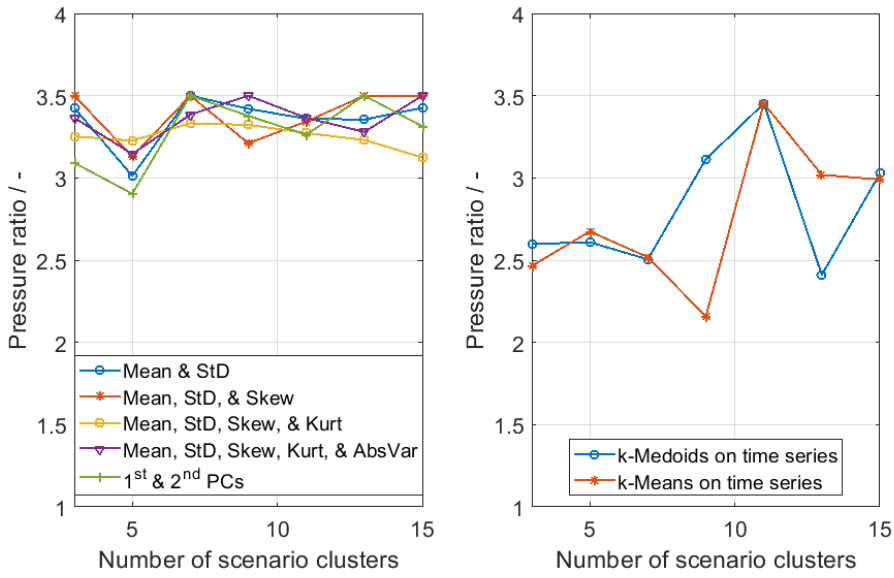


Figure C.7.: Maximum pressure ratio of the compression unit for the grid-connected PtMeOH case study for different numbers of weekly scenario clusters and clustering approaches ($N_{\mathrm{dof,\,sched}} = 18$). Left: Multi-feature clustering via k-medoids based on mean, standard deviation (StD), skewness (Skew), kurtosis (Kurt), the mean of the absolute variation between consecutive time steps (AbsVar), and principal components (PCs). Right: k-medoids and k-means clustering applied to the original scenario time series.

Bibliography

[1] S. Mucci, A. Mitsos, and D. Bongartz. Power-to-X processes based on PEM water electrolyzers: A review of process integration and flexible operation. *Computers & Chemical Engineering*, 175:108260, 2023. doi:10.1016/j.compchemeng.2023.108260.

[2] S. Mucci, A. Mitsos, and D. Bongartz. Combustion versus gasification in Power- and Biomass-to-X processes: An exergetic analysis. *ACS Omega*, 9(49):48213–48231, 2024. doi:10.1021/acsomega.4c05549.

[3] S. Mucci, D. P. Goldstein, D. Bongartz, and A. Mitsos. Exergo-techno-economic comparison of Power&Biomass-to-Kerosene pathways. In F. Manenti and G. V. Reklaitis, editors, *34th European Symposium on Computer Aided Process Engineering / 15th International Symposium on Process Systems Engineering*, volume 53 of *Computer Aided Chemical Engineering*, pages 2131–2136, 2024. doi:10.1016/B978-0-443-28824-1.50356-2.

[4] S. Mucci, A. Mitsos, and D. Bongartz. Cost-optimal Power-to-Methanol: Flexible operation or intermediate storage? *Journal of Energy Storage*, 72:108614, 2023. doi:10.1016/j.est.2023.108614.

[5] S. Mucci and D. Bongartz. Stochastic optimization of Power-to-Methanol: Production cost sensitivity to process design vs. scheduling. *AIChE Journal*, 72:e70265, 2026. doi:10.1002/aic.70265.

[6] S. Mucci and D. Bongartz. Feature-based scenario clustering and selective degrees of freedom reduction for two-stage stochastic optimization of Power-to-Methanol. *Chemical Engineering Research and Design*, 223:311–330, 2025. doi:10.1016/j.cherd.2025.09.046.

[7] S. Mucci, M.-D. Stumm, M. J. Rix, and A. Mitsos. Model-based evaluation of ammonia energy storage concepts at high technological readiness level. *Applied Energy*, 377(B):124495, 2025. doi:10.1016/j.apenergy.2024.124495.

[8] S. M. Krämer, A. S. Nielsen, S. Maier, S. Mucci, M. Hillestad, and O. S. Burheim. Power- and Biomass-to-Liquid processes with fuel-assisted solid oxide electrolysis cells and water gas shift-adjusted systems: A techno-economic analysis. *Fuel*, 396:135290, 2025. doi:10.1016/j.fuel.2025.135290.

[9] S. Mucci, J. F. Pyschik, E. J. Sim, A. Mitsos, and D. Bongartz. Combined design and operation optimization of a dynamic e-syngas fermentation process. *In preparation*, 2026.

[10] C. Mehler. Literature-based potential analysis of renewable production pathways for green methanol in Germany. Bachelor's thesis, Chair of Process Systems Engineering, RWTH Aachen University, 2022.

[11] C. Mehler. Beyond standard load profiles: Capturing heterogeneity and stochasticity in residential energy demand. Master's thesis, Chair of Process Systems Engineering, RWTH Aachen University, 2025.

[12] O. Stollenwerk. Modeling and optimization of a Reverse Water Gas Shift (RWGS) unit for the production of syngas. Bachelor's thesis, Chair of Process Systems Engineering, RWTH Aachen University, 2022.

[13] B. König. Modelling, simulation and optimal operation of a living-lab building energy system with seasonal hydrogen storage. Master's thesis, Chair of Process Systems Engineering, RWTH Aachen University, 2023.

[14] C. J. van Wersch. Modeling and optimization of a pilot plant for methanol synthesis via biogas reforming. Bachelor's thesis, Chair of Process Systems Engineering, RWTH Aachen University, 2023.

[15] J. Bothe. Preliminary design and analysis of new process concepts for future steam cracker plants with zero CO_2 emissions. Master's thesis, Chair of Process Systems Engineering, RWTH Aachen University, 2023.

[16] S. M. H. Rachi. Ammonia as a key player in chemical energy storage: A model-based study of ammonia to power technologies. Master's thesis, Chair of Process Systems Engineering, RWTH Aachen University, 2024.

[17] S. M. Krämer. Modeling of a fuel assisted power and biomass to liquid process. Master's thesis, Chair of Process Systems Engineering, RWTH Aachen University, 2024.

[18] M. Vander Elst. The production and application of "green" hydrogen starting from biogas from an anaerobic digester. Master's thesis, Chemical and Biochemical Reactor Engineering and Safety division, KU Leuven, 2024.

[19] J. Danko. Dynamic simulation of the production process of sustainable aviation fuels via high-temperature Fischer-Tropsch synthesis. Master's thesis, Chair of Process Systems Engineering, RWTH Aachen University, 2025.

[20] Core Writing Team, H. Lee and J. Romero (eds.). Climate change 2023: Synthesis report. Contribution of Working Groups I, II and III to the Sixth Assessment Report of the Intergovernmental Panel on Climate Change. Technical report, Intergovernmental Panel on Climate Change (IPCC), Geneva, Switzerland, 2023. doi:10.59327/IPCC/AR6-9789291691647.

[21] International Energy Agency (IEA). Net zero roadmap: A global pathway to keep the 1.5 °C goal in reach - 2023 update. Technical report, Paris, 2023. URL: https://www.iea.org/reports/net-zero-roadmap-a-global-pathway-to-keep-the-15-0c-goal-in-reach.

[22] A. Mitsos, N. Asprion, C. A. Floudas, M. Bortz, M. Baldea, D. Bonvin, A. Caspari, and P. Schäfer. Challenges in process optimization for new feedstocks and energy sources. *Computers & Chemical Engineering*, 113:209–221, 2018. doi:10.1016/j.compchemeng.2018.03.013.

[23] International Renewable Energy Agency (IRENA). *Electricity storage and renewables: Costs and markets to 2030*. Abu Dhabi, 2017.

[24] J. Burre, D. Bongartz, L. Brée, K. Roh, and A. Mitsos. Power-to-X: Between electricity storage, e-production, and demand side management. *Chemie-Ingenieur-Technik*, 92(1-2):74–84, 2020. doi:10.1002/cite.201900102.

[25] N. Bullerdiek, U. Neuling, and M. Kaltschmitt. *Powerfuels*. Springer Nature Switzerland, 2025. URL: https://link.springer.com/10.1007/978-3-031-62411-7, doi:10.1007/978-3-031-62411-7.

[26] C. Westerwalbesloh, G. Wang, and A. Mitsos. Power-to-Heat: Opportunities in reserve market participation for flexible chemical production. In *Proceedings of the 26th European Symposium on Computer Aided Process Engineering – ESCAPE 26*, volume 38, pages 2283–2288. Elsevier Masson SAS, 2016. doi:10.1016/B978-0-444-63428-3.50385-4.

[27] A. Sternberg and A. Bardow. Life cycle assessment of Power-to-Gas: Syngas vs methane. *ACS Sustainable Chemistry and Engineering*, 4(8):4156–4165, 2016. doi:10.1021/acssuschemeng.6b00644.

[28] J. Wyndorps, H. Ostovari, and N. von der Assen. Is electrochemical CO_2 reduction the future technology for power-to-chemicals? An environmental comparison with H_2-based pathways. *Sustainable Energy and Fuels*, 5(22):5748–5761, 2021. doi:10.1039/d1se00975c.

[29] K. M. Ebeling, D. Bongartz, S. Mürtz, R. Palkovits, and A. Mitsos. Thermodynamic and economic potential of glycerol oxidation to replace oxygen evolution in water electrolysis. *Industrial and Engineering Chemistry Research*, 63(18):8250–8260, 2024. doi:10.1021/acs.iecr.3c03615.

[30] L. Allgoewer, V. Becattini, A. Patt, P. Grandjean, J. F. Wiegner, M. Gazzani, and C. Moretti. Cost-effective locations for producing fuels and chemicals from carbon dioxide and low-carbon hydrogen in the future. *Industrial and Engineering Chemistry Research*, 63(31):13660–13676, 2024. doi:10.1021/acs.iecr.4c01287.

[31] D. Bongartz, L. Doré, K. Eichler, T. Grube, B. Heuser, L. E. Hombach, M. Robinius, S. Pischinger, D. Stolten, G. Walther, and A. Mitsos. Comparison of light-duty transportation fuels produced from renewable hydrogen and green carbon dioxide. *Applied Energy*, 231:757–767, 2018. doi:10.1016/j.apenergy.2018.09.106.

[32] S. Brynolf, M. Taljegard, M. Grahn, and J. Hansson. Electrofuels for the transport sector: A review of production costs. *Renewable and Sustainable Energy Reviews*, 81(5):1887–1905, 2018. doi:10.1016/j.rser.2017.05.288.

[33] V. Dieterich, A. Buttler, A. Hanel, H. Spliethoff, and S. Fendt. Power-to-Liquid via synthesis of methanol, DME or Fischer–Tropsch-fuels: A review. *Energy and Environmental Science*, 13(10):3207–3252, 2020. doi:10.1039/d0ee01187h.

[34] A. C. Ince, C. O. Colpan, A. Hagen, and M. F. Serincan. Modeling and simulation of Power-to-X systems: A review. *Fuel*, 304(1):121354, 2021. doi:10.1016/j.fuel.2021.121354.

[35] C. Wulf, P. Zapp, and A. Schreiber. Review of Power-to-X demonstration projects in Europe. *Frontiers in Energy Research*, 8(191):1–12, 2020. doi:10.3389/fenrg.2020.00191.

[36] G. Wang, A. Mitsos, and W. Marquardt. Conceptual design of ammonia-based energy storage system: System design and time-invariant performance. *AIChE Journal*, 63(5):1620–1637, 2017. doi:10.1002/aic.15660.

[37] T. Brown and J. Hampp. Ultra-long-duration energy storage anywhere: Methanol with carbon cycling. *Joule*, pages 1–7, 2023. doi:10.1016/j.joule.2023.10.001.

[38] N. Von Der Assen, L. J. Müller, A. Steingrube, P. Voll, and A. Bardow. Selecting CO_2 sources for CO_2 utilization by environmental-merit-order curves. *Environmental Science and Technology*, 50(3):1093–1101, 2016. doi:10.1021/acs.est.5b03474.

[39] A. König, K. Ulonska, A. Mitsos, and J. Viell. Optimal applications and combinations of renewable fuel production from biomass and electricity. *Energy and Fuels*, 33:1659–1672, 2019. doi:10.1021/acs.energyfuels.8b03790.

[40] Q. Zhang and I. E. Grossmann. Enterprise-wide optimization for industrial demand side management: Fundamentals, advances, and perspectives. *Chemical Engineering Research and Design*, 116:114–131, 2016. doi:10.1016/j.cherd.2016.10.006.

[41] P. Gabrielli, M. Gazzani, E. Martelli, and M. Mazzotti. Optimal design of multi-energy systems with seasonal storage. *Applied Energy*, 219:408–424, 2018. doi:10.1016/j.apenergy.2017.07.142.

[42] M. E. Wajeh, A. Mhamdi, and A. Mitsos. Optimal design and flexible operation of a fully electrified biodiesel production process. *Industrial & Engineering Chemistry Research*, 63:1487–1500, 2024. doi:10.1021/acs.iecr.3c03074.

[43] A. Caspari, C. Offermanns, P. Schäfer, A. Mhamdi, and A. Mitsos. A flexible air separation process: 1. Design and steady-state optimizations. *AIChE Journal*, 65(11), 2019. doi:10.1002/aic.16705.

[44] P. Mößle, T. Herrmannsdörfer, M. Welzl, D. Brüggemann, and M. A. Danzer. Economic optimization for the dynamic operation of a grid-connected and battery-supported electrolyzer. *International Journal of Hydrogen Energy*, 100:749–759, 2025. doi:10.1016/j.ijhydene.2024.12.216.

[45] C. Chen and A. Yang. Power-to-Methanol: The role of process flexibility in the integration of variable renewable energy into chemical production. *Energy Conversion and Management*, 228:113673, 2021. doi:10.1016/j.enconman.2020.113673.

[46] T. Svitnič and K. Sundmacher. Renewable methanol production: Optimization-based design, scheduling and waste-heat utilization with the FluxMax approach. *Applied Energy*, 326:120017, 2022. doi:10.1016/j.apenergy.2022.120017.

[47] H. Teichgraeber and A. R. Brandt. Optimal design of an electricity-intensive industrial facility subject to electricity price uncertainty: Stochastic optimization and scenario reduction. *Chemical Engineering Research and Design*, 163:204–216, 2020. doi:10.1016/j.cherd.2020.08.022.

[48] M. Carmo, D. L. Fritz, J. Mergel, and D. Stolten. A comprehensive review on PEM water electrolysis. *International Journal of Hydrogen Energy*, 38(12):4901–4934, 2013. doi:10.1016/j.ijhydene.2013.01.151.

[49] M. Kopp, D. Coleman, C. Stiller, K. Scheffer, J. Aichinger, and B. Scheppat. Energiepark Mainz: Technical and economic analysis of the worldwide largest Power-to-Gas plant with PEM electrolysis. *International Journal of Hydrogen Energy*, 42(19):13311–13320, 2017. doi:10.1016/j.ijhydene.2016.12.145.

[50] International Energy Agency (IEA). The Future of Hydrogen. Technical Report June, Paris, 2019. doi:10.1787/1e0514c4-en.

[51] J. Gorre, F. Ruoss, H. Karjunen, J. Schaffert, and T. Tynjälä. Cost benefits of optimizing hydrogen storage and methanation capacities for Power-to-Gas plants in dynamic operation. *Applied Energy*, 257(October 2019):113967, 2020. doi:10.1016/j.apenergy.2019.113967.

[52] S. Shiva Kumar and V. Himabindu. Hydrogen production by PEM water electrolysis - A review. *Materials Science for Energy Technologies*, 2(3):442–454, 2019. doi:10.1016/j.mset.2019.03.002.

[53] M. Bernt, A. Hartig-Weiß, M. F. Tovini, H. A. El-Sayed, C. Schramm, J. Schröter, C. Gebauer, and H. A. Gasteiger. Current challenges in catalyst development for PEM Water Electrolyzers. *Chemie Ingenieur Technik*, 92(1-2):31–39, 2020. doi:10.1002/cite.201900101.

[54] P. Shirvanian and F. van Berkel. Novel components in Proton Exchange Membrane (PEM) Water Electrolyzers (PEMWE): Status, challenges and future needs. A mini review. *Electrochemistry Communications*, 114:106704, 2020. doi:10.1016/j.elecom.2020.106704.

[55] A. H. Abdol Rahim, A. S. Tijani, S. K. Kamarudin, and S. Hanapi. An overview of polymer electrolyte membrane electrolyzer for hydrogen production: Modeling and mass transport. *Journal of Power Sources*, 309:56–65, 2016. doi:10.1016/j.jpowsour.2016.01.012.

[56] B. Bensmann and R. Hanke-Rauschenbach. Engineering modeling of PEM water electrolysis: A survey. *ECS Transactions*, 75(14):1065–1072, 2016. doi:10.1149/07514.1065ecst.

[57] D. Falcão and A. Pinto. A review on PEM electrolyzer modelling: Guidelines for beginners. *Journal of Cleaner Production*, 261:121184, 2020. doi:10.1016/j.jclepro.2020.121184.

[58] A. Buttler and H. Spliethoff. Current status of water electrolysis for energy storage, grid balancing and sector coupling via Power-to-Gas and Power-to-Liquids: A review. *Renewable and Sustainable Energy Reviews*, 82(2):2440–2454, 2018. doi:10.1016/j.rser.2017.09.003.

[59] H. Sayed-Ahmed, Á. Toldy, and A. Santasalo-Aarnio. Dynamic operation of proton exchange membrane electrolyzer - Critical review. *Renewable and Sustainable Energy Reviews*, 189:113883, 2024. doi:10.1016/j.rser.2023.113883.

[60] M. Götz, J. Lefebvre, F. Mörs, A. McDaniel Koch, F. Graf, S. Bajohr, R. Reimert, and T. Kolb. Renewable Power-to-Gas: A technological and economic review. *Renewable Energy*, 85:1371–1390, 2016. doi:10.1016/j.renene.2015.07.066.

[61] R. Peters, M. Baltruweit, T. Grube, R. C. Samsun, and D. Stolten. A techno economic analysis of the power to gas route. *Journal of CO_2 Utilization*, 34:616–634, 2019. doi:10.1016/j.jcou.2019.07.009.

[62] S. Rönsch, J. Schneider, S. Matthischke, M. Schlüter, M. Götz, J. Lefebvre, P. Prabhakaran, and S. Bajohr. Review on methanation - From fundamentals to current projects. *Fuel*, 166:276–296, 2016. doi:10.1016/j.fuel.2015.10.111.

[63] S. R. Foit, I. C. Vinke, L. G. J. de Haart, and R.-A. Eichel. Power-to-Syngas: An enabling technology for the transition of the energy system? *Angewandte Chemie International Edition*, 56(20):5402–5411, 2017. doi:10.1002/anie.201607552.

[64] S. Mbatha, R. C. Everson, N. M. Musyoka, H. W. Langmi, A. Lanzini, and W. Brilman. Power-to-Methanol process: a review of electrolysis, methanol catalysts, kinetics, reactor designs and modelling, process integration, optimisation, and techno-economics. *Sustainable Energy & Fuels*, 5(14):3490–3569, 2021. doi:10.1039/D1SE00635E.

[65] M. Pérez-Fortes, J. C. Schöneberger, A. Boulamanti, and E. Tzimas. Methanol synthesis using captured CO_2 as raw material: Techno-economic and environmental assessment. *Applied Energy*, 161:718–732, 2016. doi:10.1016/j.apenergy.2015.07.067.

[66] B. Lee, H. Lee, D. Lim, B. Brigljević, W. Cho, H.-S. Cho, C.-H. Kim, and H. Lim. Renewable methanol synthesis from renewable H_2 and captured CO_2: How can Power-to-Liquid technology be economically feasible? *Applied Energy*, 279:115827, 2020. doi:10.1016/j.apenergy.2020.115827.

[67] M. A. Adnan and M. G. Kibria. Comparative techno-economic and life-cycle assessment of Power-to-Methanol synthesis pathways. *Applied Energy*, 278:115614, 2020. doi:10.1016/j.apenergy.2020.115614.

[68] A. Álvarez, A. Bansode, A. Urakawa, A. V. Bavykina, T. A. Wezendonk, M. Makkee, J. Gascon, and F. Kapteijn. Challenges in the greener production of formates/-formic acid, methanol, and DME by heterogeneously catalyzed CO_2 hydrogenation processes. *Chemical Reviews*, 117(14):9804–9838, 2017. doi:10.1021/acs.chemrev.6b00816.

[69] S. Saeidi, S. Najari, V. Hessel, K. Wilson, F. J. Keil, P. Concepción, S. L. Suib, and A. E. Rodrigues. Recent advances in CO_2 hydrogenation to value-added products - Current challenges and future directions. *Progress in Energy and Combustion Science*, 85:100905, 2021. doi:10.1016/j.pecs.2021.100905.

[70] J. Ikäheimo, J. Kiviluoma, R. Weiss, and H. Holttinen. Power-to-Ammonia in future North European 100 % renewable power and heat system. *International Journal of Hydrogen Energy*, 43(36):17295–17308, 2018. doi:10.1016/j.ijhydene.2018.06.121.

[71] S. Fahr, R. Kender, J.-P. Bohn, S. Rehfeldt, A. Peschel, and H. Klein. Dynamic simulation of a highly load-flexible Haber–Bosch plant. *International Journal of Hydrogen Energy*, 102:1231–1242, 2025. doi:10.1016/j.ijhydene.2025.01.039.

[72] A. Tremel, P. Wasserscheid, M. Baldauf, and T. Hammer. Techno-economic analysis for the synthesis of liquid and gaseous fuels based on hydrogen production via electrolysis. *International Journal of Hydrogen Energy*, 40(35):11457–11464, 2015. doi:10.1016/j.ijhydene.2015.01.097.

[73] E. Bargiacchi, M. Antonelli, and U. Desideri. A comparative assessment of Power-to-Fuel production pathways. *Energy*, 183:1253–1265, 2019. doi:10.1016/j.energy.2019.06.149.

[74] E. Bargiacchi, N. Thonemann, J. Geldermann, M. Antonelli, and U. Desideri. Life cycle assessment of synthetic natural gas production from different CO_2 sources: A cradle-to-gate study. *Energies*, 13(17):4579, 2020. doi:10.3390/en13174579.

[75] J. C. Koj, C. Wulf, and P. Zapp. Environmental impacts of Power-to-X systems - A review of technological and methodological choices in Life Cycle Assessments. *Renewable and Sustainable Energy Reviews*, 112:865–879, 2019. doi:10.1016/j.rser.2019.06.029.

[76] G. Zang, P. Sun, A. Elgowainy, and M. Wang. Technoeconomic and life cycle analysis of synthetic methanol production from hydrogen and industrial byproduct CO_2. *Environmental Science and Technology*, 55(8):5248–5257, 2021. doi:10.1021/acs.est.0c08237.

[77] M. Grahn, E. Malmgren, A. D. Korberg, M. Taljegard, J. E. Anderson, S. Brynolf, J. Hansson, I. R. Skov, and T. J. Wallington. Review of electrofuel feasibility-cost and environmental impact. *Progress in Energy*, 4(3):032010, 2022. doi:10.1088/2516-1083/ac7937.

[78] S. Mbatha, X. Cui, P. G. Panah, S. Thomas, K. Parkhomenko, A. C. Roger, B. Louis, R. Everson, P. Debiagi, N. Musyoka, and H. Langmi. Comparative evaluation of

the Power-to-Methanol process configurations and assessment of process flexibility. *Energy Advances*, 3:2245–2270, 2024. doi:10.1039/d4ya00433g.

[79] M. Qi, D. N. Vo, H. Yu, C.-M. Shu, C. Cui, Y. Liu, J. Park, and I. Moon. Strategies for flexible operation of Power-to-X processes coupled with renewables. *Renewable and Sustainable Energy Reviews*, 179:113282, 2023. doi:10.1016/j.rser.2023.113282.

[80] International Energy Agency (IEA). Global hydrogen review 2025. Technical report, Paris, 2025.

[81] J. Brauns and T. Turek. Alkaline water electrolysis powered by renewable energy: A review. *Processes*, 8(2):248, 2020. doi:10.3390/pr8020248.

[82] J. E. Park, S. Y. Kang, S. H. Oh, J. K. Kim, M. S. Lim, C. Y. Ahn, Y. H. Cho, and Y. E. Sung. High-performance anion-exchange membrane water electrolysis. *Electrochimica Acta*, 295:99–106, 2019. doi:10.1016/j.electacta.2018.10.143.

[83] X. Shen, X. Zhang, G. Li, T. T. Lie, and L. Hong. Experimental study on the external electrical thermal and dynamic power characteristics of alkaline water electrolyzer. *International Journal of Energy Research*, 42(10):3244–3257, 2018. doi:10.1002/er.4076.

[84] Siemens Energy. Elyzer plant [online]. URL: https://p3.aprimocdn.net/siemensenergy/ea4fa194-2ce8-4645-bdea-b35300798c29/Electrolyzer-Factsheet-Elyzer-plant-100MW-pdf_Original%20file.pdf [last access: 02.03.2026].

[85] A. Tremel. *Electricity-based Fuels*. SpringerBriefs in Applied Sciences and Technology. Springer International Publishing, Cham, 2018. doi:10.1007/978-3-319-72459-1.

[86] J. Hemauer, S. Rehfeldt, H. Klein, and A. Peschel. Performance and cost modelling taking into account the uncertainties and sensitivities of current and next-generation PEM water electrolysis technology. *International Journal of Hydrogen Energy*, 48(66):25619–25634, 2023. doi:10.1016/j.ijhydene.2023.03.050.

[87] A. H. Reksten, M. S. Thomassen, S. Møller-Holst, and K. Sundseth. Projecting the future cost of PEM and alkaline water electrolysers; a CAPEX model including electrolyser plant size and technology development. *International Journal of Hydrogen Energy*, 47:38106–38113, 2022. doi:10.1016/j.ijhydene.2022.08.306.

[88] P. Millet and S. Grigoriev. Water Electrolysis Technologies. In *Renewable Hydrogen Technologies*, pages 19–41. Elsevier, 2013. doi:10.1016/B978-0-444-56352-1.00002-7.

[89] C. Minke, M. Suermann, B. Bensmann, and R. Hanke-Rauschenbach. Is iridium demand a potential bottleneck in the realization of large-scale PEM water electrolysis? *International Journal of Hydrogen Energy*, 46(46):23581–23590, 2021. doi:10.1016/j.ijhydene.2021.04.174.

[90] M. Maier, K. Smith, J. Dodwell, G. Hinds, P. R. Shearing, and D. J. Brett. Mass transport in PEM water electrolysers: A review. *International Journal of Hydrogen Energy*, 47(1):30–56, 2021. doi:10.1016/j.ijhydene.2021.10.013.

[91] J. J. C. Mancera, F. S. Manzano, J. M. Andújar, F. J. Vivas, and A. J. Calderón. An optimized balance of plant for a medium-size PEM electrolyzer. Design, control and physical implementation. *Electronics*, 9(5):871, 2020. doi:10.3390/electronics9050871.

[92] X. Wang, L. Zhang, G. Li, G. Zhang, Z. G. Shao, and B. Yi. The influence of ferric ion contamination on the solid polymer electrolyte water electrolysis performance. *Electrochimica Acta*, 158:253–257, 2015. doi:10.1016/j.electacta.2015.01.140.

[93] F. Andolfatto, R. Durand, A. Michas, P. Millet, and P. Stevens. Solid polymer electrolyte water electrolysis: Electrocatalysis and long-term stability. *International Journal of Hydrogen Energy*, 19(5):421–427, 1994. doi:10.1016/0360-3199(94)90018-3.

[94] B. Bensmann, R. Hanke-Rauschenbach, G. Müller-Syring, M. Henel, and K. Sundmacher. Optimal configuration and pressure levels of electrolyzer plants in context of Power-to-Gas applications. *Applied Energy*, 167:107–124, 2016. doi:10.1016/j.apenergy.2016.01.038.

[95] G. Tjarks, A. Gibelhaus, F. Lanzerath, M. Müller, A. Bardow, and D. Stolten. Energetically-optimal PEM electrolyzer pressure in Power-to-Gas plants. *Applied Energy*, 218(September 2017):192–198, 2018. doi:10.1016/j.apenergy.2018.02.155.

[96] Siemens Energy. Silyzer 300: The next paradigm of PEM electrolysis [online]. URL: https://assets.siemens-energy.com/siemens/assets/api/uuid:a193b68f-7ab4-4536-abe2-c23e01d0b526/datasheet-silyzer300.pdf [last access: 2025-01-31].

[97] NEL Hydrogen. Water electrolysers [online]. URL: https://nelhydrogen.com/water-electrolysers-hydrogen-generators/ [last access: 2025-02-05].

[98] V. Ruuskanen, J. Koponen, A. Kosonen, M. Hehemann, R. Keller, M. Niemelä, and J. Ahola. Power quality estimation of water electrolyzers based on current and voltage measurements. *Journal of Power Sources*, 450:227603, 2020. doi:10.1016/j.jpowsour.2019.227603.

[99] J. Koponen, V. Ruuskanen, M. Hehemann, E. Rauls, A. Kosonen, J. Ahola, and D. Stolten. Effect of power quality on the design of proton exchange membrane water electrolysis systems. *Applied Energy*, 279(3):115791, 2020. doi:10.1016/j.apenergy.2020.115791.

[100] L. Zachert, M. Suermann, B. Bensmann, and R. Hanke-Rauschenbach. Energetic evaluation and optimization of hydrogen generation and compression pathways considering PEM water electrolyzers and electrochemical hydrogen compressors. *Journal of The Electrochemical Society*, 168(1):014504, 2021. doi:10.1149/1945-7111/abcf1a.

[101] L. Bornemann, J. Lange, and M. Kaltschmitt. Optimizing temperature and pressure in PEM electrolyzers: A model-based approach to enhanced efficiency in integrated energy systems. *Energy Conversion and Management*, 325:119338, 2025. doi:10.1016/j.enconman.2024.119338.

[102] M. Suermann, T. J. Schmidt, and F. N. Büchi. Cell performance determining parameters in high pressure water electrolysis. *Electrochimica Acta*, 211:989–997, 2016. doi:10.1016/j.electacta.2016.06.120.

[103] G. I. Prokopou, M. L. Mödden, A. Mitsos, and D. Bongartz. Energetic comparison of electrochemical versus mechanical compression of hydrogen. In F. Manenti and G. V. Reklaitis, editors, *34th European Symposium on Computer Aided Process Engineering / 15th International Symposium on Process Systems Engineering*, volume 53 of *Computer Aided Chemical Engineering*, pages 2047–2052, 2024. doi:10.1016/B978-0-443-28824-1.50342-2.

[104] G. I. Prokopou, J. M. Faust, A. Mitsos, and D. Bongartz. Cost-optimal design and operation of hydrogen refueling stations with mechanical and electrochemical hydrogen compressors. *Computers & Chemical Engineering*, 192:108862, 2025. doi:10.1016/j.compchemeng.2024.108862.

[105] M. Suermann, T. Kiupel, T. J. Schmidt, and F. N. Büchi. Electrochemical hydrogen compression: Efficient pressurization concept derived from an energetic evaluation. *Journal of The Electrochemical Society*, 164(12):F1187–F1195, 2017. doi:10.1149/2.1361712jes.

[106] P. Trinke, B. Bensmann, S. Reichstein, R. Hanke-Rauschenbach, and K. Sundmacher. Impact of pressure and temperature on hydrogen permeation in PEM water electrolyzers operated at asymmetric pressure conditions. *ECS Transactions*, 75(14):1081–1094, 2016. doi:10.1149/07514.1081ecst.

[107] B. Yodwong, D. Guilbert, M. Phattanasak, W. Kaewmanee, M. Hinaje, and G. Vitale. Faraday's efficiency modeling of a proton exchange membrane electrolyzer based on experimental data. *Energies*, 13(18):4792, 2020. doi:10.3390/en13184792.

[108] A. S. Tijani and A. A. Rahim. Numerical modeling the effect of operating variables on Faraday efficiency in PEM electrolyzer. *Procedia Technology*, 26:419–427, 2016. doi:10.1016/j.protcy.2016.08.054.

[109] F. Scheepers, M. Stähler, A. Stähler, E. Rauls, M. Müller, M. Carmo, and W. Lehnert. Improving the efficiency of PEM electrolyzers through membrane-specific pressure optimization. *Energies*, 13(3):612, 2020. doi:10.3390/en13030612.

[110] C. Klose, P. Trinke, T. Böhm, B. Bensmann, S. Vierrath, R. Hanke-Rauschenbach, and S. Thiele. Membrane interlayer with Pt recombination particles for reduction of the anodic hydrogen content in PEM water electrolysis. *Journal of The Electrochemical Society*, 165(16):F1271–F1277, 2018. doi:10.1149/2.1241814jes.

[111] A. Weiß, A. Siebel, M. Bernt, T.-H. Shen, V. Tileli, and H. A. Gasteiger. Impact of intermittent operation on lifetime and performance of a PEM water electrolyzer.

Journal of The Electrochemical Society, 166(8):F487–F497, 2019. doi:10.1149/2.0421908jes.

[112] D. Gusain, M. Cvetković, R. Bentvelsen, and P. Palensky. Technical assessment of large scale PEM electrolyzers as flexibility service providers. In *2020 IEEE 29th International Symposium on Industrial Electronics (ISIE)*, pages 1074–1078, 2020. doi:doi:10.1109/ISIE45063.2020.9152462.

[113] F. Alshehri, V. García Suarez, J. L. Rueda Torres, A. Perilla, and M. A. M. M. van der Meijden. Modelling and evaluation of PEM hydrogen technologies for frequency ancillary services in future multi-energy sustainable power systems. *Heliyon*, 5:e01396, 2019. doi:10.1016/j.heliyon.2019.e01396.

[114] N. Veerakumar, Z. Ahmad, M. E. Adabi, J. R. Torres, P. Palensky, M. van der Meijden, and F. Gonzalez-Longatt. Fast active power-frequency support methods by large scale electrolyzers for multi-energy systems. In *2020 IEEE PES Innovative Smart Grid Technologies Europe (ISGT-Europe)*, pages 151–155. IEEE, 2020. doi:10.1109/ISGT-Europe47291.2020.9248949.

[115] A. M. De Corato, S. Riaz, and P. Mancarella. Impact of hydrogen electrolyzers on flexibility and network voltage profiles of a virtual power plant. In *2020 Australasian Universities Power Engineering Conference (AUPEC)*, pages 1–6, 2020. URL: https://ieeexplore.ieee.org/document/9344505.

[116] J. Koponen, A. Kosonen, V. Ruuskanen, K. Huoman, M. Niemelä, and J. Ahola. Control and energy efficiency of PEM water electrolyzers in renewable energy systems. *International Journal of Hydrogen Energy*, 42(50):29648–29660, 2017. doi:10.1016/j.ijhydene.2017.10.056.

[117] B. Guinot, F. Montignac, B. Champel, and D. Vannucci. Profitability of an electrolysis based hydrogen production plant providing grid balancing services. *International Journal of Hydrogen Energy*, 40(29):8778–8787, 2015. doi:10.1016/j.ijhydene.2015.05.033.

[118] S. Deutz and A. Bardow. Life-cycle assessment of an industrial direct air capture process based on temperature–vacuum swing adsorption. *Nature Energy*, 6(2):203–213, 2021. doi:10.1038/s41560-020-00771-9.

[119] R. M. Cuéllar-Franca and A. Azapagic. Carbon capture, storage and utilisation technologies: A critical analysis and comparison of their life cycle environmental impacts. *Journal of CO_2 Utilization*, 9:82–102, 2015. doi:10.1016/j.jcou.2014.12.001.

[120] M. Lyons, P. Durrant, and K. Kochhar. Reaching zero with renewables capturing carbon. Technical report, International Renewable Energy Agency (IRENA), 2021. URL: https://irena.org/-/media/Files/IRENA/Agency/Technical-Papers/IRENA_Capturing_Carbon_2021.pdf.

[121] International Energy Agency (IEA). About CCUS. Technical report, Paris, 2021. URL: https://www.iea.org/reports/about-ccus.

[122] A. Lewandowska-Bernat and U. Desideri. Opportunities of Power-to-Gas technology in different energy systems architectures. *Applied Energy*, 228(May):57–67, 2018. doi:10.1016/j.apenergy.2018.06.001.

[123] K. Roh, A. Bardow, D. Bongartz, J. Burre, W. Chung, S. Deutz, D. Han, M. Heßelmann, Y. Kohlhaas, A. König, J. S. Lee, R. Meys, S. Völker, M. Wessling, J. H. Lee, and A. Mitsos. Early-stage evaluation of emerging CO_2 utilization technologies at low technology readiness levels. *Green Chemistry*, 22(12):3842–3859, 2020. doi:10.1039/c9gc04440j.

[124] U. Lee, J. Burre, A. Caspari, J. Kleinekorte, A. M. Schweidtmann, and A. Mitsos. Techno-economic optimization of a green-field post-combustion CO_2 capture process using superstructure and rate-based models. *Industrial & Engineering Chemistry Research*, 55(46):12014–12026, 2016. doi:10.1021/acs.iecr.6b01668.

[125] H. Yu, G. Qi, Q. Xiang, S. Wang, M. Fang, Q. Yang, L. Wardhaugh, and P. Feron. Aqueous ammonia based post combustion capture: Results from pilot plant operation, challenges and further opportunities. *Energy Procedia*, 37:6256–6264, 2013. doi:10.1016/j.egypro.2013.06.554.

[126] J. Gaspar, L. R. Sandoval, J. B. Jørgensen, and P. L. Fosbøl. Design, economics and parameter uncertainty in dynamic operation of post-combustion CO_2 capture using piperazine (PZ) and MEA. *Energy Procedia*, 114:1444–1452, 2017. doi:10.1016/j.egypro.2017.03.1269.

[127] M. Salman, B. Beguin, T. Nyssen, and G. Léonard. Techno-economic analysis of AMP/PZ solvent for CO_2 capture in a biomass CHP plant: Towards net negative emissions. *Frontiers in Energy Research*, 12:1–18, 2024. doi:10.3389/fenrg.2024.1325212.

[128] H. Herzog. Assessing the feasibility of capturing CO_2 from the air, Publication No. LFEE 2003-002 WP. Technical report, Massachusetts Institute of Technology, Laboratory for Energy and the Environment, 2003. URL: https://www.ocf.berkeley.edu/$\sim$step/Journal_Club/paper1_02092010.pdf.

[129] K. Li, A. Cousins, H. Yu, P. Feron, M. Tade, W. Luo, and J. Chen. Systematic study of aqueous monoethanolamine-based CO_2 capture process: Model development and process improvement. *Energy Science and Engineering*, 4(1):23–39, 2016. doi:10.1002/ese3.101.

[130] H. J. Yoon and K. B. Lee. Introduction of chemically bonded zirconium oxide in CaO-based high-temperature CO_2 sorbents for enhanced cyclic sorption. *Chemical Engineering Journal*, 355:850–857, 2019. doi:10.1016/j.cej.2018.08.148.

[131] S. B. Jo, J. H. Woo, J. H. Lee, T. Y. Kim, H. I. Kang, S. C. Lee, and J. C. Kim. CO_2 green technologies in CO_2 capture and direct utilization processes: methanation, reverse water-gas shift, and dry reforming of methane. *Sustainable Energy and Fuels*, 4(11):5543–5549, 2020. doi:10.1039/d0se00951b.

[132] S. B. Jo, J. H. Woo, J. H. Lee, T. Y. Kim, H. I. Kang, S. C. Lee, and J. C. Kim. A novel integrated CO_2 capture and direct methanation process using Ni/-CaO catal-sorbents. *Sustainable Energy and Fuels*, 4(9):4679–4687, 2020. doi:10.1039/d0se00760a.

[133] H. Zeng, X. Qu, D. Xu, and Y. Luo. Porous adsorption materials for carbon dioxide capture in industrial flue gas. *Frontiers in Chemistry*, 10:939701, 2022. doi:10.3389/fchem.2022.939701.

[134] X. Zhang, M. Sun, Y. Wang, H. Zhang, J. Du, and A. Chen. Integrated CO_2 capture and electrochemical reduction: From mechanism understanding to gas diffusion electrode and catalyst design. *Journal of Energy Chemistry*, 106:81–100, 2025. doi:10.1016/j.jechem.2025.02.017.

[135] J. Gaspar, J. B. Jørgensen, and P. L. Fosbøl. Control of a post-combustion CO_2 capture plant during process start-up and load variations. *IFAC-PapersOnLine*, 28(8):580–585, 2015. doi:10.1016/j.ifacol.2015.09.030.

[136] J. Dickinson, G. Puxty, A. Percy, and T. V. Verheyen. Further developments in dynamic modelling of CO_2 capture from flue gas. *IFAC-PapersOnLine*, 28(1):216–221, 2015. doi:10.1016/j.ifacol.2015.05.067.

[137] J. Gaspar, J. B. Jørgensen, and P. L. Fosbøl. A dynamic mathematical model for packed columns in carbon capture plants. In *2015 European Control Conference, ECC 2015*, pages 2738–2743. Institute of Electrical and Electronics Engineers Inc., 2015. doi:10.1109/ECC.2015.7330952.

[138] J. Gaspar, L. Ricardez-Sandoval, J. B. Jørgensen, and P. L. Fosbøl. Controllability and flexibility analysis of CO_2 post-combustion capture using piperazine and MEA. *International Journal of Greenhouse Gas Control*, 51:276–289, 2016. doi:10.1016/j.ijggc.2016.06.003.

[139] J. Gaspar, L. Ricardez-Sandoval, J. B. Jorgensen, and P. L. Fosbøl. Dynamic simulation and analysis of a pilot-scale CO_2 post-combustion capture unit using piperazine and MEA. *IFAC-PapersOnLine*, 49(7):645–650, 2016. doi:10.1016/j.ifacol.2016.07.246.

[140] M. Mostafa, C. Varela, M. B. Franke, and E. Zondervan. Dynamic modeling and control of a simulated carbon capture process for sustainable Power-to-X. *Applied Sciences*, 11(20):9574, 2021. doi:10.3390/app11209574.

[141] J. Fagerlund, R. Zevenhoven, J. Thomassen, M. Tednes, F. Abdollahi, L. Thomas, C. J. Nielsen, T. Mikoviny, A. Wisthaler, L. Zhu, C. Biliyok, and A. Zhurkin. Performance of an amine-based CO_2 capture pilot plant at the Klemetsrud waste incinerator in Oslo, Norway. *International Journal of Greenhouse Gas Control*, 106:103242, 2021. doi:10.1016/j.ijggc.2020.103242.

[142] J. Gaspar, A. Gladis, J. B. Jørgensen, K. Thomsen, N. Von Solms, and P. L. Fosbøl. Dynamic operation and simulation of post-combustion CO_2 capture. *Energy Procedia*, 86:205–214, 2016. doi:10.1016/j.egypro.2016.01.021.

[143] Carbon Recycling International (CRI). A proven carbon utilisation solution [online]. URL: https://carbonrecycling.com/ [last access: 2025-02-05].

[144] BSE engineering. Power-to-Methanol at small-scale: FlexMethanol 10&20 MW module [online]. URL: http://www.wfbe.de/BSE-Flyer-BASF-DB_web.pdf [last access: 08.08.2025].

[145] F. V. Vázquez, J. Koponen, V. Ruuskanen, C. Bajamundi, A. Kosonen, P. Simell, J. Ahola, C. Frilund, J. Elfving, M. Reinikainen, N. Heikkinen, J. Kauppinen, and P. Piermartini. Power-to-X technology using renewable electricity and carbon dioxide from ambient air: SOLETAIR proof-of-concept and improved process concept. *Journal of CO_2 Utilization*, 28:235–246, 2018. doi:10.1016/j.jcou.2018.09.026.

[146] M. Bailera, P. Lisbona, L. M. Romeo, and S. Espatolero. Power to Gas projects review: Lab, pilot and demo plants for storing renewable energy and CO_2. *Renewable and Sustainable Energy Reviews*, 69:292–312, 2017. doi:10.1016/j.rser.2016.11.130.

[147] J. Uebbing, L. K. Rihko-Struckmann, and K. Sundmacher. Exergetic assessment of CO_2 methanation processes for the chemical storage of renewable energies. *Applied Energy*, 233-234:271–282, 2019. doi:10.1016/j.apenergy.2018.10.014.

[148] B. R. de Vasconcelos and J. M. Lavoie. Recent advances in Power-to-X technology for the production of fuels and chemicals. *Frontiers in Chemistry*, 7:1–24, 2019. doi:10.3389/fchem.2019.00392.

[149] R. Gaikwad, S. N. Villadsen, J. P. Rasmussen, F. B. Grumsen, L. P. Nielsen, G. Gildert, P. Møller, and P. L. Fosbøl. Container-sized CO_2 to methane: Design, construction and catalytic tests using raw biogas to biomethane. *Catalysts*, 10(12):1–13, 2020. doi:10.3390/catal10121428.

[150] L. Jürgensen, E. A. Ehimen, J. Born, and J. B. Holm-Nielsen. Dynamic biogas upgrading based on the Sabatier process: Thermodynamic and dynamic process simulation. *Bioresource Technology*, 178:323–329, 2015. doi:10.1016/j.biortech.2014.10.069.

[151] J. Lefebvre, M. Götz, S. Bajohr, R. Reimert, and T. Kolb. Improvement of three-phase methanation reactor performance for steady-state and transient operation. *Fuel Processing Technology*, 132:83–90, 2015. doi:10.1016/j.fuproc.2014.10.040.

[152] R. T. Zimmermann, J. Bremer, and K. Sundmacher. Load-flexible fixed-bed reactors by multi-period design optimization. *Chemical Engineering Journal*, 428:130771, 2022. doi:10.1016/j.cej.2021.130771.

[153] M. Held, D. Schollenberger, S. Sauerschell, S. Bajohr, and T. Kolb. Power-to-Gas: CO_2 methanation concepts for SNG production at the Engler-Bunte-Institut. *Chemie Ingenieur Technik*, 92(5):595–602, 2020. doi:10.1002/cite.201900181.

[154] A. El Sibai, L. Rihko-Struckmann, and K. Sundmacher. Synthetic methane from CO_2: Dynamic optimization of the Sabatier process for Power-to-Gas applications. In *12^{th} International Symposium on Process Systems Engineering and 25^{th}*

European Symposium on Computer Aided Process Engineering. 31 May – 4 June 2015, Copenhagen, Denmark, volume 37, pages 1157–1162. Elsevier, 2015. doi:10.1016/B978-0-444-63577-8.50038-3.

[155] A. El Sibai, L. K. Rihko Struckmann, and K. Sundmacher. Model-based optimal Sabatier reactor design for Power-to-Gas applications. *Energy Technology*, 5(6):911–921, 2017. doi:10.1002/ente.201600600.

[156] L. Wei, H. Azad, W. Haije, H. Grenman, and W. de Jong. Pure methane from CO_2 hydrogenation using a sorption enhanced process with catalyst/zeolite bifunctional materials. *Applied Catalysis B: Environmental*, 297:120399, 2021. doi:10.1016/j.apcatb.2021.120399.

[157] A. Bensmann, R. Hanke-Rauschenbach, R. Heyer, F. Kohrs, D. Benndorf, U. Reichl, and K. Sundmacher. Biological methanation of hydrogen within biogas plants: A model-based feasibility study. *Applied Energy*, 134:413–425, 2014. doi:10.1016/j.apenergy.2014.08.047.

[158] G. Luo, S. Johansson, K. Boe, L. Xie, Q. Zhou, and I. Angelidaki. Simultaneous hydrogen utilization and in situ biogas upgrading in an anaerobic reactor. *Biotechnology and Bioengineering*, 109(4):1088–1094, 2012. doi:10.1002/bit.24360.

[159] J. Uebbing, L. Rihko-Struckmann, S. Sager, and K. Sundmacher. CO_2 methanation process synthesis by superstructure optimization. *Journal of CO_2 Utilization*, 40(7):101228, 2020. doi:10.1016/j.jcou.2020.101228.

[160] K. L. Fischer and H. Freund. On the optimal design of load flexible fixed bed reactors: Integration of dynamics into the design problem. *Chemical Engineering Journal*, 393:124722, 2020. doi:10.1016/j.cej.2020.124722.

[161] J. Bremer, K. H. G. Rätze, and K. Sundmacher. CO_2 methanation: Optimal start-up control of a fixed-bed reactor for Power-to-Gas applications. *AIChE Journal*, 63(1):23–31, 2017. doi:10.1002/aic.15496.

[162] S. Matthischke, S. Roensch, and R. Güttel. Start-up time and load range for the methanation of carbon dioxide in a fixed-bed recycle reactor. *Industrial & Engineering Chemistry Research*, 57(18):6391–6400, 2018. doi:10.1021/acs.iecr.8b00755.

[163] S. Rönsch, A. Ortwein, and S. Dietrich. Start-and-stop operation of fixed-bed methanation reactors – Results from modeling and simulation. *Chemical Engineering and Technology*, 40(12):2314–2321, 2017. doi:10.1002/ceat.201700229.

[164] D. Sun and D. S. Simakov. Thermal management of a Sabatier reactor for CO_2 conversion into CH_4: Simulation-based analysis. *Journal of CO_2 Utilization*, 21:368–382, 2017. doi:10.1016/j.jcou.2017.07.015.

[165] J. Bremer and K. Sundmacher. Operation range extension via hot-spot control for catalytic CO_2 methanation reactors. *Reaction Chemistry and Engineering*, 4(6):1019–1037, 2019. doi:10.1039/c9re00147f.

[166] S. Matthischke, R. Krüger, S. Rönsch, and R. Güttel. Unsteady-state methanation of carbon dioxide in a fixed-bed recycle reactor - Experimental results for transient flow rate ramps. *Fuel Processing Technology*, 153:87–93, 2016. doi:10.1016/j.fuproc.2016.07.021.

[167] R. T. Zimmermann, J. Bremer, and K. Sundmacher. Optimal catalyst particle design for flexible fixed-bed CO_2 methanation reactors. *Chemical Engineering Journal*, 387:123704, 2020. doi:10.1016/j.cej.2019.123704.

[168] F. Herrmann, M. Grünewald, T. Meijer, U. Gardemann, and J. Riese. Performance of a laboratory-scale methanation plant with catalyst dilution under dynamic operating conditions. *Industrial and Engineering Chemistry Research*, 61(27):9644–9657, 2022. doi:10.1021/acs.iecr.2c00871.

[169] J. Gorre, F. Ortloff, and C. van Leeuwen. Production costs for synthetic methane in 2030 and 2050 of an optimized Power-to-Gas plant with intermediate hydrogen storage. *Applied Energy*, 253:113594, 2019. doi:10.1016/j.apenergy.2019.113594.

[170] B. Kreitz, J. Brauns, G. D. Wehinger, and T. Turek. Modeling the dynamic Power-to-Gas process: Coupling electrolysis with CO_2 methanation. *Chemie Ingenieur Technik*, 92(12):1992–1997, 2020. doi:10.1002/cite.202000019.

[171] M. Hervy, J. Maistrello, L. Brito, M. Rizand, E. Basset, Y. Kara, and M. Maheut. Power-to-Gas: CO_2 methanation in a catalytic fluidized bed reactor at demonstration scale, experimental results and simulation. *Journal of CO_2 Utilization*, 50:101610, 2021. doi:10.1016/j.jcou.2021.101610.

[172] R. Güttel. Study of unsteady-state operation of methanation by modeling and simulation. *Chemical Engineering and Technology*, 36(10):1675–1682, 2013. doi:10.1002/ceat.201300223.

[173] O. S. Joo, K. D. Jung, I. Moon, A. Y. Rozovskii, G. I. Lin, S. H. Han, and S. J. Uhm. Carbon dioxide hydrogenation to form methanol via a reverse-water-gas-shift reaction (the CAMERE process). *Industrial and Engineering Chemistry Research*, 38(5):1808–1812, 1999. doi:10.1021/ie9806848.

[174] B. Anicic, P. Trop, and D. Goricanec. Comparison between two methods of methanol production from carbon dioxide. *Energy*, 77:279–289, 2014. doi:10.1016/j.energy.2014.09.069.

[175] F. Nestler, A. R. Schütze, M. Ouda, M. J. Hadrich, A. Schaadt, S. Bajohr, and T. Kolb. Kinetic modelling of methanol synthesis over commercial catalysts: A critical assessment. *Chemical Engineering Journal*, 394:124881, 2020. doi:10.1016/j.cej.2020.124881.

[176] F. Pontzen, W. Liebner, V. Gronemann, M. Rothaemel, and B. Ahlers. CO_2-based methanol and DME - Efficient technologies for industrial scale production. *Catalysis Today*, 171(1):242–250, 2011. doi:10.1016/j.cattod.2011.04.049.

[177] P. Maksimov, A. Laari, V. Ruuskanen, T. Koiranen, and J. Ahola. Methanol synthesis through sorption enhanced carbon dioxide hydrogenation. *Chemical Engineering Journal*, 418:129290, 2021. doi:10.1016/j.cej.2021.129290.

[178] F. Samimi, D. Karimipourfard, and M. R. Rahimpour. Green methanol synthesis process from carbon dioxide via reverse water gas shift reaction in a membrane reactor. *Chemical Engineering Research and Design*, 140:44–67, 2018. doi:10.1016/j.cherd.2018.10.001.

[179] F. Manenti and G. Bozzano. Optimal control of methanol synthesis fixed-bed reactor. *Industrial and Engineering Chemistry Research*, 52(36):13079–13091, 2013. doi:10.1021/ie401511e.

[180] F. Manenti, S. Cieri, M. Restelli, and G. Bozzano. Dynamic modeling of the methanol synthesis fixed-bed reactor. *Computers and Chemical Engineering*, 48:325–334, 2013. doi:10.1016/j.compchemeng.2012.09.013.

[181] F. Nestler, V. P. Müller, M. Ouda, M. J. Hadrich, A. Schaadt, S. Bajohr, and T. Kolb. A novel approach for kinetic measurements in exothermic fixed bed reactors: Advancements in non-isothermal bed conditions demonstrated for methanol synthesis. *Reaction Chemistry and Engineering*, 6(6):1092–1107, 2021. doi:10.1039/d1re00071c.

[182] C. Seidel, D. Nikolić, M. Felischak, M. Petkovska, A. Seidel-Morgenstern, and A. Kienle. Optimization of methanol synthesis under forced periodic operation. *Processes*, 9:872, 2021. doi:10.3390/pr9050872.

[183] C. Seidel, A. Jörke, B. Vollbrecht, A. Seidel-Morgenstern, and A. Kienle. Kinetic modeling of methanol synthesis - Impact of catalyst deactivation. *Computer Aided Chemical Engineering*, 43(1):85–90, 2018. doi:10.1016/B978-0-444-64235-6.50017-6.

[184] C. Seidel, A. Jörke, B. Vollbrecht, A. Seidel-Morgenstern, and A. Kienle. Kinetic modeling of methanol synthesis from renewable resources. *Chemical Engineering Science*, 175:130–138, 2018. doi:10.1016/j.ces.2017.09.043.

[185] J. Leipold, D. Nikolic, A. Seidel-Morgenstern, and A. Kienle. Optimization of methanol synthesis under forced periodic operation in a non-isothermal fixed-bed reactor. *Computers & Chemical Engineering*, 196:109040, 2025. doi:10.1016/j.compchemeng.2025.109040.

[186] S. A. Velardi and A. A. Barresi. Methanol synthesis in a forced unsteady-state reactor network. *Chemical Engineering Science*, 57(15):2995–3004, 2002. doi:10.1016/S0009-2509(02)00181-1.

[187] E. Mancusi, P. Altimari, L. Russo, and S. Crescitelli. Multiplicities of temperature wave trains in periodically forced networks of catalytic reactors for reversible exothermic reactions. *Chemical Engineering Journal*, 171(2):655–668, 2011. doi:10.1016/j.cej.2011.04.026.

[188] D. Mignard and C. Pritchard. On the use of electrolytic hydrogen from variable renewable energies for the enhanced conversion of biomass to fuels. *Chemical Engineering Research and Design*, 86(5):473–487, 2008. doi:10.1016/j.cherd.2007.12.008.

[189] F. Ausfelder, A. Bund, A. Fischer, H. A. Gasteiger, T. E. Hamedinger, G. Harp, D. Hoormann, M. Jahn, R. Krähnert, F. Klaucke, F. Köster, U. Krewer, K. Mangold, A. Mitsos, M. Reuter, R. Schütte, T. Sörgel, M. Trennhaus, T. Turek, C. Unger, K. Wagemann, M. Waidhas, S. Waldvogel, G. Wang, and R. Weber. Elektrifizierung chemischer Prozesse: Diskussionpapier. Technical report, DECHEMA Gesellschaft für Chemische Technik und Biotechnologie e.V., Frankfurt/Main, 2015.

[190] T. Haas, R. Krause, R. Weber, M. Demler, and G. Schmid. Technical photosynthesis involving CO_2 electrolysis and fermentation. *Nature Catalysis*, 1(1):32–39, 2018. doi:10.1038/s41929-017-0005-1.

[191] L. Dittrich, M. Nohl, E. E. Jaekel, S. Foit, L. (Bert) de Haart, and R.-A. Eichel. High-temperature co-electrolysis: A versatile method to sustainably produce tailored syngas compositions. *Journal of The Electrochemical Society*, 166(13):F971–F975, 2019. doi:10.1149/2.0581913jes.

[192] P. Kaiser, R. B. Unde, C. Kern, and A. Jess. Production of liquid hydrocarbons with CO_2 as carbon source based on reverse water-gas shift and Fischer-Tropsch synthesis. *Chemie-Ingenieur-Technik*, 85(4):489–499, 2013. doi:10.1002/cite.201200179.

[193] Y. A. Daza and J. N. Kuhn. CO_2 conversion by reverse water gas shift catalysis: Comparison of catalysts, mechanisms and their consequences for CO_2 conversion to liquid fuels. *RSC Advances*, 6(55):49675–49691, 2016. doi:10.1039/c6ra05414e.

[194] M. González-Castaño, B. Dorneanu, and H. Arellano-García. The reverse water gas shift reaction: a process systems engineering perspective. *Reaction Chemistry & Engineering*, 6(6):954–976, 2021. doi:10.1039/D0RE00478B.

[195] A. Maggi, M. Wenzel, and K. Sundmacher. Mixed-integer linear programming (MILP) approach for the synthesis of efficient Power-to-Syngas processes. *Frontiers in Energy Research*, 8, 2020. doi:10.3389/fenrg.2020.00161.

[196] É. S. Van-Dal and C. Bouallou. Design and simulation of a methanol production plant from CO_2 hydrogenation. *Journal of Cleaner Production*, 57:38–45, 2013. doi:10.1016/j.jclepro.2013.06.008.

[197] M. Wenzel, L. Rihko-Struckmann, and K. Sundmacher. Thermodynamic analysis and optimization of RWGS processes for solar syngas production from CO_2. *AIChE Journal*, 63(1):15–22, 2017. doi:10.1002/aic.15445.

[198] M. Wenzel, N. V. Aditya Dharanipragada, V. V. Galvita, H. Poelman, G. B. Marin, L. Rihko-Struckmann, and K. Sundmacher. CO production from CO_2 via reverse water-gas shift reaction performed in a chemical looping mode: Kinetics on modified iron oxide. *Journal of CO_2 Utilization*, 17:60–68, 2017. doi:10.1016/j.jcou.2016.10.015.

[199] N. Utsis, M. V. Landau, A. Erenburg, and M. Herskowitz. Reverse water gas shift by chemical looping with iron-substituted hexaaluminate catalysts. *Catalysts*, 10:1082, 2020. doi:10.3390/catal10091082.

[200] M. Wenzel, L. Rihko-Struckmann, and K. Sundmacher. Continuous production of CO from CO_2 by RWGS chemical looping in fixed and fluidized bed reactors. *Chemical Engineering Journal*, 336:278–296, 2018. doi:10.1016/j.cej.2017.12.031.

[201] S. Adelung, S. Maier, and R.-U. Dietrich. Impact of the reverse water-gas shift operating conditions on the Power-to-Liquid process efficiency. *Sustainable Energy Technologies and Assessments*, 43:100897, 2021. doi:10.1016/j.seta.2020.100897.

[202] I. Hannula, N. Kaisalo, and P. Simell. Preparation of synthesis gas from CO_2 for Fischer–Tropsch synthesis—comparison of alternative process configurations. *C Journal of Carbon Research*, 6(3):55, 2020. doi:10.3390/c6030055.

[203] M. Marchese, G. Buffo, M. Santarelli, and A. Lanzini. CO_2 from direct air capture as carbon feedstock for Fischer-Tropsch chemicals and fuels: Energy and economic analysis. *Journal of CO_2 Utilization*, 46:101487, 2021. doi:10.1016/j.jcou.2021.101487.

[204] G. Scio', M. Ermini, M. Verna, V. Bernardini, and L. Campana. Comprehensive analysis on green hydrogen production in Italy and oxygen sale impact on LCOH. *International Journal of Hydrogen Energy*, 137:1042–1055, 2025. doi:10.1016/j.ijhydene.2025.02.247.

[205] L. C. Brée, K. Perrey, A. Bulan, and A. Mitsos. Demand side management and operational mode switching in chlorine production. *AIChE Journal*, 65(7):e16352, 2019. doi:10.1002/aic.16352.

[206] K. Roh, L. C. Brée, K. Perrey, A. Bulan, and A. Mitsos. Flexible operation of switchable chlor-alkali electrolysis for demand side management. *Applied Energy*, 255:113880, 2019. doi:10.1016/j.apenergy.2019.113880.

[207] L. C. Brée, A. Bulan, R. Herding, J. Kuhlmann, A. Mitsos, K. Perrey, and K. Roh. Techno-economic comparison of flexibility options in chlorine production. *Industrial and Engineering Chemistry Research*, 59(26):12186–12196, 2020. doi:10.1021/acs.iecr.0c01775.

[208] K. Roh, L. C. Brée, K. Perrey, A. Bulan, and A. Mitsos. Optimal oversizing and operation of the switchable chlor-alkali electrolyzer for demand side management. In *Computer Aided Chemical Engineering*, volume 46, pages 1771–1776. Elsevier B.V., 2019. doi:10.1016/B978-0-12-818634-3.50296-4.

[209] T. Kato, M. Kubota, N. Kobayashi, and Y. Suzuoki. Effective utilization of by-product oxygen from electrolysis hydrogen production. *Energy*, 30(14):2580–2595, 2005. doi:10.1016/j.energy.2004.07.004.

[210] S. K. Sansaniwal, K. Pal, M. A. Rosen, and S. K. Tyagi. Recent advances in the development of biomass gasification technology: A comprehensive review. *Renewable*

and Sustainable Energy Reviews, 72:363–384, 2017. doi:10.1016/j.rser.2017.01.038.

[211] A. S. Nielsen, M. Ostadi, B. Austbø, M. Hillestad, G. del Alamo, and O. S. Burheim. Enhancing the efficiency of Power- and Biomass-to-Liquid fuel processes using fuel-assisted solid oxide electrolysis cells. *Fuel*, 321:123987, 2022. doi:10.1016/j.fuel.2022.123987.

[212] A.-L. Galvan-Cara and D. Bongartz. Rethinking electrolyzer design for optimal waste-heat utilization. *Applied Energy*, 398:126367, 2025. doi:10.1016/j.apenergy.2025.126367.

[213] S. Quoilin, M. V. D. Broek, S. Declaye, P. Dewallef, and V. Lemort. Techno-economic survey of organic rankine cycle (ORC) systems. *Renewable and Sustainable Energy Reviews*, 22:168–186, 2013. doi:10.1016/j.rser.2013.01.028.

[214] F. Herrmann, M. Grünewald, and J. Riese. Flexibility of Power-to-Gas plants: A case study. *Chemie Ingenieur Technik*, 92(12):1983–1991, 2020. doi:10.1002/cite.202000063.

[215] J. Riese and M. Grünewald. Challenges and opportunities to enhance flexibility in design and operation of chemical processes. *Chemie-Ingenieur-Technik*, 92(12):1887–1897, 2020. doi:10.1002/cite.202000057.

[216] S. Fahr, M. Schiedeck, J. Schwarzhuber, S. Rehfeldt, A. Peschel, and H. Klein. Design and thermodynamic analysis of a large-scale ammonia reactor for increased load flexibility. *Chemical Engineering Journal*, 471:144612, 2023. doi:10.1016/j.cej.2023.144612.

[217] O. Osman, S. Sgouridis, and A. Sleptchenko. Scaling the production of renewable ammonia: A techno-economic optimization applied in regions with high insolation. *Journal of Cleaner Production*, 271:121627, 2020. doi:10.1016/j.jclepro.2020.121627.

[218] J. Li, J. Lin, and Y. Song. Capacity optimization of hydrogen buffer tanks in renewable Power to Ammonia (P2A) system. In *2020 IEEE Power & Energy Society General Meeting (PESGM)*, pages 1–5. IEEE, 2020. doi:10.1109/PESGM41954.2020.9282084.

[219] F. Cherubini and A. H. Stromman. Production of biofuels and biochemicals from lignocellulosic biomass: Estimation of maximum theoretical yields and efficiencies using matrix algebra. *Energy & Fuels*, 24(4):2657–2666, 2010. doi:10.1021/ef901379s.

[220] E. J. Cho, L. T. P. Trinh, Y. Song, Y. G. Lee, and H.-J. Bae. Bioconversion of biomass waste into high value chemicals. *Bioresource Technology*, 298:122386, 2020. doi:10.1016/j.biortech.2019.122386.

[221] A. Voll and W. Marquardt. Reaction network flux analysis: Optimization-based evaluation of reaction pathways for biorenewables processing. *AIChE Journal*, 58(6):1788–1801, 2012. doi:10.1002/aic.12704.

[222] P. Azadi, O. R. Inderwildi, R. Farnood, and D. A. King. Liquid fuels, hydrogen and chemicals from lignin: A critical review. *Renewable and Sustainable Energy Reviews*, 21:506–523, 2013. doi:10.1016/j.rser.2012.12.022.

[223] M. Shahbaz, A. AlNouss, I. Ghiat, G. Mckay, H. Mackey, S. Elkhalifa, and T. Al-Ansari. A comprehensive review of biomass based thermochemical conversion technologies integrated with CO_2 capture and utilisation within BECCS networks. *Resources, Conservation and Recycling*, 173:105734, 2021. doi:10.1016/j.resconrec.2021.105734.

[224] S. M. Perera, C. Wickramasinghe, B. Samarasiri, and M. Narayana. Modeling of thermochemical conversion of waste biomass – A comprehensive review. *Biofuel Research Journal*, 8(4):1481–1528, 2021. doi:10.18331/BRJ2021.8.4.3.

[225] M. Hillestad, M. Ostadi, G. Alamo Serrano, E. Rytter, B. Austbø, J. Pharoah, and O. S. Burheim. Improving carbon efficiency and profitability of the biomass to liquid process with hydrogen from renewable power. *Fuel*, 234:1431–1451, 2018. doi:10.1016/j.fuel.2018.08.004.

[226] M. Dossow, V. Dieterich, A. Hanel, H. Spliethoff, and S. Fendt. Improving carbon efficiency for an advanced Biomass-to-Liquid process using hydrogen and oxygen from electrolysis. *Renewable and Sustainable Energy Reviews*, 152:111670, 2021. doi:10.1016/j.rser.2021.111670.

[227] F. Habermeyer, E. Kurkela, S. Maier, and R.-U. Dietrich. Techno-economic analysis of a flexible process concept for the production of transport fuels and heat from biomass and renewable electricity. *Frontiers in Energy Research*, 9:1–15, 2021. doi:10.3389/fenrg.2021.723774.

[228] L. Wang, C. L. Weller, D. D. Jones, and M. A. Hanna. Contemporary issues in thermal gasification of biomass and its application to electricity and fuel production. *Biomass and Bioenergy*, 32(7):573–581, 2008. doi:10.1016/j.biombioe.2007.12.007.

[229] E. G. Pereira, J. N. Da Silva, J. L. De Oliveira, and C. S. Machado. Sustainable energy: A review of gasification technologies. *Renewable and Sustainable Energy Reviews*, 16(7):4753–4762, 2012. doi:10.1016/j.rser.2012.04.023.

[230] D. Brown, M. Gassner, T. Fuchino, and F. Maréchal. Thermo-economic analysis for the optimal conceptual design of biomass gasification energy conversion systems. *Applied Thermal Engineering*, 29(11-12):2137–2152, 2009. doi:10.1016/j.applthermaleng.2007.06.021.

[231] K. Sandeep and S. Dasappa. First and second law thermodynamic analysis of air and oxy-steam biomass gasification. *International Journal of Hydrogen Energy*, 39(34):19474–19484, 2014. doi:10.1016/j.ijhydene.2014.09.134.

[232] A. Hanel, V. Dieterich, S. Bastek, H. Spliethoff, and S. Fendt. Entrained flow gasification-based Biomass-to-X processes: An energetic and technical evaluation. *Energy Conversion and Management*, 274:116424, 2022. doi:10.1016/j.enconman.2022.116424.

[233] V. Codina Gironès, S. Moret, E. Peduzzi, M. Nasato, and F. Maréchal. Optimal use of biomass in large-scale energy systems: Insights for energy policy. *Energy*, 137:789–797, 2017. doi:10.1016/j.energy.2017.05.027.

[234] B. Todic, T. Bhatelia, G. F. Froment, W. Ma, G. Jacobs, B. H. Davis, and D. B. Bukur. Kinetic model of Fischer-Tropsch synthesis in a slurry reactor on Co-Re/Al_2O_3 catalyst. *Industrial and Engineering Chemistry Research*, 52(2):669–679, 2013. doi:10.1021/ie3028312.

[235] A. de Klerk. *Fischer-Tropsch Refining*. Wiley-VCH Verlag GmbH & Co. KGaA, 2011. doi:10.1002/9783527635603.

[236] A. Elwalily, E. Verkama, F. Mantei, A. Kaliyeva, A. Pounder, J. Sauer, and F. Nestler. Sustainable aviation fuel production via the methanol pathway: a technical review. *Sustainable Energy & Fuels*, 9:5151–5180, 2025. doi:10.1039/D5SE00231A.

[237] S. V. Vassilev, D. Baxter, L. K. Andersen, and C. G. Vassileva. An overview of the chemical composition of biomass. *Fuel*, 89(5):913–933, 2010. doi:10.1016/j.fuel.2009.10.022.

[238] C. Sheng and J. L. Azevedo. Estimating the higher heating value of biomass fuels from basic analysis data. *Biomass and Bioenergy*, 28(5):499–507, 2005. doi:10.1016/j.biombioe.2004.11.008.

[239] A. J. Pimm, T. T. Cockerill, and W. F. Gale. Reducing industrial hydrogen demand through preheating with very high temperature heat pumps. *Applied Energy*, 347:121464, 2023. doi:10.1016/j.apenergy.2023.121464.

[240] E. van der Roest, R. Bol, T. Fens, and A. van Wijk. Utilisation of waste heat from PEM electrolysers – Unlocking local optimisation. *International Journal of Hydrogen Energy*, 48:27872–27891, 2023. doi:10.1016/j.ijhydene.2023.03.374.

[241] G. Bercic and J. Levec. Catalytic dehydration of methanol to dimethyl ether. Kinetic investigation and reactor simulation. *Industrial & Engineering Chemistry Research*, 32(11):2478–2484, 1993. doi:10.1021/ie00023a006.

[242] P. Schmidt, V. Batteiger, A. Roth, W. Weindorf, and T. Raksha. Power-to-Liquids as renewable fuel option for aviation: A review. *Chemie Ingenieur Technik*, 90(1):127–140, 2018. doi:10.1002/cite.201700129.

[243] V. Batteiger, K. Ebner, A. Hebersetzer, L. Moser, P. Schmidt, W. Weindorf, and T. Raksha. Power-to-Liquids: a scalable and sustainable fuel supply perspective for aviation. Technical report, German Environment Agency, 2022. URL: https://www.umweltbundesamt.de/en/publications.

[244] C. Panzone, R. Philippe, A. Chappaz, P. Fongarland, and A. Bengaouer. Power-to-Liquid catalytic CO_2 valorization into fuels and chemicals: focus on the Fischer-Tropsch route. *Journal of CO_2 Utilization*, 38:314–347, 2020. doi:10.1016/j.jcou.2020.02.009.

[245] A. Bernardi, D. B. Casan, A. Symes, and B. Chachuat. Enviro-economic assessment of sustainable aviation fuel production from direct CO_2 hydrogenation. In A. Kokossis, M. C. Georgiadis, and E. N. Pistikopoulos, editors, *33rd European Symposium on Computer Aided Process Engineering*, volume 52 of *Computer Aided Chemical Engineering*, pages 2345–2350. Elsevier Masson SAS, 2023. doi:10.1016/B978-0-443-15274-0.50373-5.

[246] A. Bernardi, D. Danaci, A. Symes, and B. Chachuat. Alternative pathways to sustainable aviation fuel from CO_2 and H_2: An enviro-economic assessment. In F. Manenti and G. V. Reklaitis, editors, *34th European Symposium on Computer Aided Process Engineering / 15th International Symposium on Process Systems Engineering*, volume 53 of *Computer Aided Chemical Engineering*, pages 2149–2154, 2024. doi:10.1016/B978-0-443-28824-1.50359-8.

[247] K. Atsonios, J. Li, and V. J. Inglezakis. Process analysis and comparative assessment of advanced thermochemical pathways for e-kerosene production. *Energy*, 278(A):127868, 2023. doi:10.1016/j.energy.2023.127868.

[248] S. Bube, N. Bullerdiek, S. Voß, and M. Kaltschmitt. Kerosene production from power-based syngas - A technical comparison of the Fischer-Tropsch and methanol pathway. *Fuel*, 366:131269, 2024. doi:10.1016/j.fuel.2024.131269.

[249] F. Habermeyer, J. Weyand, S. Maier, E. Kurkela, and R.-U. Dietrich. Power Biomass to Liquid - An option for Europe's sustainable and independent aviation fuel production. *Biomass Conversion and Biorefinery*, 14:16199–16217, 2023. doi:10.1007/s13399-022-03671-y.

[250] S. Voß, S. Bube, and M. Kaltschmitt. Hybrid biomass- and electricity-based kerosene production - A techno-economic analysis. *Energy and Fuels*, 38(6):5263–5278, 2024. doi:10.1021/acs.energyfuels.3c04876.

[251] ASTM D7566. Standard specification for aviation turbine fuel containing synthesized hydrocarbons [online]. URL: https://www.astm.org/d7566-21.html [last access: 2025-08-28].

[252] ASTM D1655. Standard specification for aviation turbine fuels [online]. URL: https://www.astm.org/d1655-24b.html [last access: 2025-03-14].

[253] T. Lecomte, J. de la Fuente, F. Neuwahl, M. Canova, A. Pinasseau, I. Jankov, T. Brinkmann, S. Roudier, and L. Delgado Sancho. Best available techniques (BAT): Reference document for large combustion plants – Industrial Emissions Directive 2010/75/EU (integrated pollution prevention and control). Technical report, European Commission, 2017. doi:10.2760/949.

[254] L. Strömberg, G. Lindgren, J. Jacoby, R. Giering, M. Anheden, U. Burchhardt, H. Altmann, F. Kluger, and G. N. Stamatelopoulos. Update on Vattenfall's 30 MW_{th} oxyfuel pilot plant in Schwarze Pumpe. *Energy Procedia*, 1:581–589, 2009. doi:10.1016/j.egypro.2009.01.077.

[255] M. F. Santos, S. F. Interlenghi, A. E. Bresciani, N. L. Ferreira, G. S. Bassani, and R. M. de Brito Alves. Modeling and simulation of a PSA process for CO_2/syngas separation. In *33rd European Symposium on Computer Aided Process Engineering*, volume 52 of *Computer Aided Chemical Engineering*, pages 2069–2074. Elsevier B.V., 2023. doi:10.1016/B978-0-443-15274-0.50329-2.

[256] C. Gambaro, V. Calemma, D. Molinari, and J. Denayer. Hydrocracking of Fischer-Tropsch waxes: Kinetic modeling via LHHW approach. *AIChE Journal*, 57(3):711–723, 2011. doi:10.1002/aic.12291.

[257] M. A. Fahim, T. A. Alsahhaf, and A. Elkilani. Chapter 7 - Hydroconversion. In *Fundamentals of Petroleum Refining*, pages 153–198. Elsevier, 2010. doi:10.1016/B978-0-444-52785-1.00007-3.

[258] N. Nesterenko, J. Aguilhon, P. Bodart, D. Minoux, and J. P. Dath. Methanol to olefins: An insight into reaction pathways and products formation. In *Zeolites and Zeolite-like Materials*, pages 189–263. Elsevier Inc., 2016. doi:10.1016/B978-0-444-63506-8.00006-9.

[259] P. L. Spath and D. C. Dayton. Preliminary screening – Technical and economic assessment of synthesis gas to fuels and chemicals with emphasis on the potential for biomass-derived syngas. Technical report, National Renewable Energy Laboratory (NREL), 2003. URL: http://www.osti.gov/servlets/purl/15006100/, doi:10.2172/15006100.

[260] P. Dutta, S. Roy, L. Nandi, P. Samuel, S. M. Pillai, B. Bhat, and M. Ravindranathan. Synthesis of lower olefins from methanol and subsequent conversion of ethylene to higher olefins via oligomerisation. *Journal of Molecular Catalysis A: Chemical*, 223(1-2):231–235, 2004. doi:10.1016/j.molcata.2003.11.043.

[261] W. Monama, E. Mohiuddin, B. Thangaraj, M. M. Mdleleni, and D. Key. Oligomerization of lower olefins to fuel range hydrocarbons over texturally enhanced ZSM-5 catalyst. *Catalysis Today*, 342:167–177, 2020. doi:10.1016/j.cattod.2019.02.061.

[262] M. Díaz, E. Epelde, Z. Tabernilla, A. Ateka, A. T. Aguayo, and J. Bilbao. Operating conditions to maximize clean liquid fuels yield by oligomerization of 1-butene on HZSM-5 zeolite catalysts. *Energy*, 207:118317, 2020. doi:10.1016/j.energy.2020.118317.

[263] M. Cowley. Conversion of n-pentenes over H-ZSM-5. Master's thesis, University of Cape Town, 2002.

[264] K. Brooks, L. Snowden-Swan, S. Jones, M. Butcher, G.-S. Lee, D. Anderson, J. Frye, J. Holladay, J. Owen, L. Harmon, F. Burton, I. Palou-Rivera, J. Plaza, R. Handler, and D. Shonnard. *Low-Carbon Aviation Fuel Through the Alcohol to Jet Pathway.* Elsevier Inc., 2016. doi:10.1016/b978-0-12-804568-8.00006-8.

[265] I. Boumanchar, Y. Chhiti, F. E. M. Alaoui, A. Sahibed-dine, F. Bentiss, C. Jama, and M. Bensitel. Municipal solid waste higher heating value prediction from ultimate analysis using multiple regression and genetic programming techniques. *Waste Management and Research*, 37:578–589, 2019. doi:10.1177/0734242X18816797.

[266] J. Isaksson, A. Åsblad, and T. Berntsson. Pretreatment methods for gasification of biomass and Fischer-Tropsch crude production integrated with a pulp and paper mill. *Clean Technologies and Environmental Policy*, 16(7):1393–1402, 2014. doi:10.1007/s10098-014-0815-7.

[267] E. Monteiro and S. Ferreira. Some perspectives for the gasification process in the energy transition world scenario. *Energies*, 16(14):5543, 2023. doi:10.3390/en16145543.

[268] M. Rezaei, M. Sameti, and F. Nasiri. Biomass-fuelled combined heat and power: integration in district heating and thermal-energy storage. *Clean Energy*, 5(1):44–56, 2021. doi:10.1093/ce/zkaa031.

[269] K. Ulonska, A. König, M. Klatt, A. Mitsos, and J. Viell. Optimization of multi-product biorefinery processes under consideration of biomass supply chain management and market developments. *Industrial and Engineering Chemistry Research*, 57(20):6980–6991, 2018. doi:10.1021/acs.iecr.8b00245.

[270] Y. Gao, M. Wang, A. Raheem, F. Wang, J. Wei, D. Xu, X. Song, W. Bao, A. Huang, S. Zhang, and H. Zhang. Syngas production from biomass gasification: Influences of feedstock properties, reactor type, and reaction parameters. *ACS Omega*, 8(35):31620–31631, 2023. doi:10.1021/acsomega.3c03050.

[271] M. Asadullah. Biomass gasification gas cleaning for downstream applications: A comparative critical review. *Renewable and Sustainable Energy Reviews*, 40:118–132, 2014. doi:10.1016/j.rser.2014.07.132.

[272] N. Yesilova, O. Tezer, A. Ongen, and A. Ayol. Enhancing biomass gasification: A comparative study of catalyst applications in updraft and modifiable-downdraft fixed bed reactors. *International Journal of Hydrogen Energy*, 2024. doi:10.1016/j.ijhydene.2024.05.075.

[273] A. Bridgwater, A. Toft, and J. Brammer. A techno-economic comparison of power production by biomass fast pyrolysis with gasification and combustion. *Renewable and Sustainable Energy Reviews*, 6(3):181–246, 2002. doi:10.1016/S1364-0321(01)00010-7.

[274] G. Graaf, E. Stamhuis, and A. Beenackers. Kinetics of low-pressure methanol synthesis. *Chemical Engineering Science*, 43:3185–3195, 1988. doi:10.1016/0009-2509(88)85127-3.

[275] Global Petrol Prices. Kerosene prices [online]. URL: https://www.globalpetrolprices.com/kerosene_prices/ [last access: 12.03.2026].

[276] International Renewable Energy Agency (IRENA). *Future of Solar Photovoltaic: Deployment, investment, technology, grid integration and socio-economic aspects*. Abu Dhabi, 2019. URL: https://www.irena.org/publications/2019/Nov/Future-of-Solar-Photovoltaic.

[277] International Renewable Energy Agency (IRENA). *Future of Wind: Deployment, investment, technology, grid integration and socio-economic aspects*. Abu Dhabi, 2019. URL: https://www.irena.org/publications/2019/Oct/Future-of-wind.

[278] P. Schäfer, T. M. Daun, and A. Mitsos. Do investments in flexibility enhance sustainability? a simulative study considering the German electricity sector. *AIChE Journal*, 66:1–14, 2020. doi:10.1002/aic.17010.

[279] L. Valverde, C. Bordons, and F. Rosa. Integration of fuel cell technologies in renewable-energy-based microgrids optimizing operational costs and durability. *IEEE Transactions on Industrial Electronics*, 63(1):167–177, 2016. doi:10.1109/TIE.2015.2465355.

[280] A. Allman, M. J. Palys, and P. Daoutidis. Scheduling-informed optimal design of systems with time-varying operation: A wind-powered ammonia case study. *AIChE Journal*, 65(7):e16434, 2019. doi:10.1002/aic.16434.

[281] C. Chen, A. Yang, and R. Bañares-Alcántara. Renewable methanol production: Understanding the interplay between storage sizing, renewable mix and dispatchable energy price. *Advances in Applied Energy*, 2:100021, 2021. doi:10.1016/j.adapen.2021.100021.

[282] A. Khajavirad and N. V. Sahinidis. A hybrid LP/NLP paradigm for global optimization relaxations. *Mathematical Programming Computation*, 10:383–421, 2018. doi:10.1007/s12532-018-0138-5.

[283] S. Schulte Beerbühl, M. Fröhling, and F. Schultmann. Combined scheduling and capacity planning of electricity-based ammonia production to integrate renewable energies. *European Journal of Operational Research*, 241(3):851–862, 2015. doi:10.1016/j.ejor.2014.08.039.

[284] A. Allman and P. Daoutidis. Optimal scheduling for wind-powered ammonia generation: Effects of key design parameters. *Chemical Engineering Research and Design*, 131:5–15, 2018. doi:10.1016/j.cherd.2017.10.010.

[285] International Energy Agency (IEA). *World energy outlook 2021*. Paris, 2021.

[286] M.-R. Tahan. Recent advances in hydrogen compressors for use in large-scale renewable energy integration. *International Journal of Hydrogen Energy*, 47(83):35275–35292, 2022. doi:10.1016/j.ijhydene.2022.08.128.

[287] R. Moradi and K. M. Groth. Hydrogen storage and delivery: Review of the state of the art technologies and risk and reliability analysis. *International Journal of Hydrogen Energy*, 44(23):12254–12269, 2019. doi:10.1016/j.ijhydene.2019.03.041.

[288] A. M. Elberry, J. Thakur, A. Santasalo-Aarnio, and M. Larmi. Large-scale compressed hydrogen storage as part of renewable electricity storage systems. *International Journal of Hydrogen Energy*, 46(29):15671–15690, 2021. doi:10.1016/j.ijhydene.2021.02.080.

[289] M. Hirscher. *Handbook of Hydrogen Storage*. Wiley-VCH Verlag GmbH & Co. KGaA, Weinheim, Germany, 2010. doi:10.1002/9783527629800.

[290] X. Cui, S. K. Kær, and M. P. Nielsen. Energy analysis and surrogate modeling for the green methanol production under dynamic operating conditions. *Fuel*, 307:121924, 2022. doi:10.1016/j.fuel.2021.121924.

[291] A. Gonzalez-Castellanos, D. Pozo, and A. Bischi. Detailed Li-ion battery characterization model for economic operation. *International Journal of Electrical Power & Energy Systems*, 116:105561, 2020. doi:10.1016/j.ijepes.2019.105561.

[292] C. Maxwell. Cost Indices [online]. 2024. URL: https://toweringskills.com/financial-analysis/cost-indices/ [last access: 25.09.2024].

[293] L. Järvinen, P. Puranen, A. Kosonen, V. Ruuskanen, J. Ahola, P. Kauranen, and M. Hehemann. Automized parametrization of PEM and alkaline water electrolyzer polarisation curves. *International Journal of Hydrogen Energy*, 47(75):31985–32003, 2022. doi:10.1016/j.ijhydene.2022.07.085.

[294] L. T. Biegler, I. E. Grossmann, and A. W. Westerberg. *Systematic Methods of Chemical Process Design*. Prentice Hall PTR, 1997.

[295] Y. He, H. Chen, Y. Xu, and J. Deng. Compression performance optimization considering variable charge pressure in an adiabatic compressed air energy storage system. *Energy*, pages 349–359, 2018. doi:10.1016/j.energy.2018.09.168.

[296] R. G. Frank, C. Wacker, and R. Niehuis. Loss characterization of advanced VIGV configurations with adjustable blade geometry. *Journal of Turbomachinery*, 144(3):031012, 2022. doi:10.1115/1.4052409.

[297] M. Hoffmann, L. Kotzur, D. Stolten, and M. Robinius. A review on time series aggregation methods for energy system models. *Energies*, 13:641, 2020. doi:10.3390/en13030641.

[298] P. Schäfer, A. M. Schweidtmann, P. H. Lenz, H. M. Markgraf, and A. Mitsos. Wavelet-based grid-adaptation for nonlinear scheduling subject to time-variable electricity prices. *Computers & Chemical Engineering*, 132:106598, 2020. doi:10.1016/j.compchemeng.2019.106598.

[299] ENTSO-E Transparency Platform. Electricity price profiles [online]. 2024. URL: https://transparency.entsoe.eu/dashboard/show [last access: 30.09.2024].

[300] BDEW Bundesverband der Energie- und Wasserwirtschaft. Strompreisanalyse Juli 2025 [online]. URL: https://www.bdew.de/service/daten-und-grafiken/bdew-strompreisanalyse/ [last access: 2025-09-28].

[301] International Renewable Energy Agency (IRENA). *Renewable power generation costs in 2021*. Abu Dhabi, 2022. URL: https://www.irena.org/-/media/Files/IRENA/Agency/Publication/2018/Jan/IRENA_2017_Power_Costs_2018.pdf.

[302] International Renewable Energy Agency (IRENA) and Methanol Institute. *Innovation outlook: Renewable methanol*. Abu Dhabi, 2021.

[303] M. Bai, S. Liu, M. Qi, M. Kim, S. Liu, I. Moon, and W. Feng. A novel multi-period proactive flexible load management strategy for low-cost off-grid green methanol production. *Energy*, 320:135446, 2025. doi:10.1016/j.energy.2025.135446.

[304] A. Caspari, C. Offermanns, P. Schäfer, A. Mhamdi, and A. Mitsos. A flexible air separation process: 2. Optimal operation using economic model predictive control. *AIChE Journal*, 65(11), 2019. doi:10.1002/aic.16721.

[305] IMARC. Methanol Price Trend, Index and Forecast [online]. URL: https://www.imarcgroup.com/methanol-pricing-report [last access: 02.03.2026].

[306] S. Sollai, A. Porcu, V. Tola, F. Ferrara, and A. Pettinau. Renewable methanol production from green hydrogen and captured CO_2: A techno-economic assessment. *Journal of CO_2 Utilization*, 68:102345, 2023. doi:10.1016/j.jcou.2022.102345.

[307] F. Kunz and A. Zerrahn. Benefits of coordinating congestion management in electricity transmission networks: Theory and application to Germany. *Utilities Policy*, 37:34–45, 2015. doi:10.1016/j.jup.2015.09.009.

[308] P. Schäfer, H. G. Westerholt, A. M. Schweidtmann, S. Ilieva, and A. Mitsos. Model-based bidding strategies on the primary balancing market for energy-intense processes. *Computers & Chemical Engineering*, 120:4–14, 2019. doi:10.1016/j.compchemeng.2018.09.026.

[309] P. Schäfer, N. Hansmann, S. Ilieva, and A. Mitsos. Model-based bidding strategies for simultaneous optimal participation in different balancing markets. *Computer Aided Chemical Engineering*, 46:1639–1644, 2019. doi:10.1016/B978-0-12-818634-3.50274-5.

[310] M. Taslimi and A. Khosravi. Flexibility and profitability in Power-to-Methanol plants: Integrating storage solutions and reserve market participation. *Energy*, 327:136438, 2025. doi:10.1016/j.energy.2025.136438.

[311] C. Papadimitriou, J. C. Schulze, and A. Mitsos. A practical scenario generation method for electricity prices on day-ahead and intraday spot markets. *Computers & Chemical Engineering*, 199:109118, 2025. doi:10.1016/j.compchemeng.2025.109118.

[312] J. R. Birge and F. Louveaux. *Introduction to Stochastic Optimization*. Springer New York, 2011. doi:10.1007/978-1-4614-0237-4.

[313] A. J. Conejo, M. Carrión, and J. M. Morales. Stochastic Programming Fundamentals. In *International Series in Operations Research and Management Science*, volume 153, pages 27–62. Springer New York LLC, 2010. doi:10.1007/978-1-4419-7421-1_2.

[314] C. Li and I. E. Grossmann. A review of stochastic programming methods for optimization of process systems under uncertainty. *Frontiers in Chemical Engineering*, 2, 2021. doi:10.3389/fceng.2020.622241.

[315] L. A. Roald, D. Pozo, A. Papavasiliou, D. K. Molzahn, J. Kazempour, and A. Conejo. Power systems optimization under uncertainty: A review of methods and applications. *Electric Power Systems Research*, 214:108725, 2023. doi:10.1016/j.epsr.2022.108725.

[316] D. Han and J. H. Lee. Two-stage stochastic programming formulation for optimal design and operation of multi-microgrid system using data-based modeling of renewable energy sources. *Applied Energy*, 291:116830, 2021. doi:10.1016/j.apenergy.2021.116830.

[317] C. Li, D. E. Bernal, K. C. Furman, M. A. Duran, and I. E. Grossmann. Sample average approximation for stochastic nonconvex mixed integer nonlinear programming via outer-approximation. *Optimization and Engineering*, 22:1245–1273, 2021. doi:10.1007/s11081-020-09563-2.

[318] J. J. Torres, C. Li, R. M. Apap, and I. E. Grossmann. A review on the performance of linear and mixed integer two-stage stochastic programming software. *Algorithms*, 15:103, 2022. doi:10.3390/a15040103.

[319] X. Li, A. Tomasgard, and P. I. Barton. Nonconvex generalized Benders decomposition for stochastic separable mixed-integer nonlinear programs. *Journal of Optimization Theory and Applications*, 151:425–454, 2011. doi:10.1007/s10957-011-9888-1.

[320] R. Rahmaniani, T. G. Crainic, M. Gendreau, and W. Rei. Accelerating the Benders decomposition method: Application to stochastic network design problems. *SIAM Journal on Optimization*, 28:875–903, 2018. doi:10.1137/17M1128204.

[321] F. García-Muñoz, S. Dávila, and F. Quezada. A Benders decomposition approach for solving a two-stage local energy market problem under uncertainty. *Applied Energy*, 329:120226, 2023. doi:10.1016/j.apenergy.2022.120226.

[322] M. Langiu, M. Dahmen, D. Bongartz, and A. Mitsos. MUSE-BB: A decomposition algorithm for nonconvex two-stage problems using strong multisection branching. *Journal of Global Optimization*, 92:837–888, 2025. doi:10.1007/s10898-025-01489-2.

[323] H. Zhang, I. E. Grossmann, and A. Tomasgard. Decomposition methods for multi-horizon stochastic programming. *Computational Management Science*, 21:1–24, 2024. doi:10.1007/s10287-024-00509-y.

[324] P. Liu, E. N. Pistikopoulos, and Z. Li. Decomposition based stochastic programming approach for polygeneration energy systems design under uncertainty. *Industrial and Engineering Chemistry Research*, 49:3295–3305, 2010. doi:10.1021/ie901490g.

[325] T. Heo, D. S. Mallapragada, and R. Macdonald. A decomposition algorithm using multiple linear approximations to solve integrated design and scheduling optimization frameworks — Case study of nuclear based co-production of electricity and hydrogen. *Computers & Chemical Engineering*, 202:109213, 2025. doi:10.1016/j.compchemeng.2025.109213.

[326] N. Baumgärtner, F. Temme, M. Hennen, B. Bahl, D. Hollermann, and A. Bardow. RiSES^4 rigorous synthesis of energy supply systems with seasonal storage by relaxation and time-series aggregation to typical periods. In *Proceedings of ECOS 2019 - The 32nd international conference on efficiency, cost, optimization, simulation and environmental impact of energy systems*, pages 263–274, Wroclaw, Poland, 2019.

[327] Y. Wang, M. Volkmer, D. F. Hagedorn, C. Reinert, and N. von der Assen. RiNSES^4: Rigorous nonlinear synthesis of energy systems for seasonal energy supply and storage. In *Proceedings of the 10th International Conference on Foundations of Computer-Aided Process Design FOCAPD 2024*, volume 3, pages 604–611, 2024. doi:10.69997/sct.105466.

[328] E. Raheli, Y. Werner, and J. Kazempour. A conic model for electrolyzer scheduling. *Computers & Chemical Engineering*, 179:108450, 2023. doi:10.1016/j.compchemeng.2023.108450.

[329] M. Martín. Methodology for solar and wind energy chemical storage facilities design under uncertainty: Methanol production from CO_2 and hydrogen. *Computers & Chemical Engineering*, 92:43–54, 2016. doi:10.1016/j.compchemeng.2016.05.001.

[330] A. Maggi, J. Bremer, and K. Sundmacher. Multi-period optimization for the design and operation of a flexible Power-to-Methanol process. *Chemical Engineering Science*, 281:119202, 2023. doi:10.1016/j.ces.2023.119202.

[331] B. Bahl, T. Söhler, M. Hennen, and A. Bardow. Typical periods for two-stage synthesis by time-series aggregation with bounded error in objective function. *Frontiers in Energy Research*, 5:35, 2018. doi:10.3389/fenrg.2017.00035.

[332] L. Kotzur, P. Markewitz, M. Robinius, and D. Stolten. Impact of different time series aggregation methods on optimal energy system design. *Renewable Energy*, 117:474–487, 2018. doi:10.1016/j.renene.2017.10.017.

[333] H. Zebian and A. Mitsos. Pressurized oxy-coal combustion: Ideally flexible to uncertainties. *Energy*, 57:513–526, 2013. doi:10.1016/j.energy.2013.05.026.

[334] N. Baumgärtner, B. Bahl, M. Hennen, and A. Bardow. RiSES^3: Rigorous synthesis of energy supply and storage systems via time-series relaxation and aggregation. *Computers & Chemical Engineering*, 127:127–139, 2019. doi:10.1016/j.compchemeng.2019.02.006.

[335] J. H. Merrick. On representation of temporal variability in electricity capacity planning models. *Energy Economics*, 59:261–274, 2016. doi:10.1016/j.eneco.2016.08.001.

[336] X. Deng, L. Kang, and C. D. Lin. Design of experiments for emulations: A selective review from a modeling perspective. *arXiv*, 8 2025. doi:10.48550/arXiv.2505.09596.

[337] Liu, Shen. Distance correlation function [online]. URL: https://www.mathworks.com/matlabcentral/fileexchange/39905-distance-correlation [last access: 24.09.2025].

[338] P. Schäfer, A. M. Schweidtmann, P. H. Lenz, H. M. Markgraf, and A. Mitsos. Wavelet-based grid-adaptation for nonlinear scheduling subject to time-variable electricity prices. *Computers & Chemical Engineering*, 132:106598, 2020. doi:10.1016/j.compchemeng.2019.106598.

[339] Y. Cao, C. L. Swartz, and J. Flores-Cerrillo. Optimal dynamic operation of a high-purity air separation plant under varying market conditions. *Industrial and Engineering Chemistry Research*, 55(37):9956–9970, 2016. doi:10.1021/acs.iecr.6b02090.

[340] R. Karuppiah, M. Martín, and I. E. Grossmann. A simple heuristic for reducing the number of scenarios in two-stage stochastic programming. *Computers & Chemical Engineering*, 34:1246–1255, 8 2010. doi:10.1016/j.compchemeng.2009.10.009.

[341] A. Belderbos and E. Delarue. Accounting for flexibility in power system planning with renewables. *International Journal of Electrical Power & Energy Systems*, 71:33–41, 10 2015. doi:10.1016/j.ijepes.2015.02.033.

[342] K. Poncelet, H. Hoschle, E. Delarue, A. Virag, and W. D'haeseleer. Selecting representative days for capturing the implications of integrating intermittent renewables in generation expansion planning problems. *IEEE Transactions on Power Systems*, 32:1936–1948, 5 2017. doi:10.1109/TPWRS.2016.2596803.

[343] F. J. De Sisternes and M. D. Webster. ESD working paper series: Optimal selection of sample weeks for approximating the net load in generation planning problems, 2013. URL: http://hdl.handle.net/1721.1/102959.

[344] H. Teichgraeber and A. R. Brandt. Clustering methods to find representative periods for the optimization of energy systems: An initial framework and comparison. *Applied Energy*, 239:1283–1293, 4 2019. doi:10.1016/j.apenergy.2019.02.012.

[345] S. Pfenninger. Dealing with multiple decades of hourly wind and PV time series in energy models: A comparison of methods to reduce time resolution and the planning implications of inter-annual variability. *Applied Energy*, 197:1–13, 2017. doi:10.1016/j.apenergy.2017.03.051.

[346] Y. Zhang, V. Cheng, D. S. Mallapragada, J. Song, and G. He. A model-adaptive clustering-based time aggregation method for low-carbon energy system optimization. *IEEE Transactions on Sustainable Energy*, 14(1):55–64, 2023. doi:10.1109/TSTE.2022.3199571.

[347] J. Hu and H. Li. A new clustering approach for scenario reduction in multi-stochastic variable programming. *IEEE Transactions on Power Systems*, 34:3813–3825, 9 2019. doi:10.1109/TPWRS.2019.2901545.

[348] H. Heitsch and W. Römisch. Scenario reduction algorithms in stochastic programming. *Computational Optimization and Applications*, 24:187–206, 2003. doi:10.1023/A:1021805924152.

[349] J. Dupačová, N. Gröwe-Kuska, and W. Römisch. Scenario reduction in stochastic programming an approach using probability metrics. *Mathematical Programming, Series B*, 95:493–511, 3 2003. doi:10.1007/s10107-002-0331-0.

[350] H. Heitsch and W. Römisch. Scenario tree reduction for multistage stochastic programs. *Computational Management Science*, 6:117–133, 5 2009. doi:10.1007/s10287-008-0087-y.

[351] K. Bruninx and E. Delarue. Scenario reduction techniques and solution stability for stochastic unit commitment problems. In *2016 IEEE International Energy Conference (ENERGYCON)*, pages 1–7. IEEE, 4 2016. doi:10.1109/ENERGYCON.2016.7514074.

[352] S. H. Germscheid, A. Mitsos, and M. Dahmen. Scenario reduction methods for risk-averse demand response scheduling under price uncertainty. *Computer Aided Chemical Engineering*, 53:3223–3228, 2024. doi:10.1016/B978-0-443-28824-1.50538-X.

[353] A. Almaimouni, A. Ademola-Idowu, J. N. Kutz, A. Negash, and D. Kirschen. Selecting and evaluating representative days for generation expansion planning. In *Power Systems Computation Conference (PSCC)*, pages 1–7. IEEE, 6 2018. doi:10.23919/PSCC.2018.8442580.

[354] Y. Dvorkin, Y. Wang, H. Pandzic, and D. Kirschen. Comparison of scenario reduction techniques for the stochastic unit commitment. In *2014 IEEE PES General Meeting | Conference & Exposition*, pages 1–5. IEEE, 2014. doi:10.1109/PESGM.2014.6939042.

[355] N. Helistö, J. Kiviluoma, and H. Reittu. Selection of representative slices for generation expansion planning using regular decomposition. *Energy*, 211:118585, 11 2020. doi:10.1016/j.energy.2020.118585.

[356] A. Y. Raya-Tapia, F. J. López-Flores, J. Tovar-Facio, and J. M. Ponce-Ortega. Comparative framework of representative weeks selection methods for the optimization of power systems. *Computers & Chemical Engineering*, 194:108985, 3 2025. doi:10.1016/j.compchemeng.2024.108985.

[357] T. Warren Liao. Clustering of time series data - a survey. *Pattern Recognition*, 38:1857–1874, 2005. doi:10.1016/j.patcog.2005.01.025.

[358] K. Phillips. *Efficiently capturing spatio-temporal variability in power system planning models*. Ph.D. thesis, KU Leuven, Belgium, 2024.

[359] M. Sun, F. Teng, X. Zhang, G. Strbac, and D. Pudjianto. Data-driven representative day selection for investment decisions: A cost-oriented approach. *IEEE Transactions on Power Systems*, 34(4):2925–2936, 2019. doi:10.1109/TPWRS.2019.2892619.

[360] B. Jürgens, H. Seele, H. Schricker, C. Reinert, and N. von der Assen. Decision-based vs. distribution-driven clustering for stochastic energy system design optimization. *ArXiv*, 7 2024. URL: `http://arxiv.org/abs/2407.11457`.

[361] M. Barandas, D. Folgado, L. Fernandes, S. Santos, M. Abreu, P. Bota, H. Liu, T. Schultz, and H. Gamboa. TSFEL: Time Series Feature Extraction Library. *SoftwareX*, 11:100456, 2020. `doi:10.1016/j.softx.2020.100456`.

[362] D. Bongartz and A. Mitsos. Deterministic global optimization of process flowsheets in a reduced space using McCormick relaxations. *Journal of Global Optimization*, 69:761–796, 2017. `doi:10.1007/s10898-017-0547-4`.

[363] H. Teichgraeber, C. P. Lindenmeyer, N. Baumgärtner, L. Kotzur, D. Stolten, M. Robinius, A. Bardow, and A. R. Brandt. Extreme events in time series aggregation: A case study for optimal residential energy supply systems. *Applied Energy*, 275(1):115223, 2020. `doi:10.1016/j.apenergy.2020.115223`.

[364] P. Schäfer, A. M. Schweidtmann, and A. Mitsos. Nonlinear scheduling with time-variable electricity prices using sensitivity-based truncations of wavelet transforms. *AIChE Journal*, 66, 2020. `doi:10.1002/aic.16986`.

[365] C. Papadimitriou, T. Varelmann, C. Schröder, A. Jupke, and A. Mitsos. Globally optimal scheduling of an electrochemical process via data-driven dynamic modeling and wavelet-based adaptive grid refinement. *Optimization and Engineering*, 25:1719–1757, 2023. `doi:10.1007/s11081-023-09860-6`.

[366] T. Karia. *Tailored formulations to accelerate deterministic global optimisation of mixed-integer nonlinear programs*. Ph.D. thesis, Imperial College London, United Kingdom, November 2024.

[367] N. Baumgärtner, B. Bahl, M. Hennen, and A. Bardow. RiSES^3: Rigorous synthesis of energy supply and storage systems via time-series relaxation and aggregation. *Computers & Chemical Engineering*, 127:127–139, 2019. `doi:10.1016/j.compchemeng.2019.02.006`.

[368] F. Neumann and T. Brown. The near-optimal feasible space of a renewable power system model. *Electric Power Systems Research*, 190:106690, 2021. `doi:10.1016/j.epsr.2020.106690`.

[369] EPEX Spot. 15-minute products in Market Coupling [online]. URL: `https://www.epexspot.com/en/15-minute-products-market-coupling#regulatory-framework` [last access: 2025-09-28].

[370] T. J. Kotas. *The Exergy Method of Thermal Plant Analysis*. Krieger Publishing Company, 1995.

[371] G. Lopez, M. Artetxe, M. Amutio, J. Alvarez, J. Bilbao, and M. Olazar. Recent advances in the gasification of waste plastics. A critical overview. *Renewable and Sustainable Energy Reviews*, 82:576–596, 2018. `doi:10.1016/j.rser.2017.09.032`.

[372] B. Raho, G. Colangelo, M. Milanese, and A. de Risi. A critical analysis of the oxy-combustion process: From mathematical models to combustion product analysis. *Energies*, 15(18):6514, 2022. doi:10.3390/en15186514.

[373] T. Lecomte, J. F. F. de la Fuente, F. Neuwahl, M. Canova, A. Pinasseau, I. Jankov, T. Brinkmann, S. Roudier, and L. D. Sancho. Best available techniques (BAT) reference document for large combustion plants. Technical report, Publications Office of the European Union, 2017. URL: https://eippcb.jrc.ec.europa.eu/sites/default/files/2019-11/JRC_107769_LCPBref_2017.pdf, doi:10.2760/949.

[374] J. Deng, X. Wang, Z. Wei, L. Wang, C. Wang, and Z. Chen. A review of NO_x and SO_x emission reduction technologies for marine diesel engines and the potential evaluation of liquefied natural gas fuelled vessels. *Science of The Total Environment*, 766:144319, 2021. doi:10.1016/j.scitotenv.2020.144319.

[375] K. M. Vanden Bussche and G. F. Froment. A steady-state kinetic model for methanol synthesis and the water gas shift reaction on a commercial $Cu/ZnO/Al_2O_3$. *Journal of Catalysis*, 161(1):1–10, 1996. doi:10.1006/jcat.1996.0156.

[376] F. Vidal Vázquez, P. Pfeifer, J. Lehtonen, P. Piermartini, P. Simell, and V. Alopaeus. Catalyst screening and kinetic modeling for CO production by high pressure and temperature reverse water gas shift for Fischer-Tropsch applications. *Industrial and Engineering Chemistry Research*, 56(45):13262–13272, 2017. doi:10.1021/acs.iecr.7b01606.

[377] Álvaro A. Ramírez-Santos, C. Castel, and E. Favre. Utilization of blast furnace flue gas: Opportunities and challenges for polymeric membrane gas separation processes. *Journal of Membrane Science*, 526:191–204, 2017. doi:10.1016/j.memsci.2016.12.033.

[378] M. M. F. Hasan, R. C. Baliban, J. A. Elia, and C. A. Floudas. Modeling, simulation, and optimization of postcombustion CO_2 capture for variable feed concentration and flow rate. 1. chemical absorption and membrane processes. *Industrial & Engineering Chemistry Research*, 51(48):15642–15664, 2012. URL: https://pubs.acs.org/doi/10.1021/ie301571d, doi:10.1021/ie301571d.

[379] U.S. Department of energy (DOE). Technical targets for hydrogen delivery [online]. URL: https://www.energy.gov/eere/fuelcells/doe-technical-targets-hydrogen-delivery [last access: 2023-05-19].

[380] K. Guthrie. Data and techniques for preliminary capital cost estimating. *Chemical Engineering*, 3:114–142, 1969.

[381] ADI Analytics LLC, Houston, Texas. Natural gas utilization via small scale methanol technologies [online]. 2015. URL: http://www.sgicc.org/uploads/8/4/3/1/8431164/bftp_methanol_white_paper_vf.pdf [last access: 2023-07-19].

[382] International Energy Agency (IEA). World energy outlook 2023. Technical report, Paris, 2023. URL: https://www.iea.org/reports/world-energy-outlook-2023.